Conception et mise en oeuvre de méthodes vortex hybrides-frontières immergées pour des milieux solides-fluides-poreux. Application au contrôle passif d'écoulements.

Chloé Mimeau

UNIVERSITÉ DE GRENOBLE

THÈSE

Pour obtenir le grade de

DOCTEUR DE L'UNIVERSITÉ DE GRENOBLE

Spécialité : **Mathématiques Appliquées**

Arrêté ministériel : 7 aout 2006

Présentée par

Chloé Mimeau

Thèse dirigée par **Georges-Henri Cottet**
et codirigée par **Iraj Mortazavi**

préparée au sein du **Laboratoire Jean Kuntzmann**
et de **École Doctorale Mathématiques, Sciences et Technologies de l'Information, Informatique**

Conception and implementation of a hybrid vortex penalization method for solid-fluid-porous media: application to the passive control of incompressible flows

Thèse soutenue publiquement le **7 juillet 2015** ,
devant le jury composé de :

M. Serge Huberson
Professeur, Université de Poitiers, Président
M. Richard Pasquetti
Directeur de Recherche CNRS, Université de Nice Sophia-Antipolis, Rapporteur
M. Roberto Verzicco
Professeur, Université de Rome "Tor Vergata", Rapporteur
Mme Heloïse Beaugendre
Maître de conférence, Université Bordeaux 1, Examinatrice
Mme Stéfania Cherubini
Maître de conférence, Arts et Métiers ParisTech, Examinatrice
M. Petros Koumoutsakos
Professeur, ETH Zürich, Examinateur
M. Georges-Henri Cottet
Professeur, Université Joseph Fourier, Directeur de thèse
M. Iraj Mortazavi
Professeur, Centre National des Arts et Métiers, Co-Directeur de thèse
M. Federico Galizzio
Docteur, OPTIMAD Engineering Srl, Invité

Conception and implementation of a hybrid vortex penalization method for solid-fluid-porous media: application to the passive control of incompressible flows

Thèse présentée et soutenue publiquement par :

Chloé Mimeau

le 7 juillet 2015

Composition du jury :

Président :
Serge Huberson,
Professeur, Université de Poitiers

Rapporteurs :
Richard Pasquetti,
Directeur de Recherche CNRS, Université de Nice Sophia-Antipolis
Roberto Verzicco,
Professeur, Université de Rome "Tor Vergata"

Examinateurs :
Heloïse Beaugendre,
Maître de conférence, Université Bordeaux 1
Stéfania Cherubini,
Maître de conférence, Arts et Métiers ParisTech
Petros Koumoutsakos,
Professeur, ETH Zürich
Georges-Henri Cottet,
Professeur, Université Joseph Fourier (Directeur de thèse)
Iraj Mortazavi,
Professeur, Centre National des Arts et Métiers (Co-directeur de thèse)

Invité :
Federico Galizzio,
Docteur, OPTIMAD Engineering Srl

Thèse préparée au sein du Laboratoire Jean Kuntzmann
et de l'école doctorale MSTII : Mathémaiques, Sciences
et Technologies de l'Information, Informatique.

Remerciements

Je tiens en premier lieu à remercier mes deux rapporteurs, Richard Pasquetti et Roberto Verzicco pour leur lecture très attentive de mes travaux ainsi que pour leurs nombreuses remarques et recommandations.

Tout au long de ces années de thèse, j'ai eu l'occasion d'interagir avec de nombreuses personnes dont l'aide et les conseils ont pleinement participé à la construction de ce travail et à son aboutissement. Parmi ces personnes je souhaite tout d'abord remercier Federico Gallizio qui en me transmettant son code de calcul m'a fourni une base robuste pour les débuts de cette thèse. Federico est une personne avec qui j'ai pris beaucoup de plaisir à collaborer durant ces années de par sa grande disponibilité, sa rigueur scientifique et sa gentillesse.

Je remercie également très chaleureusement tous les membres du groupe de travail du LJK : Christophe, Franck, Eric, Jean-Baptiste et Jean-Matthieu. Les nombreuses heures de discussions passées en salle 46 de la tour IRMA ont eu un rôle prépondérant dans l'avancée de cette thèse. Je remercie tout particulièrement Franck et Christophe pour le temps précieux qu'ils ont accordé à la relecture minutieuse de mon manuscrit et Jean-Matthieu pour avoir toujours pris le temps de répondre clairement et pédagogiquement aux multiples questions de sa co-bureau !

Dans le cadre de ma co-direction j'ai également eu la chance d'échanger longuement avec nombre de mes anciens professeurs de l'Institut de Mathématiques de Bordeaux. Parmi eux je remercie Lisl Weynans, Michel Bergmann, Angelo Iollo, Charles-Henri Bruneau et surtout Heloïse Beaugendre qui m'a été d'une grande aide en cette fin de thèse. Un grand merci également aux doctorants Florian, Guillaume, Alexia, Étienne, Michaël et Yoann avec qui j'ai passé d'excellents moments lors de mes nombreuses visites à l'IMB.

Je tiens aussi à remercier Petros Koumoutsakos de l'ETH Zürich ainsi que ses étudiants Mattia, Wim et Christian avec qui j'ai pris grand plaisir à continuer de collaborer suite à mon stage de master au CSE lab. Leurs travaux représentent pour moi d'inconditionnelles références.

Enfin, c'est au CNAM que j'ai eu plus récemment l'opportunité de rencontrer de brillants chercheurs. Je remercie tout particulièrement Amélie Danlos et ses étudiants Renaud et Vincent pour leur immense efficacité dans la mise en œuvre d'un dispositif expérimental capable de reproduire les études menées numériquement dans cette thèse concernant le contrôle passif avec l'ajout d'une couche poreuse.

Je termine ce paragraphe dédié aux personnes avec qui j'ai eu le plaisir de collaborer en mentionnant les enseignants qui m'ont épaulé au cours de mon service d'enseignement à l'UJF et à l'UPMF. Je suis en particulier très reconnaissante envers Benoît Kloeckner, Remi Drouilhet et Jean-François Coeurjolly.

Au sein du LJK, la liste des personnes à citer est également conséquente. Tout d'abord, je remercie tout le personnel ITA qui s'illustre au quotidien par sa véritable efficacité. J'accorde une mention particulière à mes deux assistantes d'équipe Juana et Laurence qui ont toujours fait preuve d'une grande amabilité et d'un véritable dynamisme malgré les nombreuses irruptions dans leur bureau pour établir des ordres de missions !

Un grand merci bien-entendu à l'ensemble de l'équipe du service informatique que j'ai beaucoup sollicitée au cours de cette thèse et qui a toujours su répondre à mes besoins en des temps record, en particulier Franck, Fred, Caroline, Patrice, Bruno et Bruno (!).

Mes derniers remerciements « ljkaïens » se dirigent naturellement vers tous les doctorants/-postdoc/ingénieurs sans qui mon séjour grenoblois n'aurait jamais été aussi intéressant, lumineux et festif : Jean-Matthieu, Thomas, Madison, Samuel, Berti, Euriell, Roland, Amin, Kolé, Abdoulaye, Mahamar, Pierre-Yves, Jean-Yves, Gaëlle, Alexandre J., Jérémie, Gilles, Lukàs, Morgane, Romain, Kevin, Federico Z., Federico P., Charles, Rémi, Sevkan, Nelson, Margaux, Roland P., Olivier, Noé, Pierre-Jean, Jean-Baptiste, Alexandre H., Ester, Cécile, Charlotte, Pierre, Burak, Adrien, Abdel, Dmitri, Chi, Meriem (à qui je fais dans cette parenthèse une petite mention

spéciale pour ne pas la contrarier mais aussi par chauvinisme parce que c'est une bordelaise et surtout parce qu'elle est une amie et que sa présence au labo a beaucoup compté pour moi), Vincent et Pierro (qui sont bien plus que des compagnons de route, leur amitié m'est très chère et leur soutien fut immense) et enfin Matthias dont la présence à mes côtés a été le moteur principal de cette thèse.

J'adresse d'immenses remerciements à ma jolie famille : mes parents, Louise, mes grands-parents Mimi et Riton, Sylvie, Dominique, Anthony et Nathan. S'il peut être parfois difficile de reconnaître l'intérêt d'une thèse lorsqu'on la considère d'un point de vue extérieur, ce n'est jamais le sentiment que ma famille m'a laissé entrevoir. Elle fut à mes côtés pendant ces quasi quatre années de travail et son soutien a toujours été entier et identique au premier jour. La robustesse des liens qui unissent cette famille représente la base de mon épanouissement et du chemin que j'ai eu la chance de parcourir jusqu'ici.

Je remercie également mes amis les plus chers : Let, Camillou, Jo, Caro, Matchou, Lulu, Finou, Cess, Kaka, Anna, Soso, Ben et Mika. Leurs encouragements et tout simplement leur présence ont été absolument essentiels malgré l'éloignement géographique.

Une pensée également envers tous les membres de la troupe de théâtre de Seyssinet, et plus particulièrement envers Emy, Cécile et Elvire avec qui j'ai tant appris, entre autres à me familiariser avec la formidable respiration ventrale, si utile lors d'une conférence ou d'une soutenance !

Enfin, j'adresse mes derniers remerciements à ceux à qui je dois véritablement cette thèse : mes deux directeurs Georges-Henri et Iraj. Malheureusement, seules les personnes ayant eu la chance de travailler à leurs côtés peuvent comprendre l'immense honneur que j'ai eu de pouvoir réaliser ces travaux sous leur direction. Iraj et Georges-Henri ont su faire preuve de beaucoup de disponibilité, de confiance, de patience et de pédagogie à mon égard. Leur complémentarité a rendu cette co-direction extrêmement riche. J'ai énormément appris à leur côté et leur suis infiniment reconnaissante.

Résumé

Dans cette thèse nous mettons en œuvre une méthode vortex hybride pénalisée (HVP) afin de simuler des écoulements incompressibles autour de corps non profilés dans des milieux complexes solides-fluides-poreux. Avec cette approche particulaire hybride, le phénomène de convection est modélisé à l'aide d'une méthode vortex afin de bénéficier du caractère peu diffusif et naturel des méthodes particulaires. Un remaillage des particules est alors réalisé systématiquement sur une grille cartésienne sous-jacente afin d'éviter les phénomènes de distorsion. D'autre part, les effets diffusifs et d'étirement ainsi que le calcul de la vitesse sont traités sur la grille cartésienne, à l'aide de schémas eulériens. Le traitement des conditions de bords aux parois de l'obstacle est effectué à l'aide d'une technique de pénalisation, particulièrement bien adaptée au traitement de milieux solides-fluides-poreux.

Cette méthode HVP est appliquée au contrôle passif d'écoulement. Cette étude de contrôle est effectuée respectivement en 2D et en 3D autour d'un demi-cylindre et d'un hémisphère par l'ajout d'un revêtement poreux à la surface de l'obstacle. La présence de cette couche poreuse modifiant la nature des conditions aux interfaces, permet de régulariser l'écoulement global et de diminuer la traînée aérodynamique de l'obstacle contrôlé. A travers des études paramétriques sur la perméabilité, l'épaisseur et la position du revêtement poreux, ce travail vise à identifier des dispositifs de contrôles efficaces pour des écoulements autour d'obstacles comme des rétroviseurs automobiles.

Mot clés :

Méthode vortex hybride, méthode de pénalisation, contrôle passif d'écoulements, milieux poreux.

Abstract

In this work we use a hybrid vortex penalization method (HVP) to simulate incompressible flows past bluff bodies in complex solid-fluid-porous media. In this hybrid particle approach, the advection phenomenon is modeled through a vortex method in order to benefit from the natural description of the flow supplied by particle methods and their low numerical diffusion features. A particle remeshing is performed systematically on an underlying Cartesian grid in order to prevent distortion phenomena. On the other hand, the viscous and stretching effects as well as the velocity calculation are discretized on the mesh through Eulerian schemes. Finally, the treatment of boundary conditions is handled with a penalization method that is well suited for the treatment of solid-fluid-porous media.

The HVP method is applied to passive flow control. This flow control study is realized past a 2D semi-circular cylinder and a 3D hemisphere by adding a porous layer on the surface of the body. The presence of such porous layer modifies the characteristics of the conditions at the interfaces and leads to a regularization of the wake and to a decrease of the aerodynamic drag of the controlled obstacle. Through parametric studies on the permeability, the thickness and the position of the porous coating, this works aims to identify efficient control devices for flows around obstacles like the rear-view mirrors of a ground vehicle.

Keywords :

Hybrid vortex method, penalization method, passive flow control, porous media.

Contents

Introduction

In recent years, advances in computing enabled a large enhancement of numerical simulations related to Computational Fluid Dynamics (CFD). These simulations allow to predict the physical behavior of fluid flows and constitute a real economic issue when applied to bio-medical or engineering problems. In this thesis, we will particularly focus on incompressible Newtonian fluid flows past obstacles, which have been and are still subject to many investigations due to their close relation to aerodynamic efficiency.

Among the numerous numerical approaches used in CFD, particle methods occupy an important place thanks to their intuitive and natural description of the flow as well as their low numerical diffusion and their stability. Vortex methods [Cottet and Koumoutsakos, 2000] belong to this class of Lagrangian approaches and will constitute the key point of the present work. In the last three decades, the wide range of research works performed on these methods allowed to highlight their robustness and accuracy while providing a solid mathematical framework with convergence analysis and studies on conservation features. On the other side, a lot of efforts have been devoted to overcome their main intrinsic difficulties, mostly relying in the treatment of the boundary conditions and the modeling of the viscous effects due to particle distortion. The remeshing technique [Huberson and Jollès, 1990, Koumoutsakos and Leonard, 1995] may be considered as one of the most efficient and popular method to bypass the inherent problem of particle distortion. It consists in periodically redistributing the particles onto an underlying Cartesian grid in order to ensure their overlapping and thus the convergence of the solution. Following the introduction of this remeshing procedure, hybrid vortex methods emerged. These semi-Lagrangian approaches are characterized by the fact that the vorticity transport equations and the velocity equation are both handled on the particles field and on a Cartesian grid. They allow to benefit from the strengths of vortex schemes to handle convection phenomenon and from the one of grid-based methods, like immersed boundary methods, to model boundary conditions. Based on these different improvements, vortex methods have matured and now offer a robust framework able to compete with pure Eulerian methods in the handling of challenging problems. Besides the numerical approach, vortex methods also need computational competitiveness to pretend for being used in the CFD community. A lot of investigations related to algorithmic issues were therefore carried out in order to achieve this goal. Nowadays, a very few number of high performance scientific libraries using hybrid vortex methods exist. Based on this analysis, the present work is in line with a desire to demonstrate the effectiveness of a hybrid vortex method through the implementation of a dedicated scientific library, parallel, flexible, portable and modular.

The hybrid vortex method considered in this thesis is coupled with an immersed boundary method in order to account for the presence of obstacles in the flow and to model the boundary conditions. The method chosen here is the Brinkman penalization technique [Caltagirone, 1994, Angot et al., 1999, Kevlahan and Ghidaglia, 2001]. The underlying idea is to extend the fluid velocity inside the solid body and to solve the flow equations with a penalization term, depending on the intrinsic permeability, to enforce rigid motion inside the solid, using a vorticity formulation. Beyond the advantages specific to immersed boundary methods, the penalization approach

allows to handle solid-fluid-porous media. The differentiation between the three different media is indeed easily performed defining the value of the penalization parameter without prescribing a boundary condition at the solid boundary or a condition at the porous-fluid interface. This point is the main issue of the numerical application handled in this thesis, dealing with passive flow control around bluff bodies.

In recent years, applications related to flow control widely developed, especially in the automotive industry. A striking example is that of trucks companies, for which 25% of the overall budget is spent on fuel, while it is estimated that 60% of the truck engine power is dedicated to fight the drag force at speed of 90-100 km/h [Mohamed-Kassim and Filippone, 2010]. Drag reduction therefore appears as a real issue. For this purpose many flow control devices have been developed. They may be classified in two categories: the active and the passive techniques. The first ones consist in modifying the flow by supplying energy to the system and the passive devices rely on the change of structural and morphological configuration of the controlled body. In this thesis we aim at performing flow control past the rear-view mirrors of a ground vehicle. The latter, in spite of the fact that they only represent 0.5% of the projected surface of the vehicle, are responsible for about 10% of the total aerodynamic drag because of their spanwise position. Due to the size and the geometry of rear-view mirrors, passive control devices appear as the most suited. The passive technique considered here in order to smooth the flow dynamics involves porous media. As highlighted in [Pluvinage et al., 2014], it is interesting to mention that flow throughout porous media may be observed in multiple applications, like tennis balls [Mehta and Pallis, 2001] or carbon-nanotubes-based flow sensors [Vaseashta and Dimova-Malinovska, 2005], as well as natural structures like vegetation canopies [Gosselin, 2009], birds' covert feathers [Venkataraman and Bottaro, 2012] or endothelial glycocalyx (i.e. "sweet shield") of blood vessels [Secomb et al., 2001]. The presence of such porous layers enables a damping of the flow-induced surface instabilities, therefore modifying the flow behavior in the vicinity of the solid-porous-fluid interface. Based on the works of [Bruneau and Mortazavi, 2004, Bruneau and Mortazavi, 2006, Bruneau et al., 2008], the passive flow control device designed in the present work relies in a total or partial coating of the rear-view mirror surface with a porous layer. Under optimal conditions related to the permeability of the added porous layer, its thickness and its position, the modifications of the flow induced by the presence of such device may lead to a regularization of the wake and to a drag reduction.

The main objective of this thesis is to demonstrate the relevance and efficiency of the presented hybrid vortex penalization method in the context of two- and three-dimensional complex flows involving solid, porous and fluid media. It particularly requires the implementation of a parallel library which conception must take into account important considerations like flexibility, robustness or portability on different architectures and systems. The completeness of the proposed study also involves, in a second place, a careful analysis of the numerical results from a validation as well as a flow control application point of view. The present numerical method is based on a DNS (Direct Numerical Simulations) model, which limits the choice of the Reynolds number. The modeling of realistic fully turbulent flows, characterized by high Reynolds numbers, would require unaffordable computational resources in the context of DNS. Nevertheless, the presently performed simulations constitute a necessary step in order to validate and understand the physical phenomena involved in solid-porous-fluid media, considering all length scales, before tackling turbulence models of industrial scope.

This thesis is organized as follows. In the first chapter we propose a survey on vortex methods. By retracing the history of these particle methods from their introduction in the 1930's through calculations by hand until nowadays, with the apparition of the first highly efficient parallel vortex-methods libraries, this state of art aims to precisely define the scientific context

and the numerical issues of the thesis. The second chapter will be dedicated to the description of the hybrid vortex method considered in this work. We will first express the continuous governing equations before introducing the algorithm and numerical schemes designed in order to discretize the problem. A full description of the co-implemented scientific library designed to solve the problem will be given at the end of the chapter. In chapter three, we will perform a validation study of the proposed method for two- and three-dimensional flows past different bluff bodies. The analysis of the validation and convergence results will be preceded by a description of the physical mechanisms involved in incompressible viscous flows past bluff bodies. The understanding of these phenomena is necessary for a correct interpretation of the obtained validation results and the one related to flow control. This latter point will be addressed in chapter four. This chapter reports all the 2D and 3D numerical passive flow control results obtained using porous media around bluff bodies with a square back wall. In this study, we will carry out several parametric studies on the porous layer permeability, thickness or position, intending to determine the optimal devices in terms of drag reduction and global flow regularization. Finally, some perspectives related to the present work will be outlined in chapter five.

1

Literature survey on vortex methods

Contents

Résumé 1

Afin de situer les travaux de cette thèse dans leur contexte scientifique et afin d'en comprendre les enjeux, nous proposons dans ce premier chapitre un état de l'art des méthodes vortex. Dès leur création dans les années 1930, ces méthodes particulaires ont su susciter un attrait dans la communauté de la mécanique des fluides numérique de par leur capacité à modéliser de façon précise, robuste et naturelle des écoulements où le phénomène convectif est dominant. Cependant, leur utilisation à grande échelle fut freinée par leur difficulté à modéliser les conditions d'adhérence sur la paroi d'un solide immergé ainsi qu'à traiter les effets dus à la viscosité de l'écoulement. Ce dernier point s'explique par le phénomène de distorsion, caractéristique des méthodes lagrangiennes, se manifestant par une accumulation ou une raréfaction des particules dans les zones de forts gradients. Malgré de multiples études

menées entre 1973 et le début des années 90 afin de remédier à ces faiblesses, les méthodes vortex ne parvinrent pas à s'imposer dans leur contexte initial. C'est avec l'apparition de schémas de remaillage et leur utilisation dans le cadre de méthodes hybrides eulériennes/lagrangiennes que les méthodes vortex réussirent à contourner leurs difficultés intrinsèques, tout en conservant leurs atouts d'origine, et gagnèrent en compétitivité. En effet, la procédure de remaillage permit de redistribuer les particules sur une grille sous-jacente assurant ainsi leur recouvrement, et l'utilisation de méthodes eulériennes sur la grille facilita le traitement des effets visqueux mais aussi des conditions limites avec par exemple l'introduction de méthodes aux frontières immergées. Ce nouveau cadre semi-lagrangien suscita alors de nombreux efforts, notamment en termes de développement algorithmique et de calcul haute performance. Rendues ainsi plus rapides et plus efficaces, les méthodes vortex devinrent alors capables de traiter des problèmes ayant des enjeux industriels ou biologiques. C'est dans ce contexte semi- lagrangien que s'inscrit la méthode proposée dans cette thèse ayant pour but d'être appliquée, à terme, à la modélisation de contrôle passif d'écoulement pour des problèmes d'aérodynamique automobile.

Through the first vortex sheet computations of [Prager, 1928] and [Rosenhead, 1931] in the 1930's, the Vortex Methods (VM), which stem from particle methods, actually correspond to the first numerical method ever used in the Computational Fluid Dynamics community. This can be explained by their very natural framework, close to the physics, which make them particularly well suited for advection dominated flow problems.

In particle methods, the physical quantities involved in the simulated problem are discretized onto a set of particles evolving spatially in the domain according to the problem dynamics. The particles are therefore characterized by their position in the computational domain and the value of the physical quantity they are carrying. Since they are intrinsically close to the physics that they aim to model, the Lagrangian methods have been widely used to simulate problems related to astrophysics, solid mechanics and fluid mechanics, hence providing a relevant alternative to grid-based methods.

In vortex methods, the particles discretize the Navier-Stokes equations in their velocity-vorticity formulation. This formulation allows to directly point to the essence of vorticity dynamics in incompressible flows, which is characterized by advection and diffusion as well as stretching and change of orientation. As we aim in this work to perform DNS of incompressible flows with application to flow control, the choice of a vortex method is first justified by the fact that the vorticity formulation of the Navier-Stokes equations is a natural framework to address questions related to flow control. Indeed, the vorticity is a signature of wakes in bluff body flows and, as such, is related to aerodynamic performance of obstacles. Furthermore, we aim to deal with moderate and high Reynolds numbers and under these regimes, the vorticity advection is predominant, which motivates the use of particle schemes to discretize these equations.

This chapter proposes a literature survey of the vortex methods from their introduction in the 1930's until nowadays. We will start with the presentation of the VM in the context of two-dimensional inviscid flows, that is to say the context in which they arose, before detailing their extension to the three-dimensional case. We will then introduce step by step the different approaches which were developed in order to model viscous effects as well as the presence of immersed boundaries in the fluid flow, until we reach recent hybrid VM allowing to solve accurately and efficiently the Navier-Stokes equations for incompressible flows past bluff bodies. The next part will present the outlines of the hybrid penalization vortex method used in the present work and the last section of this chapter will be dedicated to the algorithmic issues related to hybrid vortex methods.

1.1 Vortex methods for inviscid incompressible flows

Before introducing the initial version of vortex method, which was given in the case of inviscid flows, let us first define the vorticity. From the physical point of view, the vorticity measures the local rotation of the fluid flow. It is obtained by taking the curl of the velocity field:

$$\boldsymbol{\omega} \equiv \nabla \times \mathbf{u}. \tag{1.1}$$

In the case of a two dimensional flow, the vorticity is perpendicular to the flow plane and corresponds to a scalar field. We note it by ω in that case. In the Cartesian coordinates system, the vorticity respectively expresses in 2D and 3D as follows:

$$\omega = \omega_z = \frac{\partial u_y}{\partial x} - \frac{\partial u_x}{\partial y} \quad , \qquad \boldsymbol{\omega} = (\omega_w, \omega_y, \omega_z) = \left(\frac{\partial u_z}{\partial y} - \frac{\partial u_y}{\partial z} \ , \ \frac{\partial u_x}{\partial z} - \frac{\partial u_z}{\partial x} \ , \ \frac{\partial u_y}{\partial x} - \frac{\partial u_x}{\partial y} \right). \tag{1.2}$$

The circulation Γ corresponds to the macroscopic rotation of the flow. It is a scalar field defined as the line integral of the velocity field along a closed path. Using the Stokes theorem, the circulation associated to a patch of vorticity $\mathcal{A}$, bounded by a closed path $\mathcal{L}$, is defined by:

$$\Gamma = \oint_{\mathcal{L}} \mathbf{u} \ ds = \int_{\mathcal{A}} \boldsymbol{\omega} \ d\mathbf{x}. \tag{1.3}$$

In other words, the vorticity may be defined as the microscopic rotation of the flow at a given point, while the circulation may be considered as a vorticity flux.

1.1.1 Two dimensional vortex methods

As mentioned in the introduction of this thesis, the first calculations based on vortex methods were performed, by hand, independently by [Prager, 1928] and [Rosenhead, 1931]. For that purpose, they discretized the flow into elements, namely the particles, each carrying a local circulation α. These calculations were limited in terms of number of flow elements as well as in computational time. Based on these pioneer works, the method described in the sequel corresponds to the general definition of vortex methods, first introduced in the 1970's.

Vortex blob method

The design of vortex methods for inviscid two-dimensional incompressible flows is based on vorticity-velocity formulation of the Euler equations:

$$\frac{\partial \omega}{\partial t} + (\mathbf{u} \cdot \nabla)\omega = 0 \tag{1.4}$$

$$\text{div } \mathbf{u} = 0 \tag{1.5}$$

$$\omega(\cdot, 0) = \omega_0 \tag{1.6}$$

$$|\mathbf{u}| \to \mathbf{u}_\infty \tag{1.7}$$

where $(\mathbf{u} \cdot \nabla)\omega$ denotes the advection term in the conservation momentum equation 1.4 and equation 1.5 corresponds to the incompressibility condition. The idea of vortex blob method was originally introduced by [Chorin and Bernard, 1973]. Let a regular approximation ω^h of ω, and $\mathbf{x}_p^h$ the trajectories of the particles transported by the flow. This approximated vorticity ω^h may be numerically expressed at time t by:

$$\omega^h(\mathbf{x}, t) = \sum_p \alpha_p \delta[\mathbf{x} - \mathbf{x}_p^h(t)], \tag{1.8}$$

where α_p corresponds to the local circulation around $\mathbf{x}_p^h$. We note that this requirement directly comes from the Kelvin's theorem on which the vortex methods are based. This theorem states

that in an inviscid flow the circulation around a closed curve, enclosing the same fluid elements, remains constant in time when moving with the fluid, which mathematically writes:

$$\frac{\partial \Gamma}{\partial t} = \frac{\partial}{\partial t} \int_{V(t)} \omega(\cdot, t)\ d\mathbf{x} = 0. \tag{1.9}$$

At all times, the velocity field $\mathbf{u}$ is coupled with the vorticity ω through the Poisson equation:

$$\Delta \mathbf{u} = -\nabla \times \omega, \tag{1.10}$$

obtained from the definition of the vorticity (eq. 1.1) and the incompressibility condition (eq. 1.5), as follows:

$$\nabla \times \omega = \nabla \times (\nabla \times \mathbf{u}) = -\Delta \mathbf{u} + \nabla(\nabla \cdot \mathbf{u}). \tag{1.11}$$

Considering periodic boundary conditions, the solution of equation 1.10 is recovered solving the following Biot-Savart equation:

$$\mathbf{u} = \mathbf{K} \star \omega, \tag{1.12}$$

where $\star$ denotes the convolution and $\mathbf{K}$ is the rotational counterpart of the periodic Green's function of the Poisson equation 1.10. The velocity field recovered from ω^h is thus given by:

$$\mathbf{u}^h(\mathbf{x}) = \mathrm{curl}(\mathbf{G}(\mathbf{x}, \mathbf{x}') \star w^h(\mathbf{x})) + \mathbf{u}^h_\infty(\mathbf{x}) = \int -\nabla \mathbf{G}(\mathbf{x}, \mathbf{x}')\ \omega^h(\mathbf{x}')\ d\mathbf{x} + \mathbf{u}^h_\infty(\mathbf{x}), \tag{1.13}$$

where the Green's function $\mathbf{G}$ satisfies

$$\nabla^2 \mathbf{G}(\mathbf{x}, \mathbf{x}') = \delta(\mathbf{x} - \mathbf{x}'). \tag{1.14}$$

In 2D, the fundamental solution of the above equation yields:

$$\mathbf{G}(\mathbf{x}, \mathbf{x}') = \frac{1}{2\pi} \ln(|\mathbf{x} - \mathbf{x}'|), \tag{1.15}$$

and the Poisson equation kernel, denoted $\mathbf{K}$, is then equal to:

$$\mathbf{K}(\mathbf{x}, \mathbf{x}') = \nabla \mathbf{G}(\mathbf{x}, \mathbf{x}') = \frac{1}{2\pi} \frac{(y - y', -(x - x'))}{|\mathbf{x} - \mathbf{x}'|}. \tag{1.16}$$

Consequently, at any time, the velocity field $\mathbf{u}^h$ is related to the vorticity ω^h through the Biot-Savart law:

$$\mathbf{u}^h(\mathbf{x}) = -\int \mathbf{K}(\mathbf{x}, \mathbf{x}')\ \omega^h(\mathbf{x}')\ d\mathbf{x} + \mathbf{u}^h_\infty(\mathbf{x}) \tag{1.17}$$

$$= \mathbf{K}(\mathbf{x}, \mathbf{x}') \star \omega(\mathbf{x}') + \mathbf{u}^h_\infty(\mathbf{x}). \tag{1.18}$$

According to equation 1.16, a singularity appears in the kernel $\mathbf{K}$ when the distance between two particles becomes too small. Faced with this problem, the idea of a global regularization of $\mathbf{K}$ arose. This is the creation of the vortex blob method which now basically stands for most of the commonly used vortex methods. In this numerical approach, the vorticity of a flow element is distributed on a blob, that is to say on a disk of finite radius ε. This vorticity distribution is defined by a smooth cutoff function ζ.

Definition 1.1

One calls cutoff function of order r a radially-symmetric function ζ, satisfying the following r-ordered moment properties:

$$\begin{cases} \int \zeta(\mathbf{x})d\mathbf{x} = 1 \\ \int \mathbf{x}^s \zeta(\mathbf{x})d\mathbf{x} = 0, \qquad 1 \leq |s| \leq r-1, \quad r \geq 2 \\ \int |\mathbf{x}|^r |\zeta(\mathbf{x})|d\mathbf{x} < \infty \end{cases} \tag{1.19}$$

If the blob radius ε is small enough, one denotes ζ_ε the mollified function defined by:

$$\zeta_\varepsilon = \frac{1}{\varepsilon^2}\, \zeta\left(\frac{\mathbf{x}}{\varepsilon}\right). \tag{1.20}$$

The vorticity ω_ε^h of the mollified particles is then given by:

$$\omega_\varepsilon^h(\mathbf{x}) = \sum_p \alpha_p \zeta_\varepsilon(\mathbf{x} - \mathbf{x}_p^h), \tag{1.21}$$

where the numerical particles locations $\mathbf{x}_p^h(t)$ are obtained by solving the following ODEs:

$$\frac{\partial \mathbf{x}_p^h(t)}{\partial t} = \mathbf{u}^h(\mathbf{x}_p^h(t), t) \tag{1.22}$$

with

$$\mathbf{u}^h = \mathbf{K}_\varepsilon \star \omega^h = (\mathbf{K} \star \zeta_\varepsilon) \star \omega^h \tag{1.23}$$

which, using a discrete integral estimation, may be expressed by:

$$\mathbf{u}^h(\mathbf{x}) = \sum_p \alpha_p \mathbf{K}_\varepsilon(\mathbf{x} - \mathbf{x}_p^h). \tag{1.24}$$

Among the possible cutoff functions, the Gaussian-based ones are often favored because of their smoothness property and their fast decay. Let us first give the example of the first-order Gaussian cutoff function, which is defined by:

$$\zeta_\varepsilon(r) = \frac{e^{-r^2/\varepsilon^2}}{\pi\varepsilon^2}, \tag{1.25}$$

where $r = |\mathbf{x} - \mathbf{x}'|$ and where the proportionality factor allows the integral of the above function to be equal to 1 over the infinite plane. One can notice that this function approaches the Dirac function as $\varepsilon \to 0$ (the vortex blob narrows to a single point and the vorticity amplitude goes to ∞) and its area integral remains unity. Moreover, the behavior of a point vortex is mimicked as we move away from the center. In the case of Gaussian-based cutoffs, the corresponding velocity kernel is given in explicit algebraic form. For the first-order function (equation 1.25), one obtains:

$$\mathbf{K}_\varepsilon = \frac{1}{2\pi r^2}(-y, x)\left(1 - e^{-r/\varepsilon^2}\right). \tag{1.26}$$

Concerning high-order cutoff functions, [Beale and Majda, 1982] constructed smooth functions at any order. These functions are defined by:

$$\Gamma_l(\mathbf{x}) = c_l \mathcal{F}^{-1}\left(e^{-|\boldsymbol{\xi}|^{2l}}\right), \tag{1.27}$$

where $l \geq 1$ denotes the order of the cutoff, $\mathcal{F}^{-1}$ is the inverse Fourier transform, and c_l are normalization coefficients ensuring that the first property of definition 1.1 to be satisfied. If $l = 1$ one recovers equation 1.25.

1.1.2 Three dimensional vortex methods

The resolution of three dimensional inviscid flows mainly relies on two classes of vortex methods: the vortex filament method and the vortex particle method. The first one appeared in the 80's, introduced by Leonard [Leonard, 1975, Leonard, 1980, Leonard, 1985]. This method leans on the theorems of Helmholtz and Kelvin, stating that tubes of vorticity retain their identity and move as material elements in an inviscid flow. In this approach, the quantity carried by the Lagrangian elements is a scalar, as in two dimensions, and the elements are now deformable lines instead of discrete points. As for two-dimensional vortex schemes, the circulation of the particles remains constant in time.

The second method, called particle vortex method, was introduced later by [Cottet, 1988a, Anderson and Greengard, 1985]. It can be considered as a direct extension of the two-dimensional vortex schemes since the vorticity is still carried by a set of points (the particles). The difference with the two-dimensional case lies in the fact that the quantity transported by particles is a vector instead of a scalar and that the circulation is no more constant in time because of the presence of the stretching term in the vorticity equation. Before presenting these two approaches, let us first define the Euler equations governing a three-dimensional inviscid flow.

In three dimensions, the vorticity $\boldsymbol{\omega} = \nabla \times \mathbf{u}$ is a vector. The vorticity-velocity formulation of the Euler equations writes:

$$\frac{\partial \boldsymbol{\omega}}{\partial t} + (\mathbf{u} \cdot \nabla)\boldsymbol{\omega} - (\boldsymbol{\omega} \cdot \nabla)\mathbf{u} = 0 \tag{1.28}$$

$$\boldsymbol{\omega}(\cdot, 0) = \boldsymbol{\omega}_0 \tag{1.29}$$

$$\mathbf{u} = \mathbf{K} \star \boldsymbol{\omega}, \tag{1.30}$$

where $\mathbf{K}$ is the non-regularized matrix-valued function given by:

$$\mathbf{u}(\mathbf{x}) = \mathbf{K} \star \boldsymbol{\omega}(\mathbf{x}) = -\frac{1}{4\pi} \int \frac{\mathbf{x} - \mathbf{x}'}{|\mathbf{x} - \mathbf{x}'|^3} \times \boldsymbol{\omega}(\mathbf{x}')\, d\mathbf{x} = \mathrm{curl}(\mathbf{G} \star \boldsymbol{\omega}) \tag{1.31}$$

and where $\mathbf{G}$ is the Green function of Poisson equation 1.30 given in 3D by $\mathbf{G} = (4\pi|\mathbf{x}|)^{-1}$. The equation 1.28 is a transport-deformation equation for the vorticity field and $(\boldsymbol{\omega} \cdot \nabla)\mathbf{u} = [\nabla \mathbf{u}][\boldsymbol{\omega}]$, the vector of component $\omega_j\, \partial u_i / \partial x_j$, corresponds to the stretching term. A conservative vortex scheme can be derived considering the conservative formulation of the stretching term, which stands as:

$$\mathrm{div}(\boldsymbol{\omega} : \mathbf{u}) = (\boldsymbol{\omega} \cdot \nabla)\mathbf{u} - \mathbf{u}(\mathrm{div}\ \boldsymbol{\omega}). \tag{1.32}$$

According to the fundamental laws of fluid mechanics, the vorticity is a solenoidal field ($\mathrm{div}\ \boldsymbol{\omega} \equiv 0$). Therefore equation 1.32 corresponds to the conservative form of the stretching term, which means that is does not contribute to the creation of circulation. Physically, the vortex stretching phenomenon corresponds to the lengthening of vortices in the three-dimensional fluid flow, associated with an increase of the component of vorticity in the stretching direction. For incompressible flow, the volume conservation of fluid elements implies that the longitudinal stretching goes together with the shrinking of the fluid elements in the directions perpendicular to the stretching direction. This reduces the radial length scale of the associated vorticity and explains the fact that the vorticity stretching is considered as the mechanism responsible for the energy transfer from the large scales to the small scales of the flow.

1.1.2.1 Vortex filament method

The vortex filament method relies on a very natural framework, which explains their earliest historical apparition [Leonard, 1975]. Instead of dealing with single points it considers deformable line vortices on which the circulation is conserved, according to the Kelvin's theorem. Intuitively, it seems clear that a vorticity distribution along a line can experience lengthening and deformation (caused by the stretching term), whereas it is impossible to model such a phenomenon

through the point-particles handled in the vortex particle method. Concretely, a filament vortex method consists in following the discrete markers of a Lagrangian curve (the filament) which model the vorticity field distribution and then in reconstructing the corresponding curves at each time step.

From the geometrical point of view, the vortex filament is defined as a vorticity field that is concentrated on a tube of radius ε and of infinitesimal cross section with a singularity at the center (Figure 1.1). A vortex line cannot end in the fluid: it must form a closed path or extend to infinity. The direction of a vortex filament is tangent at each point of its constitutive curve, and its circulation Γ is equal to the vorticity flux through a cross section of the filament:

$$\Gamma = \int_{\text{tube}} \omega \; dA = \oint_{\mathcal{L}} \mathbf{u} \; ds = \mathbf{u}_\theta(2\pi\varepsilon), \tag{1.33}$$

where $\mathbf{u}_\theta$ denotes the tangential velocity. According to the first Helmholtz theorem, this flux is independent of the considered cross section and from Kelvin's observations we know that the circulation of a vortex line does not change along its length. Therefore, this eliminates the need to calculate the stretching component of the vorticity equation and explains why the first three-dimensional vortex simulations were performed using vortex filament methods.

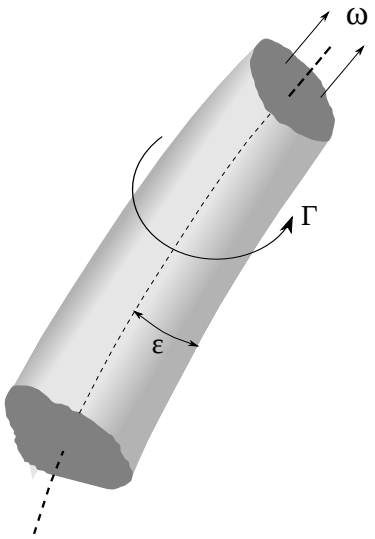

Figure 1.1: Geometrical representation of a vortex filament. The dashed line characterizes the filament singularity.

Let us now present the definition of a vortex filament and the solution of equation 1.28 using this approach. The mathematical description presented here follows the one detailed in [Cottet and Koumoutsakos, 2000]. Let us consider a smooth closed oriented curve $\mathcal{L}$ in $\mathbb{R}^3$. A vortex filament with unit circulation supported by $\mathcal{L}$ is the vector-valued measure $\boldsymbol{\mu}_{\mathcal{L}}$ defined by:

$$\langle \boldsymbol{\mu}_{\mathcal{L}}, \varphi \rangle = \int_{\mathcal{L}} \frac{\partial \gamma}{\partial \xi} \cdot \varphi[\gamma(\xi)] \; d\xi \tag{1.34}$$

where $\gamma(\xi)$ corresponds to a parametrization of $\mathcal{L}$, preserving its orientation, and φ is a continuous test function. Then, according to the Kelvin's circulation theorem, the unique solution of equation 1.28 is the vortex filament:

$$\boldsymbol{\omega}^h(\mathbf{x}, t) = \sum_p \boldsymbol{\alpha}_p \boldsymbol{\mu}_{\mathcal{L}_p^h(t)}, \tag{1.35}$$

which, coupled with the filament dynamics:

$$\frac{\partial \mathcal{L}_p^h}{\partial t} = \mathbf{u}^h(\mathcal{L}_p^h, t) = \mathbf{K}_\varepsilon \star \boldsymbol{\omega}^h, \tag{1.36}$$

defines the vortex filament methods. The mollified Poisson equation kernel $\mathbf{K}_\varepsilon$ is computed as usual with a cutoff function ζ. If this function has a spherical symmetry, then the velocity field can be explicitly recovered with the following formula:

$$\mathbf{u}^h(\mathcal{L}_p^h, t) = -\sum_q \boldsymbol{\alpha}_q \int_{\mathcal{L}_q} \frac{\rho\left[\frac{\gamma_p - \gamma_q(\xi)}{\varepsilon}\right]}{|(\gamma_p - \gamma_q)|^3} [\gamma_p - \gamma_q(\xi)] \times \frac{\partial \gamma_q}{\partial \xi}\, d\xi, \tag{1.37}$$

where

$$\rho(r) = \int_0^r \zeta(s) s^2\, ds \tag{1.38}$$

In practice, vortex filament methods were chosen to perform one of the first 3D simulation in CFD [Leonard, 1980] and were also used more recently by [Angelidis and Neyret, 2005] in graphic works. However, they suffer from several weaknesses: first of all, they are most of the time quite difficult to initialize for a given flow. Only specific problems like vorticity rings and jets are spared from this trouble. Also, some filament "surgeries" might become necessary in order to avoid tiny loops or to reconnect neighboring filaments, which make the method complex to use. Eventually, there is no straightforward way to include the diffusion effects in the model with filament method. All these major drawbacks led to the introduction of vortex point method to handle three dimensional inviscid flows in a pure Lagrangian way.

1.1.2.2 Vortex particle method

Proceeding in the same spirit as with the two dimensional case, the vortex particle method proposed by [Anderson and Greengard, 1985, Cottet, 1988a] is obtained by approximating the vorticity field as follows:

$$\boldsymbol{\omega}^h(\mathbf{x}, t) = \sum_p \boldsymbol{\alpha}_p^h(t)\ \delta[\mathbf{x} - \mathbf{x}_p^h(t)], \tag{1.39}$$

where the particles $\mathbf{x}_p^h$ follow the trajectories defined by the vector field $\mathbf{u}^h$ according to the three dimensional form of equation 1.22 and where $\boldsymbol{\alpha}_p^h$ are vectors satisfying the following ODEs:

$$\frac{\partial \boldsymbol{\alpha}_p^h}{\partial t} = \boldsymbol{\alpha}_p^h \cdot \nabla \mathbf{u}^h(\mathbf{x}_p^h, t). \tag{1.40}$$

As we can see, the presence of the stretching term in the vorticity transport equation 1.28 modifies the circulation of the particles.

As in two dimensions, the velocity field $\mathbf{u}^h$ is recovered from the vorticity field solving the Biot-Savart equation 1.30 for a mollified vorticity field. This mollification of the vorticity distribution is achieved using a cutoff function ζ which satisfies the moment conditions given in definition 1.1. Then one has:

$$\zeta_\varepsilon(\mathbf{x}) = \varepsilon^{-3}\zeta(\mathbf{x}/\varepsilon), \qquad \mathbf{G}_\varepsilon = \mathbf{G} \star \zeta_\varepsilon, \qquad \mathbf{K}_\varepsilon = \nabla \mathbf{G}_\varepsilon, \tag{1.41}$$

and finally, the velocity field is given by:

$$\mathbf{u}^h = \mathbf{K}_\varepsilon \star \boldsymbol{\omega}^h \tag{1.42}$$

The computation of the mollified kernel $\mathbf{K}_\varepsilon$ is performed in the same way as in two dimensions. For example, if ζ is a spherical symmetric cutoff function, one gets:

$$\mathbf{K}_\varepsilon(\mathbf{x}) = -\frac{\mathbf{x}}{|\mathbf{x}|^3} f\left(\frac{\mathbf{x}}{\varepsilon}\right) \tag{1.43}$$

with

$$f(r) = \int_0^r \zeta(s) s^2 ds \tag{1.44}$$

This approach, further developed by [Beale and Majda, 1985, Gustafasson and Sethian, 1991] was also adopted by [Beale et al., 1991] who tested it for several formulations of the stretching term, in particular $[\nabla \mathbf{u}^h][\boldsymbol{\alpha}_p^h]$ and the transpose scheme $[\nabla \mathbf{u}^h]^T[\boldsymbol{\alpha}_p^h]$ [Choquin and Cottet, 1988]. They applied it to model a vortex ring with swirl. It was also used for the same application in [Lifschitz et al., 1996]. Compared to vortex filament methods, the vortex particle methods are certainly less natural from a physical point of view but they remain easier to handle and to implement since they are more generic. In that sense they are much more suitable to model viscous flows. This point will be addressed in section (1.2) of this chapter.

1.1.3 Convergence of vortex methods

What distinguishes vortex methods from grid-based methods is the fact that they are build in such a way that many inviscid flow invariants are conserved. This makes them particularly interesting from a fluid mechanics point of view since they ensure a correct qualitative answer, even in the case of underresolved simulations. Besides this important feature, vortex methods indisputably belong to the category of plain numerical methods by means of their complete numerical analysis.

Historically, the first complete proof of convergence was given by [Hald, 1979] as part of the vortex blob methods. This analysis included the influence of the numerical parameters involved in the model, namely the blob radius ε (that is to say the cutoff width) and the particle spacing, denoted h. It turned out that, in two dimensions, the vortex blob trajectories tend to the exact one when the number of eddies increases. But this statement relies on a restrictive overlapping condition (i.e $h \ll \varepsilon$) and on several assumptions about the considered cutoff function ζ. One has to wait until 1982 with the work of [Beale and Majda, 1982] to get a generalized convergence analysis, in the sense of $h = \mathcal{O}(\varepsilon)$. These results allow to reach high orders of convergence in two dimensions. An extension to the three dimension case is also proposed in this study, giving birth to new high orders three dimensional vortex methods. An other convergence analysis of three-dimensional vortex methods was further given in [Cottet, 1988a]. On the other hand, Cottet identified a minimal smoothness requirement for the cutoff function ζ and proposed a simplified consistency analysis based on quadrature estimates [Cottet, 1982]. In 1985, the time discretization is added for the first time in the convergence analysis of the 2D and 3D Euler equations [Anderson and Greengard, 1985]. Until then, the vortex methods had only been analyzed in terms of semi-discretized schemes. The most important result which came out from this study is the fact that these methods do not suffer from any Courant-Friedricks-Levy (CFL) condition, which constraints the time step to be related to the minimal grid size in Eulerian methods. Indeed, in vortex methods the stability constraint on the time step only depends on the velocity gradient:

$$\Delta t \leq \frac{C}{\|\nabla \mathbf{u}\|_\infty}, \tag{1.45}$$

where the constant C, also called LCFL number (for Lagrangian CFL), must be lower or equal to 1. This condition provides a much less restrictive constraint for the time step compared to purely grid-based schemes. This outcome is of great importance, especially when considering turbulent flows for which highly resolved simulations are needed. We will come back in details on these time step concerns in the next chapters of this thesis.

The convergence proof of the so-called vortex point method (where $\varepsilon = 0$) for incompressible Euler equations was only brought in 1990 and 1991 respectively by [Goodman et al., 1990] and [Hou et al., 1991]. This method was shown to converge quadratically to the exact solution, provided it is smooth enough. To achieve this convergence analysis, the authors relied on the techniques used in the early work of [Beale and Majda, 1982].

1.2 Viscous vortex methods

One of the main applications that vortex methods aim to model, and which correspond to those considered throughout this thesis, are the incompressible flows past bluff bodies. In order to numerically solve such flows, it is essential to include the viscous effects which, along with the presence of the obstacle's boundaries, are responsible for the creation of vorticity. To understand this phenomenon, it is important to recall that the viscosity of a fluid is a measure of its resistance to gradual deformations by shear stress. Thus when a fluid encounters a solid body, the intermolecular forces, due to the viscosity, oblige the fluid to decelerate very rapidly in a thin layer (called boundary layer) surrounding the body. High tangential constraints then occur in this region, thus creating circulation and consequently, vorticity. Under the action of viscosity, this vorticity diffuses away in the flow, where no vorticity used to exist before. Therefore, an accurate resolution of flow past bluff bodies implies to carefully take into account the viscous effects, at least in the vicinity of the solid walls. The first numerical schemes including viscous effects in vortex methods were designed with the desire to conserve the Lagrangian framework. They were consequently purely based on particles.

In this section we will present in details two main existing viscous vortex methods, namely the Random Walk method (RW) and the Particle Strength Exchange method (PSE). The first one proposes a stochastic approach to model the vorticity diffusion phenomenon in the Navier-Stokes equations, whereas the second one is a pure deterministic method and is based on the integral approximation of the diffusion equation. Before starting with the description of the Random Walk method, which was historically the first viscous vortex method developed by [Chorin, 1973], it is necessary to introduce the concept of viscous splitting of the Navier-Stokes equations. Indeed, in order to handle the diffusion term, it seemed natural to separate the inertial term from the diffusive one within the time-stepping scheme, and to solve them independently. The first subsection below is thus dedicated to the presentation of the viscous splitting algorithm.

1.2.1 Viscous splitting method

The original concept of viscous splitting was first introduced at the beginning of the 20^{th} century by [Prandtl, 1904]. However, its design within the framework of vortex methods was originally proposed in the early 70's by [Chorin, 1973] in order to develop his Random Walk Method suited to model the diffusive phenomenon.

In a two-dimensional viscous flow, the transport of vorticity is governed by the Navier-Stokes equations, expressed in their velocity-vorticity formulation $(\mathbf{u}, \omega)$, written:

$$\frac{\partial \omega}{\partial t} + (\mathbf{u} \cdot \nabla)\omega = \nu \Delta \omega, \tag{1.46}$$

where ν denotes the viscosity of the fluid. This equation is coupled with the Poisson equation $\Delta \mathbf{u} = -\nabla \times \omega$ in order to recover the velocity field from the vorticity.
The viscous splitting algorithm consists in performing substeps in which the convective and the diffusive effects, respectively governed by $(\mathbf{u} \cdot \nabla \omega)$ and $(\nu \Delta \omega)$, are handled successively. Thus, the two steps of the viscous splitting algorithm for a two-dimensional flow are the following:

1) convection:

$$\frac{\partial \omega}{\partial t} + (\mathbf{u} \cdot \nabla)\omega = 0, \tag{1.47}$$

2) diffusion:

$$\frac{\partial \omega}{\partial t} = \nu \Delta \omega. \tag{1.48}$$

In a Lagrangian frame, the viscous splitting algorithm stands as follows:

1) convection:

$$\frac{d\mathbf{x}_p}{dt} = \mathbf{u}(\mathbf{x}_p) \tag{1.49}$$

$$\frac{d\omega_p}{dt} = 0, \tag{1.50}$$

2) diffusion:

$$\frac{d\mathbf{x}_p}{dt} = 0 \tag{1.51}$$

$$\frac{d\omega_p}{dt} = \nu\Delta\omega(\mathbf{x}_p), \tag{1.52}$$

where in the first step, the particles locations ($\mathbf{x}_p$) are updated using the local flow velocity and in the second one the vorticity of the flow is modified at these new positions (ω_p) by the diffusion.

The convergence of the viscous splitting method was proved by [Beale and Majda, 1981] and is given by the re-formulated theorem [Cottet and Koumoutsakos, 2000]:

Theorem 1.1

Let ω^n denote an approximation of the exact solution $\omega(\cdot, t_n)$. If $\omega_0 \in W^{3,\infty}(\mathbb{R}^2) \bigcap W^{3,1}(\mathbb{R}^2)$, then the following estimate holds for all $p \in [1, +\infty]$:

$$\|\omega^n - \omega(\cdot, t_n)\|_{0,p} \leq C(T)\nu\Delta t. \tag{1.53}$$

1.2.2 Random Walk method (RW)

The method of Random Walk [Chorin, 1973] is based on the probabilistic interpretation of the Green's function, solution of the diffusion equation:

$$\omega(\mathbf{x}, t) = \int G(\mathbf{x} - \mathbf{y}, \nu t)\omega_0(\mathbf{y})\ d\mathbf{y}, \tag{1.54}$$

which, in d-dimensions is known to be explicitly equal to:

$$G(\mathbf{x} - \mathbf{y}, \nu t) = \frac{1}{(4\pi\nu\Delta t)^{d/2}}\ \exp\left(\frac{-\|\mathbf{x} - \mathbf{y}\|^2}{4\nu\Delta t}\right). \tag{1.55}$$

As mentioned previously, the RW method is inherently related to the viscous splitting approach since the vorticity field obtained after the advection step is assigned to the initial condition of the diffusion equation. The diffusion effects are then modeled imposing a Brownian motion to the flow particles which positions are updated over a time step Δt according to the following scheme:

$$\mathbf{x}^{n+1} = \mathbf{x}^n + \Delta t\mathbf{u}^n + \mathbf{g}, \tag{1.56}$$

where $\mathbf{g}$ is a vector of independent random variables obtained through a Gaussian probability distribution with zero mean and a variance $\sigma = 2\nu\Delta t$:

$$\mathcal{N}_p^n(0, 2\nu\Delta t) = \frac{1}{(2\pi\sigma)^{d/2}}\ \exp\left(\frac{-\|\mathbf{x}\|^2}{2\sigma}\right). \tag{1.57}$$

Moving the particles in such a way creates a concentration field that converges to the above Green's function solution of the diffusion equation, as the number of particles tends to infinity. [Marchioro and Pulvirenti, 1982], [Goodman, 1987] and [Long, 1988] successively proved the convergence of the Random Walk method.

Thank to its main advantages, namely its simplicity, its capability to easily handle flows around complicated boundaries and its property to conserve the total circulation, this method has been extensively used during the last thirty years of the 20^{th} century. In terms of applications related to the one considered in this thesis, we can cite the works of [Chorin, 1973, Chorin, 1989], [van Dommelen, 1986] and [Smith and Stansby, 1988, Smith and Stansby, 1989] who applied the Random Walk method for the simulations of flows around cylinders. We can also refer to [Wang, 1995] who studied in his thesis several active flow control techniques to prevent the dynamic stall of airfoils and to [Lewis, 1990] who used the Random Walk method to simulate flows over airfoil cascades. However, this viscous vortex method is a stochastic method: it therefore presents several drawbacks. First, it does not exactly conserve the mean position of the vorticity in free space. Next, the computed solutions are noisy due to the statistical errors. Indeed, increasing the viscosity ν makes the variance of the random variables larger and consequently deteriorates the solution. In flow control studies, these statistical errors could mask the effects of variation in the control parameters. The statistical errors can also cause symmetric flows to turn asymmetric erroneously which could also corrupt the flow control analysis. Finally, the stochastic feature of the Random Walk method limits its convergence capability. The error is indeed proportional to $1/\sqrt{N}$ [Milinazzo and Saffman, 1977], where N is the number of particles. Therefore, accurate simulations need a very large number of fluid elements, which increases the computational cost. In conclusion, one can state that Random Walk methods that use rather small number of elements should be considered as methods delivering a qualitative behavior of the flow, instead of a way to approximate the Navier-Stokes equations.

1.2.3 Particle Strength Exchange method (PSE)

The origin of this deterministic viscous vortex method comes from a previous type of methods called Resampling Methods first developed by [Cottet and Mas-Gallic, 1983] for linear equations and further proposed in a conservative formulation by [Choquin and Huberson, 1989] and then extended to the Navier-Stokes equations by [Cottet and Mas-Gallic, 1990]. These resampling methods use viscous/inviscid splitting of the vorticity equation where the resolution of the diffusion equation is performed exactly using the fundamental solution of the heat equation and resampling the vorticity field induced by one particle on its neighbors. Unlike the RW method, resampling methods are characterized by the fact that diffusion is modeled by a change in the strength of the particles and not their positions.

Based on the same idea, the Particle Strength Exchange method was later introduced by [Degond and Mas-Gallic, 1989]. It is based on a deterministic approach allowing to approximate the Navier-Stokes equations. The mathematical description of the PSE method is here given in a two-dimensional framework but the main ideas of this approach remain the same in three dimensions:

1. Approximate the diffusion operator $\Delta\boldsymbol{\omega}_p$ by an integral operator. This approach is motivated by the fact that integrals are better suited to handle particle methods compared to second-order differential operators.

2. Consider the strength (circulation) of each particle as an unknown quantity that changes with time due to diffusion effects. We recall that the circulation associated to a particle corresponds to the product of the vorticity by the volume of the particle: $\boldsymbol{\alpha}_p = \mathbf{v}_p\boldsymbol{\omega}_p$.

3. Discretize the integral operator of step 1 using the particle positions as quadrature points.

First of all, let us consider a mollified diffusion kernel $\eta_\varepsilon(\mathbf{x}) = \varepsilon^{-2}\eta(\mathbf{x}/\varepsilon)$ where η is of order of

r, that is to say satisfying the following moment properties:

$$\begin{cases} \int x_i x_j \eta(\mathbf{x}) d\mathbf{x} = 2\delta_{ij}, & \text{for } i,j = 1,2 \\ \int x_1^{i_1} x_2^{i_2} \eta(\mathbf{x}) d\mathbf{x} = 0, & i_1 + i_2 = 1 \text{ or } 3 \leq i_1 + i_2 \leq r+1 \\ \int |\mathbf{x}|^{r+2} |\eta(\mathbf{x})| d\mathbf{x} < \infty \end{cases} \tag{1.58}$$

According to Proposition 1.1, the Laplacian operator may be replaced by:

$$\Delta_\varepsilon \omega(\mathbf{x}) = \varepsilon^{-2} \int [\omega(\mathbf{y}) - \omega(\mathbf{x})] \eta_\varepsilon(\mathbf{y} - \mathbf{x}) \, d\mathbf{y}. \tag{1.59}$$

Proposition 1.1

Assuming that $\omega \in W^{r+2,\infty}(\mathbb{R}^2)$, then the following estimate holds:

$$\|\Delta_\varepsilon \omega - \Delta\omega\|_{0,\infty} \leq C\varepsilon^r \|\omega\|_{r+2,\infty}. \tag{1.60}$$

The resulting discrete scheme is written as:

$$\omega^h(\mathbf{x}, t) = \sum_p v_p \ \omega_p^h(t) \ \delta(\mathbf{x} - \mathbf{x}_p), \tag{1.61}$$

and using the numerical integration of Δ_ε (equation 1.59) we finally obtain the following system of ODEs allowing to get a particle approximation of the diffusion effects:

$$\frac{d\omega_p^h}{dt} = \nu\varepsilon^{-2} \sum_q (v_q \omega_q^h - v_q \omega_p^h) \ \eta_\varepsilon(\mathbf{x}_q^h - \mathbf{x}_p^h). \tag{1.62}$$

This equation can be interpreted as changes in the strength of particles due to the neighboring particles. We refer to the works of [Degond and Mas-Gallic, 1989] regarding the construction of the kernel η, but one possibility is to use $\eta = \Delta\zeta$ (where η statisfies the conditions 1.58 if ζ is a cutoff function of the order of r - see Definition 1.1 -).

The main advantages of the PSE method rely on its deterministic approach and on the integral framework used to obtained the approximation of the viscous effects. These two aspects make the method more accurate compared to the Random Walk method presented previously. The reliability of the method is also based on its capability to conserve the natural invariants of the flow, which is not the case with non corrected Resampling Methods (see [Cottet and Koumoutsakos, 2000]). Eventually, the PSE method is not based on the viscous splitting algorithm, contrary to Resampling Methods, which therefore discards the intrinsic error of the splitting process (see Theorem 1.2). However, a major disadvantage of this approach lies on the necessity to achieve a significant overlap of the vortices needed to ensure a great convergence of the method. This requirement reduces the ability of the method in resolving the smallest scales since it noticeably increases the computational cost.

From the pioneer works of [Koumoutsakos and Leonard, 1995] who applied the PSE method to impulsively started and stopped flows around translating and rotating cylinders for Reynolds numbers ranging from 40 to 9500, a wide range of applications related to bluff body flows have been handled based on this deterministic approach.

The problem consisting in modeling viscous effects in vortex methods has been subject to numerous works between 1980 and 2000, and besides the famous RVM and PSE methods one can also cite other approaches like the Core Expansion Method [Leonard, 1980], the Fishelov's Method [Fishelov, 1990a], the Diffusion Velocity Method [Fronteau and Combis, 1984],

the Free-Lagrange Method [Borgers and Peskin, 1987, Rees and Morton, 1991] or the Redistribution Scheme [Shankar and van Dommelen, 1996]. However, most of these methods proved unable to handle three-dimensional problems.

Apart from the RVM and PSE methods, one of the rare approach that has been successfully applied to model the diffusion term in the three-dimensional Navier-Stokes equations is the Diffusion Velocity Method (DVM) of [Rivoalen et al., 1997]. This method, first introduced by [Fronteau and Combis, 1984], relies on the idea that the diffusion of vorticity is handled within the convective process by absorbing the diffusion term into the convection one in the Navier-Stokes equations 1.46. This process gives rise to two different velocities: the convection velocity and the diffusion velocity. The latter can be considered as an artificial velocity. Thus, the transport of vorticity (due to convection and diffusion effects) is modeled by the vortices' movement provoked by the convection velocities and the diffusion velocities. However, the DVM is subject to lack of accuracy, even numerical instability, in the regions of the flow with high vorticity gradients or vanishing vorticity. The method requires the particle size *eps* to be large in these regions in order to achieve an important particle overlapping and thus a higher accuracy.

In order to conclude this section, one can highlight the fact that, regardless of the type of approach, the viscous vortex methods show some difficulties in efficiently and accurately modeling the diffusion effects in a pure Lagrangian framework. A common drawback is the need of a large particle overlapping to prevent numerical instabilities. This problem will be treated in section (1.4).

1.3 Treatment of the boundary conditions

In this thesis we aim to model incompressible viscous flows past obstacles. It is therefore of great importance to carefully handle the question of boundary conditions at the solid walls. Furthermore, as explained at the beginning of section (1.2), the boundaries and the flow viscosity are the only source of vorticity, which explains the efforts made in order to design a method able to accurately model the flow behavior in this region, essentially governed by the no-slip boundary condition. The major difficulty lies in the fact that the no-slip boundary condition only involves the velocity field in its expression whereas the vortex methods are based on a vorticity formulation of the Navier-Stokes equations. In this section we will give a global description of all the main approaches dealing with boundary conditions in the vortex methods framework. We will therefore consider the velocity-vorticity formulation of the Navier-Stokes equations and we will restrict this survey to solid and rigid obstacles. Before introducing these approaches, we start by giving the expression of the no-slip boundary condition as a function of the velocity field.

1.3.1 The no-slip boundary condition

The no-slip boundary condition results from the kinematics and the molecular viscosity. On one hand, the kinematics force the normal component of the flow velocity $\mathbf{u}$ to be equal to the normal velocity of the body $\mathbf{u}_s$, at any location on the solid surface ($\mathbf{x}_s$):

$$\mathbf{u}(\mathbf{x}_s) \cdot \mathbf{n} = \mathbf{u}_s \cdot \mathbf{n}. \tag{1.63}$$

On the other hand, the molecular viscosity dictates that, at their interface, the tangential component of the flow velocity must be equal to the body velocity:

$$\mathbf{u}(\mathbf{x}_s) \cdot \mathbf{s} = \mathbf{u}_s \cdot \mathbf{s}. \tag{1.64}$$

The coupling of equations 1.63 and 1.64 gives the no-slip boundary conditions:

$$\mathbf{u}(\mathbf{x}_s) = \mathbf{u}_s. \tag{1.65}$$

Under this condition, the fluid elements present in the vicinity of the solid walls experience a net torque imparting a rotational motion to the surrounding fluid. This phenomenon corresponds to the creation of vorticity at the boundaries.

In the context of vortex methods, we aim to express the boundary conditions in terms of the vorticity field, equivalent to the no-slip boundary condition 1.65. To write these boundary conditions one may choose a Dirichlet formulation (wall vorticity) or a Neumann formulation (wall-normal vorticity flux). The Neumann form is often preferred since it directly governs the local production of vorticity at a solid wall. Indeed, the wall-normal vorticity flux, given by:

$$\frac{\partial \boldsymbol{\omega}}{\partial \mathbf{n}}, \tag{1.66}$$

measures the vorticity that enters the flow from the boundaries. This flux is actually responsible for the total production of vorticity at the no-slip wall. It will be taken into account in all the different methods we will present. These approaches, designed to model the boundary conditions with a vorticity formulation, will be introduced respecting their historical order of appearance. The first family of methods belongs to the ones based on viscous splitting that mimic the vortex creation at the interface. The second group of methods gathers the ones dealing with exact formulation of vorticity boundary conditions. The last type of method presented hereafter consists in defining vorticity flux boundary conditions in order to create vorticity at the wall boundary and thus to enforce the no-slip.

1.3.2 Methods based on viscous splitting and vorticity creation

1.3.2.1 The Chorin's vortex sheet method

The first successful approach designed to handle the boundary conditions in vortex methods for fluid flows is due to [Chorin, 1973]. The method he introduced uses the fractional step technique (described previously in section (1.2.1)) and relies on creating a vortex sheet at the solid boundary in order to vanish the slip velocity and thus to enforce the required no-slip boundary condition. Practically, the wall is discretized into segments. Each of these segments is associated to a local slip velocity where vortex blob elements are created at each time step to cancel it. We detail the different steps of the algorithm used in the method proposed in [Chorin, 1973] to discretize the Navier-Stokes equations, with boundary conditions. In the following, Ω and $\mathcal{S}$ refer respectively to the whole domain and the solid surface, and $\boldsymbol{\omega}_n$ denotes the vorticity approximation at time $t_n = n\Delta t$:

1. **Resolution of the inviscid part**
   The Euler equation is solved, coupled with a no-through-flow boundary condition (1.68):

$$\frac{\partial \omega}{\partial t} + \mathbf{u} \cdot \nabla \omega = 0 \qquad \text{in } \Omega, \tag{1.67}$$

$$\mathbf{u} \cdot \mathbf{n} = 0 \qquad \text{on } \mathcal{S}. \tag{1.68}$$

   At the end of this first step, one has the expression of the intermediate vorticity, denoted $\omega_{n+1/2}$, associated to the velocity $\mathbf{u}_{n+1/2}$ whose normal component is equal to zero at the solid boundary.

2. **Enforcement of the no-slip boundary condition (vorticity creation)**
   The no-slip boundary condition is obtained by creating a vortex sheet across the wall. This operation is performed adding an odd extension to the velocity field along the boundary, as depicted in Figure 1.2. The generated vortex sheet then has a strength equal to $\gamma = \mathbf{u}_{n+1/2} \cdot \mathbf{s} \otimes \delta_{\mathcal{S}}$, which corresponds to the jump of the tangential component of the velocity field. At the end of this step, the vorticity is known in the fluid and a vortex sheet has been created at the solid surface. As the vortex sheet γ may be considered as interior vorticity

(contrary to external vorticity, that is vorticity of the flow), the resulting vorticity, leading to velocity cancellation, is:

$$\tilde{\omega}_{n+1/2} = \omega_{n+1/2} - \mathbf{u}_{n+1/2} \cdot \mathbf{s} \ \otimes \delta_{\mathcal{S}} \tag{1.69}$$

Let us mention here that this result is inspired by the pioneer works of [Lighthill, 1963] who already gave in 1963 the expression 1.69 of the new vorticity. At that time, Lighthill ended the description of his vorticity creation model assuming that the vortex sheet was slightly impinging on the domain Ω and that, consequently, the velocity associated to $\tilde{\omega}$ satisfied the no-slip boundary conditions, experiencing a jump inside the domain. But this first model suffered from the fact that the vortex sheet strength γ was not explicitly taken into account in a vorticity-type boundary condition. This is precisely the point on which Chorin focused to improve the model. This point is described in the third step of the present algorithm.

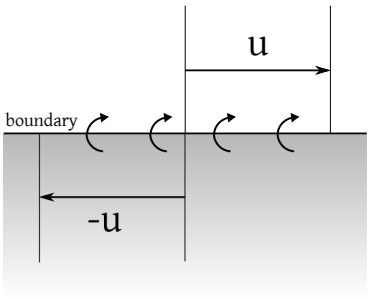

Figure 1.2: Odd extension of the velocity field at the wall boundary leading to the creation of a vortex sheet.

3. **Resolution of the viscous part with homogeneous Neumann boundary condition**
The diffusion equation is solved in the whole domain Ω taking $\tilde{\omega}_{n+1/2}$ as initial condition, and an homogeneous Neumann boundary condition is imposed on the surface $\mathcal{S}$:

$$\frac{\partial \omega}{\partial t} - \nu \Delta \omega = 0 \qquad \text{in } \Omega, \tag{1.70}$$

$$\omega(\cdot, 0) = \tilde{\omega}_{n+1/2} \qquad \text{in } \Omega, \tag{1.71}$$

$$\frac{\partial \omega}{\partial \mathbf{n}} = 0 \qquad \text{on } \mathcal{S} \tag{1.72}$$

This Stokes step conserves the symmetry of the velocity across the solid wall and thus provides an even and smooth vorticity field along the boundary. Therefore, the vorticity satisfies $\partial\omega/\partial\mathbf{n} = 0$ on $\mathcal{S}$ and the discontinuous velocity of step 2. is regularized, establishing a boundary layer (see Figure 1.3).

The success of this method is due to its efficiency and its user-friendliness. Nevertheless, establishing a proof of convergence for such an algorithm is far from being so easy. Indeed, in this approach the step dealing with inviscid part only handles the no-through-flow boundary condition. Thus, the two following steps in the algorithm are biased by the fact that the velocity field violates its boundary condition. The convergence proof of this splitting scheme given by [Chorin et al., 1978, Benfatto and Pulvirenti, 1986] is then much more advanced than the one corresponding to the result of Theorem 1.2. The main drawback of the method lies in the fact that the creation of vortex blobs at the boundary is responsible for an increase of the global numerical dissipation of the algorithm. Indeed, adding such blobs near the surface artificially smooths the vorticity field in this region.

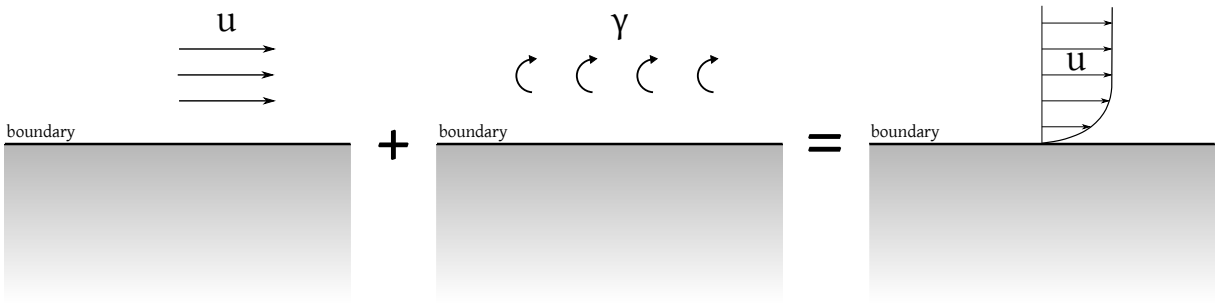

Figure 1.3: Pattern of no-slip velocity acquisition at the solid wall using Chorin's vortex sheet method.

In order to overcome this weakness and to recover accuracy, [Chorin, 1978] presented an improved approach consisting in coupling the Prandtl boundary-layer equations near the surface and the Navier-Stokes equations everywhere else. This method is also known as the vortex sheet/vortex blob method.

1.3.2.2 The vortex sheet/vortex blob method

The outline of the algorithm proposed by [Chorin, 1978] is the same as the one just presented, with the addition of two main elements. The first one is the use of segments of vortex sheets (that is to say flat vortex sheets) instead of vortex blobs, in the boundary layer. It leads to a more natural discretization of the created vortex sheets in step 2. The second main ingredient added in this approach is the consideration of the Prandtl boundary-layer equations to model the flow fields near the surface of the body. These equations rely on the assumption that, in the boundary region, vorticity diffusion mainly occurs in the direction normal to the wall and high velocity gradients are essentially along the component tangential to the wall. In order to take into account these assumptions, the Prandtl equations are expressed in a coordinate system where x and y respectively denote the tangential and the normal coordinates, and where (u, v) corresponds to the velocity vector field in this system. The wall is assumed to be at $y = 0$ and the fluid domain is defined by the half-space $y \geq 0$. The Prandtl boundary-layer equations are then given by:

$$\frac{\partial \omega}{\partial t} + u\frac{\partial \omega}{\partial x} + v\frac{\partial \omega}{\partial y} = \nu\frac{\partial^2 \omega}{\partial y^2} \tag{1.73}$$

$$\omega = -\frac{\partial u}{\partial y}, \tag{1.74}$$

They are completed by the continuity equation and the following boundary conditions:

$$\mathbf{u} = 0 \quad \text{at} \quad y = 0, \tag{1.75}$$

$$u(x, y_\infty) = U_\infty(x), \tag{1.76}$$

where equation 1.75 imposes the no-slip boundary condition at $y = 0$ and equation 1.76 expresses a far-field condition for the u component when $y \geq y_\infty$. The value y_∞ is often taken of the order of the boundary layer thickness.

Let us now consider a set of N elements S_i of vortex sheets, of strengths α_i. These elements should be seen as segments of a straight line, parallel to the x axis and of length ε, such that the two values of u at the extremities of S_i differ from each other by α_i. According to this definition, the vortex sheet approximation of ω is given by:

$$\omega \simeq \sum_j \alpha_j b_\varepsilon(x - x_j)\delta(y - y_j), \tag{1.77}$$

where b_ε is a one-dimensional cutoff function given by $b_\varepsilon = \varepsilon^{-1} b(x/\varepsilon)$ and where δ is the one-dimensional Dirac mass in the normal direction.

The u component of S_i, due to the presence of the other surrounding segments, is then obtained from a direct integration of equation 1.74, using the right-hand side of the above ω approximation (Eq. 1.77):

$$u(x,y) = U_\infty(x) + \sum_j \alpha_j b_\varepsilon(x - x_j) H(y_j - y) \tag{1.78}$$

where H is the Heavyside function. The expression of v can then be deduced from u, using the continuity equation:

$$v(x,y) = -\frac{\partial U_\infty(x)}{\partial x} y - \sum_j \alpha_j b'_\varepsilon(x - x_j) \min(y, y_j) \tag{1.79}$$

One is now able to give the substeps constituting the algorithm of the Chorin's vortex sheet/vortex blob method:

1. Evaluation of the u and v components from formulations 1.78, 1.79 and convection of the vortex sheets with this velocity field.

2. Computation of u on the wall ($y = 0$) and creation of new sheets at the boundary with strengths $\alpha_i = -u(x_i)dl$ in order to impose the no-slip boundary condition (these strength values directly come from the integration of equation 1.74). As explained in [Chorin, 1978], the velocity field is here extended across the wall by the anti-symmetry $u(x,-y) = -u(x,y)$. As a consequence $\omega(x,-y) = \omega(x,y)$ and a vortex sheet is generated at $y = 0$. This anti-symmetry replaces the vorticity creation process used in [Chorin, 1973].

3. Diffusion of the vortex sheets in the y direction using a random walk approach (see section (1.2.2)). If a sheet arises in the far-field region ($y \geq y_\infty$), it is transformed into a vortex blob. If a sheet crosses the boundary, moving into the body, it is reflected on the other side.

Each of these steps are depicted in Figure 1.4.

Thanks to its more natural framework, this random vortex sheet/vortex blob method turned out to be widely used to model slightly viscous flow past obstacles. For example, one can refer again to the work of [Smith and Stansby, 1988] who studied flows around cylinder, to [Sethian and Ghoniem, 1988] who performed a validation study of this technique for flow past a backward-facing step at different regimes or to [Cheer, 1983] who carried out simulations of flows past airfoils and blunt bodies. All these studies demonstrate the capability of the method to supply the qualitative behaviors of the flows. However, [Anderson and Reider, 1994] has shown numerically that the Prandtl-Navier-Stokes coupling is not consistent.

About 3D version

The three dimensional version of the vortex sheet/vortex blob method was introduced shortly after by [Chorin, 1980]. In this version, the vortex sheets within the boundary-layer region are now defined as "tiles". These tiles are rectangles, parallel to the wall and their motion is dictated by the straightforward extension of equation 1.74, that is:

$$\omega_x = -\frac{\partial u_y}{\partial z}, \qquad \omega_y = \frac{\partial u_x}{\partial z}. \tag{1.80}$$

Like in two dimensions, the tiles undergo random walk. They are transformed into vortex blobs (also referred to as vortex segments in 3D, as opposed to vortex filaments) when they leave the boundary layer. This method was successfully used in several studies, for instance by

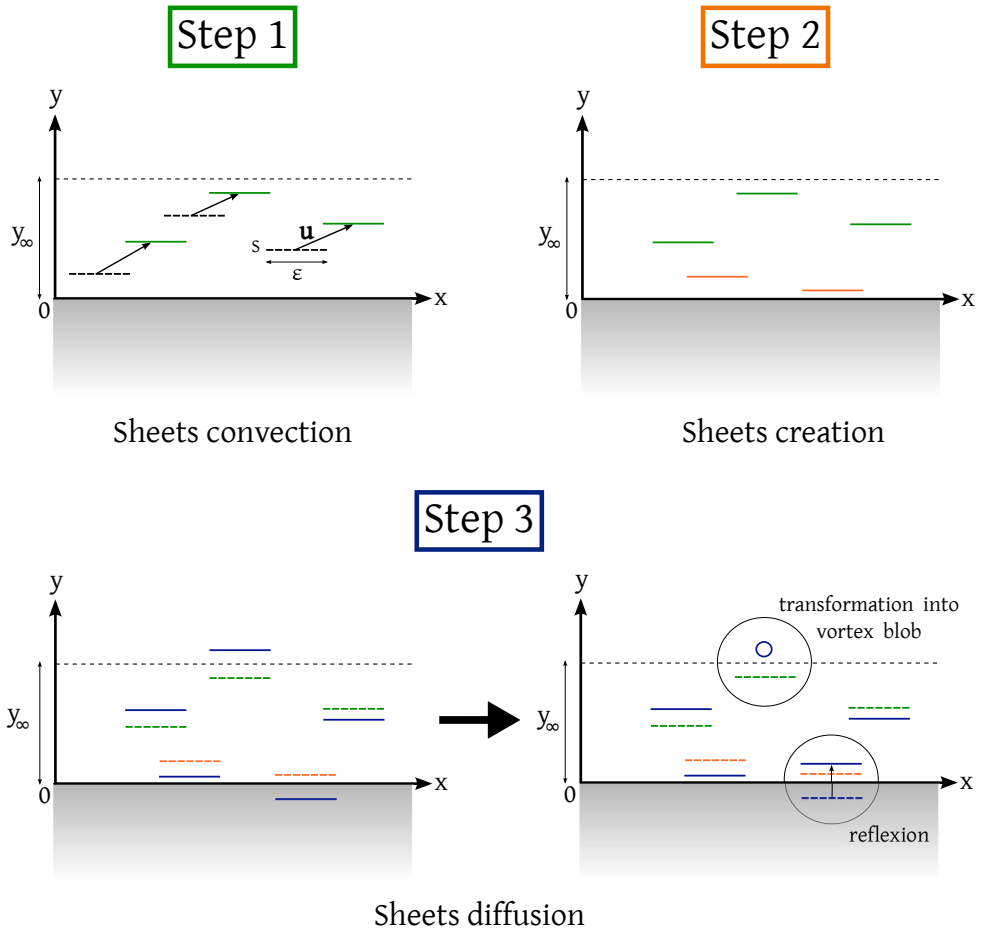

Figure 1.4: Steps of the vortex sheet/vortex blob algorithm.

[Fishelov, 1990b, Gharakhani and Ghoniem, 1998], who respectively dealt with flow past infinite plate and flow inside a cylinder equipped with an eccentric inlet port and a driven piston. However, and besides the lack of consistency highlighted numerically by Anderson and Reider in two dimensions, some other limitations arise in 3D. For example, the divergence free condition for the vorticity field is only satisfied approximately, which prevents from getting accurate application of vortex methods to three-dimensional flows. All these remarks therefore make this procedure limited.

The next subsection is dedicated to the methods using exact formulation of the vorticity boundary conditions. Their development is motivated by the wish to derive vorticity boundary conditions free of any *ad hoc* parameters.

1.3.3 Methods based on exact formulation of vorticity boundary conditions

In the literature, the problem of expressing exact formulation of vorticity boundary conditions was first addressed in order to solve the two-dimensional Navier-Stokes equations in a domain with rigid walls, in the vorticity (ω)-stream function (ψ) formulation:

$$\frac{\partial \omega}{\partial t} + (\mathbf{u} \cdot \nabla)\omega = \nu \Delta \omega \tag{1.81}$$

$$\Delta \psi = -\omega, \tag{1.82}$$

where $\nabla \times \psi \equiv \mathbf{u}$. In this formulation of the Navier-Stokes equations, one must prescribe at the walls two boundary conditions in terms of the stream function:

$$\psi = 0 \tag{1.83}$$

$$\partial\psi/\partial\mathbf{n} = 0, \tag{1.84}$$

where 1.83 models the no-through flow boundary condition, and 1.84 specifies the no-slip boundary conditions. There is no direct explicit boundary condition on the vorticity. The first and the most common approach to express the vorticity value on the boundary consists in using the normal derivative condition [Roache, 1972, Orszag and Israeli, 1974, Peyret and Taylor, 1983]. In this type of approach, often dealing with finite-differences space approximations along with time marching to satisfy the boundary conditions, a lack of accuracy is often observed with a vorticity field that may be only of order one. Other approaches have been considered in order to overcome this difficulty. One can for instance cite the works of [Quartapelle, 1981] and [Anderson, 1989] who considered that the vorticity boundary conditions have to be global. In other words, one has to solve a system of equations coupling all points located on the boundary together to achieve the boundary value of vorticity. Then one gets vorticity conditions of integrodifferential type (non local) instead of boundary value type (local).

Finally, one can also refer to the approach proposed by [Cottet, 1988b], which completely fits into the vortex methods realm and which allows to formulate either a Dirichlet or a Neumann boundary condition on the vorticity. It consists in evaluating the velocity as the solution of the following Poisson equation, supplemented with the no-slip boundary condition expressed in terms of the velocity:

$$-\Delta\mathbf{u} = \nabla \times \omega \quad \text{in} \quad V, \tag{1.85}$$

$$\mathbf{u} = 0 \quad \text{on} \quad S. \tag{1.86}$$

The Dirichlet boundary condition on the vorticity is then given by:

$$\omega = \nabla \times \mathbf{u} \quad \text{on} \quad S, \tag{1.87}$$

ensuring the incompressibility condition div $\mathbf{u} = 0$. A Neumann-type boundary condition on the vorticity was also derived in [Cottet, 1988b], defined as:

$$\frac{\partial\omega}{\partial\mathbf{n}} = \frac{\partial}{\partial\mathbf{n}}(\nabla \times \mathbf{u}) - \frac{1}{|S|}\int_S \frac{\partial}{\partial\mathbf{n}}\left[\nabla \times \mathbf{u}(\mathbf{y})\right]\, d\mathbf{y}, \tag{1.88}$$

where the second term of the right-hand side is a constant whose subtraction ensures the conservation of circulation at all time (see Kelvin's theorem).

The major weakness of the approaches detailed in this section lies in the lack of associated stability analysis and energy estimate necessary to quantify the impact of the errors made though the vorticity boundary condition on the velocity computation and thus on the discretization of the governing equations.

1.3.4 Vorticity creation methods using vorticity flux boundary conditions

The type of method presented in this section was designed later and re-use the framework of algorithms based on viscous splitting and vorticity creation. However, contrary to the Chorin's methods, detailed in sections (1.3.2.1) and (1.3.2.2), it handles vorticity flux boundary conditions to enforce the no-slip condition on the walls, instead of vortex blobs or vortex sheets. In a first part we will give the expression of the corresponding continuous problem and secondly we will focus on the numerical schemes and techniques used to approximate the integral solution of this continuous problem. Unlike the models based on the formulation of exact vorticity boundary conditions, we will see that the methods relying on vorticity flux boundary conditions provide energy estimates, ensuring the stability of the numerical schemes.

1.3.4.1 The continuous problem

2D formulation

The idea of a vorticity creation method based on a vorticity flux boundary condition was independently proposed by [Cottet, 1994] and [Koumoutsakos et al., 1994]. The so-called vorticity flux boundary condition is characterized by a relation between the normal derivative of the vorticity and the time derivative of the tangential component of the velocity. To derive the global Navier-Stokes problem, we follow the development described in [Cottet, 1994] starting with the Stokes problem. Let us consider two vorticity fields ω_1 and ω_2 in the same time interval $[t_n, t_{n+1}]$. Each time step is initialized by the exact initial vorticity field ω_n and provide at the end the solution ω_{n+1} where ω_1 and ω_2 are the solutions of the 2 following sub-problems within the interval $[t_n, t_{n+1}]$:

Sub-problem 1:

$$\begin{cases} \dfrac{\partial \omega_1}{\partial t} - \nu \Delta \omega_1 = 0 \quad \text{in} \quad V, \\ \omega_1(\cdot, t_n) = \omega_n \quad \text{in} \quad V, \\ \dfrac{\partial \omega_1}{\partial \mathbf{n}} = 0 \quad \text{on} \quad S \end{cases} \tag{1.89}$$

Sub-problem 2:

$$\begin{cases} \dfrac{\partial \omega_2}{\partial t} - \nu \Delta \omega_2 = 0 \quad \text{in} \quad V, \\ \omega_2(\cdot, t_n) = \omega_n \quad \text{in} \quad V, \\ \nu \dfrac{\partial \omega_2}{\partial \mathbf{n}} = -\dfrac{\partial}{\partial t}(\mathbf{u}_1 \cdot \mathbf{s}) \quad \text{on} \quad S, \end{cases} \tag{1.90}$$

where $\mathbf{s}$ denotes the tangent vector to the surface S and $\mathbf{u}_1$ corresponds to the velocity field associated with ω_1. According to the following explicit Euler discretization:

$$\frac{\partial \mathbf{u}}{\partial t}(t_n + \Delta t) = \frac{\mathbf{u}(t_n + \Delta t) - \mathbf{u}(t_n)}{\Delta t} + \mathcal{O}(\Delta t) = \frac{\mathbf{u}(t_n + \Delta t)}{\Delta t} + \mathcal{O}(\Delta t), \tag{1.91}$$

one can then write the approximated formulation of 1.90:

$$\begin{cases} \dfrac{\partial \omega_2}{\partial t} - \nu \Delta \omega_2 = 0 \quad \text{in} \quad V, \\ \omega_2(\cdot, t_n) = \omega_n \quad \text{in} \quad V, \\ \nu \dfrac{\partial \omega_2}{\partial \mathbf{n}} = -\dfrac{\mathbf{u}_1 \cdot \mathbf{s}}{\Delta t} \quad \text{on} \quad S. \end{cases} \tag{1.92}$$

In summary, in sub-problem 1, the Stokes equations are solved with an homogeneous Neumann boundary condition, that is to say without creating any vortex sheet on the walls. Then, in sub-problem 2, vorticity is produced at the boundary thus enabling to cancel the slip resulting from sub-problem 1. At the end of the time step, ω_{n+1} is set to $\omega_2(\cdot, t_{n+1})$. We respectively refer to parts 2.1 and 2.3 of [Cottet, 1994] for the proof of equivalence with Chorin's algorithm and the proof of convergence using energy estimates. The generalization of the present algorithm to the Navier-Stokes problem is straightforward. It simply consists in adding the advection term in equations 1.89 and 1.90 and in replacing the vorticity flux boundary condition of 1.90 by:

$$\nu \frac{\partial \omega_2}{\partial \mathbf{n}} = -\left[\frac{\partial \mathbf{u}_1}{\partial t} + (\mathbf{u}_1 \cdot \nabla)\mathbf{u}_1 \right] \cdot \mathbf{s} \tag{1.93}$$

3D formulations

In three dimensions, as the vorticity has three components, three boundary conditions are now needed instead of one.

The half-plane case

The first three dimensional extension of the above algorithm was given in the specific case of a flat plate, that is to say for a body with no curvature. We propose here to give the outline of the algorithm detailed in [Cottet and Koumoutsakos, 2000]. The plate is located at $z = 0$ and the x and the y axis are parallel to the surface S, where $\mathbf{x} = (x, y, z)$ denotes the coordinates in a Cartesian system. In these coordinates, one has:

$$\boldsymbol{\omega} = \nabla \times \mathbf{u} = (\omega_w, \omega_y, \omega_z) = \left(\frac{\partial u_z}{\partial y} - \frac{\partial u_y}{\partial z} \; ; \; \frac{\partial u_x}{\partial z} - \frac{\partial u_z}{\partial x} \; ; \; \frac{\partial u_y}{\partial x} - \frac{\partial u_x}{\partial y} \right). \tag{1.94}$$

If one assumes that the velocity vanishes at the walls, i.e. $u_x = u_y = 0$, then the normal component of the vorticity also vanishes:

$$\omega_z = 0 \quad \text{on} \quad z = 0. \tag{1.95}$$

Concerning the tangential components of the vorticity, ω_x, ω_y, it seems natural to extend the 2D vorticity flux boundary condition, in other words to impose the no-slip for the velocity components u_x and u_y by creating vorticity for the components ω_x and ω_y respectively. Discarding the subscripts $\cdot_1$ and $\cdot_2$ for the sake of clarity, the two sub-problems presented before then become:

Sub-problem 1:

The convection-diffusion equation is solved for the three components of the vorticity field using the homogeneous Dirichlet boundary condition for ω_z and homogeneous Neumann boundary conditions for ω_x, ω_y:

$$\begin{cases} \dfrac{\partial \boldsymbol{\omega}}{\partial t} - \nu \Delta \boldsymbol{\omega} = 0 \quad \text{in} \quad V, \\ \boldsymbol{\omega}(\cdot, t_n) = \boldsymbol{\omega}_n \quad \text{in} \quad V, \\ \omega_z = 0 \quad \text{on} \quad S, \\ \dfrac{\partial \omega_x}{\partial z} = \dfrac{\partial \omega_y}{\partial z} = 0 \quad \text{on} \quad S. \end{cases} \tag{1.96}$$

Sub-problem 2:

After computing the slip (u_x, u_y) at the walls, resulting from convection, the sub-problem 1 is repeated with the new Neumann boundary condition for the tangential component of the vorticity:

$$\begin{cases} \dfrac{\partial \boldsymbol{\omega}}{\partial t} - \nu \Delta \boldsymbol{\omega} = 0 \quad \text{in} \quad V, \\ \boldsymbol{\omega}(\cdot, t_n) = \boldsymbol{\omega}_n \quad \text{in} \quad V, \\ \omega_z = 0 \quad \text{on} \quad S, \\ \nu \dfrac{\partial \omega_x}{\partial z} = -\dfrac{u_y}{\Delta t} \quad \text{on} \quad S, \\ \nu \dfrac{\partial \omega_y}{\partial z} = +\dfrac{u_x}{\Delta t} \quad \text{on} \quad S. \end{cases} \tag{1.97}$$

We note that in 3D, one must ensure that the vorticity is divergence free in order to satisfy the fundamental laws of the fluid mechanics. This algorithm do guarantee this condition and we refer to [Cottet and Koumoutsakos, 2000] for the proof. However, if the considered body has a non-zero curvature, this statement is not true anymore. One then has to modify the problem 1.97 adding a corrective curvature term.

Curvature effects

Let us consider in this part the case of a cylinder, with curvature $\kappa = 1/R$. The natural coordinate system to consider herein is the cylindrical coordinate system where we denote by $(\mathbf{e}_r, \mathbf{e}_z, \mathbf{e}_\theta)$ the basis vectors, respectively corresponding to the unit normal vector $(\mathbf{e}_r)$ and the tangent vectors to the cylinder surface $(\mathbf{e}_z, \mathbf{e}_\theta)$. According to [Poncet, 2001, Cottet and Poncet, 2003] it appears that the divergence free condition is ensured if the boundary condition on the tangential component ω_θ (previously referred to as ω_y in 1.97) is modified into a Robin type boundary condition. The correct continuous problem thus yields:

$$\left\{\begin{array}{rl} \dfrac{\partial \boldsymbol{\omega}}{\partial t} - \nu\Delta\boldsymbol{\omega} = 0 & \text{in } V, \\ \boldsymbol{\omega}(\cdot, t_n) = \boldsymbol{\omega}_n & \text{in } V, \\ \boldsymbol{\omega}\cdot\mathbf{e}_r = \boldsymbol{\omega}\cdot\mathbf{n} = 0 & \text{on } S, \\ \nu\dfrac{\partial \boldsymbol{\omega}}{\partial \mathbf{n}}\cdot\mathbf{e}_z = -\dfrac{\mathbf{u}\cdot\mathbf{e}_\theta}{\Delta t} & \text{on } S, \\ \nu\left(\kappa\boldsymbol{\omega} + \dfrac{\partial \boldsymbol{\omega}}{\partial \mathbf{n}}\right)\cdot\mathbf{e}_\theta = +\dfrac{\mathbf{u}\cdot\mathbf{e}_z}{\Delta t} & \text{on } S. \end{array}\right. \iff \left\{\begin{array}{rl} \dfrac{\partial \boldsymbol{\omega}}{\partial t} - \nu\Delta\boldsymbol{\omega} = 0 & \text{in } V, \\ \boldsymbol{\omega}(\cdot, t_n) = \boldsymbol{\omega}_n & \text{in } V, \\ \omega_r = 0 & \text{on } S, \\ \nu\dfrac{\partial \omega_z}{\partial \mathbf{n}} = -\dfrac{u_\theta}{\Delta t} & \text{on } S, \\ \nu\left(\kappa\omega_\theta + \dfrac{\partial \omega_\theta}{\partial \mathbf{n}}\right) = +\dfrac{u_z}{\Delta t} & \text{on } S. \end{array}\right. \tag{1.98}$$

One can notice that if $\kappa = 0$, then one recovers problem 1.97.

1.3.4.2 The integral approach

The issue now lies on the resolution of the continuous problems derived above in order to obtain an explicit expression of the approximated vorticity field, such that the no-slip boundary condition is satisfied. The successive substeps of the general existing algorithms stand as follows: first, the particles are advected and the diffusion is solved in the domain with a PSE scheme. Then the vorticity flux boundary condition is expressed in terms of an integral formulation and finally the PSE scheme in complemented by distributing this vorticity flux onto the existing vortex blobs so that vorticity enters the domain. In this last step, particles just experience a change in their strength without multiplying themselves, like in Chorin's methods. In the following, we will focus on the different approximations of the continuous diffusion problems described previously.

The 2D solution

The method presented hereafter to solve the continuous problem 1.90 was introduced and validated by [Koumoutsakos et al., 1994, Koumoutsakos and Leonard, 1995]. We re-write the problem 1.90 by considering the vorticity diffusion equation supplemented with an homogeneous initial condition and a Neumann boundary condition:

$$\frac{\partial \omega}{\partial t} - \nu\Delta\omega = 0 \quad \text{in } V \times [0,\ t], \tag{1.99}$$

$$\omega(\mathbf{x}, 0) = 0 \quad \text{in } V, \tag{1.100}$$

$$\nu\frac{\partial \omega}{\partial \mathbf{n}} = F(\mathbf{x}, t) = -\frac{\partial}{\partial t}(\mathbf{u}\cdot\mathbf{s}) \quad \text{on } S \times [0,\ t]. \tag{1.101}$$

The integral solution of equation 1.101 for the vorticity involves integrals over the surface S only. To discretize this integral, a boundary integral method is employed by defining S as a set of discrete panels, denoted with index i, length d and centered in $\mathbf{x}_i$. Then, the vorticity induced by a panel i can be given by the following integral:

$$\omega_i(\mathbf{x},t) = \frac{1}{2}\int_0^t \mu_i(\tau)\phi(\mathbf{x}-\mathbf{x}_i, t-\tau)\ d\tau, \tag{1.102}$$

where, if one defines a coordinate system $\mathbf{x} = (x, y)$ with the x axis parallel to the surface, the ϕ function yields:

$$\phi(\mathbf{x}, t-\tau) = \frac{e^{\frac{-y^2}{4\nu(t-\tau)}}}{\sqrt{4\pi\nu(t-\tau)}}\left\{\mathrm{erf}\left[\frac{d+x}{\sqrt{4\nu(t-\tau)}}\right] + \mathrm{erf}\left[\frac{d-x}{\sqrt{4\nu(t-\tau)}}\right]\right\}, \tag{1.103}$$

and where $\mu(\mathbf{x}, t)$, the diffusion potential, can be approximated for points s along S by:

$$\mu_i(s) \approx -2F_i(s)\left[1-\kappa(s)\sqrt{\pi\nu\Delta t}\right]^{-1} \approx -2\left(-\frac{(\mathbf{u}\cdot\mathbf{s})}{\Delta t}(s_i)\right)\left[1-\kappa(s)\sqrt{\pi\nu\Delta t}\right]^{-1}, \tag{1.104}$$

where $\gamma_i = -\dfrac{(\mathbf{u}\cdot\mathbf{s})}{\Delta t}(s_i)$ corresponds to the vortex sheet strength derived from 1.101. We refer the reader to [Koumoutsakos et al., 1994] for a full description of the integral evaluation of equation 1.102.

Then, the strength $\Gamma_j = \omega(\mathbf{x}_j)v_j$ of the particles are modified by distributing the vorticity flux:

$$\Gamma_j(t) = \Gamma_j(0) + \frac{v_j\Delta t}{2}\sum_{i=1}^{N}\mu_i\phi\Big((\mathbf{x}_j-\mathbf{x}_i), \Delta t\Big), \tag{1.105}$$

with N denoting the number of panels on the surface of the body. Finally, replacing μ_i by approximation 1.104 in the above equation, the prescription of the no-slip boundary condition is performed through the following particle strength update:

$$\Gamma_j^{n+1} = \Gamma_j^n + v_j\Delta t\sum_{i=1}^{N}\frac{\gamma_i}{\Big(1-\kappa(s)\sqrt{\pi\nu\Delta t}\Big)}\phi\Big((\mathbf{x}_j-\mathbf{x}_i), \Delta t\Big). \tag{1.106}$$

The 3D solutions

The half-plane case

An analysis similar to the one just detailed above was performed in three dimensions by [Casciola et al., 1996] in order to solve the problem 1.97. First of all, this study supplies the expression of the integral equation for the vorticity creation. An approximation of such integral equation is then given and identified as the slip velocity at the surface of the body. Moreover, this work exposes an error estimate of the proposed approximation and also proves that the vorticity generated at the wall and then diffused in the flow is solenoidal.

Curvature effects

Finally, the tri-dimensional numerical scheme giving the solution of 1.98 is derived by [Poncet, 2001, Cottet and Poncet, 2003]. In these studies, the initial continuous problem is split in two sub-equations, respectively referred to as:

the *axial* equation:

$$\begin{cases} \dfrac{\partial\omega_z}{\partial t} - \nu\Delta\omega_z = 0 \quad \text{in } V, \\ \omega_z(\cdot, t_n) = \omega_z^n \quad \text{in } V, \\ \nu\dfrac{\partial\omega_z}{\partial\mathbf{n}} = -\dfrac{u_\theta}{\Delta t} \quad \text{on } S, \end{cases} \tag{1.107}$$

and the *azimuthal* equation:

$$\begin{cases} \dfrac{\partial \boldsymbol{\omega}}{\partial t} - \nu \Delta \boldsymbol{\omega} = 0 \quad \text{in} \quad V, \\ \boldsymbol{\omega}(\cdot, t_n) = \boldsymbol{\omega}_n \quad \text{in} \quad V, \\ \omega_r = 0 \quad \text{on} \quad S, \\ \nu \left(\kappa \omega_\theta + \dfrac{\partial \omega_\theta}{\partial \mathbf{n}} \right) = + \dfrac{u_z}{\Delta t} \quad \text{on} \quad S. \end{cases} \tag{1.108}$$

The final solution is expressed as the synthesis of the two sub-solutions of 1.107 and 1.108. We refer the reader to [Poncet, 2001] for the complete formulation of the resulting solution along with a full description and validation of the integral techniques used to solve the problem. This validation, performed in the case of a ring impinging on a 3D cylinder at $Re = 400$, shows the accuracy of the vorticity flux boundary conditions in terms of the flow diagnostics.

All the different approaches presented in this section highlight the important efforts which have been made between the early 1970's until the mid 1990's in order to design methods able to model the no-slip boundary condition. The successful idea of the pioneer approach, introduced by Chorin in 1973 and further improved in 1978, was based on the mimicking of the physical creation of vorticity at the boundary due to viscosity. However, the difficulties of this method in modeling fully separated flow and in providing a consistent numerical model led to consider exact formulations of the vorticity boundary conditions. However, because of the lack of related energy estimate and stability analysis, the latter did not really manage to be adopted. The handling of the no-slip boundary condition using vorticity flux formula finally stands as the most suitable method. It indeed allows to treat in an accurate way the high velocity gradients at the solid-fluid interface while overcoming the main drawbacks of the prior approaches.

1.4 Distortion of particle distribution, remeshing and hybrid methods

1.4.1 The particle overlapping

In pure Lagrangian method, the particle distribution may undergo distortion, that manifests itself by the clustering or spreading of the flow elements in high strain regions. This accumulation or dispersion phenomenon is then translated in inaccurate computations because of a deteriorated communication between particles, which is actually the keypoint of the vortex methods. As meaningful illustrations of the distortion effect one can cite the test case of the axisymmetric inviscid vortex patch, illustrated in [Cottet and Koumoutsakos, 2000]. In this example, one can observe the distortion of the initial and uniform particle distribution due to the important shear. One can also refer to [Henshaw et al., 1989, Krasny, 1986] for comparable observations concerning the appearance of non-physical small scales in vortex sheet calculations in the context of two dimensional inviscid flows. Concerning viscous flows and as already mentioned in section (1.2.3), the use of particle strength exchange may increase the difficulty in getting accurate simulations, since the particles can not diffuse their vorticity if they do not overlap, that is to say if the cutoff size ε is not at least of the order of h, the distance between particles. More precisely, the numerical analysis given in [Cottet and Koumoutsakos, 2000] provides the following convergence result, already mentioned in section (1.1.3):

Theorem 1.2

Assume that ζ is a cutoff function of the order r in the sense of definition 1.1. Assume also that there exists $s > 0$ such that $h/\varepsilon \leq \varepsilon^s$, then for h small enough the following estimate holds for $t \in [0,\ T]$:

$$\|\omega^n - \omega_\varepsilon^h\|_{L^p(\Omega)} \leq C(T)\varepsilon^r \tag{1.109}$$

where ω^n refers to the vortex point approximation 1.8 and ω_ε^h to the vortex blob approximation 1.21. In other words, this theorem means that the overlapping of particles ($h/\varepsilon \to 0$) is necessary in order to ensure the convergence of ω_ε^h towards ω^n.

Several solutions have been designed in order to overcome the distortion problem. One can separate these methods in two different classes.

The first class deals with methods involving a change in particle strength in order to correct the vorticity field without modifying the particle location. Among these methods one can first refer to the approach developed by [Beale, 1988] which consists in correcting the circulation at each time step, through an iterative procedure. This technique has been successfully used by [Choquin and Lucquin-Desreux, 1988] to model incompressible viscous flow with a PSE scheme. However, the iterative process may be slow to converge in case of particle clustering or irregularities in the vorticity fields. A second type of methods one can mention, and which was already cited in the section dedicated to viscous vortex methods, are the Free-Lagrange methods. They were not initially designed to tackle the distortion problem but they actually offer a good framework to handle it. They consist in creating a triangulation, whose nodes are the particles locations, which is then used to interpolate the circulation carried by the flow elements. For instance, the Delaunay triangulation, suggested by [Russo and Strain, 1994] and obtained connecting the particles when they belong to adjacent polygons in a Voronoi diagram, enables one to successfully avoid the distortion of the particle distribution and provides a second-order accurate vortex scheme. An other example one can cite among these Free-Lagrange methods is the adaptive quadrature method introduced by [Strain, 1997]. This approach allows to increase the order of accuracy of the usual triangulation methods by considering sub-elements that would combine several triangles together. Finally, one can cite the strategy introduced by [Schrader et al., 2010] which can be considered as a generalization of the PSE method. It indeed proposes to correct the method given by [Eldredge et al., 2002] consisting in approximating the derivatives on scattered particles locations. This corrected framework of the PSE scheme enables one to achieve the convergence without any overlapping condition and regardless of the resolution. However, the convergence of the latter was limited to a certain range of resolutions.

The second class of methods designed in order to remedy the distortion problem are based on a frequent re-location of the particles onto new positions where the overlapping condition is satisfied. These methods allow to directly control the distance between the particles, thus ensuring the convergence of the solution. Historically, this approach first appeared in the framework of vortex filament methods, where the connectivity of the particles along the filament was used for refinement/regridding when the distance between particles became critical. Since the positions of markers along the filament are known at all times, it was indeed easy to create a new particle between two consecutive markers whenever their distance exceeds a given threshold. This curve reconstruction strategy was originally introduced by [Rehbach, 1978] and thoroughly used since then. More recently, [Farjoun and Seibold, 2009] proposed a similar approach, first of all motivated by the will to satisfy the conservation laws. It consists in inserting new particles in under-resolved regions and merging particles in the clustering parts of the flow. We can note that this technique has been also widely used with Smooth Particle Hydrodynamics methods (SPH) in order to achieve realistic visual effects as well as improvements in computational performance [Adams et al., 2007, Dongli and Hong, 2012].

The following section is dedicated to the description of another re-location method, called the remeshing technique, on which the vortex method considered in this thesis is based.

1.4.2 The remeshing procedure

From the pioneer work of [Huberson and Jollès, 1990, Koumoutsakos and Leonard, 1995], this approach has been widely and is still successfully used in vortex methods [Koumoutsakos, 1997, Ould-Salihi et al., 2000, Cottet and Poncet, 2003, Koumoutsakos, 2005, Cottet and Weynans, 2006, Chatelain et al., 2008, van Rees et al., 2013]. Since we will also handle the remeshing process in the numerical method proposed in this thesis, a whole section is here dedicated to the global and historical description of this technique, which represents an efficient way to control the distance between particles. More details will be provided in the following chapter of this thesis concerning the practical use of the remeshing step in our case.

The remeshing technique consists in redistributing the particles on an underlying Cartesian grid. The description of the regridding process is here proposed for the one-dimensional case. Let us denote by $\tilde{x}_q$ the position of the particle q carrying the circulation $\tilde{\Gamma}_q$. These particles are remeshed at the grid points x_k of a uniform Cartesian grid, with spacing h, using the interpolation kernel W of support $[-M_s,\ +M_s]$ like follows:

$$\Gamma_k = \sum_q \tilde{\Gamma}_q W\left(\frac{x_k - \tilde{x}_q}{h}\right). \tag{1.110}$$

In other words, this procedure means that every grid point k receives the sum of the weighted values of the circulation carried by the particles for which k is included in the interpolation support.

Let us recall that one of the strong advantages of the vortex methods lies in their capability to satisfy the conservation properties. In order to preserve this important feature, the interpolation kernel has to be constructed such that the successive moments are conserved. For instance, to satisfy the total circulation invariance (and more generally, the conservation of mass), W must ensure:

$$\sum_k W\left(\frac{x - x_k}{h}\right) = 1. \tag{1.111}$$

The conservation of the first p moments is given by the following conditions:

$$\sum_q x_q^\alpha\ W\left(\frac{x_q - x}{h}\right) = x^\alpha, \quad 0 \leq |\alpha| \leq p-1, \tag{1.112}$$

and W is therefore an interpolation kernel of order p (we refer to [Cottet and Koumoutsakos, 2000] for the proof of this assessment). For $p = 0, 1$ and 2, the conservation of the total circulation, the linear impulse and the angular impulse are respectively ensured.

In the following, we will describe the different kernel families, detailing their construction as well as their properties.

1.4.2.1 The ordinary interpolation kernels

This class includes the kernels whose construction is only based on the satisfaction of conditions 1.112. These kernels, denoted Λ_p where p refers to the maximum order of conserved moments, are piecewise polynomial functions of degree p. Their construction requires the calculation of $p(p+1)$ coefficients, obtained from the relations 1.112. For $p = 1$, one gets the linear interpolation kernel, satisfying mass conservation:

$$\Lambda_1(x) = \begin{cases} 1 - |x| & \text{if} \quad |x| \leq 1 \\ 0 & \text{otherwise.} \end{cases} \tag{1.113}$$

As can be seen on Figure 1.5a where are also plotted Λ_2, Λ_3 and Λ_4, this type of kernels suffer from a lack of regularity. One can notice that Λ_2 is not even continuous, which is expected to lead to inaccurate solutions. In order to reduce the creation of oscillations due to the poor regularity of the kernels, [Cottet and Magni, 2009, Magni and Cottet, 2012] proposed to insert correction formulas in the expression of Λ_p.

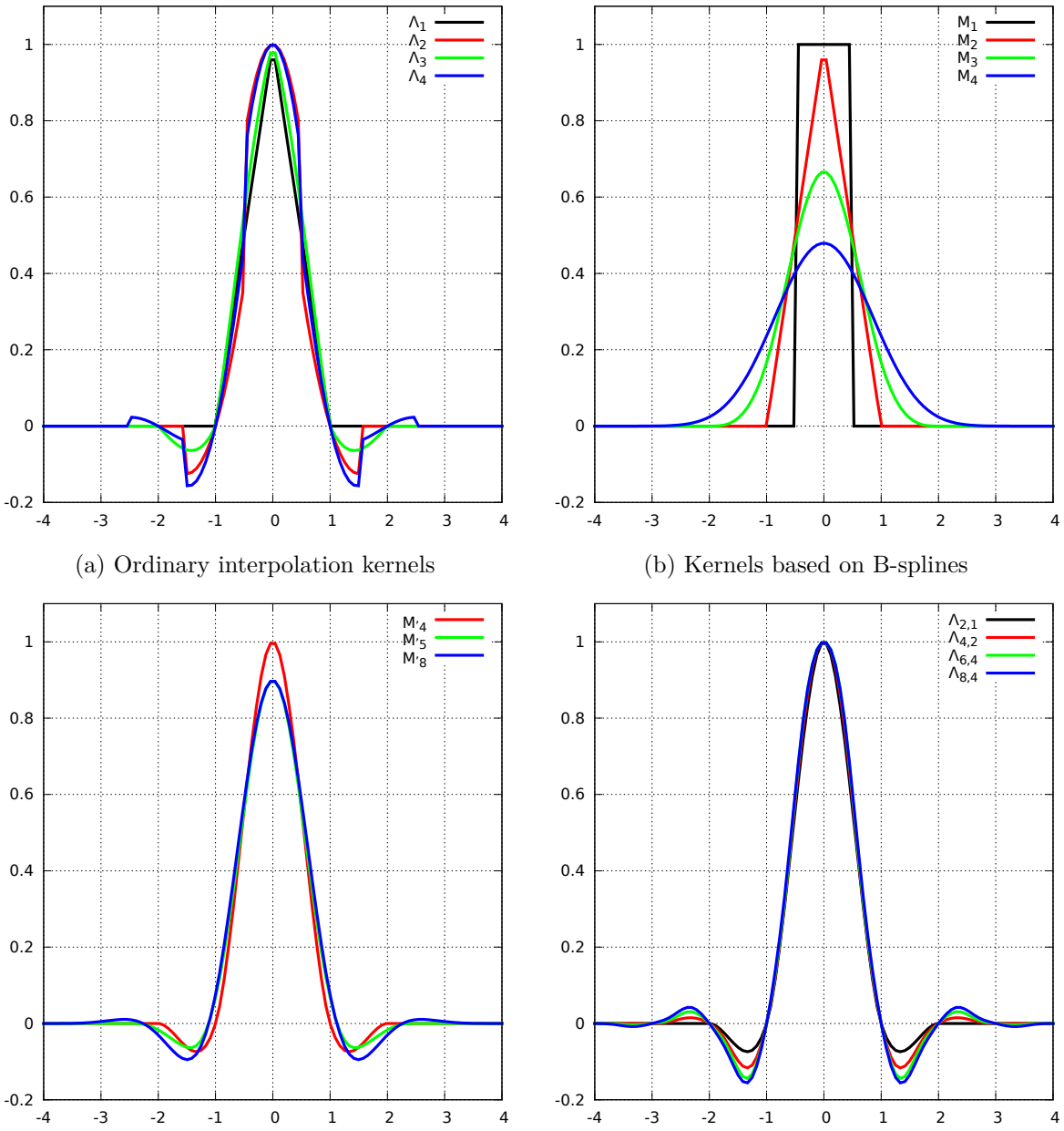

(a) Ordinary interpolation kernels

(b) Kernels based on B-splines

(c) Extrapolation of B-splines kernels

(d) High order kernels

Figure 1.5: Remeshing kernels

1.4.2.2 The B-splines-based kernels

Smooth kernels, denoted M_p, may be obtained using B-splines [Schoenberg, 1946]:

$$M_p(x) = \frac{1}{2\pi} \int_{-\infty}^{\infty} \left(\frac{\sin \xi/2}{\xi/2} \right)^p e^{ix\xi} \, d\xi \tag{1.114}$$

For $p = 1$ one gets the top-hat function, M_1. The p-order kernels M_p thus correspond to the successive convolutions of M_1: $M_p = M_1^{(*p)}$ and each kernel M_p is of class $\mathcal{C}^{p-2}$ (Figure 1.5b). M_3 and M_5 particularly distinguish themselves for their non-oscillatory properties, as illustrated in [Magni, 2011]. Nevertheless, the M_p kernels only ensure the conservation of the two first moments, which strongly limits the accuracy of the remeshing procedure.

1.4.2.3 Extrapolation of B-splines-based kernels

In order to achieve higher order remeshing schemes while preserving their smoothness properties, an extrapolation of the M_p kernels is proposed by [Monaghan, 1985]. It consists in deriving linear combinations of the M_p kernels and their derivatives, more precisely $W = \sum_{l=0}^{p/2} \alpha_{l+1} x^l M_j^{(l)}$, such that the successive continuous moments of W are canceled:

$$\int y^\alpha W(y) \, dy = \begin{cases} 1 & \text{if} \quad \alpha = 0 \\ 0 & \text{if} \quad 1 \leq \alpha \leq p. \end{cases} \tag{1.115}$$

With this approach, [Monaghan, 1985] obtained the so-called M_4' kernel defined by:

$$W = M_4' = \frac{1}{2} \left(3M_4(x) + x \frac{dM_4}{dx}(x) \right) \tag{1.116}$$

$$= \begin{cases} 1 - \frac{5}{2}|x|^2 + \frac{3}{2}|x|^3 & \text{if} \quad |x| \leq 1 \\ \frac{1}{2}(1-|x|)(2-|x|)^2 & \text{if} \quad 1 \leq |x| \leq 2 \\ 0 & \text{otherwise.} \end{cases} \tag{1.117}$$

This kernel is of class $\mathcal{C}^1$, it is piecewise cubic, and its support is of size 4 on $[-2, \, 2]$. Locally this kernel offers a third-order accurate scheme, although its global order is 2. In practice, the M_4' is a very good compromise between regularity, accuracy and computational cost: that is the reason why it is still used to simulate vortex flows [Gazzola et al., 2011, Gazzola et al., 2012, Gazzola et al., 2014]. However, these extrapolated smooth kernels do not systematically satisfy the following interpolation property:

$$W(i) = \begin{cases} 1 & \text{if} \quad i = 0 \\ 0 & \text{otherwise.} \end{cases} \tag{1.118}$$

For instance, the M_4' kernel does satisfy this condition, but it is not the case of the one derived from M_8 (Figure 1.5c). Nevertheless, this property is essential since its dictates the algebraic conservation of the exact solution if the velocity is zero (that is to say if the particles do not move from their original location on the grid).

1.4.2.4 High order kernels

Recently, [Bergdorf and Koumoutsakos, 2006] proposed a higher order kernel, called M_6' and in 2014 [Cottet et al., 2014] used high order kernels in a systematic way, also providing proofs of stability for remeshing problems. These high order kernels satisfy simultaneously the interpolation property, the smoothness and the moment conditions to any desired order. Their construction thus relies on the satisfaction of the five following properties:

- P1: W has support in $[-M_s,\ +M_s]$,
- P2: W is even and piecewise polynomial of degree M in intervals of the form $[i,\ i+1]$,
- P3: W is of class $\mathcal{C}^r$,
- P4: W satisfies the moment properties 1.112 for a given value of p
- P5: W satisfies the interpolation property 1.118.

In [Cottet et al., 2014], a new global notation is proposed for these high order remeshing kernels and stands as $\Lambda_{p,r}$ where p denotes the order to which moment conditions are satisfied and r refers to the regularity of the kernel. Figure 1.5d depicts some of these kernels. We particularly focus the attention of the reader on kernels $\Lambda_{2,1}$ and $\Lambda_{4,2}$, which respectively correspond to M'_4 previously mentionned and M'_6 proposed by [Bergdorf and Koumoutsakos, 2006], since they will be the two different kernels mainly used in the present thesis.

1.4.2.5 The directional splitting

For multiresolution problems, the remeshing step is classically performed through a tensorial product of the chosen 1D kernel formula. It is the case for instance for all the studies cited at the beginning of section (1.4.2). For example, if the desired kernel has a 1D-support of $S = 2M_s$ points, then the number of operations needed to interpolate one particle on the grid is proportional to S^2 for a two-dimensional problem and to S^3 for a three-dimensional one. Recently, a new method was proposed in [Magni and Cottet, 2012] for the particle redistribution procedure. Based on a viscous splitting (see section (1.2.1)), it consists in successively solving monodirectional sub-problems, including the advection and the remeshing step. In other words for a N-dimensional problem, one applies the following algorithm for each particle:

for d $\in \{1, ..., N\}$:

- advection in the direction d
- remeshing in the direction d

We refer to Figure 1.6 for a comparative pattern of tensorial product and directional splitting methods. As a consequence, if the chosen kernel contains S points in its 1D-support, the number of operations with the directional splitting method goes from $\mathcal{O}(S^2)$ to $\mathcal{O}(2S)$ in 2D and from $\mathcal{O}(S^3)$ to $\mathcal{O}(3S)$ in 3D. If we consider the three-dimensional case, a meaningful example is the one of the $\Lambda_{8,4}$ interpolation kernel (Figure 1.5d). Indeed, as its support includes 10 points, the directional splitting method allows to divide the number of operations by more than 33! For kernels $\Lambda_{2,1}$ ($S = 4$) and $\Lambda_{4,2}$ ($S = 6$), the ratios are respectively ~ 5 and 12. This directional splitting consequently allows for a drastic reduction of the computational cost in terms of regridding operations.

To remedy the main drawback of this approach, which lies in the fact that the increase of the time-order of the method is more complicated than for the traditional tensorial approach, [Magni and Cottet, 2012] also proposed the so-called Strang splitting method, which was successfully used afterward by [Cottet et al., 2014] in the context of passive scalar advection problems. This method consists in performing the directional advection/remeshing step using half time steps, except for the last direction where one can gather the operations on $[t_n;\ t_{n+1/2}[$ and $[t_{n+1/2};\ t_{n+1}[$ together. It is therefore of order 2 in time. The different substeps of this approach are respectively given below for the 2D and the 3D case:

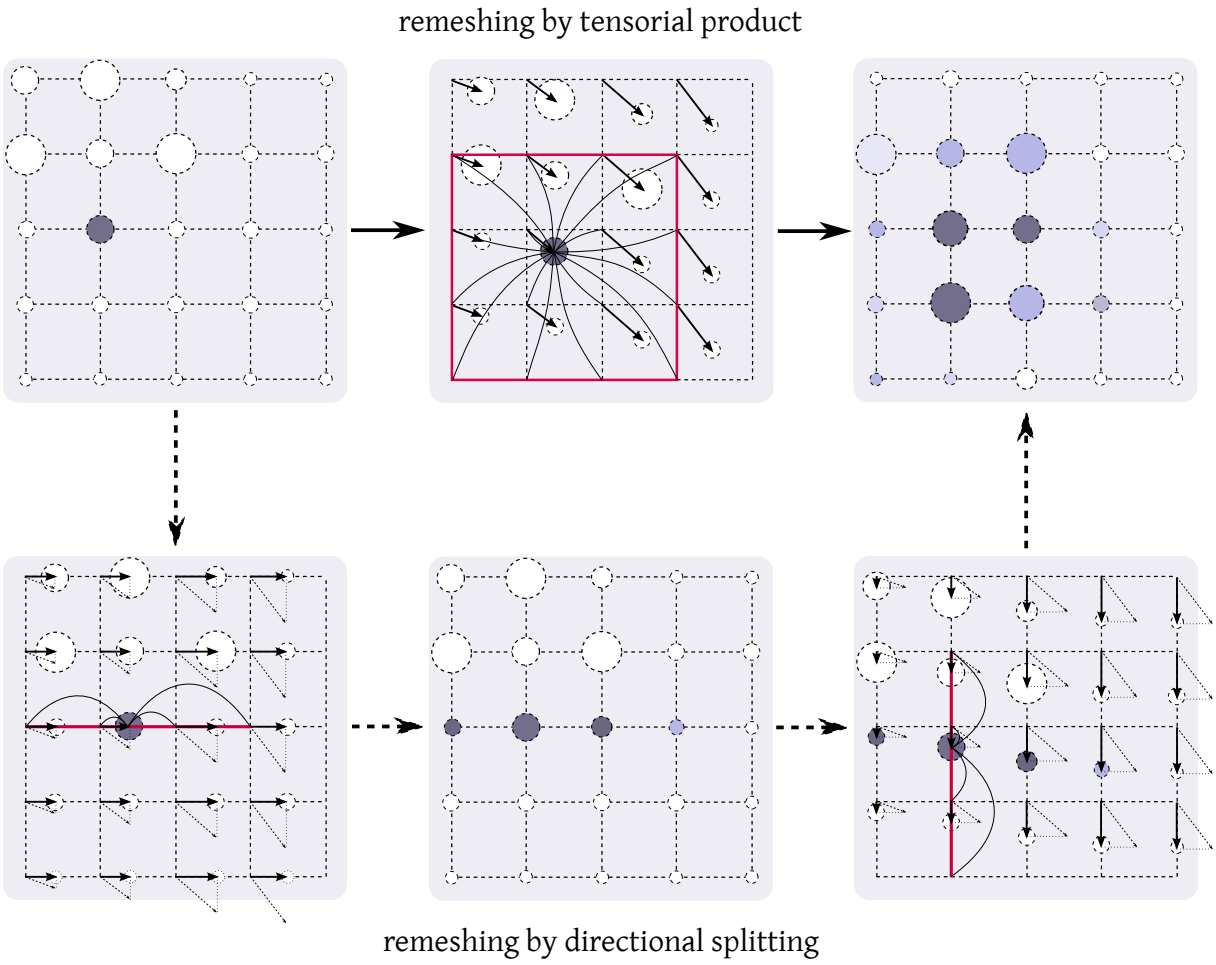

Figure 1.6: Remeshing procedure using a tensorial product (on top, depicted by plain arrows) and a directional splitting (on bottom, depicted by dashed arrows). The red lines indicate the support of the remeshing kernel. In this example, the kernel has a 1D-support of 4 points.

2D case

- advection + remeshing in the X-direction on $[t_n;\ t_{n+1/2}[$
- advection + remeshing in the Y-direction on $[t_n;\ t_{n+1}[$
- advection + remeshing in the X-direction on $[t_{n+1/2};\ t_{n+1}[$

3D case

- advection + remeshing in the X-direction on $[t_n;\ t_{n+1/2}[$
- advection + remeshing in the Y-direction on $[t_n;\ t_{n+1/2}[$
- advection + remeshing in the Z-direction on $[t_n;\ t_{n+1}[$
- advection + remeshing in the Y-direction on $[t_{n+1/2};\ t_{n+1}[$
- advection + remeshing in the X-direction on $[t_{n+1/2};\ t_{n+1}[$

With the Strang splitting method, a multidimensional remeshing thus costs $\mathcal{O}(3S)$ (respectively $\mathcal{O}(5S)$) operations per particle in 2D (respectively in 3D).

The introduction of an underlying grid in order to ensure particle overlapping modifies the essence of the original vortex methods since Lagrangian vortex particles and Cartesian mesh now coexist. As a first type of vortex method using the existence of an underlying grid, one can cite the one proposed by [Ploumhans et al., 2002]. This method, which is a 3D extension of the two dimensional vortex PSE method derived for viscous flows, involves a regular indicial lattice in order to remesh the vortex particles. Among the other vortex methods that use grids, there are the semi-Lagrangian methods, also called hybrid vortex methods in this context. In this type of approach, Lagrangian and Eulerian schemes are alternatively used in order to solve the governing equations. The last part of this section is dedicated to the description of the two main hybrid vortex methods, namely the domain decomposition method and the Vortex-In-Cell (VIC) method.

1.4.3 Hybrid vortex methods

Hybrid vortex methods were developed in order to overcome the main weaknesses of the pure Lagrangian vortex methods which essentially lie in the treatment of the viscous effects (see section (1.2)) and the near wall boundary conditions (see section (1.3)). In order to preserve the robustness of the global scheme, characterized by minimal numerical dissipation, these methods still involve a Lagrangian framework for the convection process but they also handle a fixed Cartesian grid. The presence of this grid facilitates the prescription of the no-slip boundary conditions as well as the modeling of the diffusive term, using Eulerian schemes, and ensures the particle overlapping condition. Concerning these Eulerian schemes, we will often refer in the following to finite-differences schemes, but it should be noticed that any type of grid-based schemes may also be used, like finite-volumes, finite-elements or spectral methods. To summarize, in the following we will consider a vortex method as *hybrid* whenever the resolution of the vorticity transport equation and the velocity Poisson equation will be handled both on the particles and on an underlying Cartesian grid.

The first hybrid vortex method presented here relies on the fact that grid methods and Lagrangian methods are used in different parts of the computational domain, where Eulerian schemes are implemented in the near wall region while a grid-free vortex method is chosen to solve the wake region. This Eulerian-Lagrangian domain decomposition method distinguishes itself from the Vortex-In-Cell (VIC) method which alternatively uses grid schemes or vortex methods to handle the different sub-equations of the viscous splitting algorithm (see section (1.2.1)). The VIC method will be further introduced in this section.

Before introducing these two particle-grid approaches, we need to define the common thread between all hybrid methods which stands in the way to exchange information between Eulerian and Lagrangian schemes. More precisely, hybrid methods require on one hand to transfer the values of the flow fields $\mathbf{a}$ from the particles to the grid points (we will denote it the *P2M* process, for *Particle to Mesh*) and on the other hand to transfer the values of $\mathbf{a}$ from mesh points to the particle distribution (we will denote it the *M2P* process, for *Mesh to Particle*).

Let us first define the *P2M* scheme, also called the assignment scheme. This process can be considered as a particular case of the remeshing procedure presented previously and is defined by the following scheme:

$$\mathbf{a}_k = \frac{1}{\mathbf{V}_k} \sum_p v_p \mathbf{a}_p \phi_k(\mathbf{x}_p), \tag{1.119}$$

where $\mathbf{V}_k$ corresponds to the volume surrounding the grid point $\mathbf{x}_k$ (this volume equals to h^3 if the mesh is Cartesian with a uniform mesh size h) and the basis function ϕ_k is defined by:

$$\phi_k(\mathbf{x}_p) = \phi\left(\frac{\mathbf{x}_p - \mathbf{x}_k}{h}\right), \tag{1.120}$$

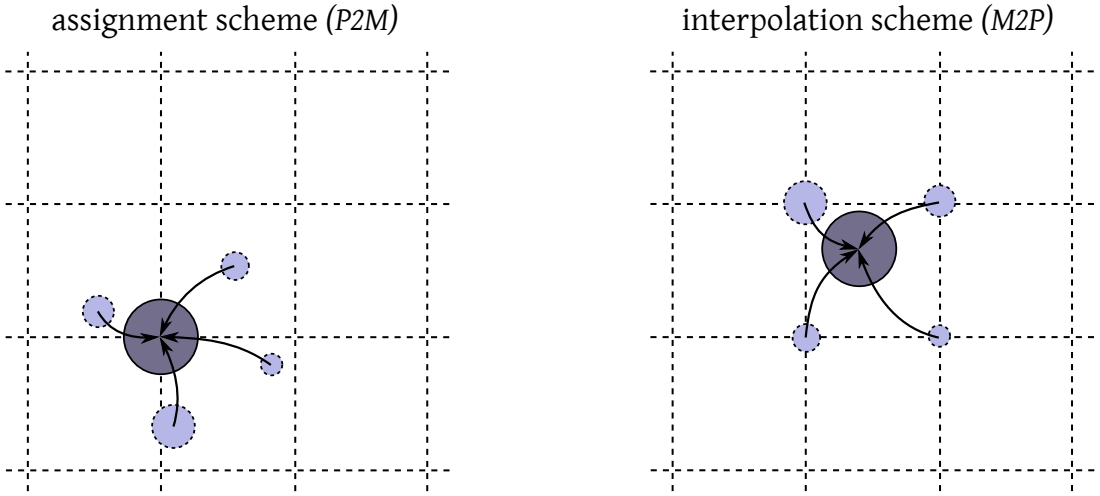

Figure 1.7: Assignment and interpolation schemes.

and satisfies:

$$\sum_k \phi_k \equiv 1. \tag{1.121}$$

If the considered grid is Cartesian, the basis function ϕ may be taken as one of the M_p, M'_p or $\Lambda_{r,p}$ functions described in the previous section.

On the other hand, the *M2P* scheme, also called the interpolation scheme, yields:

$$\mathbf{a}_p = \sum_k \mathbf{a}_k \phi_k(\mathbf{x}_p) \tag{1.122}$$

These *P2M* and *M2P* formula lead to conservative schemes. They are depicted in Figure 1.7.

1.4.3.1 The Eulerian-Lagrangian domain decomposition methods

With this type of hybrid methods, the idea is to benefit from the respective strengths of grid-based and vortex schemes. On one hand the grid-based method, which is used in the flow regions containing obstacles, enables one to accurately impose the no-slip boundary conditions and on the other hand the vortex method, which is implemented elsewhere, ensures an accurate modeling of the convection-diffusion effects and also provides a simplified treatment of the far-field boundary conditions. Following the idea of [Cottet, 1991], who first proposed this approach in the context of inviscid flows, we detail hereafter a domain decomposition algorithm allowing to solve the Navier-Stokes equations with overlapping domains. Let us respectively denote by Ω_1 and Ω_2 the Eulerian (grid-based) and Lagrangian (grid-free) domains. S_1 and S_2 respectively refer to the outer boundary of Ω_1 and the inner boundary of Ω_2; they define the boundaries of the overlapping zone (Figure 1.8).

The algorithm, based on viscous splitting, consists in solving in a first time the Poisson equation for the velocity and in a second part the convection-diffusion equation.

In Ω_1 these equation express as:

$$\text{(Poisson equation)} \qquad \Delta\boldsymbol{\psi} = -\boldsymbol{\omega}, \tag{1.123}$$

$$\mathbf{u} = \nabla \times \boldsymbol{\psi}, \tag{1.124}$$

$$\text{(Convection-diffusion)} \qquad \frac{\partial \boldsymbol{\omega}}{\partial t} + (\mathbf{u}\cdot\nabla)\boldsymbol{\omega} - (\boldsymbol{\omega}\cdot\nabla)\mathbf{u} = 0, \qquad \frac{\partial \boldsymbol{\omega}}{\partial t} = \nu\Delta\boldsymbol{\omega}, \tag{1.125}$$

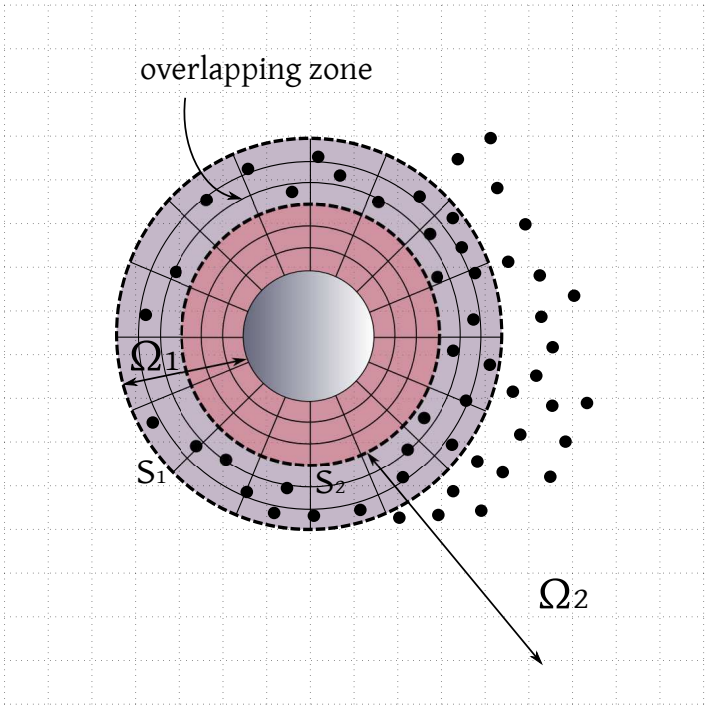

Figure 1.8: Domain decomposition for flow past a circular obstacle with overlapping Eulerian Ω_1 and Lagrangian Ω_2 domains. In this case, inspired from [Cottet et al., 2000], Ω_1 is defined by a polar mesh and a uniform Cartesian grid lies in Ω_2 for particle remeshing.

and in Ω_2 as:

$$\text{(Poisson equation)} \qquad \boldsymbol{\psi} = \int_{\Omega_2} G(\mathbf{x}-\mathbf{y})\boldsymbol{\omega}(\mathbf{y})\ d\mathbf{y} + \int_{S_2} \frac{\partial G}{\partial \mathbf{n}_x}(\mathbf{x}-\mathbf{y})\boldsymbol{\psi}(\mathbf{y})\ d\mathbf{y} + \int_{S_2} G(\mathbf{x}-\mathbf{y})\frac{\partial \boldsymbol{\psi}}{\partial \mathbf{n}}(\mathbf{y})\ d\mathbf{y}, \tag{1.126}$$

$$\mathbf{u} = \nabla \times \boldsymbol{\psi}, \tag{1.127}$$

$$\text{(Convection-diffusion)} \qquad \frac{d\mathbf{x}_p}{dt} = \mathbf{u}, \qquad \frac{d\boldsymbol{\omega}_p}{dt} = (\boldsymbol{\omega}\cdot\nabla)\mathbf{u} + \nu\Delta\boldsymbol{\omega}_p \tag{1.128}$$

The Poisson equation is commonly solved using a Schwarz alternative method. The later relies in computing firstly the solution in Ω_1 using the boundary conditions on S_1 obtained in Ω_2 at the previous iteration (let us call them $S^{n-1}_{1_{\Omega_2}}$) and then in computing the solution in Ω_2 using the boundary conditions on S_2 obtained in Ω_1 at the current iteration (let us call them $S^{n}_{2_{\Omega_1}}$). Then, once the convergence of the Schwarz algorithm is achieved, the convection-diffusion equation is solved in each domain where the respective boundary conditions are evaluated using assignment (*P2M*) and interpolation (*M2P*) formulas (1.119 and 1.122).

Finally, the complete algorithm yields as follows:

1. **Poisson equation**

   Schwarz iterative method

   (a) Solve 1.123 in Ω_1 using a grid solver, with $\boldsymbol{\psi}$ on $S^{n-1}_{1_{\Omega_2}}$

   (b) Deduce the values of $\boldsymbol{\psi}$ and $\partial\boldsymbol{\psi}/\partial\mathbf{n}$ (for source terms of integral equation 1.126) on fixed grid points on S_2 (i.e. $\boldsymbol{\psi}$ and $\partial\boldsymbol{\psi}/\partial\mathbf{n}$ on $S^{n}_{2_{\Omega_1}}$)

   (c) Solve 1.126 in Ω_2 with an integral solver and deduce $\boldsymbol{\psi}$ on S_1 (i.e. $\boldsymbol{\psi}$ on $S^{n}_{1_{\Omega_2}}$)

Velocity computation

(d) After Schwarz algorithm convergence, compute final velocity field:

$$\mathbf{u} = \underbrace{(\nabla \times \boldsymbol{\psi}_{\Omega_1})}_{\text{in } \Omega_1} + \underbrace{(\nabla \times \boldsymbol{\psi}_{\Omega_2})}_{\text{in } \Omega_2 - \Omega_1}$$

(e) Evaluate velocities on particles in $\Omega_1 \cap \Omega_2$ using a *M2P* formula.

2. **Convection-diffusion equation**

(a) Update $\boldsymbol{\omega}_1$ in Ω_1 solving 1.125 with an Eulerian solver.
For boundary values of $\boldsymbol{\omega}_1$ on grid points of S_1, assign to these grid points the vorticity of the closest particles in Ω_2 through a *P2M* formula. The distance from S_1 to S_2 must then be larger or equal to the width of the assignment function ϕ.

(b) Update $\boldsymbol{\omega}_2$ in Ω_2 solving 1.128 with a remeshed PSE scheme.
This update depends on the particles surrounding S_2. These particles are located around S_2 in a layer called Ω_{12} whose width depends on the size of the support of the kernel η used in PSE formula (see [Cottet and Koumoutsakos, 2000]). Particle vorticity values are thus computed in Ω_{12} through a *M2P* formula.

We note that the remeshing procedure performed in step 2.(b) is not as crucial in this context as in a pure Lagrangian framework (see section (1.2.3)). Indeed, the distortion effects mainly occur in the vicinity of the wall boundaries, where the highest velocity gradients are observed. In the far wake, where the PSE scheme is here applied to solve the convection-diffusion, these gradients are smoothed and the particle distribution on an underlying Cartesian grid may not be necessary.

Let us precise that the present algorithm, successfully applied in [Cottet et al., 2000] to model flow past several cylinders, corresponds to a particular version of the domain-decomposition method. Several variations may be brought to this model, while keeping the same base lines. First, this algorithm only deals with overlapping domains but one can also cite the works of [Guermond et al., 1993] who considered matching domains. This type of decomposition makes the definition of interface boundary conditions more challenging but enables a reduction of computational operations. Secondly, we handled here a problem involving a unique obstacle, included in Ω_1. For sure, this algorithm may be derived for several bodies, where the flow in the vicinity of each body is discretized on an independent grid domain [Manickathan, 2014]. Then, the Eulerian method used to solve 1.125 in this algorithm is based on an explicit time integration scheme. An implicit scheme can for sure be implemented in this domain [Cottet and Koumoutsakos, 2000] and we refer to the works of [E and Liu, 1996] for a complete comparison between implicit and explicit advancing schemes in the context of finite-differences methods. Finally, this method is based on a velocity-vorticity formulation of the Navier-Stokes equations in the whole computational domain. A velocity-pressure formulation may also be used on the grid domains for a more flexible and natural treatment of the viscous boundary conditions. Concerning these different aspects we refer the reader to the chapter 2 of [Ould-Sahili, 1998].

1.4.3.2 The Vortex-In-Cell (VIC) methods

This hybrid vortex method, proposed in the pioneer studies of [Christiansen, 1973], relies in dealing with an underlying grid while solving the governing equations with a particle vortex method. Then, Eulerian schemes or Lagrangian schemes are used to solve the different parts of the equations, according to their respective strengths. Concretely, in a VIC method, the advection is performed by updating the trajectories and the vorticity of the Lagrangian particles

through a set of ODEs. On the other hand, Eulerian schemes are handled on the underlying grid to efficiently compute the particle velocities and to solve the diffusion terms for which pure vortex method encounter difficulties (see section (1.2)). For three dimensional flows, the stretching term is often resolved on the mesh for the sake of simplicity.

The general Vortex-In-Cell algorithm can thus be described as follows:

1. **Poisson equation**:
   (a) Assign particle vorticity values to the grid using a *P2M* formula.
   (b) Compute the velocity field solving the following equation on the grid:
   $$\Delta\boldsymbol{\psi} = -\boldsymbol{\omega}. \tag{1.129}$$
   (c) Solve $\Delta\mathbf{u} = \nabla \times \boldsymbol{\psi}$ on the grid.
2. **Convection**:
   (a) Interpolate the velocity field on the particles using a *M2P* formula.
   (b) Perform a Lagrangian advection of the particles and get their new positions and vorticity values:
   $$\frac{d\mathbf{x}_p}{dt} = \mathbf{u}_p, \qquad \frac{d\boldsymbol{\omega}}{dt} = 0 \tag{1.130}$$
   (c) Assign vorticity values and cell volumes to the grid using a *P2M* formula.
3. **Stretching**:
   (a) Solve the stretching equation on the grid by differentiation of the velocity field:
   $$\frac{\partial\boldsymbol{\omega}}{\partial t} = (\boldsymbol{\omega}\cdot\nabla)\mathbf{u} \tag{1.131}$$
   Note: One can also write the stretching term in its conservative form:
   $$\frac{\partial\boldsymbol{\omega}}{\partial t} = \mathrm{div}(\boldsymbol{\omega} : \mathbf{u}) \tag{1.132}$$
4. **Diffusion**:
   (a) Solve the diffusion equation on the grid and get the final grid values for the vorticity field:
   $$\frac{\partial\boldsymbol{\omega}}{\partial t} = \nu\Delta\boldsymbol{\omega} \tag{1.133}$$
   (b) Interpolate the particle values from the grid using a *M2P* formula.

Let us precise that this algorithm corresponds to the original version of the VIC algorithm, following the idea of [Christiansen, 1973]. We note that this initial version of the VIC method actually suffers from the same difficulties as the one experienced by purely Lagrangian approaches because of the distortion effects provoked by the Lagrangian resolution of the convection equation (step 2). The emergence of the remeshing technique in the mid 1990's allowed to overcome this problem and the VIC method then became particularly attractive.

Concerning the grid-based solver used to solve steps 3 and 4, a finite-differences scheme is often chosen [Ould-Salihi et al., 2000, Gallizio, 2009, van Rees et al., 2011]. A more challenging problem relies in the choice of the Poisson solver handled in step 1. The resolution of the

Poisson equation actually stands as the most expensive operation in the present algorithm. Indeed, for N particles, the classical discretization of equation 1.129 through the Biot-Savart Law 1.17 implies to compute the interactions between each particles and all the others, leading to a $\mathcal{O}(N^2)$ complexity.

In order to decrease this number of operations, several grid-based Poisson solvers were designed. They are called fast Poisson solvers, as opposed to the traditional "slow" solvers based for instance on Jacobi, Gauss-Seidel, Conjugate Gradients or Successive Over Relaxation (SOR) methods. These fast Poisson solvers can be defined as hierarchical methods and among them, one can distinguish the direct solvers from the iterative one. The most popular direct solvers are the Fast Fourier Transform method, which consists in solving exactly the Poisson solver in the Fourier space using FFT, and the Cyclic Reduction method, consisting in discretizing the Poisson equation by means of finite-differences method over a rectangle by a successive splitting of the initial problem (see [Buzbee et al., 1970]). These two direct grid-based Poisson solvers present a $\mathcal{O}(N\ logN)$ complexity. On the other hand, one of the most famous iterative solver relies on the Multigrid method, which recursively uses coarse discretizations of the Poisson problem to approximate its solution (see [Brandt, 1977]). The complexity of Multigrid algorithms is $\mathcal{O}(N)$, which makes them very attractive in terms of computational cost. However, they may require more efforts in terms of implementation and use.

An other very famous Fast Poisson solver, also having a $\mathcal{O}(N)$ complexity, is based on the Fast Multipole Method (FMM). However, contrary to all the solvers mentioned above, this one is grid-free and consequently does not take place in the framework of Vortex-In-Cell methods. As this method is part of the most efficient one nowadays, we shortly depict its outlines: this technique, introduced by [Greengard and Rokhlin, 1987], exploits the geometrical distributions of the vortices to evaluate the velocity. The key point is that the velocity field induced by a group of particles clustered around a center does not need to be computed directly from its individual members, but it can be approximated by a finite number of multipole expansions. This approach has been widely used in the context of vortex methods like in [Marzouk and Ghoniem, 2005, Yokota et al., 2009, Rossinelli, 2011].

This section only supplied a detailed description of two semi-Lagrangian methods, namely the domain decomposition and the VIC approach, but it is important to mention the existence of other hybrid vortex methods, like for instance the one recently designed by [Kornev et al., 2013], consisting in representing the large scale field on the grid, whereas the small scale field is evaluated through a pure Lagrangian vortex method.

In the context of the present work we will use the remeshed VIC method. This hybrid technique was indeed chosen for its relevant advantages that we recapitulate in the following list:

- ✓ Lowest computational cost of the Fast Poisson solvers compared to the classical particle-particle interactions,
- ✓ Easy treatment of the viscous effects using finite-differences schemes on the grid (or finite-volumes schemes, spectral schemes) for the resolution of the diffusion equation,
- ✓ Easiness of implementation compared to domain decomposition methods,
- ✓ Conservation of the less restrictive stability condition on the time step (eq. 1.45),
- ✓ Satisfaction of the particle overlapping condition all along the simulation through remeshing procedures, whose computational cost may be greatly decreased by the use of directional splitting schemes (see subsection (1.4.2.5)),
- ✓ Limitation of the diffusive effects in the convection/remeshing step.

For all these reasons, the remeshed VIC method has been extensively used in DNS to discretize the Navier-Stokes equations [Liu, 2001, Cottet and Poncet, 2003], especially in the case of highly transitional regimes with Reynolds numbers ranging from 1000 to 10000. One can mention for example the work of [van Rees et al., 2011] who carried out periodic vortical flows at $Re = 1600$ are compared their results to the one obtained with spectral methods, as well as the studies of [Morgenthal and Walther, 2007, Kudela and Kozlowski, 2009] where the VIC method is used to model incompressible flows past cylinders up to $Re = 3000$ and $Re = 9500$ respectively. In terms of engineering applications, [Gallizio, 2009] used a VIC method in order to model incompressible flows past a vertical axis turbine with a Reynolds number scaling up to $Re = 10000$ and [Gazzola et al., 2014] made use of this approach to study fish schooling for energy harnessing issues. All these problems successfully solved with the VIC method show its competitive features.

However, the Cartesian mesh makes difficult the simulation of flows over complex geometries. The coupling of the remeshed VIC scheme with an immersed boundary method thus appears as an interesting solution to handle such problems. The last section of this survey is dedicated to the so-called hybrid vortex penalization method, which is part of the Vortex-In-Cell/immersed boundary methods and on which the present thesis is based.

1.5 A vortex immersed boundary method

As discussed in the previous sections, the treatment of the boundary conditions may be handled in different ways in the context of vortex methods. First, we presented boundary element methods to which belong the Chorin's vortex sheet approaches. We also highlighted the accuracy provided by the vorticity flux boundary conditions detailed in section (1.3.4). Finally, we can mention the strategy consisting in handling a body-fitted underlying mesh, as for instance the polar mesh usually employed in Eulerian-Lagrangian domain decomposition methods (see Figure 1.8). However, the ease of use of these methods strongly depends on the obstacle geometry, and in the case of body-conforming grids, the computational time needed to build such meshes might become important, even prohibitive if moving obstacles are considered.

In order to overcome the difficulties related to the body geometry, while ensuring an accurate enforcement of the boundary conditions, immersed boundary methods are often chosen. In the following we give a general description of the main categories of immersed boundary methods before focusing on the method of interest in this thesis: the hybrid vortex penalization method.

1.5.1 Families of immersed boundary methods (IBM)

Among the most famous categories of immersed boundary methods, one can cite the three following one: the continuous forcing method, the discrete (or direct) forcing method and the cut-cell method. The two former are based on the introduction of a forcing function in the momentum equation in order to model the presence of an immersed body in the fluid. The latter consists in reshaping the Cartesian cells located on the immersed boundaries such that they coincide with the surface geometry.

1.5.1.1 The continuous forcing method

This immersed boundary method was introduced by Peskin in 1972 and presented as a new technique enabling to easily model fluid-structure interactions. In its original context, this method was used to simulate blood flow inside deformable human heart valves [Peskin, 1972, Peskin, 1977]. This technique is based on an Eulerian-Lagrangian approach where the fluid is represented on a uniform Cartesian grid and the structure is defined by a set of points, also called fibers in the original context of elastic heart valves, which do not necessary fit with the regular mesh. The method invented by Peskin to model the presence of the structure boundaries

consists in defining the force $\mathbf{f}(\mathbf{x}, t)$ applied by the immersed structure to the surrounding fluid and in distributing this force from each Lagrangian fiber over its neighboring grid nodes (Figure 1.9a). The forcing function $\mathbf{f}$ is then inserted in the right-hand-side of the governing momentum equations of the neighboring points before discretization. The main distinction between all the existing continuous forcing methods lies in the definition of the forcing function $\mathbf{f}$, which is often desired to be smooth in order to prevent oscillations at the fluid-structure interface.

Contrary to the two following IBM, the main advantage of the continuous forcing approach relies in the fact that it does not depend on the discretization scheme used on the underlying grid, which makes this technique generic and easy to set up on a given grid-based/hybrid Navier-Stokes solver.

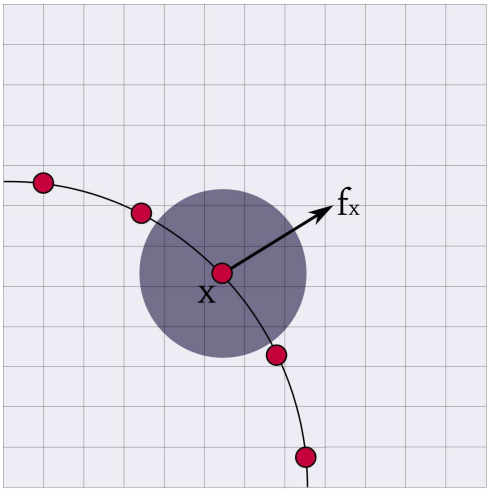

(a) Application of forcing $\mathbf{f}$ from Lagrangian point to neighboring fluid points.

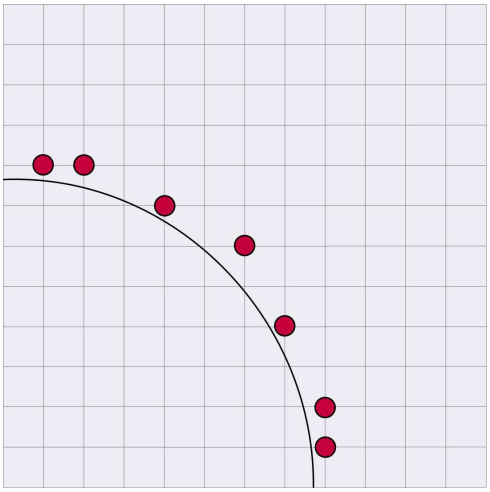

(b) Direct forcing is applied on the red grid points from velocities interpolated from next grid nodes.

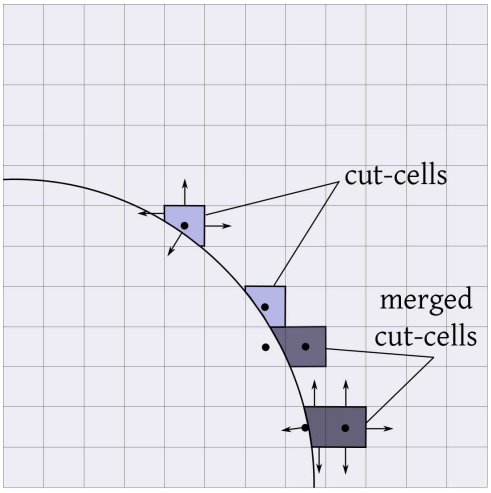

(c) Fluxes for different types of cut-cells

Figure 1.9: Immersed boundary methods

1.5.1.2 The discrete forcing method

Whereas the continuous method consists in adding a forcing term in the momentum equations before their discretization, the discrete forcing approach, introduced by [Mohd-Yusof, 1997], proceeds in the opposite way since the forcing is now computed from the discretized Navier-Stokes equations. One advantage resides in the workaround of the stiffness problem encountered by the function $\mathbf{f}$ used in the continuous approach. The outlines of the discrete forcing algorithm are given hereafter following the one reported by [Balaras, 2004]. Let us first consider the

incompressible Navier-Stokes equations in their velocity-pressure formulation. Including the forcing term, they are expressed by:

$$\frac{\partial \mathbf{u}}{\partial t} + (\mathbf{u}\cdot\nabla)\mathbf{u} + \nabla p - \nu\Delta\mathbf{u} = \mathbf{f}, \quad \text{in } \Omega\times(0,\ T) \tag{1.134}$$

$$\text{div } \mathbf{u} = 0, \quad \text{in } \Omega\times(0,\ T) \tag{1.135}$$

$$\mathbf{u} = \bar{\mathbf{u}}, \quad \text{on } \partial\Omega \tag{1.136}$$

After time discretization, one can write the body force on grid point i as follows:

$$\frac{\mathbf{u}_i^{n+1} - \mathbf{u}_i^n}{\Delta t} = \text{RHS}_i + \mathbf{f}_i \tag{1.137}$$

where the RHS includes the convection, the diffusion and the pressure gradient terms. Knowing that the role of the forcing function $\mathbf{f}$ is to enforce the desired boundary conditions at the immersed boundary, then it must impose $\mathbf{u}_i^{n+1} = \bar{\mathbf{u}}_i^{n+1}$ on $\partial\Omega$, and therefore $\mathbf{f}$ is defined by:

$$\mathbf{f}_i = \begin{cases} \dfrac{\bar{\mathbf{u}}_i^{n+1} - \mathbf{u}_i^n}{\Delta t} - \text{RHS}_i & \text{near } \partial\Omega, \\ 0 & \text{elsewhere.} \end{cases} \tag{1.138}$$

We give here the algorithm for the $\mathbf{f}$ computation in the general case where the boundary does not fit with the mesh:

1. Compute $\mathbf{u}^*$ from equation 1.134, without the forcing term $\mathbf{f}$. The fluid is then allowed to enter inside the solid and the velocity $\mathbf{u}^*$ does not satisfy the correct boundary conditions.

2. Interpolate the velocity $\bar{\mathbf{u}}$ on the forcing points from the surrounding nodes (Figure 1.9b) and compute $\mathbf{f}$ from equation 1.138, taking $\mathbf{u}^*$ for the computation of the RHS term.

3. Compute $\mathbf{u}_i^{n+1}$ from equation 1.134, with the forcing term $\mathbf{f}$ resulting from the previous step. This velocity now ensures the correct boundary conditions.

Many variations of this algorithm have been derived. They mainly focus on how to determine the forcing points of step 2. and how to interpolate $\bar{\mathbf{u}}$ on these points. On that subject, one can for instance cite the works of [Mohd-Yusof, 1997, Balaras, 2004] and [Verzicco et al., 2000, Fadlun et al., 2000, Iaccarino and Verzicco, 2003] where, in the latter ones, the direct forcing method is used in the framework of finite-differences Large Eddy Simulations (LES), proving the efficiency of IBM in the treatment of turbulent incompressible flows.

1.5.1.3 The cut-cell method

A different approach, not relying on the momentum forcing technique, was proposed by Ye et al [Ye et al., 1999]. Based on a finite-volumes framework, it consists in cutting the Cartesian cells crossed by the immersed boundary according to the following rule: if the center of the cell is located in the fluid region, the cell is reshaped by removing the portion that lies in the solid part. On the contrary, if the cell center lies in the solid, then the remaining part located in the fluid can be absorbed by the surrounding cells to overcome stability problems. These cut cells of trapezoidal shape then define the new control volumes in the vicinity of the immersed boundary for the finite-volumes discretization scheme (Figure 1.9c). The modeling and computational efforts then mainly lie on the evaluation of the fluxes on the sides of reshaped cells [Udaykumar et al., 1999, Ye et al., 1999, Udaykumar et al., 2001].

The cut-cell methods are particularly accurate in the treatment of the boundary conditions since they often rely on second-order schemes. However, their implementation requires a lot

of efforts. More generally, these features (accuracy and difficulty of implementation) are also verified for the continuous and direct forcing immersed boundary methods.

For a complete description and comparison of the different immersed boundary methods with their respective improved versions, we suggest the works of [Mittal and Iaccarino, 2005, Bandringa, 2010].

1.5.1.4 The penalization method

The penalization technique, firstly proposed by [Caltagirone, 1994] and further developed by [Angot et al., 1999], is actually part of the continuous forcing immersed boundary methods and relies on the simple following idea: the fluid in which the flow evolves is assumed to be a porous medium of infinite permeability while, on the other hand, the solid obstacles immersed in the fluid are considered as media with zero permeability. A flow evolving in such media may be modeled by the Brinkman-Navier-Stokes equations, which stands for the whole domain and which contains an additional term with respect to classical Navier-Stokes equations, acting as a forcing term. The latter, called the penalization term, directly comes from the Darcy equations that govern flows in porous media. In the velocity-pressure formulation, the Brinkman-Navier-Stokes equations yield:

$$\frac{\partial \mathbf{u}}{\partial t} + (\mathbf{u}\cdot\nabla)\mathbf{u} + \nabla p - \nu\Delta\mathbf{u} = \mathbf{f}, \quad \text{in } \Omega\times(0,\ T) \tag{1.139}$$

$$\text{div } \mathbf{u} = 0, \quad \text{in } \Omega\times(0,\ T), \tag{1.140}$$

where $\mathbf{f}$ corresponds to the penalization term, equal to:

$$\mathbf{f} = -\frac{\mathbf{u}}{K}, \tag{1.141}$$

where K is a coefficient mainly depending on the permeability of the medium. This K coefficient is consequently set to infinity in the fluid region and to zero in the solid ones. In that way the force is therefore activated only inside the solids, making the velocity vanishing in these regions, and the no-slip boundary conditions are automatically satisfied. In case of moving obstacles, the penalization term is given by $(\bar{\mathbf{u}} - \mathbf{u})/K$, where $\bar{\mathbf{u}}$ denotes the velocity of the moving obstacle. The condition $\mathbf{u} = \bar{\mathbf{u}}$ is thus prescribed on the boundary and rigid motion is ensured within the solid.

One can also mention an alternative to this method proposed by [Pasquetti et al., 2008] and called the pseudo-penalization method. In this approach, no penalization term is involved in the governing equations such that no penalization coefficient explicitly appears. The pseudo-penalization technique is finally equivalent to consider the Navier-Stokes equations in the fluid domain coupled to penalized steady Stokes equations in the solid domain. This coupling is performed through the prescription of natural transmission conditions. This approach has been successfully applied to the control of turbulent wake flows in the very recent works of [Pasquetti and Peres, 2015].

1.5.2 The hybrid vortex penalization method

When they are used with Cartesian meshes, remeshed Vortex In Cell methods turn out to be robust and reasonable in terms of computational cost. They should therefore definitely benefit from immersed boundaries approaches, that would allow to supply flexibility in their application.

Historically, the first type of vortex immersed boundary methods consisted in imposing a specific treatment, namely imposing the no-slip boundary conditions, on the computational cells intersecting the boundary. The identification of these cells was realized through corrected interpolation formula, enabling to quantify the overlapping of the boundary and the cells, in the spirit of Volume of Fluid (VOF) methods. This approach was successfully used in particular

by [Ploumhans and Winckelmans, 2000, Ploumhans et al., 2002] to handle complex 2D and 3D geometries, at highly transitional flow regimes.

A second class of vortex immersed boundary methods was then introduced, in which the boundary conditions are in the form of local forcing terms in the right-hand side of the momentum equations. In this approach, the flow equations are discretized in a unique way in the computational domain, independently of the nature of the cells (i.e fluid, solid or mixed cells). One can particularly cite the approach proposed by [Cottet and Poncet, 2003] where the no-slip boundary condition is enforced from source points that are located on the boundary itself on all grid points that are at a distance less than the grid-size from the boundary. In this way the boundary conditions are prescribed on the body boundary regardless of the position where the flow particles are initialized and remeshed.

More recently, a third class of vortex immersed boundary method was proposed, consisting in using the penalization technique to enforce the boundary conditions. The hybrid method handled in this thesis belongs to this class and is called the hybrid vortex penalization method. This approach simply consists in coupling the $\mathbf{u} - p$ penalization method presented in the previous paragraph with the Vortex-In-Cell method. For that purpose, one needs to express the Brinkman-Navier-Stokes equations 1.139-1.140 in their vorticity formulation. Setting $K = \frac{1}{\lambda}\chi$, where χ denotes the characteristic function of the solid bodies and λ is the penalization parameter related to the medium permeability, and taking the curl of equation 1.139, we obtain the following vorticity-penalization equations, originally proposed by [Kevlahan and Ghidaglia, 2001]:

$$\frac{\partial \boldsymbol{\omega}}{\partial t} + (\mathbf{u}\cdot\nabla)\boldsymbol{\omega} - (\boldsymbol{\omega}\cdot\nabla)\mathbf{u} - \nu\Delta\boldsymbol{\omega} = \nabla\times[\lambda\chi(\bar{\mathbf{u}} - \mathbf{u})], \qquad \text{in } \Omega\times(0,\ T) \tag{1.142}$$

$$\text{div } \mathbf{u} = 0, \qquad \text{in } \Omega\times(0,\ T) \tag{1.143}$$

With this formulation, the zone variation is performed by changing the value of the λ parameter: a λ-value tending to infinity will model a solid region and, on the contrary, a λ-value equal to zero will model the fluid part.

In the last decade, the hybrid vortex penalization method has been used successfully for different types of applications. First, we can cite the works of [Gallizio, 2009, Morency et al., 2012] who coupled the penalization technique with a level-set method in order to handle moving bodies. Then, [Rasmussen et al., 2011] proposed a multiresolution VIC algorithm with Brinkman penalization and validated it in the case of classical benchmarks involving bluff bodies. In terms of fluid-structure interactions, we can cite the works of [Coquerelle and Cottet, 2008] who coupled the penalization method with a level-set method and a collision model to simulate the interaction of an incompressible flow with rigid bodies, as well as those of [Gazzola et al., 2014] (and all prior related studies from the same authors) dealing with fish schooling, where the penalization method is combined to a projection approach allowing to model the action of the fluid on the deforming fishes. Finally, [Hejlesen et al., 2015] introduced very recently an iterative vortex-Brinkman penalization method in order to enhance its accuracy while allowing larger time steps.

In terms of numerical advantages, besides the one already cited concerning remeshed Vortex-In-Cell methods, the present hybrid vortex penalization method first naturally exhibits the ones of the immersed boundary methods, that is the absence of explicit prescription of the boundary conditions, the existence of a unique equation for the whole domain and the possibility to handle complex geometries. Nevertheless, on this last point, it distinguishes itself from some other IBM since its implementation is totally independent of the obstacles' shape, which is not the case for example with the previously presented direct forcing method where high curvatures in the immersed boundary require more sophisticated interpolations and fluxes computations. Then, the Brinkman penalization method is particularly easy to implement: the only thing to do is changing the value of λ in the penalization term. Finally, we directly benefit from the variable-permeability background of the method to handle passive flow control. Indeed, as the objective

of this work is to perform passive flow control by covering the surface of the immersed obstacle with porous areas, the penalization technique will particularly ease the implementation and the handling of such bodies since we will simply have to set λ to an intermediate permeability value in these areas.

The major drawback of the present penalization method is its first-order accuracy. Nevertheless, we will see in the next chapters that it still provides a precise behavior of the flow in the boundaries region.

The next chapter will be fully dedicated to the mathematical description, the discretization and the implementation of the hybrid vortex penalization method adopted in this thesis in the context of passive flow control applications.

The last point that remains to evoke in this survey concerns the algorithmic issues related to vortex methods. The question related to the computational performance of the library in which they are implemented are indeed crucial since they determine the capability of these methods to handle challenging problems.

1.6 Algorithmic issues

Besides the aspects related to accuracy and particle distortion, the low expansion of pure particle methods in the CDF community is also explained by their computational implementation. The main limitations indeed rely in the fact that particle methods are difficult to parallelize efficiently and that most of the relevant scientific libraries are incompatible with such approach. In recent years, with the appearance of efficient hybrid vortex methods, a lot of efforts were dedicated to the design of competitive algorithms and the first parallel codes based on remeshed vortex methods arose. In this last section, we present two main scientific libraries that clearly enhance the challenging features of the vortex methods in modeling complex fluid dynamics problems.

The first one is the so-called Parallel Particle-Mesh (PPM) library. As explained by its authors in [Sbalzarini et al., 2006], it supplies a general-purpose parallel and portable framework that can handle particles-only, mesh-only, as well as hybrid particle–mesh systems. In terms of parallelism, the PPM library is usable on single processor machines as well as on distributed memory, shared memory, and vector parallel processors. Finally, concerning numerical methods, PPM is able to handle mesh-based solvers, evaluations of differential operators on particles, Fast Multipole Method (FMM), parallel FFT, and multi-stage ODE integrators. This library was successfully used to simulate a wide range of three-dimensional challenging problems, like the diffusion in the endoplasmic reticulum of a live cell, the reacting of compressible double shear layer or the instability of two anti-parallel vortex tubes. These applications always showed parallel efficiencies reaching or exceeding the state of the art, and satisfactory run-times on large systems.

The second library is called MRAG-I2D, for Multi-Resolution Adapted Grids for Incompressible flow simulations in 2D. This open source software was developed by [Rossinelli et al., 2015] for multiresolution simulations of two-dimensional incompressible flows on multicore architectures using remeshed particle methods. In this library, the concept of wavelet adaptivity is used in order to generate adapted grids that enable the optimization of computations for fluid flows, developing multi-spacial and temporal scales. More precisely, the set up of the multiresolution analysis of both velocity and vorticity field is performed using biorthogonal wavelets. The latter introduce a pair of analysis functions (used by the Fast Wavelet Transform) and a pair of synthesis functions (performed by the inverse FWT). A function can therefore be decomposed in scaling and detail coefficients at different levels of resolution. Each point of the adaptive grid is thus represented by a scaling and a detail coefficient. The aim is to discard the detail coefficients which, compared to a fixed threshold, do not carry relevant information about the flow field.

The space-adapted grids are also coupled with local time-stepping (LTS) integration schemes in order to speedup the computational efficiency. These schemes, exploiting the time step locality imposed by the different stability conditions, allow to integrate the coarser elements with larger time steps than the finer ones and thus enable one to perform fewer integration steps. Local time-stepping schemes are shown to speedup the computation by one order of magnitude at each level of resolution from a certain number of levels. The non-uniformity of the grid imposes the use of a Fast Multipole Method (FMM) to solve the velocity Poisson equation. The MRAG-I2D library efficiently maps these different algorithmic and numerical aspects onto modern computing architectures, in particular onto heterogeneous CPU-GPU platforms. It as been used for the simulation of bluff body flows with Reynolds numbers ranging until 40000, flow-mediated interactions between two solids, analysis of optimal shapes in anguilliform swimming and reinforcement learning in the context of self-propelled bodies.

Beyond the scope of these two software, another algorithm issue lies in multi-scales simulations. Indeed, as exposed in the previous sections, vortex methods are a natural approach to investigate the main features of incompressible turbulence, in particular the mechanisms that drive the organization of the small scales into large eddies. This concern has been addressed in the framework of vortex methods by [Cottet, 1996, Cottet and Wray, 1997], who proposed a eddy viscosity model, with anisotropic non-linear diffusion, leading to artificial viscosity schemes. This subgrid-scale model is intrinsically anisotropic and able to distinguish between vorticity and strain, which is not the case of the commonly used Smagorinsky model. As a result the artificial dissipation does not affect large eddies. A discussion related to the implementation of an eddy viscosity algorithm will be addressed at the end of this thesis as a perspective of the present work.

Conclusion 1.1

The intensive development of the vortex methods between 1973 and the mid 1990's was motivated by the will to design robust and accurate numerical schemes able to overcome the main weaknesses of traditional grid methods, especially in the case of dominant convection effects in the flows. The major advantages arising from these pure Lagrangian methods are the following: appealing physical attributes, automatic adaptivity of the discretization elements (particles), compactness of vorticity support, accurate handling of boundary conditions at infinity, low numerical diffusion, conservation of the flow invariants, relaxed stability condition on the time step and usefulness of vorticity in terms of results interpretations. However, during this period, vortex methods experienced some difficulties. First they had to face an inaccurate modeling of the viscous effects due to the particle distortion phenomenon. They were also confronted with the expensive resolution of the Poisson equation allowing to recover the velocity field from the vorticity. Finally, they failed in providing both accurate, efficient and generalized treatment of boundary conditions on solid walls due to the velocity formulation of the no-slip boundary conditions. For all these reasons, the pure vortex methods did not manage to become a common tool for the simulation of incompressible real flows. In order to bypass their intrinsic difficulties, they started to move towards hybrid formulations in the early 1990's, resulting in the introduction of underlying grids with remeshing. The presence of Cartesian grids thus enables the use of Fast Poisson solvers as well as grid-based schemes for the discretization of the diffusion term, and makes possible the handling of immersed boundary methods for the treatment of the solid bodies, while ensuring particle overlapping. In the meantime, the particle discretization of the flow allows to keep most of the advantages of the Lagrangian methods. All these advances allowed to highlight the interest and potential of VM in handling challenging CFD problems. Important efforts were therefore supplied to design efficient algorithms in the context of hybrid vortex methods and eventually gave birth to high performance scientific libraries.

Returning to the realm of the present work, aiming to deal with passive flow control around bluff bodies, the choice of the hybrid vortex penalization method is therefore jus-

tified by three main arguments: first, the framework addressed by the vortex methods is particularly well suited to the moderate and highly-transitional flow regimes that we aim to handle and allows to solve the governing equations in a fast and robust Lagrangian way. Secondly, the presence of an underlying grid in the present method enables a permanent control of the particles overlapping and allows the use of a fast summation algorithm for the Poisson solver as well as finite-differences schemes to discretize differential operators. Finally, the penalization immersed boundary method facilitates the modeling of the complex fluid-solid-porous media considered in this work.

2

The hybrid vortex penalization method

Contents

Résumé 2

Ce chapitre est dédié à la description de la méthode vortex hybride pénalisée mise en oeuvre dans cette thèse. Nous présentons dans un premier temps les équations fondamentales du problème, à savoir les équations de Navier-Stokes incompressibles exprimées dans leur formulation vitesse-vorticité. Le but de ces travaux étant de contrôler passivement un écoulement par l'ajout d'un matériau poreux à la surface de l'obstacle immergé, la construction d'un modèle d'écoulement dans un milieu solide-fluide-poreux devient alors nécessaire. Pour cela, les équations de Navier-Stokes sont alors couplées avec l'équation de pénalisation de Brinkman, où le terme de pénalisation ainsi ajouté est fonction de la perméabilité du milieu et permet de modéliser les différentes parties du système. Après avoir décrit les caractéristiques physiques d'un écoulement dans un milieu solide-fluide-poreux et après en avoir détaillé le modèle continu, nous déclinons ensuite l'algorithme général, basé sur une méthode de splitting, ainsi que les schémas de discrétisation mis en place afin de résoudre le problème. Un schéma semi-lagrangien d'advection/remaillage d'ordre élevé est utilisé afin de traiter l'équation de convection tandis que les autres opérateurs différentiels présents dans les équations du problème sont discrétisés sur une grille sous-jacente à l'aide d'une méthode de différences-finies. L'ensemble de ces schémas de discrétisation sont implémentés au sein d'un code de calcul scientifique dont une description détaillée est faite dans la dernière partie de ce chapitre.

This chapter is devoted to the description of the numerical algorithm and the implementation of the Hybrid Vortex Penalization (HVP) method that is not only appropriate to model incompressible flows past bluff bodies, but also to simulate flows in complex media involving fluid, porous and solid regions. The method proposed in the present work to handle this type of problem is based on the vortex Brinkman-penalization technique. As explained in the dedicated section (1.5.2) in chapter 1, this approach involves a unique equation for the whole domain and ensures an accurate modeling of each of the different regions thanks to the dimensionless penalization factor. In the penalization technique the system is considered as a single flow, subject to the Navier-Stokes equation with a penalization term that enforces continuity at the solid-porous and porous-fluid interfaces as well as rigid motion inside the solid. The main advantage of this method is that it needs neither the mesh to fit the boundaries nor to specify no-slip boundary conditions. This Brinkman-penalization technique has already been used successfully in its original velocity-pressure formulation under a purely Eulerian approach by Bruneau and Mortazavi in order to model 2D flows in fluid-porous-media [Bruneau and Mortazavi, 2004, Bruneau and Mortazavi, 2006, Bruneau and Mortazavi, 2008]. The present hybrid algorithm provides an extension of this penalization approach to the two- and three-dimensional $(\mathbf{u}, \boldsymbol{\omega})$-Navier-Stokes equations in order to perform passive flow control using porous media.

Moreover, aside from proving the competitiveness of the present hybrid vortex penalization method and applying it for the first time to passive flow control, a major goal of this work was also to implement the present method within a new perennial and upgradable open source library able to handle a broad spectrum of incompressible flow problems with challenging issues, based on hybrid simulations using particles.

The outline of this chapter is the following: starting from the original Brinkman Navier-Stokes equations in velocity-pressure formulation, we will first give the successive steps enabling to achieve the numerical model used in this thesis, based on a vorticity formulation. We will then present the algorithm derived in order to discretize the governing equations. This algorithm has been implemented in a computational solver that will be presented in the last part of this chapter.

We precise that all the notations introduced in this chapter will be further used in the next parts of this thesis.

2.1 Mathematical and physical description of the model

2.1.1 The Brinkman Navier-Stokes equations in velocity formulation

The three-dimensional Navier-Stokes equations governing the incompressible flow of a Newtonian fluid in a domain D, without external forces, are given by:

$$\rho \frac{\partial \mathbf{u}}{\partial t} + \rho (\mathbf{u} \cdot \nabla)\mathbf{u} + \nabla p - \mu \Delta \mathbf{u} = 0 \qquad \text{in } D \times (0,T), \tag{2.1}$$

$$\text{div } \mathbf{u} = 0 \qquad \text{in } D \times (0,T), \tag{2.2}$$

where ρ refers to the density of the fluid (considered as constant throughout this work), μ corresponds to the dynamic viscosity of the fluid, $\mathbf{u}$ is the three dimensional velocity vector field and p denotes the pressure scalar field.

As explained in section (1.5.1.4), the penalization method consists in adding a forcing term in the equation of momentum conservation. This term models the entire domain as a porous medium with different permeabilities.

In a porous medium the velocity $\mathbf{u}$ is given by the Darcy law:

$$\mathbf{u} = -\frac{k}{\mu \Phi} \boldsymbol{\nabla} p, \tag{2.3}$$

Insert 1 – Porosity and permeability

- The **porosity** Φ of a porous medium corresponds to the fraction of void space (air, water, ...) in a material. It is defined by the ratio:

$$\phi = \frac{V_{\mathrm{V}}}{V_{\mathrm{T}}} \tag{2.4}$$

  where V_{V} indicates the volume of the void-space and V_{T} is the total volume of the material, including the solid and the void parts. The porosity is therefore a value between 0 and 1.

- The **permeability** k measures the ability of a porous material to allow fluids to pass through it. High permeabilities will therefore enable a fluid to evolve fastly within a porous medium. This quantity directly derives from the Darcy equation and its unit of measure is the darcy ($Da = 0.97 \times 10^{-12}\ m^2$).

where Φ denotes the porosity of the medium and k is the intrinsic permeability (see Insert 1).

On the other hand, assuming that the Boussinesq hypothesis is satisfied for the fluid saturating the porous medium, we get the Brinkman equation that includes the diffusion inside the body and which is only valid when the porosity coefficient is close to one:

$$\nabla p = -\frac{\mu\Phi}{k}\mathbf{u} + \tilde{\mu}\Phi\Delta\mathbf{u}, \tag{2.5}$$

with $\tilde{\mu}$ denoting the Brinkman's effective viscosity. To model solid-porous-fluid media, the Brinkman equation is actually preferred to the Darcy equation since it can either model the flow in a highly porous region or the interface with the fluid (which can always be seen as a medium with a porosity close to one). The Brinkman equation prescribes similar equations on both sides of the interface, which supplies a natural coupling between the fluid model and the porous one. Concerning the effective viscosity $\tilde{\mu}$, it should be seen here as a parameter that enables the connection of the shear stress boundary conditions across the fluid/porous interface. Many studies had been carried out concerning the relation between μ and $\tilde{\mu}$. Brinkman himself originally set $\mu = \tilde{\mu}$, however this assumption is not true in the general case. [Liu and Masliyah, 2005] stated that $\tilde{\mu}$ is actually highly dependent on the considered porous medium and the strength of the flow. Nevertheless, they conclude that it is of common practice to set μ approximately equal to $\tilde{\mu}$ when high porosities (close to 1) are involved, which is the case in this study. Therefore, assuming that $\tilde{\mu} \sim \mu/\Phi$, then the Brinkman equation yields:

$$\nabla p = -\frac{\mu\Phi}{k}\mathbf{u} + \mu\Delta\mathbf{u}. \tag{2.6}$$

If the velocity of the immersed body $\mathbf{u}_b$ is non-zero, then the Brinkman equation expresses as:

$$\nabla p = \frac{\mu\Phi}{k}(\mathbf{u}_b - \mathbf{u}) + \mu\Delta\mathbf{u}. \tag{2.7}$$

Complementing this equation with the inertial terms of the Navier-Stokes equation, and following the way the Forchheimer-Navier-Stokes equation is derived by [Whitaker, 1999], we finally obtain the modified Forchheimer-Navier-Stokes equation, also called Brinkman Navier-Stokes equations ([Bruneau and Mortazavi, 2004]):

$$\frac{\partial\mathbf{u}}{\partial t} + (\mathbf{u}\cdot\nabla)\,\mathbf{u} + \frac{\nabla p}{\rho} = \frac{\mu\Phi}{k\rho}\chi_b(\mathbf{u}_b - \mathbf{u}) + \frac{\mu}{\rho}\Delta\mathbf{u} \qquad \text{in } D\times(0,T), \tag{2.8}$$

$$\operatorname{div}\mathbf{u} = 0 \qquad \text{in } D\times(0,T), \tag{2.9}$$

where χ_b is the characteristic function equal to 0 in the fluid and 1 in the body.

We now seek to express this Brinkman Navier-Stokes equation in its velocity-vorticity formulation.

2.1.2 The Brinkman Navier-Stokes equations in vorticity formulation

Taking the curl of equation 2.1 and using equation 2.2, we get the three-dimensional Helmholtz equation, also called Vorticity Transport Equation (VTE), for the vorticity $\boldsymbol{\omega} = \nabla \times \mathbf{u}$:

$$\frac{\partial \boldsymbol{\omega}}{\partial t} + (\mathbf{u} \cdot \nabla)\boldsymbol{\omega} - (\boldsymbol{\omega} \cdot \nabla)\mathbf{u} = \frac{\mu}{\rho}\Delta\boldsymbol{\omega} \qquad \text{in } D \times (0,T), \tag{2.10}$$

where the terms $(\mathbf{u} \cdot \nabla)\boldsymbol{\omega}$, $(\boldsymbol{\omega} \cdot \nabla)\mathbf{u}$ and $\mu/\rho\ \Delta\boldsymbol{\omega}$ respectively model the convection, the stretching and the diffusion of the vorticity field. This equation has to be coupled to the system giving the velocity in terms of the vorticity. It is convenient to use the Helmholtz decomposition:

$$\mathbf{u} = \nabla \times \boldsymbol{\psi} + \nabla\varphi. \tag{2.11}$$

The stream function $\boldsymbol{\psi}$ and potential φ satisfy the following systems in D:

$$-\Delta\boldsymbol{\psi} = \boldsymbol{\omega},\ \nabla \cdot \boldsymbol{\psi} = 0,\ \Delta\varphi = 0, \tag{2.12}$$

complemented with appropriate boundary conditions (we will come back to this point is the sequel). Using the incompressibility condition 2.2, the velocity may also be directly linked to the vorticity through the following relation, already mentioned in the previous chapter and justified by relations 1.11:

$$\Delta\mathbf{u} = -\nabla\times\boldsymbol{\omega}. \tag{2.13}$$

One can notice that equation 2.10 no more contains pressure term. Indeed, since the density ρ is constant in this study, the curl of $\nabla p/\rho$ vanishes. But the pressure can be recovered from the velocity field by integrating the following Poisson equation:

$$\Delta p = -\nabla \cdot (\mathbf{u} \cdot \nabla)\mathbf{u}, \quad \text{in } D, \tag{2.14}$$

which is derived from the divergence of equation 2.1.

By dividing equation 2.7 by ρ and by taking the curl of the resulting equation, one obtains the Brinkman equation in its velocity-vorticity formulation:

$$0 = \nabla \times \left(\frac{\mu\Phi}{k\rho}(\mathbf{u}_b - \mathbf{u})\right) + \frac{\mu}{\rho}\Delta\boldsymbol{\omega}. \tag{2.15}$$

Proceeding exactly in the same way as we did to get equation 2.8, one obtains from the Brinkman equation 2.15 and the VTE 2.10 the dimensional penalized Vorticity-Transport-Equations, originally proposed by [Kevlahan and Ghidaglia, 2001]:

$$\frac{\partial \boldsymbol{\omega}}{\partial t} + (\mathbf{u} \cdot \nabla)\boldsymbol{\omega} - (\boldsymbol{\omega} \cdot \nabla)\mathbf{u} = \nabla \times \Big(\lambda\ \chi_b(\mathbf{u}_b - \mathbf{u})\Big) + \nu\Delta\boldsymbol{\omega} \qquad \text{in } D \times (0,T), \tag{2.16}$$

$$\Delta\mathbf{u} = -\nabla\times\boldsymbol{\omega} \qquad \text{in } D \times (0,T), \tag{2.17}$$

where $\lambda = \mu\Phi/k\rho$ is the penalization parameter of dimension $[s^{-1}]$ and $\nu = \mu/\rho$ is the kinematic viscosity of the fluid of dimension $[m^2][s^{-1}]$.

2.1.3 The dimensionless problem

In order to get the non-dimensional formulation of equation 2.16, let us consider the following usual substitutions involving the mean velocity of the fluid $\bar{\mathbf{u}}$, the size of the body H and the reference time $\bar{t}$:

$$\boldsymbol{\omega} = \boldsymbol{\omega}' \frac{\bar{\mathbf{u}}}{H} \qquad \mathbf{u} = \mathbf{u}'\bar{\mathbf{u}} \qquad x = x'H \qquad t = t'\bar{t} = t'\frac{H}{\bar{\mathbf{u}}} \qquad \lambda = \lambda' \frac{1}{\bar{t}}. \tag{2.18}$$

From these relations, one can evaluate each term of equation 2.16 in its non-dimensional form. The detail of the computations is given in appendix (A). After substitution, one finally gets:

$$\frac{\bar{\mathbf{u}}^2}{H^2}\frac{\partial \boldsymbol{\omega}'}{\partial t'} + \frac{\bar{\mathbf{u}}^2}{H^2}(\mathbf{u}'\cdot\nabla')\boldsymbol{\omega}' - \frac{\bar{\mathbf{u}}^2}{H^2}(\boldsymbol{\omega}'\cdot\nabla')\mathbf{u}' = \nabla' \times \left(\frac{\mu\Phi\bar{\mathbf{u}}}{\rho k H}\ \chi_b(\mathbf{u}_b' - \mathbf{u}')\right) + \frac{\mu\bar{\mathbf{u}}}{\rho H^3}\ \Delta'\boldsymbol{\omega}'. \tag{2.19}$$

Multiplying the above equation by $\dfrac{H^2}{\bar{\mathbf{u}}^2}$ eventually gives:

$$\frac{\partial \boldsymbol{\omega}'}{\partial t'} + (\mathbf{u}'\cdot\nabla')\boldsymbol{\omega}' - (\boldsymbol{\omega}'\cdot\nabla')\mathbf{u}' = \nabla' \times \left(\frac{\mu\Phi H}{\rho k\bar{\mathbf{u}}}\ \chi_b(\mathbf{u}_b' - \mathbf{u}')\right) + \frac{\mu}{\rho H\bar{\mathbf{u}}}\ \Delta'\boldsymbol{\omega}', \tag{2.20}$$

where the penalization parameter $\lambda' = \mu\Phi H/\rho k\bar{\mathbf{u}}$ is indeed a non-dimensional parameter since one has $\lambda' = \lambda\ H/\bar{\mathbf{u}} = \lambda\bar{t}$ and thus $[\lambda'] = [s^{-1}].[s]$. The same conclusion holds for the quantity $\mu/\rho H\bar{\mathbf{u}}$ which actually corresponds to the inverse of the Reynolds number: $1/Re = \mu/\rho H\bar{\mathbf{u}} = \nu/H\bar{\mathbf{u}}$ and thus $[1/Re] = [m^2.s^{-1}]/[m^2.s^{-1}]$.

Finally, skipping the $(\cdot)'$ notation in equation 2.20 for the sake of clarity, one obtains the dimensionless penalized Vorticity-Transport-Equations:

$$\frac{\partial \boldsymbol{\omega}}{\partial t} + (\mathbf{u}\cdot\nabla)\boldsymbol{\omega} - (\boldsymbol{\omega}\cdot\nabla)\mathbf{u} = \nabla \times \Big(\lambda\ \chi_b(\mathbf{u}_b - \mathbf{u})\Big) + \frac{1}{Re}\Delta\boldsymbol{\omega} \qquad \text{in } D\times(0,T), \tag{2.21}$$

$$\Delta\mathbf{u} = -\nabla\times\boldsymbol{\omega} \qquad \text{in } D\times(0,T). \tag{2.22}$$

In the above equations $\lambda = \mu\Phi H/\rho k\bar{\mathbf{u}}$ denotes the non-dimensional penalization parameter and $Re = H\bar{\mathbf{u}}/\nu$ corresponds to the dimensionless Reynolds number, measuring the relative importance of the inertial effects compared to the viscous ones.

2.1.4 A vortex penalization method for solid-porous-fluid media

This section is devoted to the study of flows in solid-porous-fluid media and aims to highlight the efficiency of the present vortex penalization method to solve such problems.

For a three different media configuration composed of solid, porous and fluid parts, it is of great importance to clearly understand the flow behavior at the fluid-porous interface in order to model the physics correctly. As described in [Bruneau and Mortazavi, 2008], we can consider five different flow regions from the solid to the free flow in the fluid. First, there is the boundary layer inside the porous medium, close to the solid wall. It is very thin compared to the second region which is characterized by the homogeneous porous flow with Darcy velocity $\mathbf{u}_D$ (numbers 1 and 2 in Figure 2.1). In the vicinity of the porous-fluid interface, two transient layers can be recognized (numbers 3 and 4 in Figure 2.1). The first one corresponds to the increase of the porous layer velocity, reaching the value $\mathbf{u}_i$ at the interface, and the second one to the fluid boundary layer which extends from the interface to the free flow. The fluid boundary layer growth is then determined by $\mathbf{u}_\infty - \mathbf{u}_i$ where $\mathbf{u}_\infty$ denotes the velocity of the main fluid flow (number 5 in Figure 2.1).

Several approaches have already been proposed to deal with this problem, among which one can distinguish two main techniques. The first one, which is essentially used to model flows past

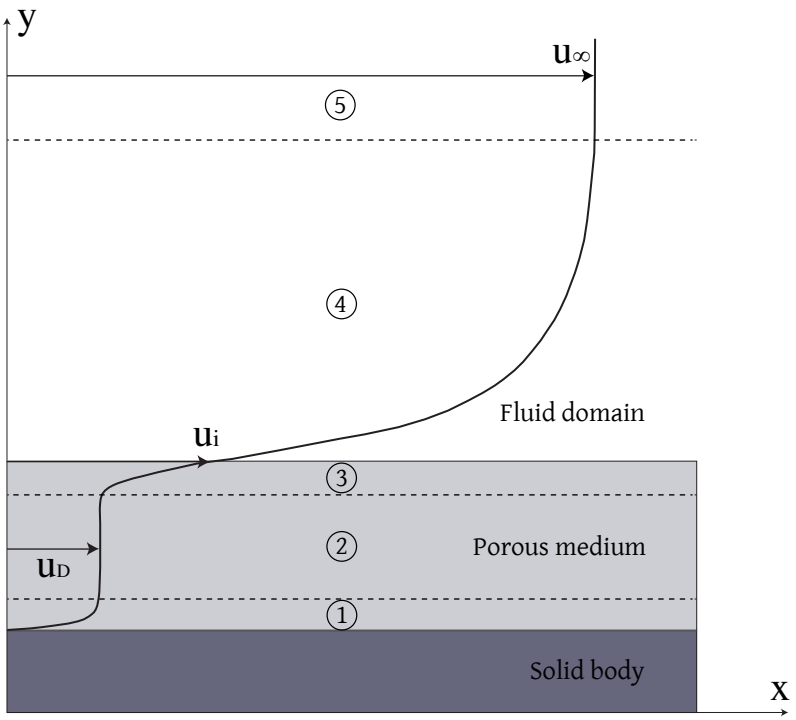

Figure 2.1: Velocity profile in the vicinity of a porous medium. $\mathbf{u}_D$ denotes the Darcy velocity of the flow within the porous medium, $\mathbf{u}_i$ is the non-zero velocity at the porous/fluid interface and $\mathbf{u}_\infty$ corresponds to the velocity of the main fluid flow.

a solid with permeable walls [Hahn et al., 2002, Jimenez et al., 2001], avoids to solve the porous flow by enforcing appropriate porous-fluid boundary conditions [Beavers and Joseph, 1967]. This method neglects the porous medium physics and does not permit to have an overall view of the problem. On the contrary, the second approach considers that the porous flow has to be accurately computed. For that purpose, it solves the governing equations in each region by coupling the Darcy equation (which governs flows in porous media) and the Navier-Stokes equations (which govern flows in free-fluids) with a right treatment at the interface [Breugem et al., 2005, Hanspal et al., 2006]. However, this approach is very difficult to handle especially because of the interface problem.

Therefore, the penalized Vorticity-Transport-Equation 2.21 appears to be very convenient to model the flow in the whole domain thanks to the dimensionless penalization factor λ, whose value allows to distinguish between the different materials. As mentioned in the previous section, λ is expressed as $\lambda = \mu\Phi H/\rho k\bar{\mathbf{u}}$ where $\bar{\mathbf{u}}$ actually corresponds to the main uniform fluid flow velocity $\mathbf{u}_\infty = (u_\infty, 0, 0)$. In this study we set $H = \rho = u_\infty = 1$ and we recall that the porosity Φ is close to 1 as imposed by the Brinkman equation ([Nield and Bejan, 1999]). Therefore λ essentially depends, in the inverse proportion, on the intrinsic permeability k of the medium. Varying the value of λ thus directly defines the different media. Indeed, in the fluid, the intrinsic permeability coefficient k goes to infinity, thus the fluid can be considered numerically as a porous media with a very high permeability. We set $lambda = 0$ in this region. As a consequence, the penalization term vanishes in equation 2.21, and we naturally recover the dimensionless Vorticity Transport Equation:

$$\frac{\partial \boldsymbol{\omega}}{\partial t} + (\mathbf{u}\cdot\nabla)\boldsymbol{\omega} - (\boldsymbol{\omega}\cdot\nabla)\mathbf{u} = \frac{1}{Re}\Delta\boldsymbol{\omega}. \tag{2.23}$$

On the contrary, the solid has a permeability coefficient k close to zero, it can be consequently modeled by fixing the penalization parameter λ to a very high value. In this study λ is set to 10^8 in the solid. It was proved in [Angot et al., 1999] that solving equation 2.21 with such a value of λ was equivalent to solve Darcy's law in the solid. Furthermore, setting the λ parameter to an

intermediate value, reasonably chosen between these two extreme values ($\lambda = 0$ and $\lambda = 10^8$), would model a porous medium in which the flow has a Darcy velocity $\mathbf{u}_D$ (Figure 2.1). Complete studies will be presented in the chapters 3 and 4 in order to determine the range of λ-values allowing to actually model a porous medium.

As a conclusion, the variation of λ corresponds to the variation of k and specifies the intrinsic porous material permeability. The following table recapitulates the settings used in this study according to the different regions of the domain:

Domain regions	λ-value and corresponding permeability	State of the velocity flow
Fluid	$\lambda = 0$ (infinite permeability)	$\mathbf{u}$ is not penalized
Solid	$\lambda = 10^8$ (vanishing permeability)	$\mathbf{u} \to 0$
Porous	$0 < \lambda < 10^8$ (intermediate permeability)	$\mathbf{u} = \mathbf{u}_D$

2.2 Forces evaluation

The accurate computation of the unsteady aerodynamic force exerted by the fluid on an immersed body is of great importance in the framework of this study (see Insert 2).

Insert 2 – Aerodynamic force

The aerodynamic force is the force exerted by a fluid on an immersed body.

It originates from the relative motion between body and fluid and arises from two causes:

- the normal force due to the **pressure** on the surface of the body
- the shear force due to the viscosity of the fluid, also known as skin **friction**, acting locally, parallel to the surface .

In three dimensions, the components of the vector force **F** are the following:

- the drag F_x: component parallel to the direction of relative motion.
- the vertical lift F_y: component normal to the direction of relative motion, vertically.
- the lateral lift F_z: component normal to the direction of relative motion, horizontally.

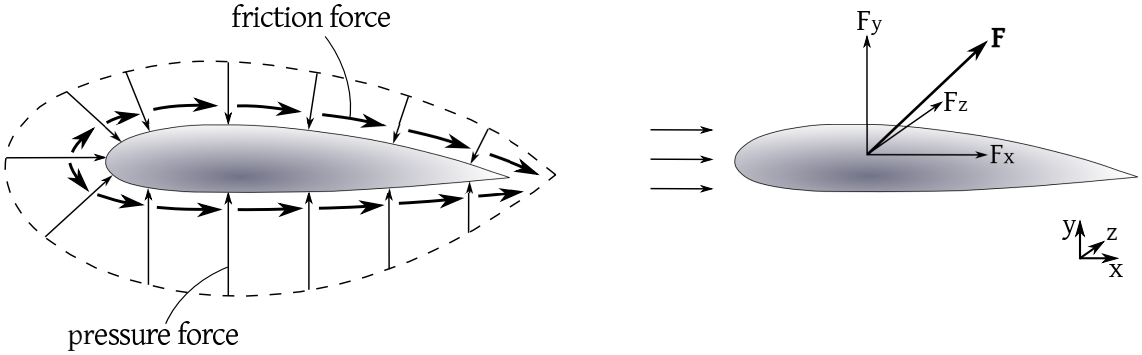

Indeed, on one hand the force provides a reliable diagnostic to validate the ability of the present method to model the problem correctly and on the other hand it represents the main physical quantity to be minimized in terms of the flow control application handled in this thesis. However, the evaluation of this force is not so simple and many works have been carried out on that subject. One can for instance refer to the studies of [Quartapelle and Napolitano, 1982,

Pan and Chew, 2002, Protas, 2007]. In this section, we will present different formulations of the aerodynamic force and we will try to highlight the one that would be suited to the present framework. For that purpose, let us assume a flow in $\mathbb{R}^N$ around a bounded body B with velocity and vorticity vanishing at infinity.

A first approach to compute the force consists in using the penalization term, since it actually corresponds to a forcing term in the Navier-Stokes equations. Indeed, the Brinkman penalization method allows to compute the pressure as a continuous field on the whole domain including the bodies when the velocity-pressure formulation is considered. It was therefore shown in [Caltagirone, 1994] that one can compute the force by integrating the penalization term on the volume of the body:

$$\mathbf{F} = \frac{1}{Re}\int_B \Delta\mathbf{u}\, d\mathbf{x} - \int_B \nabla p\, d\mathbf{x} \approx \int_D \lambda\chi_b\mathbf{u}\, d\mathbf{x}. \tag{2.24}$$

This formula is based on the velocity-pressure formulation of the penalization method. It assumes that the velocity is of the order of λ^{-1} inside the body. However, in a vorticity formulation there is no direct control of the velocity in the body. In practice one observes that the velocity in the body is small but larger than λ^{-1}. This is illustrated in Figure 2.2 showing a converged velocity in the order of 2.5×10^{-3} inside the obstacle in the case of flow past a 2D circular cylinder at $Re = 550$. In that case, we found that accurate computations of the force could

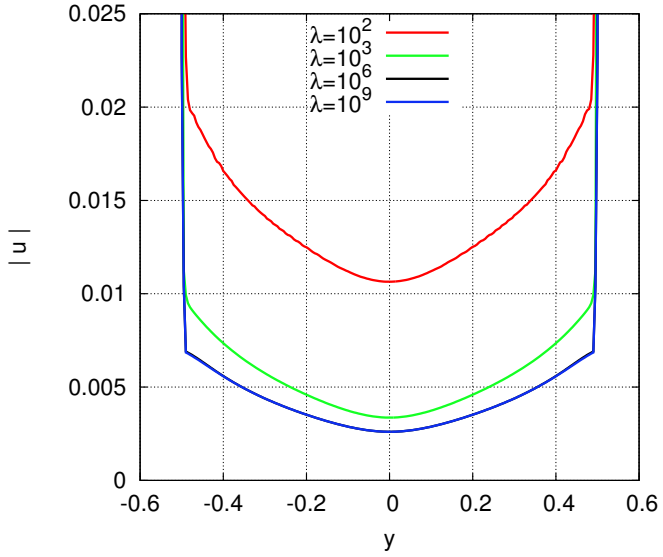

Figure 2.2: Mean velocity magnitude profiles in a section across the center of a circular cylinder, at $x = 0$, obtained for different λ values at $Re = 550$.

not be achieved using the formula 2.24. We may instead use the force evaluations in terms of vorticity distributions around the body.

The force $\mathbf{F}$ exerted by a flow on the body is given by:

$$\mathbf{F} = -\frac{d}{dt}\int_{B'} \mathbf{u}\, d\mathbf{x}, \tag{2.25}$$

where B' denotes the domain outside B. Integration by parts allows to express this force in terms of the vorticity, with N denoting the space dimension:

$$\mathbf{F} = -\frac{1}{N-1}\frac{d}{dt}\int_{S'} \mathbf{x}\times\boldsymbol{\omega}\, d\mathbf{x} - \frac{1}{N-1}\frac{d}{dt}\oint_{\partial S} \mathbf{x}\times(\mathbf{n}\times\mathbf{u}) d\mathbf{s}. \tag{2.26}$$

In the above expression, the first integral is the linear hydrodynamical impulse and the second integral is the bound vorticity (see [Saffman, 1992]). For an impulsively started obstacle at early times, the vorticity remains essentially attached to the body, and this formula can be used by taking a computational domain large enough to contain the vorticity support. When vorticity shedding occurs, this is no longer possible.

Alternatively, one may consider the method used by [Koumoutsakos and Leonard, 1995] and [Poncet, 2001]. By integrating the velocity-pressure Navier-Stokes equations on B' (the domain around B), one gets:

$$\frac{d}{dt}\int_{B'} \mathbf{u}\ d\mathbf{x} - \nu \int_{B'} \Delta\mathbf{u}\ d\mathbf{x} + \int_{B'} \nabla p\ d\mathbf{x} = 0. \tag{2.27}$$

Therefore, according to the force definition 2.25, $\mathbf{F}$ may be expressed as follows:

$$\mathbf{F} = -\nu \int_{B'} \Delta\mathbf{u}\ d\mathbf{x} + \int_{B'} \nabla p\ d\mathbf{x}, \tag{2.28}$$

where one assumes that vorticity vanishes at infinity, which in practice is always the case. Moreover, one has:

$$\int_{B'} \nabla p\ d\mathbf{x} = \int_{\partial B} p\mathbf{n}\ d\mathrm{s}, \tag{2.29}$$

and according to the Poisson equation 2.13 and the Green's formula:

$$-\nu \int_{B'} \Delta\mathbf{u}\ d\mathbf{x} = \nu \int_{B'} \nabla\times\boldsymbol{\omega}\ d\mathbf{x} = -\nu \int_{\partial B} \boldsymbol{\omega}\times\mathbf{n}\ d\mathrm{s}. \tag{2.30}$$

Finally, the expression of $\mathbf{F}$ is given by:

$$\mathbf{F} = -\nu \int_{\partial B} \boldsymbol{\omega}\times\mathbf{n}\ d\mathrm{s} + \int_{\partial B} p\mathbf{n}\ d\mathrm{s}. \tag{2.31}$$

One advantage of such expression is that it allows to distinguish friction (in the first integral) from pressure drag (in the second integral), which can be very interesting in terms of flow control issue to quantitatively determine the respective contribution of the two different components of the total drag. However, the use of this expression requires an accurate computation of the pressure term which is precisely a complicated task that vortex methods allow to bypass. To overcome this difficulty, a solution would be to perform substitutions and integrations by parts of this relation in order to remove the pressure term. In the case of a 2D circular cylinder of radius r, this yields the following formula [Koumoutsakos and Leonard, 1995]:

$$\mathbf{F} = \nu\ r \left(\int_0^{2\pi} \boldsymbol{\omega}\overrightarrow{\mathbf{e}_\theta}\ d\theta - \int_0^{2\pi} \frac{\partial\boldsymbol{\omega}}{\partial\mathbf{n}}\overrightarrow{\mathbf{e}_\theta}\ d\theta \right). \tag{2.32}$$

For a detached bluff body flow this formula can be used as long as vorticity and its normal derivatives are accurately captured at the boundary. However, the penalization method just described is derived from a method which is only first order for the velocity. It therefore does not capture vorticity values and fluxes at the boundary with enough accuracy to give reliable force evaluation through 2.32 with reasonable grid sizes. It is consequently necessary to use a method which does not involve integrals of the physical quantities on the surface of the body. The technique chosen here combines time derivatives, volume integrals of the vorticity momentum - like in formula 2.26 - and vorticity boundary values as well as fluxes on a surface away from the body, where these quantities are accurately computed.

For that purpose, we follow the approach proposed by [Noca et al., 1999] who presented some closed formulations of the incompressible Navier-Stokes equations with such properties. In this study, we mainly focus on the so-called *momentum Noca's equation* that we rewrite as follows:

$$\mathbf{F} = -\frac{d}{dt}\int_V \mathbf{u}\, d\mathbf{x} + \int_\Sigma \mathbf{n}\cdot\boldsymbol{\gamma}\, d\mathbf{x}, \tag{2.33}$$

where, as depicted in Figure 2.3, V is a control volume containing the body B, Σ denotes its boundary and

$$\begin{aligned}\boldsymbol{\gamma} = & \\ & \frac{1}{2}|\mathbf{u}|^2\mathbf{I} - \frac{1}{N-1}\mathbf{u}\cdot(\mathbf{x}\times\boldsymbol{\omega}) + \frac{1}{N-1}\boldsymbol{\omega}\cdot(\mathbf{x}\times\mathbf{u}) \\ & -\frac{1}{N-1}\left[\left(\mathbf{x}\cdot\frac{\partial\mathbf{u}}{\partial t}\right)\mathbf{I} - \mathbf{x}\cdot\frac{\partial\mathbf{u}}{\partial t}\right] + \frac{1}{N-1}\left[\mathbf{x}\cdot(\nabla\cdot\mathbf{T})\mathbf{I} - \mathbf{x}(\nabla\cdot\mathbf{T})\right] + \mathbf{T}.\end{aligned} \tag{2.34}$$

In the above equation N corresponds to the space dimension and $\mathbf{T}$ is the viscous stress tensor:

$$\mathbf{T} = \mu(\nabla\mathbf{u} + \nabla\mathbf{u}^{\mathbf{t}}), \tag{2.35}$$

where μ is the dynamic viscosity of the fluid. The main advantage of this formulation compared to equation 2.26 lies in the fact that the computation of the force is performed on a fixed control volume V, containing B and included inside the computational domain D, which does not need to adapt to the vorticity distribution. Moreover, the surface integrals involved in this Noca's formulation give rise to less difficulties than in 2.26 since they are evaluated away from the obstacle.

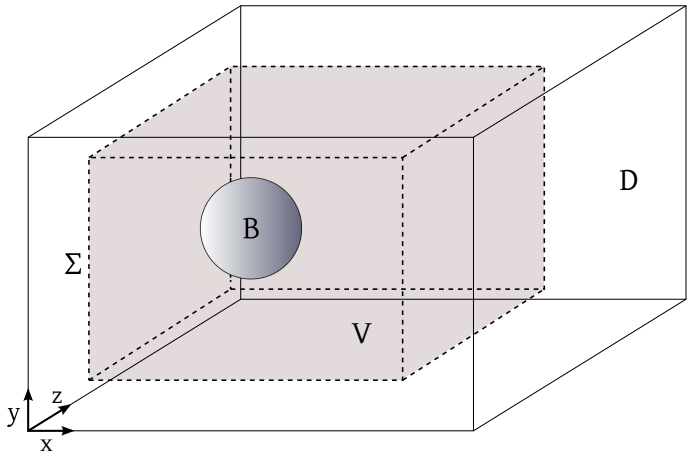

Figure 2.3: Computational domain D and control volume V around the body B.

The Noca's expressions encounter a large success both in the experimental community, where it is often used along with the Digital Particle Image Velocimetry (DPIV) technique [Sterenborg et al., 2014], and in the numerical approaches, especially when the pressure field is not explicitly computed (the pressure is indeed not involved at all in Noca's formulations). Such formulas, and in particular formula 2.33, have been for instance used successfully by [Gallizio, 2009] to accurately compute the force in the context of a two-dimensional hybrid vortex methods.

However, some questions arise about this method. For instance, one can expect that the force evaluated with Noca's formulations is sensitive to the size of the control volume V. A parametric study on that subject is precisely carried out in [Noca et al., 1999] and concludes that the force results indeed strongly depend on the size of V and on the origin taken for the values of the $\mathbf{x}$ positions involved in the formula. It emerges from this study that large control volumes (with a size of roughly the order of the computational domain) and a body centered origin represent the set of parameters leading to the most accurate results.

In any case, regardless of the results, the main issue lies in the fact that, in 3D, Noca's formula 2.33 is quite expensive to evaluate, first because of the numerous operations involved by the volume integral in V and secondly because of the complicated computations implicated in the surface integrals on Σ. Moreover, it would be preferable to discard any parameter influence

in the evaluation of the force.

The last method we propose for force evaluation is the more numerical approach introduced by [Morency et al., 2012] under the name of *change of momentum*. It is based on the fact that the time dependent force exerted by a fluid on a body of constant mass is directly proportional to the body acceleration. For unit density one has:

$$\mathbf{F} = -\frac{d}{dt}\int_B \mathbf{u}\ d\mathbf{x}. \tag{2.36}$$

If we (already) think in terms of numerical iterative process, we can consider that, at each time step, the fluid is allowed to enter inside the rigid body before the penalization term enforces the velocity $\mathbf{u}$ to be equal to $\mathbf{u}_\lambda = 0$ inside the body. Therefore, the obstacle experiences the following change of momentum:

$$\Delta\mathbf{m} = \int_B (\mathbf{u} - \mathbf{u}_\lambda)\ d\mathbf{x}, \tag{2.37}$$

and the force is finally obtained by the formula:

$$\mathbf{F} = \frac{d}{dt}\int_B (\mathbf{u} - \mathbf{u}_\lambda)\ d\mathbf{x}, \tag{2.38}$$

which indeed corresponds to the numerical acceleration of the body.

Based on the overall issues emerging from this section, we finally decided to consider the *Noca's momentum equation* 2.33 to compute the aerodynamic force in two-dimensions. This choice ensures the accuracy of the results, provided that the control volume is sufficiently large. For the three-dimensional problems addressed in this work, the *change of momentum* formula 2.38 will be preferred for its ease of use. The numerical flow solutions obtained with such approaches will be detailed in the next chapter of this thesis.

To conclude this section, we give the dimensionless quantities used to quantify the different components of the aerodynamic force. They are called the drag and lift coefficients and are defined by:

$$C_D = \frac{F_x}{q \times \mathcal{A}}, \qquad C_L = \frac{F_y}{q \times \mathcal{A}}, \qquad C_S = \frac{F_z}{q \times \mathcal{A}}, \tag{2.39}$$

where the lift coefficient is decomposed into C_L (vertical lift) and C_S (side lift), $q = \frac{1}{2}\rho u_\infty^2$ denotes the dynamic pressure and $\mathcal{A}$ is the reference area, also defined as the surface of the body "seen" by the fluid. In the case of a 2D cylinder and a 3D sphere the reference area is respectively equal to $\mathcal{A} = 2r$ and $\mathcal{A} = \pi r^2$, where r refers to the radius.
For a 2D cylinder of diameter d, the force coefficients write:

$$C_D = \frac{2F_x}{\rho u_\infty^2 d}, \qquad C_L = \frac{2F_y}{\rho u_\infty^2 d}, \qquad C_S = \frac{2F_z}{\rho u_\infty^2 d} \tag{2.40}$$

and for a 3D sphere of radius r, they are given by:

$$C_D = \frac{2F_x}{\rho u_\infty^2 \pi r^2}, \qquad C_L = \frac{2F_y}{\rho u_\infty^2 \pi r^2}, \qquad C_S = \frac{2F_z}{\rho u_\infty^2 \pi r^2} \tag{2.41}$$

2.3 Far-field boundary conditions

As mentioned in the previous section, the present study uses a bounded computational domain. Artificial boundary conditions therefore need to be prescribed at the box walls. To model flows past obstacles in bounded domains, the common and natural far-field boundary conditions are uniform-flow at the inlet and outflow type boundary condition at the outlet, usually handled

with Neumann type boundary conditions. These conditions ensure a given inlet flow. They are often coupled with Dirichlet type boundary conditions in the other directions.

In the present work, we consider periodic boundary conditions. This choice will allow us to use a Fast Fourier Transform method to solve the Poisson equation $\Delta \mathbf{u} = -\nabla \times \boldsymbol{\omega}$. The dedicated parallel `fftw` library, particularly well suited for periodic Poisson problem, can therefore be used. However, handling periodic boundary conditions implies special treatments on the flow fields in order to recover the desired uniform flow at the inlet. These treatments appear in two types of corrections that we describe here.

Eddies absorption

A first consequence of periodic boundary conditions is the emergence, in the upstream region, of eddies coming periodically from the outlet (we suppose in this study that the domain has a sufficient size in the y and z directions so that the wake do not reach the concerned boundaries). In order to discard these arising vortices, one needs to apply a specific treatment on the vorticity field. This treatment consists in an absorption, in the flow direction, of the vorticity within a band located at the outlet of the domain. The absorbed vorticity $\tilde{\boldsymbol{\omega}}$ is defined as:

$$\tilde{\boldsymbol{\omega}} = f(x)\ \boldsymbol{\omega}_{\text{periodic}}, \tag{2.42}$$

where f is the following one-dimensional smoothing function defined in the flow direction, that is to say the x-direction [Parker and Balachandar, 2001]:

$$f(x) = \begin{cases} 1 & \text{if } \ x < x_b \\ \dfrac{\tanh(\alpha(x - x_c)) - \tanh(\alpha(x_e - x_c))}{\tanh(\alpha(x_b - x_c)) - \tanh(\alpha(x_e - x_c))} & \text{if } \ x_b \leq x \leq x_e \\ 0 & \text{if } \ x > x_e \end{cases} \tag{2.43}$$

with x_b, x_c and x_e respectively referring to the beginning, the center and the end of the absorption band at the outlet (see Figure 2.4). The parameter α allows to adjust the steepness of the absorption function f.

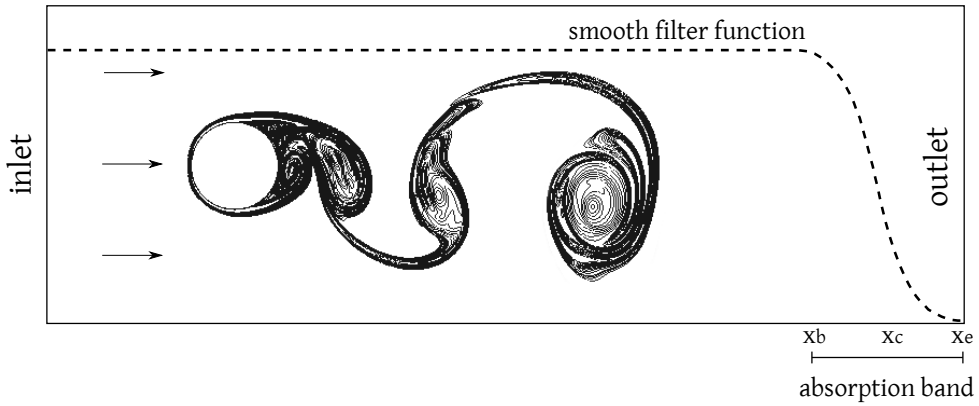

Figure 2.4: Schematic representation of the smooth vorticity absorption performed at the outlet.

In two dimensions the vorticity field has only one non-zero component, it therefore automatically satisfies the condition div $\omega = 0$. In three dimensions it is not the case and one needs to ensure the solenoidal condition in the absorption procedure.

For that purpose, let us first define the expression of the corrected velocity $\tilde{\mathbf{u}}$ allowing to recover a uniform flow field at the inlet:

$$\tilde{\mathbf{u}} = f(x)\ \mathbf{u}_{\text{periodic}} + (1 - f(x))\ \mathbf{u}_{\infty}, \tag{2.44}$$

where f is given by definition 2.43.
One then obtains:

$$\tilde{\boldsymbol{\omega}} = \nabla \times \tilde{\mathbf{u}} \tag{2.45}$$

$$= f(x)\ \boldsymbol{\omega}_{\text{periodic}} + [\nabla f(x) \times \mathbf{u}_{\text{periodic}}] + \nabla[1 - f(x)] \times \mathbf{u}_\infty \tag{2.46}$$

$$= \begin{pmatrix} \omega_x f(x) \\ \omega_y f(x) \\ \omega_z f(x) \end{pmatrix} + \begin{pmatrix} 0 \\ -f'(x)u_z \\ f'(x)u_y \end{pmatrix} + \begin{pmatrix} 0 \\ f'(x)u_{z\infty} \\ -f'(x)u_{y\infty} \end{pmatrix}. \tag{2.47}$$

Knowing that the divergence of a curl is always zero, the above absorption guarantees div $\boldsymbol{\omega} = 0$. As can be seen on Figure 2.5, a 3D vorticity absorption based on equation 2.42 instead of 2.47 would be responsible for spurious reflections at the outflow boundary, affecting the solution.

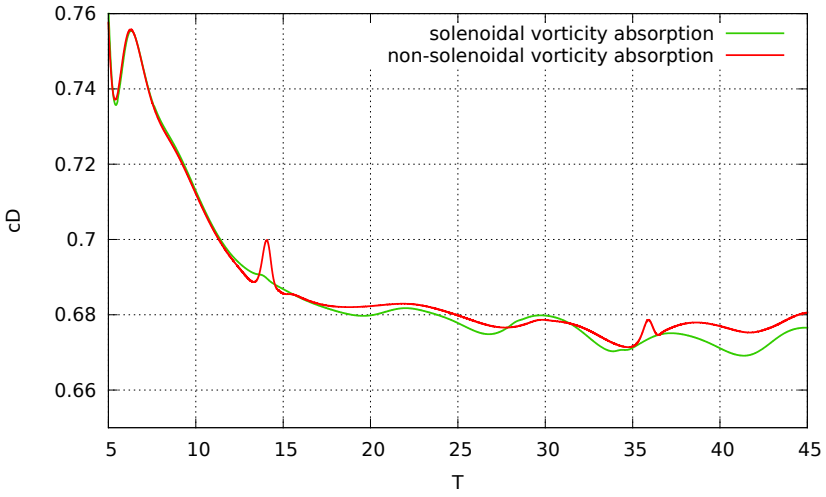

Figure 2.5: Time evolution of drag coefficient for flow past a 3D sphere at $Re = 300$: comparison of two types of 3D vorticity absorptions respectively performed with equation 2.47 (green curve) and equation 2.42 (red curve).

Velocity correction

The prescription of periodic boundary conditions also implies a zero circulation, i.e. $\int_D \boldsymbol{\omega} = 0$, which is not satisfied in our case. Solving the Poisson equation $\Delta \mathbf{u} = -\nabla \times \boldsymbol{\omega}$ with periodic boundary conditions consequently leads to a modification of the space-average velocity field. To account for non-zero circulation, a correction of the velocity is therefore necessary after the Poisson equation resolution, at each time step, by adding transverse velocities with their streamwise dependencies. This correction is performed as follows.
Let us introduce the present notation in order to express the corrected velocity:

$$\mathbf{u} = \widetilde{\mathbf{u}} + \overline{\mathbf{u}}. \tag{2.48}$$

In this relation, $\widetilde{\mathbf{u}}$ denotes the output velocity field obtained from the FFT-evaluations performed in the Fast Poisson Solver and $\overline{\mathbf{u}}$ represents the space-average velocity, that we aim to correct. The x-axis of the Cartesian system corresponds to flow direction and the velocity is initialized setting $\mathbf{u}(t = 0) = (u_{x\infty}, u_{y\infty}, u_{z\infty})$.
$\overline{u_x}$ is a spatially constant flux, therefore $\dfrac{\partial \overline{u_x}}{\partial x} = \dfrac{\partial \overline{u_x}}{\partial y} = \dfrac{\partial \overline{u_x}}{\partial z} = 0$ and the mean vorticity is given

by:

$$\overline{\omega_x} = \frac{\partial \overline{u_z}}{\partial y} - \frac{\partial \overline{u_y}}{\partial z} \tag{2.49}$$

$$\overline{\omega_y} = -\frac{\partial \overline{u_z}}{\partial x} \tag{2.50}$$

$$\overline{\omega_z} = \frac{\partial \overline{u_y}}{\partial x}. \tag{2.51}$$

First of all, a correction of the streamwise component of the velocity u_x is necessary in order to correct the flux at the inlet. This correction stands as follows:

u_x correction:

Let I be the inlet rectangular surface of the computational box, normal to the flow direction, of area $L_y L_z$. L_y and L_z respectively denote the lengths of the computational box in the y and z directions. According to the decomposition $\mathbf{u} = \widetilde{\mathbf{u}} + \overline{\mathbf{u}}$ and knowing that $\overline{u_x}$ is a constant and that the desired flow rate at the inlet is equal to $u_{x\infty} L_y L_z$, one has:

$$\underbrace{\iint_I u_x \; dydz}_{\text{desired flow rate}} = \underbrace{\iint_I \widetilde{u_x} \; dydz}_{\text{calculated flow rate}} + \iint_I \overline{u_x} \; dydz \tag{2.52}$$

$$\iff \overline{u_x} = u_{x\infty} - \frac{\iint_I \widetilde{u_x} \; dydz}{L_y L_z} \tag{2.53}$$

and finally:

$$u_x = u_{x\infty} + \widetilde{u_x} - \frac{\iint_I \widetilde{u_x} \; dydz}{L_y L_z}. \tag{2.54}$$

Next we need to correct the transverse velocities u_y and u_z in order to recover a non-zero circulation.

u_y correction:

According to relation 2.51 one has $\overline{u_y} = \overline{\omega_z} x + c_1$, with c_1 a constant value that we aim to evaluate and $\overline{\omega_z} = \dfrac{1}{L_x L_y L_z} \displaystyle\int_D \omega_z \, d\mathbf{x}$, with $L_x L_y L_z$ corresponding to the volume of the computational domain D. From the decomposition $\mathbf{u} = \widetilde{\mathbf{u}} + \overline{\mathbf{u}}$, one therefore concludes that $u_y = \widetilde{u_y} + \overline{\omega_z} x + c_1$. Thus:

$$\underbrace{\iint_I u_y \; dydz}_{\text{desired flow rate}} = \underbrace{\iint_I \widetilde{u_y} \; dydz}_{\text{calculated flow rate}} + \iint_I \overline{\omega_z} x \; dydz + \iint_I c_1 \; dydz. \tag{2.55}$$

Since the flow rate is desired to be $u_{y\infty} L_y L_z$, then:

$$u_{y\infty} L_y L_z = \iint_I \widetilde{u_y} \; dydz + \; \overline{\omega_z} x_0 L_y L_z + c_1 L_y L_z \tag{2.56}$$

$$\iff c_1 = u_{y\infty} - \frac{\iint_I \widetilde{u_y} \; dydz}{L_y L_z} - \overline{\omega_z} x_0, \tag{2.57}$$

and finally the corrected y-component of the velocity fields stands as:

$$u_y = u_{y\infty} + \widetilde{u_y} + \overline{\omega_z}(x - x_0) - \frac{\iint_I \widetilde{u_y} \; dydz}{L_y L_z}, \tag{2.58}$$

where x_0 corresponds to the x-coordinate of the inlet surface in the Cartesian system.

u_z correction:

Following the same principle, and according to the relation 2.50 one obtains $\overline{u_z} = -\overline{\omega_y}x + c_2$ with c_2 a constant value. From the decomposition $\mathbf{u} = \tilde{\mathbf{u}} + \overline{\mathbf{u}}$, one gets $u_z = \widetilde{u_z} - \overline{\omega_y}x + c_2$. Finally, mimicking the process used for u_y, one gets:

$$u_z = u_{z\infty} + \widetilde{u_z} - \overline{\omega_y}(x - x_0) - \frac{\iint_I \widetilde{u_z}\ dydz}{L_y L_z}. \tag{2.59}$$

In conclusion, for a free stream velocity equal to $\mathbf{u}_\infty = (u_{x\infty}, u_{y\infty}, u_{z\infty}) = (1, 0, 0)$, the corrected streamwise component of the velocity allowing to recover the desired flux at the inlet is:

$$u_x = 1 + \widetilde{u_x} - \frac{\iint_I \widetilde{u_x}\ dydz}{L_y L_z}, \tag{2.60}$$

and the corrected transverse components of the velocity allowing to account for a non-zero circulation are:

$$u_y = \widetilde{u_y} + \overline{\omega_z}(x - x_0) - \frac{\iint_I \widetilde{u_y}\ dydz}{L_y L_z} \tag{2.61}$$

$$u_z = \widetilde{u_z} - \overline{\omega_y}(x - x_0) - \frac{\iint_I \widetilde{u_z}\ dydz}{L_y L_z}. \tag{2.62}$$

In order to validate the use of periodic boundary conditions coupled with the above special treatments, let us consider a flow past a 3D sphere at $Re = 300$ in a bounded domain $D = [-2,\ 8.24] \times [-2.56,\ 2.56] \times [-2.56,\ 2.56]$. The free stream velocity is desired to be uniform at the inlet, with $\mathbf{u}_\infty = (1, 0, 0)$. Figure 2.6 shows upstream isocontours of u_x at the end of the simulation ($T = 75$) in the inlet YZ plane ($x = x_0 = -2$) for two different cases. In the first case (left figure), the absorption band lies from $x_b = 7.24$ until $x_e = 8.24$ and $\alpha = 10$ in the definition of f (eq. 2.43). The range of u_x values at the inlet surface is then equal to $[0.973,\ 1.009]$. In the second case (right figure), the absorption band is twice thicker ($x_b = 6.24$, $x_e = 8.24$) and $u_{x\ \text{inlet}} \in [0.977,\ 1.007]$.

The present inlet streamwise velocity thus only shows a maximum relative error of respectively 2.7% and 2.3% for the first and the second case compared to the theoretical uniform free stream flow ($u_{x\infty} = 1$). Let us also notice the symmetrical patterns of the velocity isocontours. This symmetry is explained by the periodic boundary conditions.

We also performed simulations with a domain twice longer in the x-direction, i.e. $x_b = 17.48$, $x_e = 18.48$ and obtained very similar results ($u_{x\ \text{inlet}} \in [0.975,\ 1.004]$). Finally, a simulation was carried out in the original domain D with a higher Reynolds number, $Re = 1000$, setting $x_b = 7.24$, $x_e = 8.24$ and comparable results were achieved ($u_{x\ \text{inlet}} \in [0.977,\ 1.004]$).

2.4 Complement on stability conditions

In the present numerical algorithm, the advection and the stretching schemes will be subject to a stability condition. The aim of this section will be first to express each of these conditions and secondly to identify the correct values of the involved constants in order to define a global condition on the simulation time step.

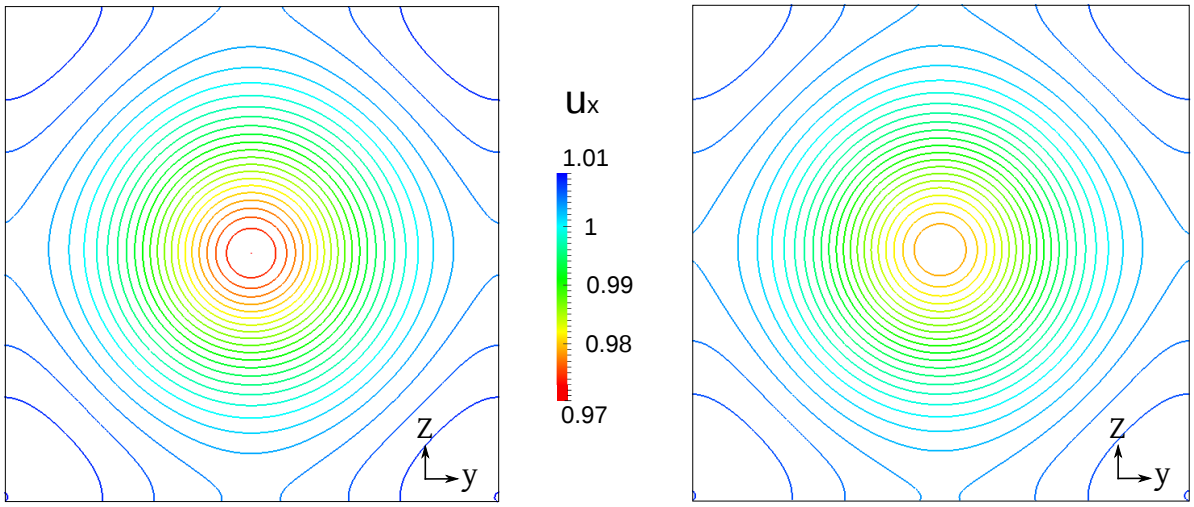

Figure 2.6: Flow past a 3D sphere: isocontours of the inlet streamwise velocity u_x in the YZ plane when imposing periodic boundary conditions coupled with adapted corrections. (Left picture) The width of the absorption band equals 1. (Right picture) The width of the absorption band equals 2.

2.4.1 Stability condition for the advection scheme

In particle methods, the non-linear stability of the convection/remeshing scheme is ensured under the following condition on the time step:

$$\Delta t_{\text{adv}} \leq \frac{\text{LCFL}}{\|\nabla \mathbf{u}\|_\infty}, \tag{2.63}$$

where the Lagrangian CFL must satisfy LCFL ≤ 1 [Cottet et al., 2014]. From a physical point of view, this stability condition imposes that particles trajectories do not cross. One can notice here that the time step in not constrained by the grid size or the distance between the particles but only by the flow strain, which often provides larger time steps compared to Eulerian grid-based schemes, constrained by the following condition:

$$\Delta t_{\text{adv}} \leq \frac{\text{CFL}\ \Delta x}{\|\mathbf{u}\|_\infty}, \qquad \text{CFL} \leq 1. \tag{2.64}$$

Another derived version of the stability condition 2.63 may also be found in literature, like for instance in [Gallizio, 2009, Gazzola, 2013]:

$$\Delta t_{\text{adv}} \leq \frac{\text{LCFL}}{\|\boldsymbol{\omega}\|_\infty}. \tag{2.65}$$

2.4.2 Stability condition for the stretching scheme

The stretching equation, which models the lengthening of vortices in a three-dimensional flow, may be given under several formulations [Cottet and Koumoutsakos, 2000]:

$$\frac{\partial \boldsymbol{\omega}}{\partial t} = \text{div}(\boldsymbol{\omega} : \mathbf{u}) \tag{2.66}$$

$$\frac{\partial \boldsymbol{\omega}}{\partial t} = [\nabla \mathbf{u}] \cdot \boldsymbol{\omega} \tag{2.67}$$

$$\frac{\partial \boldsymbol{\omega}}{\partial t} = [\nabla \mathbf{u}]^t \cdot \boldsymbol{\omega} \tag{2.68}$$

$$\frac{\partial \boldsymbol{\omega}}{\partial t} = \frac{1}{2}([\nabla \mathbf{u}] + [\nabla \mathbf{u}]^t) \cdot \boldsymbol{\omega}. \tag{2.69}$$

We note that these formulations are all equivalent at the continuous level. However, it is not the case at the discrete level. The formulation which will be retained in the present work is the conservative formulation 2.66 but for the sake of simplicity, the stability analysis is performed from equation 2.67. The details of this study are provided in Appendix (B) and we give here the resulting stability condition for the stretching scheme:

$$\Delta t_{\text{stretching}} < \frac{C}{\max\limits_{1\leq i\leq 3} \sum\limits_{1\leq j\leq 3} \left| \frac{\partial u_i}{\partial x_j} \right|}, \tag{2.70}$$

where C is a constant depending on the time integration scheme used to discretize the stretching equation. The following table gives the values of C for different time integration schemes:

Scheme	order	C
Euler	1	2
Runge-Kutta 2	2	2
Runge-Kutta 3	3	2.5127
Runge-Kutta 4	4	2.7853

2.4.3 Definition of the global simulation time step

The global simulation time step has to take into account the two conditions 2.63 and 2.70. Since these conditions both depend of the flow strain, one can define the global time step as an adaptive parameter along the simulation, like follows:

$$\Delta t^n_{\text{adapt}} = \min(\Delta t^n_{\text{adv}}, \Delta t^n_{\text{stretching}}), \tag{2.71}$$

where n denotes the current iteration. Such definition of the time step thus allows to strongly accelerate the simulation when the flow quantities present low gradients, while ensuring the stability of the overall numerical scheme.

Concerning Δt_{adv}, the theory stands that the LCFL number should be taken lower or equal to 1. In practice, this parameter is often set to LCFL= 1/4 with condition 2.65 and to LCFL= 1/8 with condition 2.63. We aim here to numerically verify the choice of such values, depending on the definition of Δt_{adv}. For that purpose we consider the test case of a flow past a 3D sphere at $Re = 300$ and we compare the adaptive time step values obtained from 2.71 for different LCFL values using conditions 2.63 and 2.65 for Δt_{adv}. The evolution of the adaptive time step is given by Figure 2.7a which is complemented by Table 2.7b. These results show that when condition 2.63 is chosen for the Δt_{adv} constraint, the value LCFL= 1/4 is too large and leads to a lack of stability. The same conclusion holds with the condition **??** and the value LCFL= 1/2. Stable solutions are obtained with condition 2.63 for LCFL= 1/8 and with condition 2.65 for LCFL= 1/4 and LCFL= 1/8. We note here that the commonly used LCFL values are justified in the case of this study. As we aim on one hand to ensure the stability of the solution and on the other hand to use time steps Δt_{adapt} as large as possible, a good compromise here according to Table 2.7b lies in defining Δt_{adv} with respect to condition 2.63 and to set the LCFL number to 1/8.

We now have to look at $\Delta t_{\text{stretching}}$. The stability condition for the stretching equation 2.70 is much less restrictive than the one for advection, which means that the stability of the solution is only dictated by the condition on Δt_{adv}. This statement is illustrated in the context of the 3D sphere test case by Figure 2.8 which clearly shows that the values of $\Delta t_{\text{stretching}}$ are much larger than the one of Δt_{adv} (see Table 2.7b) and actually depend on it.

Based on this analysis, the global adaptive time step will be defined as follows by default in all the three-dimensional simulations performed in this thesis:

$$\Delta t^n_{\text{adapt}} = \frac{1}{8 \left\| \nabla \mathbf{u} \right\|^n_\infty}. \tag{2.72}$$

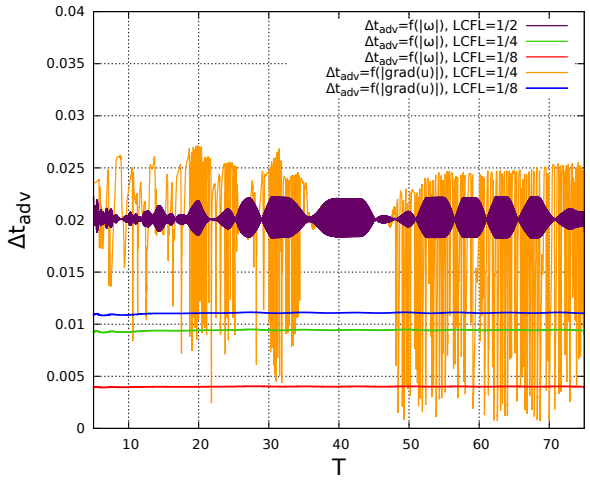

(a) Time evolution of Δt_{adv} along the simulation.

Δt_{adv} cond.	LCFL	solution	Δt_{adv}
$\text{LCFL}/\|\|\nabla \mathbf{u}\|\|_\infty$	1/4	unstable	-
$\text{LCFL}/\|\|\nabla \mathbf{u}\|\|_\infty$	1/8	stable	$\backsimeq 0.011$
$\text{LCFL}/\|\|\boldsymbol{\omega}\|\|_\infty$	1/2	unstable	$\backsimeq 0.02$
$\text{LCFL}/\|\|\boldsymbol{\omega}\|\|_\infty$	1/4	stable	$\backsimeq 0.0095$
$\text{LCFL}/\|\|\boldsymbol{\omega}\|\|_\infty$	1/8	stable	$\backsimeq 0.004$

(b)

Figure 2.7: Study of Δt_{adv} according to different stability conditions in the case of incompressible flow past a 3D sphere at $Re = 300$.

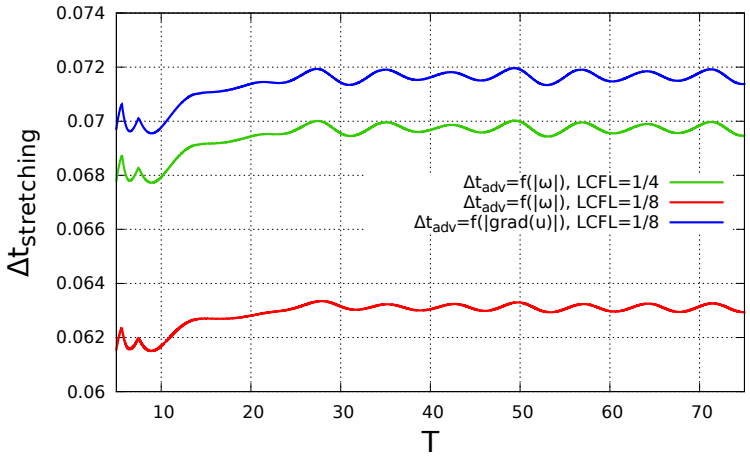

Figure 2.8: Time evolution of $\Delta t_{\text{stretching}}$ along the simulation of incompressible flow past a 3D sphere at $Re = 300$ for different definitions of Δt_{adv}.

Concerning the 2D case, as the computational cost of the overall simulation is much smaller, we can handle the more restrictive constraint 2.65 on Δt_{adv}, setting LCFL to 1/4.

2.5 Numerical discretization and sketch of algorithm

As the aim of this thesis was to first perform passive flow control in the context of two-dimensional flows before handling the three-dimensional problem, the present method has been used and discretized, in a first place, in 2D (see [Mimeau et al., 2015] in Appendix (C)). For the extension to the 3D case, the discretization of the method was improved and implemented in a new computational solver able to satisfy needs related to efficiency and memory management. This section and the following will essentially deal with the three-dimensional case.

In the current section we present the methodology adopted in order to numerically discretize the 3D penalized Vorticity-Transport-Equation:

$$\frac{\partial \boldsymbol{\omega}}{\partial t} + (\mathbf{u}\cdot\nabla)\boldsymbol{\omega} - (\boldsymbol{\omega}\cdot\nabla)\mathbf{u} = \nabla\times\Big(\lambda\,\chi_b(\mathbf{u}_b-\mathbf{u})\Big) + \frac{1}{Re}\Delta\boldsymbol{\omega} \qquad \text{in } D\times(0,T), \tag{2.73}$$

$$\Delta\mathbf{u} = -\nabla\times\boldsymbol{\omega} \qquad \text{in } D\times(0,T), \tag{2.74}$$

The above governing equations are discretized on a plane-parallel computational box. The domain is meshed with an uniform Cartesian grid and periodic boundary conditions are prescribed on the walls (see section (2.3)). Equations 2.73-2.74 are discretized through a viscous splitting algorithm, consisting in solving successively the different operators within the same time iteration (see section (1.4.3.2)). Concerning the main steps of this splitting algorithm, the particle advection is performed in a Lagrangian way and complemented at each time step by a remeshing procedure in order to redistribute the particles on the underlying grid and to avoid the distortion effects (see section (1.4)). The penalization equation is handled on the grid through an implicit time integration scheme and the diffusion equation as well as the Poisson equation are solved on the grid using the Fast Fourier Transform method. The details of the overall numerical discretization are given in the sequel. The successive steps are listed in algorithm 1 and we describe each of these steps giving for each one the involved equation and the numerical method used to discretize it.

Algorithm 1 3D case

Initialization

Preliminary velocity field (on grid) $$\mathbf{u}^0 = \mathbf{u}_\infty = (1,0,0) \tag{2.75}$$

Preliminary vorticity field (on grid) $$\boldsymbol{\omega}^0 = (0,0,0) \tag{2.76}$$

Vorticity penalization (on grid) $$\boldsymbol{\omega}_\lambda^0 = \boldsymbol{\omega}^0 + \nabla \times \left(\frac{-\lambda\chi\Delta t \mathbf{u}^0}{1+\lambda\chi\Delta t} \right) \tag{2.77}$$

Marching

Vorticity absorption (on grid) $$\boldsymbol{\omega}^n = \nabla \times [f\mathbf{u}^n + (1-f)\mathbf{u}_\infty] \tag{2.78}$$

Poisson problem (on grid) $$\Delta \mathbf{u}^n = -\nabla \times \boldsymbol{\omega}^n \tag{2.79}$$

Velocity correction (on grid) $$\mathbf{u}^n = \widetilde{\mathbf{u}}^n + \overline{\mathbf{u}}^n \tag{2.80}$$

Force computation (on grid) $$\mathbf{F} = \frac{d}{dt}\int_B (\mathbf{u}^n - \mathbf{u}_\lambda^n)\, d\mathbf{x} \tag{2.81}$$

Vorticity penalization (on grid) $$\boldsymbol{\omega}_\lambda^n = \boldsymbol{\omega}^n + \nabla \times \left(\frac{-\lambda\chi\Delta t \mathbf{u}^n}{1+\lambda\chi\Delta t} \right) \tag{2.82}$$

Stretching (on grid) $$\frac{\partial \boldsymbol{\omega}^n}{\partial t} = \mathrm{div}(\boldsymbol{\omega}^n : \mathbf{u}^n) \tag{2.83}$$

Diffusion (on grid) $$\frac{\partial \boldsymbol{\omega}^n}{\partial t} = \frac{1}{Re}\Delta \boldsymbol{\omega}^n \tag{2.84}$$

Advection (on particles) $$\frac{\partial \boldsymbol{\omega}^{n+1}}{\partial t} + (\mathbf{u}^n \cdot \nabla)\boldsymbol{\omega}^{n+1} = 0 \tag{2.85}$$

Enstrophy computation (on grid) $$Z = \int_D |\boldsymbol{\omega}^{n+1}|^2 d\mathbf{x} \tag{2.86}$$

Evaluation of $\Delta t_{\mathrm{adapt}}$ (on grid) $$\Delta t_{\mathrm{adapt}}^n = \frac{1}{8\,\|\nabla \mathbf{u}\|_\infty^n} \tag{2.87}$$

Poisson equation

The resolution of the Poisson equation:

$$\Delta \mathbf{u} = -\nabla \times \boldsymbol{\omega}, \tag{2.88}$$

corresponding to the step 2.79 in algorithm 1, is performed on the grid using the Fast Fourier Transform method (FFT). For that purpose, one has first to express $\mathbf{u}$ and $\boldsymbol{\omega}$ in terms of their

Fourier Transform. For a three-dimensional problem, it gives:

$$\mathcal{F}(\mathbf{u})(\xi) = \hat{\mathbf{u}}(\xi) = \int_{\mathbb{R}^3} e^{-2\pi i <\mathbf{x},\xi>} \mathbf{u}(\mathbf{x})\ d\mathbf{x}, \qquad \mathcal{F}(\boldsymbol{\omega})(\xi) = \hat{\boldsymbol{\omega}}(\xi) = \int_{\mathbb{R}^3} e^{-2\pi i <\mathbf{x},\xi>} \boldsymbol{\omega}(\mathbf{x})\ d\mathbf{x}$$

Then, one diagonalizes the Poisson equation in the ξ-space:

$$\mathcal{F}(\Delta\mathbf{u})(\xi) = \mathcal{F}(-\nabla\times\boldsymbol{\omega})(\xi) \tag{2.89}$$

$$\Leftrightarrow\ -|\xi|^2\mathcal{F}(\mathbf{u})(\xi) = \mathcal{F}(-\nabla\times\boldsymbol{\omega})(\xi) \tag{2.90}$$

$$\Leftrightarrow \begin{pmatrix} \widehat{u_x} \\ \widehat{u_y} \\ \widehat{u_z} \end{pmatrix}(\xi) = \frac{1}{|\xi|^2}(\widehat{\nabla\times\boldsymbol{\omega}}) = \frac{i}{|\xi|^2} \begin{pmatrix} \xi_y\widehat{\omega_z} - \xi_z\widehat{\omega_y} \\ \xi_z\widehat{\omega_x} - \xi_x\widehat{\omega_z} \\ \xi_w\widehat{\omega_y} - \xi_y\widehat{\omega_x} \end{pmatrix} \tag{2.91}$$

Finally, the real solution $\mathbf{u}(\mathbf{x})$ is given by the inverse Fourier transform:

$$\mathbf{u}(\mathbf{x}) = \mathcal{F}^{-1}(\hat{\mathbf{u}}(\xi))(\mathbf{x}) = \int_{\mathbb{R}^3} e^{2\pi i <\xi,\mathbf{x}>} \frac{\widehat{\nabla\times\boldsymbol{\omega}}(\xi)}{|\xi|^2}\ d\xi. \tag{2.92}$$

In terms of complex Fast Fourier Transform, the solution is given in 3D by:

$$\mathbf{u}_{k_x,k_y,k_z} = \mathrm{FFT}^{-1}(\hat{\mathbf{u}}_{j_x,j_y,j_z}) = \sum_{k_x=0}^{N_x-1}\sum_{k_y=0}^{N_y-1}\sum_{k_z=0}^{N_z-1} \frac{\widehat{\nabla\times\boldsymbol{\omega}}_{j_x,j_y,j_z}}{|\mathbf{k}|^2}\ e^{\frac{2\pi i}{N_x}j_xk_x}\ e^{\frac{2\pi i}{N_y}j_yk_y}\ e^{\frac{2\pi i}{N_z}j_zk_z}\ , \tag{2.93}$$

where $\hat{\mathbf{u}}_{j_x,j_y,j_z}$ and $\hat{\boldsymbol{\omega}}_{j_x,j_y,j_z}$ respectively denote the Fast Fourier Transform of $\mathbf{u}$ and $\boldsymbol{\omega}$. The evaluation of this solution is numerically carried out by the dedicated library `fftw` [Frigo and Johnson, 2005], imposing periodic boundary conditions.

In algorithm 1, the resolution of the Poisson equation is preceded by step 2.78, corresponding to the solenoidal vorticity absorption. As explained in section (2.3), this absorption is performed through the following equation:

$$\boldsymbol{\omega}^{n+1} = f(x)\ \boldsymbol{\omega}^n + [\nabla f(x) \times \mathbf{u}^n] + \nabla[1 - f(x)] \times \mathbf{u}_\infty, \tag{2.94}$$

where the discretization of the curl operator is done on the grid with a 4^{th} order centered finite-differences scheme.

The resolution of the Poisson equation is then followed by step 2.80, allowing to recover correct flux and inlet velocity conditions (see section (2.3)):

$$\mathbf{u} = \widetilde{\mathbf{u}} + \overline{\mathbf{u}}, \qquad \Longleftrightarrow \qquad \begin{aligned} u_x &= 1 + \widetilde{u_x} - \frac{\iint_I \widetilde{u_x}\ dydz}{L_yL_z} \\ u_y &= \widetilde{u_y} + \overline{\omega_z}(x - x_0) - \frac{\iint_S \widetilde{u_y}\ dydz}{L_yL_z} \\ u_z &= \widetilde{u_z} - \overline{\omega_y}(x - x_0) - \frac{\iint_S \widetilde{u_z}\ dydz}{L_yL_z}. \end{aligned} \tag{2.95}$$

The discretization of the integral terms is performed with a 1^{st} order midpoint rule.

Penalization

In its velocity-vorticity formulation, the continuous penalization equation stands as:

$$\frac{\partial\boldsymbol{\omega}}{\partial t} = \nabla \times \Big(\lambda\ \chi_b(\mathbf{u}_b - \mathbf{u})\Big). \tag{2.96}$$

In the context of this study, where the immersed obstacle is considered static in the computational domain, the body velocity $\mathbf{u}_b$ is equal to 0. One can therefore rewrite the above penalization equation as follows:

$$\frac{\partial \boldsymbol{\omega}}{\partial t} = -\nabla \times (\lambda\ \chi_b \mathbf{u}). \tag{2.97}$$

In order to discretize equation 2.97, let us first of all discretize the penalization equation for the velocity:

$$\frac{\partial \mathbf{u}}{\partial t} = -\lambda \chi_b \mathbf{u}. \tag{2.98}$$

This is done using an implicit 1^{st} order Euler scheme:

$$\frac{\mathbf{u}^{n+1} - \mathbf{u}^n}{\Delta t} = -\lambda \chi_b \mathbf{u}^{n+1} \tag{2.99}$$

$$\iff \mathbf{u}^{n+1} = \frac{\mathbf{u}^n}{1 + \lambda \chi_b \Delta t}. \tag{2.100}$$

One therefore gets the penalized velocity field that we denote $\mathbf{u}_\lambda$. Taking the curl of the above equation and then performing the following successive arrangements:

$$\begin{aligned}
\nabla \times \mathbf{u}^{n+1} &= \nabla \times \left(\frac{\mathbf{u}^n}{1 + \lambda \chi_b \Delta t} \right) \\
\iff \boldsymbol{\omega}^{n+1} &= \nabla \times \left(\mathbf{u}^n - \frac{\lambda \chi_b \Delta t\ \mathbf{u}^n}{1 + \lambda \chi_b \Delta t} \right) \\
&= \nabla \times (\mathbf{u}^n) + \nabla \times \left(\frac{-\lambda \chi_b \Delta t\ \mathbf{u}^n}{1 + \lambda \chi_b \Delta t} \right),
\end{aligned}$$

we finally obtain the conservative formulation of the discrete penalized vorticity [van Rees, 2014]:

$$\boldsymbol{\omega}^{n+1} = \boldsymbol{\omega}^n + \nabla \times \left(\frac{-\lambda \chi_b \Delta t\ \mathbf{u}^n}{1 + \lambda \chi_b \Delta t} \right). \tag{2.101}$$

The treatment of this penalization equation is realized at step 2.82 in algorithm 1, using a 4^{th} order centered finite-differences scheme for the discretization of the curl operator. We notice that the velocity field is not directly penalized in this algorithm. The velocity penalization is implicitly realized through the resolution of the Poisson problem in step 2.79 of algorithm 1.

Stretching

As mentioned in section (2.4.2), several formulations may be used to express the stretching term. In this study we choose the conservative one, given by:

$$\frac{\partial \boldsymbol{\omega}}{\partial t} = \mathrm{div}(\boldsymbol{\omega} : \mathbf{u}). \tag{2.102}$$

It corresponds to step 2.83 in algorithm 1. The time integration scheme chosen here to discretize this equation is the commonly used 3^{rd} order Runge-Kutta TVD (Total Variation Diminishing, i.e. non extra oscillations) scheme [Gottlieb and Shu, 1998]. With this time discretization, the velocity field involved in the divergence operator is not modified. The RK3 scheme approximates $\boldsymbol{\omega}$ at $t^n + \Delta t$ from an approximation of $\boldsymbol{\omega}^n$ and $\mathbf{u}^n$ at time t^n following this procedure:

$$\boldsymbol{\omega}^{(1)} = \boldsymbol{\omega}^n + \Delta t\ \mathrm{div}(\boldsymbol{\omega}^n : \mathbf{u}^n,\ t^n) \tag{2.103}$$

$$\boldsymbol{\omega}^{(2)} = \frac{3}{4}\boldsymbol{\omega}^n + \frac{1}{4}\Big(\boldsymbol{\omega}^{(1)} + \Delta t\ \mathrm{div}(\boldsymbol{\omega}^{(1)} : \mathbf{u}^n,\ t^n + \Delta t)\Big) \tag{2.104}$$

$$\boldsymbol{\omega}^{n+1} = \frac{1}{3}\boldsymbol{\omega}^n + \frac{2}{3}\Big(\boldsymbol{\omega}^{(2)} + \Delta t\ \mathrm{div}\Big(\boldsymbol{\omega}^{(2)} : \mathbf{u}^n,\ t^n + \frac{1}{2}\Delta t\Big)\Big). \tag{2.105}$$

The divergence operator is discretized through a 4^{th} order centered finite-differences scheme on the grid.

Diffusion

The diffusion equation, appearing in step 2.84 of algorithm 1, and given by:

$$\frac{\partial \boldsymbol{\omega}}{\partial t} = \frac{1}{Re}\Delta\boldsymbol{\omega}, \tag{2.106}$$

is discretized in time using an implicit 1^{st} order Euler scheme:

$$\frac{\boldsymbol{\omega}^{n+1} - \boldsymbol{\omega}^n}{\Delta t} = \frac{1}{Re}\Delta\boldsymbol{\omega}^{n+1} \tag{2.107}$$

$$\iff \Delta\boldsymbol{\omega}^{n+1} - \frac{Re}{\Delta t}\boldsymbol{\omega}^{n+1} = -\frac{Re}{\Delta t}\boldsymbol{\omega}^n. \tag{2.108}$$

This equation is solved in the Fourier space, where the solution is given by:

$$\hat{\boldsymbol{\omega}}^{n+1} = \frac{\frac{Re}{\Delta t}}{|\xi|^2 + \frac{Re}{\Delta t}}\,\hat{\boldsymbol{\omega}}^n. \tag{2.109}$$

Particle advection and remeshing procedure

The semi-Lagrangian advection performed in the 3D case is performed using a 1^{st} order directional splitting approach [Magni and Cottet, 2012] (see section (1.4.2) and Figure 1.6). This technique consists in solving the convection/remeshing problem direction by direction. In other words one has to solve here three different mono-dimensional problems. The method is therefore described in the context of a mono-dimensional vorticity transport equation:

$$\frac{\partial \omega}{\partial t} + \frac{\partial}{\partial x}(u\omega) = 0. \tag{2.110}$$

First, one solves the following ODE in order to update the new positions of particles at time t^{n+1} from the grid positions x_i^n and the velocity field u^n at time t^n:

$$\begin{cases} \dfrac{dx_p}{dt} = \mathbf{u}(x_p), & t \in [t^n,\ t^{n+1}] \\ x_p^n = x^n. \end{cases} \tag{2.111}$$

A 2^{nd} order Runge-Kutta scheme is used for the resolution of this equation:

$$x_p^{n+1} = x_p^n + \Delta t\ u^n\left(x_p^n + \frac{\Delta t}{2}u^n\right). \tag{2.112}$$

Once all the particles have been pushed in the same direction, they are remeshed on the grid, in this direction. The kernel chosen here is $\Lambda_{4,2}$ [Cottet et al., 2014] (also called M_6' [Bergdorf and Koumoutsakos, 2006]). Its 1D support includes 6 points and it satisfies 4 moment conditions, it is therefore a 4^{th} order interpolation kernel. Its definition is the following:

$$\Lambda_{4,2}(x) = \begin{cases} 1 - \frac{5}{4}|x|^2 - \frac{35}{12}|x|^3 + \frac{21}{4}|x|^4 - \frac{25}{12}|x|^5 = p_0(|x|) & 0 \le |x| < 1 \\ -4 + \frac{75}{4}|x| - \frac{245}{8}|x|^2 + \frac{545}{24}|x|^3 - \frac{63}{8}|x|^4 + \frac{25}{24}|x|^5 = p_1(|x|) & 1 \le |x| < 2 \\ 18 - \frac{153}{4}|x| + \frac{255}{8}|x|^2 - \frac{313}{24}|x|^3 + \frac{21}{8}|x|^4 - \frac{5}{24}|x|^5 = p_2(|x|) & 2 \le |x| < 3 \\ 0 & |x| \ge 3 \end{cases}$$

where $|x|$ denotes the distance between the particle and a given grid point. From this formula, one can evaluate the weights collected by each grid point involved in the kernel support. For each direction, let us first consider the distance $y = (x_p - x_i)/h$ between a particle located at

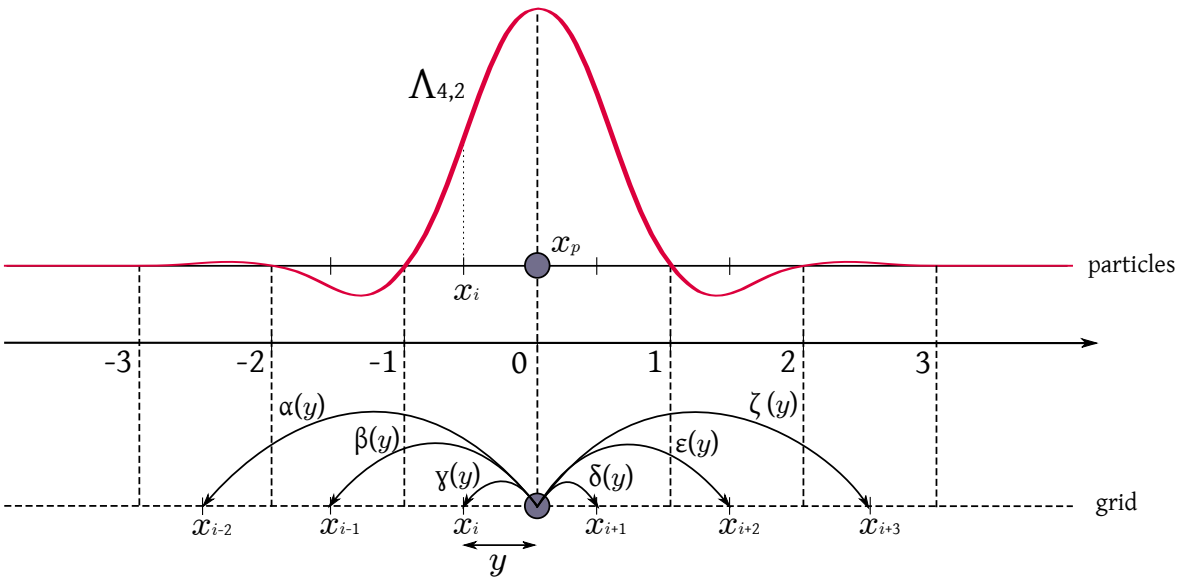

Figure 2.9: One-dimensional representation of the computation of the remeshing weights using the $\Lambda_{4,2}$ kernel.

position x_p and the closest grid point of minimum coordinate located at x_i. This distance is normalized by h, the uniform mesh size. Let us also denote $\alpha(y), \beta(y), \gamma(y), \delta(y), \varepsilon(y), \zeta(y)$ the weights respectively collected by the grid points x_{i-2}, x_{i-1}, x_i, x_{i+1}, x_{i+2} and x_{i+3} included in the kernel support.

According to the $\Lambda_{4,2}$ formula these weights are defined as follows (see the graphical representation of Figure 2.9):

$$\begin{cases} \alpha(y) = \Lambda_{4,2}(-2-y) = p_2(2+y) = \frac{1}{12}y - \frac{1}{24}y^2 - \frac{3}{8}y^3 + \frac{13}{24}y^4 - \frac{5}{24}y^5 \\ \beta(y) = \Lambda_{4,2}(-1-y) = p_1(1+y) = -\frac{2}{3}y + \frac{2}{3}y^2 + \frac{13}{8}y^3 - \frac{8}{3}y^4 + \frac{25}{24}y^5 \\ \gamma(y) = \Lambda_{4,2}(-y) = p_0(y) = 1 - \frac{15}{12}y^2 - \frac{35}{12}y^3 + \frac{63}{12}y^4 - \frac{25}{12}y^5 \\ \delta(y) = \Lambda_{4,2}(1-y) = p_0(1-y) = \frac{2}{3}y + \frac{2}{3}y^2 + \frac{11}{4}y^3 - \frac{31}{6}y^4 + \frac{25}{12}y^5 \\ \varepsilon(y) = \Lambda_{4,2}(2-y) = p_1(2-y) = -\frac{1}{12}y - \frac{1}{24}y^2 - \frac{11}{8}y^3 + \frac{61}{24}y^4 - \frac{25}{24}y^5 \\ \zeta(y) = \Lambda_{4,2}(3-y) = p_2(3-y) = \frac{7}{24}y^3 - \frac{1}{2}y^4 + \frac{5}{24}y^5 \end{cases} \tag{2.113}$$

In each direction, the remeshing scheme therefore stands as:

$$\omega_i^{n+1} = \sum_p \omega_p^n \Lambda_{4,2}\left(\frac{x_p^{n+1} - x_i}{h}\right). \tag{2.114}$$

We note that thanks to the directional splitting, the total number of weights to compute per particle in 3D is equal to 3 (number of directions) $\times 6$ (kernel support) $= 18$ instead of $6^3 = 216$ with a tensorial approach. This important saving in operations allows here to handle a 4^{th} order remeshing kernel at a much lower price than the popular 2^{nd} order kernel $\Lambda_{2,1}$ (also called M_4') used with a tensorial approach in 3D ($4^3 = 64$ weights/particle).
The particle convection/remeshing procedure is performed in step 2.85 of algorithm 1.

Diagnostics computation

Besides the resolution of the governing equations, some diagnostic computations are required in order to be able to analyze the flow behavior and to draw general conclusions in terms of flow control.

Aerodynamic force

It will represent the main criterion in quantifying the flow control efficiency in this study. As explained in section (2.2), the aerodynamic force is evaluated in 3D with respect to the *change of momentum* equation 2.38. It is evaluated on the grid with a midpoint rule:

$$\mathbf{F} = \frac{1}{\Delta t} \sum_B \left(\mathbf{u}^n - \frac{\mathbf{u}^n}{1 + \lambda \Delta t} \right) h^3, \tag{2.115}$$

where $\mathbf{u}^n$ corresponds to the non-penalized velocity and h denotes the uniform grid space. We note that the above equation is indeed equivalent to the discretized formulation of equation 2.38, since:

$$\mathbf{F} = \frac{1}{\Delta t} \sum_B \left(\mathbf{u}^n - \frac{\mathbf{u}^n}{1 + \lambda \Delta t} \right) h^3 \tag{2.116}$$

$$= \frac{1}{\Delta t} \sum_B \left(\frac{\mathbf{u}^n (1 + \lambda \Delta t) - \mathbf{u}^n}{1 + \lambda \Delta t} \right) h^3 \tag{2.117}$$

$$= \sum_B \left(\frac{\lambda \mathbf{u}^n}{1 + \lambda \Delta t} \right) h^3, \tag{2.118}$$

and if $\lambda \Delta t \gg 1$, which in practice is always verified in our case since $\lambda = 10^8$ in B and $\Delta t \geq 10^{-3}$, then:

$$\mathbf{F} = \sum_B \frac{\mathbf{u}^n}{\Delta t} \, h^3, \tag{2.119}$$

which corresponds to the 1^{st} order discretization of the *change of momentum* equation 2.38 where $\mathbf{u}_\lambda = 0$.

Let us notice that, if $\Delta t \to 0$, then:

$$\mathbf{F} = \sum_B \lambda \mathbf{u}^n \, h^3, \tag{2.120}$$

which corresponds to the discretized formulation of the force expression 2.24 proposed by [Caltagirone, 1994].

The force evaluation is performed right before the penalization step in algorithm 1 (step 2.81).

Enstrophy

An other interesting flow diagnostic is the enstrophy. This quantity indeed allows to measure the dissipation of energy in terms of kinetic energy. It is given by the following formula:

$$Z = \int_D |\boldsymbol{\omega}|^2 d\mathbf{x}, \tag{2.121}$$

and discretized with a 1^{st} order midpoint rule in step 2.86 of algorithm 1.

2.6 Implementation and libraries description

As mentioned in the introduction of the previous section, the discretization of the two-dimensional and three-dimensional problems has been implemented in two distinct computational solvers. The current section aims to describe these two solvers, giving for each of them the context in which they were created as well as the way they operate.

2.6.1 The 2D solver

The numerical solver presented in this part is purely dedicated to the simulation of two-dimensional flows past obstacles using the present hybrid vortex penalization method. It was inherited at the beginning of this thesis from Federico Gallizio who successfully used it to model incompressible flows past VAT (Vertical Axis Turbines) at different flow regimes [Gallizio, 2009]. This library is implemented in Fortran using an imperative programming paradigm. As explained previously, it is dedicated to the simulation of incompressible flows past immersed obstacles and allows to consider moving obstacles thanks to the implementation of a module dealing with a level-set function for the front capturing. The first objective of the present work was to complete and improve this 2D solver in order to further demonstrate the robustness and accuracy of the proposed numerical method and also to carry out a preliminary and detailed passive flow control study. The main goal through this two-dimensional approach was indeed to try to correctly understand the intrinsic mechanism involved in the flow control of bluff bodies using a porous medium before handling the more realistic and complex three-dimensional problem.

In this thesis, the contributions to the presented 2D solver therefore involved modifications in the implementation of numerical methods on one hand, and additions in the implementation of the passive flow control devices on the other hand. Concerning the first point, the Poisson solver was modified. The original one was using the Fishpack library [Adams et al., 1980] based on the Cyclic Reduction method, which is not maintained anymore. The FFT-based method was therefore chosen to overcome this problem. For this purpose, the Fortran `fftw` library was used [Frigo and Johnson, 2005], imposing periodic boundary conditions to close the Poisson problem. As explained previously, these changes had to go along with the implementation of an outlet vorticity absorption and a velocity correction (see section (2.3)). Concerning the passive flow control application, the required modifications and additions mainly concerned the implementation of porous areas at the surface of the considered body as well as diagnostics to analyze and quantify the control efficiency. Among the latter, we can cite the pressure field, the enstrophy, the velocity and pressure profiles and the output binary files representing the averaged and instantaneous flow fields, handled with the `VTK` library.

The numerical discretization of the governing equations in the 2D solver mainly corresponds to the two-dimensional counterpart of the discretization described previously in the 3D case. Concerning the noticeable differences between the 2D and the 3D discretization, we can first mention the force evaluation. As explained in section (2.2), the aerodynamic force is indeed computed in 2D according to the *momentum Noca's equation*. On the other hand, the remeshing procedure is performed through the *tensorial product* (see section (1.4.2) and Figure 1.6) of the one-dimensional $\Lambda_{2,1}$ kernel formula (better known as M'_4 kernel). Finally, the global time step is *fixed* and the advection stability constraint:

$$\Delta t_{\text{adv}} \leq \frac{\text{LCFL}}{\|\nabla \mathbf{u}\|_\infty}, \quad \text{with LCFL} = 1/4 \tag{2.122}$$

is specifically prescribed within the advection step, leading to sub-iterations in the convection/remeshing process when the global fixed time step is greater than Δt_{adv}. These three different points were then changed or improved in the three-dimensional version, as presented in the previous section.

As will be confirmed in the next chapter dedicated to the method validation, the numerical simulations performed with this 2D Navier-Stokes solver provide accurate results. Nevertheless, the present library offers little flexibility. For this reason, its extension to the 3D case was performed in an entirely new framework. The resulting library, that will be presented next, ensures a robust, flexible and user-friendly software while taking into account the knowledge obtained from the 2D solver.

2.6.2 The 3D solver

This library was created with the intention to supply a flexible, portable and modular scientific software able to solve a large range of problems involving partial differential equations and related to computational fluid dynamics in 2D and in 3D. The present library, called HySoP (**Hy**brid **S**imulati**o**ns using **P**articles), includes two levels of hybridization. The first one is related to the use of different types of numerical methods, namely Eulerian and Lagrangian (i.e. vortex particle) methods. The second level is related to the exploitation of different architectures on a same heterogeneous machine. HySoP indeed encompasses distributed computing on multi-cores/nodes and computation on multi-GPU's (Graphics Processing Unit). This second level of hybridization has been developed simultaneously, beyond the scope of this thesis, and is for the moment apart from the context of the present work. Nevertheless, it corresponds to a main characteristic of the HySoP library and we aim in the future to make the considered problem of flow past obstacles resolvable on such hybrid architecture in order to accelerate performances. HySoP will be soon released under a GNU GPLv3 license. In the following we describe the concepts, the characteristics and the operating of the present computational scientific library.

2.6.2.1 An object-oriented library

In order to overcome the problems due to the lack of flexibility inherent to imperative and procedural programming, the present software was developed using an object-oriented paradigm (see Insert 3). From a general point of view, this approach enables the users and the programmers to handle objects which are very close to the mathematical and physical concepts they aim to represent. To be more precise, the object-oriented paradigm provides, on one hand, robustness thanks in particular to the encapsulation principle, which allows to interact with the objects through their own methods instead of their data, and on the other hand ensures flexibility thanks to the abstraction concept. The latter has to be conscientiously considered since a good abstraction leads to a good portability. The next paragraph is dedicated to the description of the different abstraction levels present in HySoP.

Insert 3 – The object-oriented programming

Object-oriented programming (OOP) is a paradigm in which the data structures are *objects*. These objects contain on one hand data, also called *attributes*, and on the other hand procedures, often known as *methods*. The attributes can be seen as the main characteristics or properties of the objects (in the form of fields) while the methods define the behavior of the object or the actions that the object is able to perform (in the form of code). Most popular OOP-based languages use the concept of *class*, meaning that objects are instances of classes. The classes allow to determine the objects type.

The OOP paradigm is characterized by the following main features:

- **Encapsulation**: it is the packing of data and functions into a self-contained module (ex: the classes).
- **Inheritance**: classes are created in hierarchies, and inheritance enables one class (the parent class) to pass down its structure and methods to other classes (the descendant classes).
- **Abstraction**: it consists in establishing levels of complexity. The first level corresponds to the one on which a user interacts with the system. The more complex details are pushed below.

2.6.2.2 The abstraction levels

The present approach follows the one proposed by [Labbé et al., 2003] in the context of scientific libraries development. It consists in splitting the physical PDE-based problem in four different concepts: the problem itself, the operator, the variable and the domain. These concepts are respectively handled at different levels of abstraction.

Highest abstraction level (→ user)

It corresponds to the abstraction level that is close to the physics. It is proper to the user. In practice, this level corresponds to the definition of the four concepts by the user:

- **Problem**: it corresponds to the mathematical problem to be solved
  ex: the incompressible Navier-Stokes equations
- **Operator**: it represents the notion of continuous mathematical operator. It can be an elementary differential operator or a sub-problem
  ex: Laplacian operator, transport operator
- **Variable**: it represents the mathematical entities involved by the operators within the problem. It includes the specification of a type (vector or scalar) and an initial value or an exact computation formula.
  ex: velocity (vector field), pressure (scalar field)
- **Domain**: it describes the support on which the variables are defined. It includes the specification of a geometry and boundary conditions
  ex: plane-parallel box with periodic boundary conditions

Data and operator management abstraction level (→ programmer)

In this lower abstraction level we will find the implementations of the methods dedicated to the communications management between the different computer entities, namely the CPU cores/nodes (MPI) and the GPU's (OpenCL). It also includes the development of methods dedicated to the variable's data storage and distribution (topology management). Finally, it handles the interfacing between the different programming languages (see next paragraph). For further details concerning this abstraction level in the context of HySoP, we refer to [Etancelin, 2014].

Numerical method abstraction level (→ programmer)

This abstraction level encompasses all the variables and the operators discretization. In others words, this is the level at which the programmer implements all the resolution algorithms (typically, those described in the previous section (2.5)).

The main advantage of this abstract approach lies in the fact that the operations performed at one abstraction level do not depend on the operations realized at the other levels. Thus, it becomes easy for instance to change the discretization algorithm of a given operator without modifying the rest of the library. In the same spirit, face to a new type of architecture, it should be rather easy to modify the setup instead of completely re-write the code.

2.6.2.3 External modules and programming languages

A natural choice for the HySoP's programming language was Python. First, Python is first of all a language that allows the use of both imperative and object-oriented paradigms. It is also a language that is easily available on any platform. The present HySoP library is easy to install

on any machine without administrator rights. Finally, it is an interpreted language. Thanks to the absence of compilation, this feature is well suited to the source code development and prototyping.

However, the main weakness of Python language precisely lies in this absence of compilation since the numerical performances obtained in the context of a naive implementation are extremely bad compared to non-interpreted languages like C++ or Fortran. In order to achieve competitive simulation times, it becomes necessary to deal with the optimization libraries. In our case we use the `numpy` package which is specialized in the treatment and the storage of data arrays in the context of scientific computing.

As mentioned previously, Python language also offers a programmer-friendly framework to interface other language. In HySoP, this possibility enabled us to use the `fftw` Fortran library for the resolution of the Poisson equation (step 2.79 in algorithm 1) as well as the implementation in Fortran of the semi-Lagrangian advection method, developed by [Lagaert et al., 2014] under the name of `scales` library [1] (step 2.85 in algorithm 1). Finally, the input/output files describing the flow fields are treated with `HDF5` format through the `H5py` package.

A graphical representation of the resolution of the penalized Navier-Stokes equations using the HySoP library is given by Figure 2.10. The contributions of this thesis to the overall library development take place for most of them at the *highest* and the *numerical method* abstraction levels.

The use of optimized packages, external modules and programming interfaces allows to greatly enhance the library performances which then become comparable to those obtained with compiled languages, like Fortran or C++. It is important to mention that HySoP is a research library in development, it is therefore perfectible and further optimizations may be done. We consider for instance the use of the `Cython` module in order to improve the library performances by simplifying the implementation of compiled parts in the code.

Conclusion 2.1

In this chapter we described in details the hybrid vortex penalization (HVP) method which will be applied for the first time to passive flow control past bluff bodies, using porous media. In the context of this application, the governing equations and the physical description of the problem were first presented before introducing the numerical discretization method handled to solve the problem. This method has been implemented in the two-dimensional and the three-dimensional cases. The 3D code was developed in the context of a library, called HySoP, that uses an object-oriented paradigm. It provides flexibility as well as portability and in that way, HySoP could be used for the resolution of many types of PDE-based problems on different types of architectures, by simply adding the corresponding source code. This software, like preceding or current developments made in particular at ETH Zürich (i.e. PPM [Sbalzarini et al., 2006] and MRAG [Rossinelli et al., 2015] presented in chapter 1), is a key ingredient to develop and maintain numerical algorithms able to handle billions of particles for accurate DNS of complex flows.

[1] This library was developed in the framework of a collaborative work with the LEGI Grenoble (Laboratoire des Ecoulements Géophysiques et Industriels)

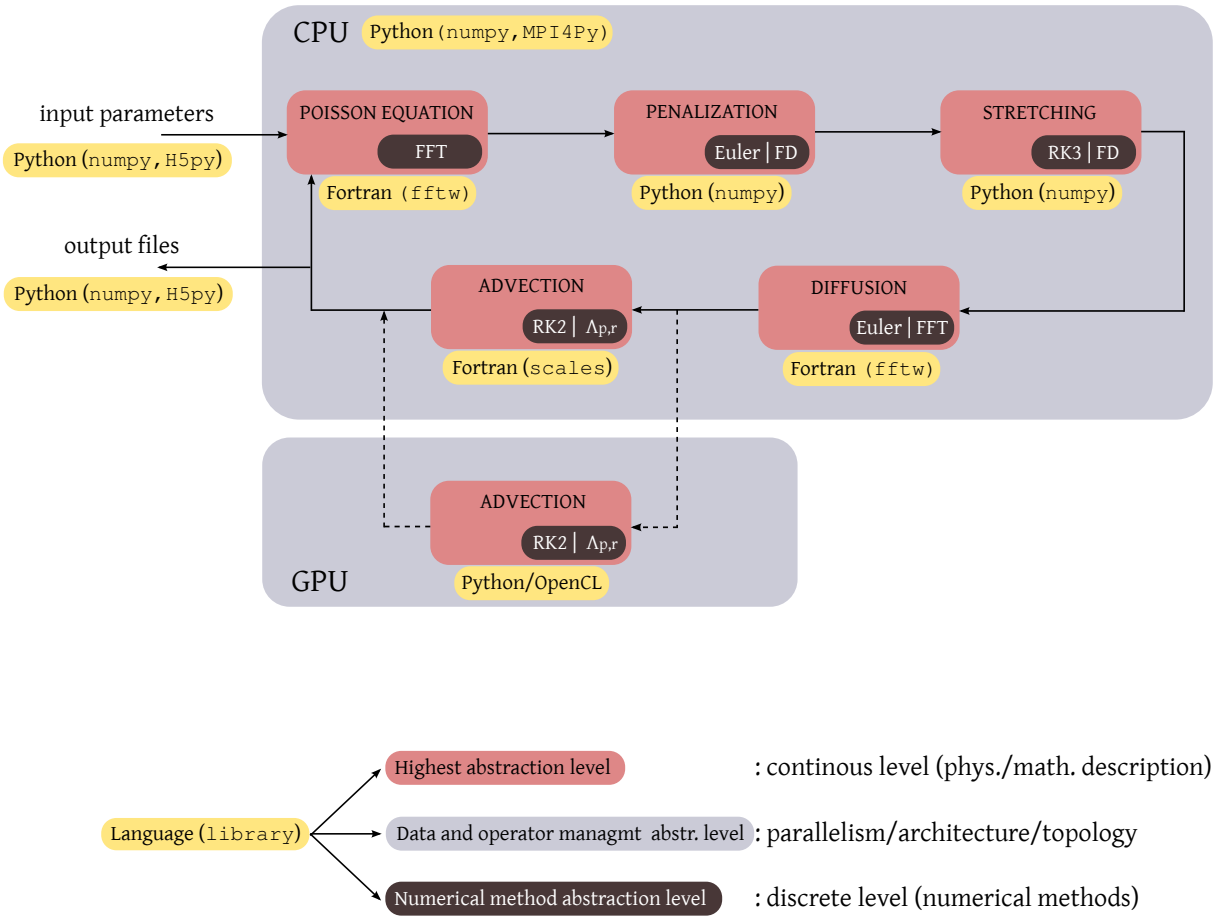

Figure 2.10: Example of resolution of the penalized Navier-Stokes equations in HySoP.

3

Numerical validations for bluff body flows

Contents

Résumé 3

Nous proposons dans ce chapitre une étude de validation de la méthode vortex hybride pénalisée. Cette étude, visant à analyser la convergence ainsi que la précision de notre méthode, est effectuée dans un cadre similaire à celui qui sera considéré dans l'application au contrôle d'écoulements. Nous nous intéressons à des écoulements 2D et 3D autour d'un demi-cylindre et d'un hémisphère, respectivement. En effet, le contrôle d'écoulements étant destiné à être effectué autour d'un rétroviseur automobile, le demi-cylindre (en 2D) et l'hémisphère (en 3D) peuvent être considérés comme une géométrie simplifiée de cet obstacle. Le nombre de travaux portant sur des écoulements autour d'un demi-cylindre ou d'un hémisphère étant très faible nous complèterons cette étude de validation par des simulations d'écoulements autour d'un cylindre (2D) et d'une sphère (3D) qui constituent des écoulements de référence pour lesquelles de nombreux résultats numériques et expérimentaux sont disponibles. Ce chapitre est introduit par une description des phénomènes physiques mis en jeu au niveau de la surface du corps immergé. La connaissance de ces mécanismes est nécessaire afin d'être en mesure de valider les résultats obtenus numériquement mais aussi afin d'analyser ultérieurement l'efficacité du contrôle passif. Les résultats issus de cette étude de validation démontrent la convergence de l'algorithme ainsi que sa capacité à rendre compte de façon précise des comportements des écoulements 2D et 3D étudiés. Cette étude permet par ailleurs de mettre en exergue la différence notable entre le sillage développé à l'aval d'une sphère et celui d'un hémisphère, venant ainsi confirmer les rares études analogues.

In this chapter we propose a validation study of the HVP method. Its convergence and accuracy are numerically analyzed in the 2D and the 3D cases for flows past different bluff bodies. Simulations will be first performed in 2D around a semi-circular cylinder and then in 3D around a hemisphere. For both of them, the bluff-surface faces the upstream flow and the flat one is oriented downstream. The main reason for choosing such a geometrical configuration is its similarity with the sideview mirrors of a ground vehicle and the possible engineering extension of the control study to reduce their drag. However, to our knowledge, very little research has been conducted concerning incompressible flows past semi-circular cylinders and hemispheres. For the sake of completeness, this validation study will therefore be supplemented with the analysis of flows past a circular-cylinder in 2D and a sphere in 3D. These obstacles indeed represent very classical benchmarks offering a lot of results in the literature. Before presenting the validation results of the numerical method, a first introductory part is dedicated to the description of viscous flows around bluff bodies.

3.1 Physical description of viscous flows past bluff bodies

A knowledge of flows past bluff bodies is absolutely essential in the context of the present study. It will enable us in a first place to understand and validate the results obtained numerically and, secondly, to precisely analyze the efficiency of the passive flow control in the last chapter. First of all we give a description of the physical phenomena happening in the immediate vicinity of the obstacle's bounding surface.

3.1.1 Boundary layer, flow separation and drag production

3.1.1.1 Boundary layers

In the region of the obstacle's surface, where the effects of viscosity are the most important, a layer of fluid appears: it is the boundary layer. This layer starts from the stagnation point, that is to say from the point where the local fluid velocity is zero, and its thickness increases as the flow continues back. One can distinguish two different types of boundary layers: the laminar (Figure 3.1a) and the turbulent one (Figure 3.1b). In the laminar boundary layer, the flow is very smooth and takes place in layers on a microscopic scale. Any exchange of momentum occurs only between adjacent layers. But the laminar boundary layer is not stable, and when the Reynolds number reaches a certain threshold, it can turn to a turbulent state. The turbulent boundary layer is characterized by swirls or "eddies" which come from the mixing across several layers, on a macroscopic scale. The exchange of momentum and energy therefore happens on a much larger scale compared to a laminar boundary layer.

3.1.1.2 Mechanism of flow separation

In viscous flows, when the Reynolds number reaches a certain threshold - more or less equal to 5 - the boundary layer detaches from the surface of the bluff body. In order to understand the flow separation phenomenon, it is first important to highlight the effects of the viscosity. The presence of a bluff body immersed in the flow forces the fluid to bypass it, that is to say to travel a longer way, in the same amount of time (otherwise, accumulation would occur). Consequently, the thicker will be the obstacle to bypass, the higher will be the flow acceleration. This is what would happen with inviscid flows. Nevertheless, with viscosity, things get more complicated: the latter is actually responsible for a deficit in the dynamic acceleration of the flow compared to the potential acceleration obtained in the inviscid case. The pressure gradient is a predominant factor in this situation. Indeed, a negative pressure gradient will counteract the retarding effect of the shear stress due to viscosity in the boundary layer. A negative pressure gradient is then called a *favorable* pressure gradient. A positive pressure gradient has the opposite effect and is defined as *adverse* pressure gradient. The geometry of a bluff body's surface involves a favorable

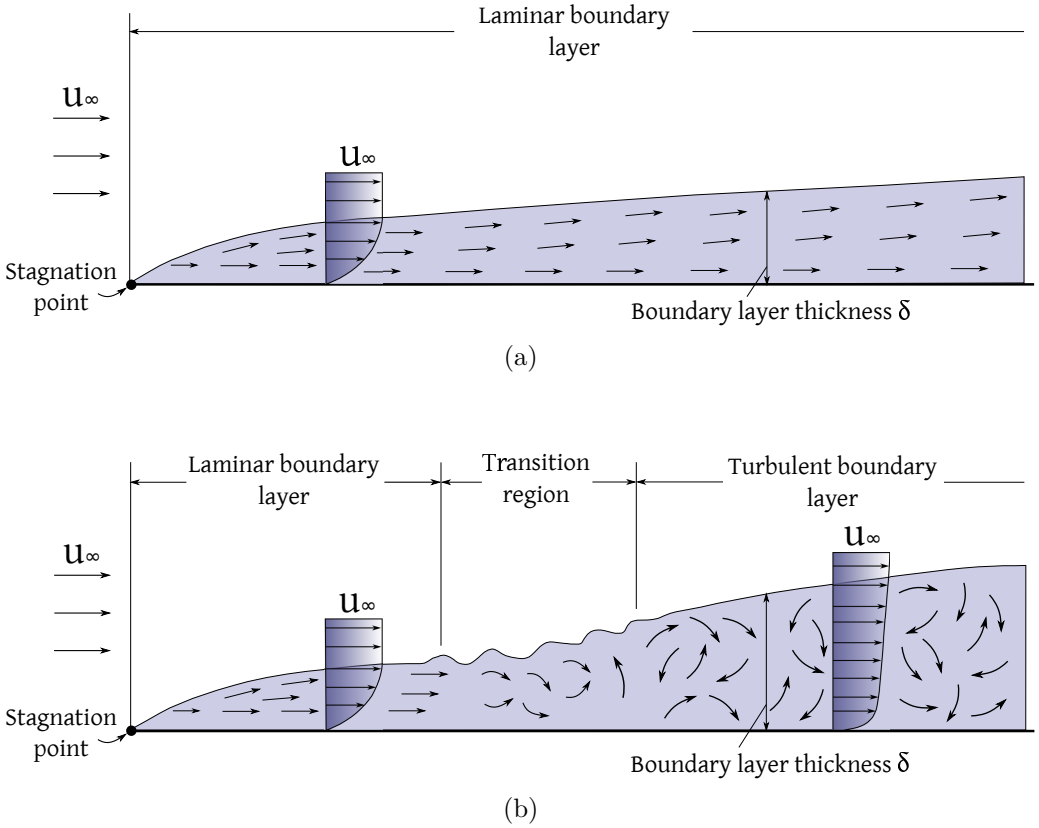

Figure 3.1: (a) Laminar boundary layer. (b) Transition from laminar to turbulent boundary layer

pressure gradient from the stagnation point to the point denoted P in Figure 3.2. An adverse pressure gradient then appears downstream of P and starts to retard the flow. As a consequence, the velocity in the vicinity of the wall decreases and the boundary layer thickens (see the velocity profiles in Figure 3.2). A continuous deceleration of the flow leads the wall shear stress to vanish at the point S. This is the separation point. From this S position, the flow no longer attaches to the contour of the body and a recirculation zone develops.

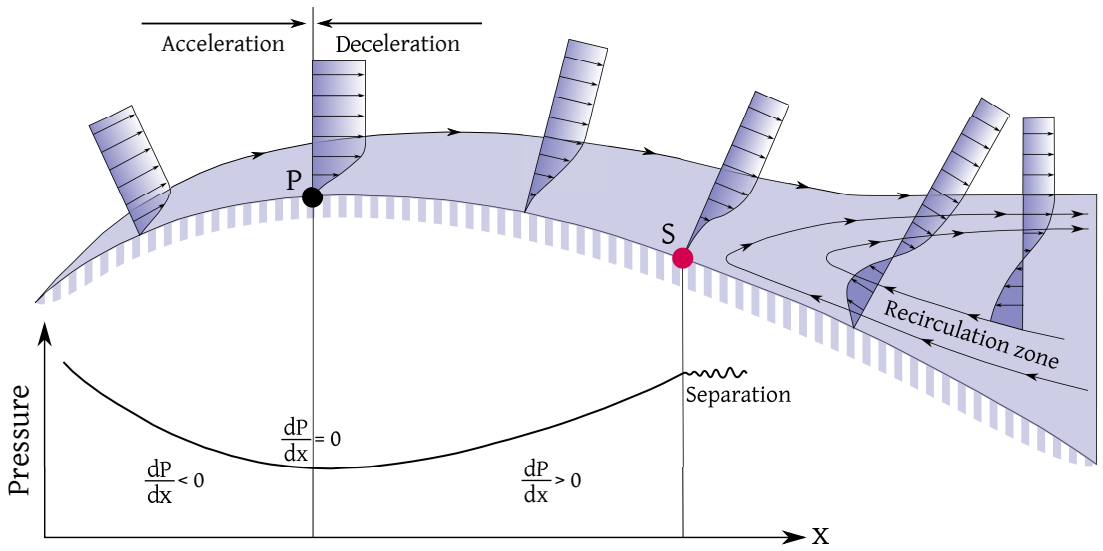

Figure 3.2: Flow separation on a bluff body profile.

3.1.1.3 Drag production

In aerodynamics, boundary layer separation is a crucial physical phenomenon since it contributes to enhance the drag force acting on the bluff body. It can be explained by the fact that the pressure formed downstream due to the separation is relatively low. In the absence of flow separation, the pressure force on the front side of the obstacle is the exact opposite to that on the back side, leading to zero net drag acting on the body. When the flow detaches, the resultant pressure force acting on the front side is greater in magnitude than the oppositely directed force on the back side, giving rise to non-zero drag force.

A main issue in aerodynamics research consists in optimizing the shape of the obstacle in order to delay the separation and increase the downstream pressure. The control application performed in this work and presented in the next chapter will not involve shape optimization but only passive devices using porous media in order to achieve these goals.

3.1.2 Incompressible flow regimes

The different flow regimes past an obstacle are determined by the shape of the body and by the nature of the boundary layer, which in turn completely depends on the non-dimensional Reynolds number:

$$Re = \frac{\text{inertial forces}}{\text{viscous forces}} = \frac{\mathbf{u}_\infty L}{\nu}, \tag{3.1}$$

where $\mathbf{u}_\infty$ is the free stream velocity, $\nu = \mu/\rho$ is the kinematic viscosity and L denotes the characteristic length traveled by the fluid (in the case of a circular obstacle, the characteristic length would be the diameter).

In this section we detail the different regimes characterizing an incompressible flow past a circular cylinder. These flow regimes are listed in Table 3.1 and detailed in the sequel:

Creeping flow

When $Re < 5$, the friction constraints are not sufficient to create a significant boundary layer. Consequently, the flow field bypasses the cylinder with a perfect symmetry along the longitudinal axis, without any separation. The behavior of such flows is identical to the one of inviscid flows.

Steady separated flow

For $5 < Re < 48$, because of the increase of the inertial forces, the boundary layer cannot attach to the cylinder anymore. A flow separation happens at the top and bottom of the solid, forming a fixed and symmetric pair of counter-rotating vortices. The reattachment point, enclosing this recirculation zone, moves away from the cylinder when increasing the Reynolds number [Batchelor, 1967].

Unsteady laminar flow

When $48 < Re < 180$, an intrinsic bi-dimensional instability appears and the flow becomes unsteady. The pair of vortices then looses its symmetry with respect to the longitudinal axis and the latter start to detach alternatively from the cylinder. This regime of alternated eddies was studied by Von Kármán [von Kármán, 1912], who gave his name to this periodic formation of vorticity in the wake. The eddies of the Von Kármán alley constitute a stable block which is convected by the flow.

Transitional regime

At $180 < Re < 300$, the flow becomes three-dimensional and the transition to turbulence occurs in the wake. This region of transition moves towards the cylinder when increasing the

Reynolds number. The experimental studies of [Gerrard, 1978, Williamson, 1988] show that the two-dimensional features observed at the previous flow regime in the vortex shedding are now clearly three-dimensional, with vortices shed in the spanwise direction.

Subcritical regime

When the Reynolds number is higher than 300, the wake is fully turbulent and the eddies cannot be distinguished from each others. A large wake therefore forms at a separation angle of about 80 degrees with respect to the stagnation point. The important shear exerted in the detachment zone amplifies the Kelvin-Helmholtz instability. When the Reynolds number becomes larger ($Re > 2600$), this instability increases and leads to the creation of small eddies interacting with the elementary ones. This regime is called sub-critical since the boundary layer is still laminar at the separation point.

Critical regime

In the critical regime, characterized by Reynolds numbers ranging approximately between 10^5 and 10^6, the transition to turbulence happens in the boundary layer itself. This transition first takes place at the location where the boundary layer separates, and as the Reynolds increases, the transition region moves along the cylinder surface towards the stagnation point, making the laminar boundary layer diminishing. This regime is consequently characterized by the fact that the boundary layer is turbulent when the separation happens. We note by the way that at this regime the separation occurs at a larger angle, which is approximately equal to 120 degrees, leading to the formation of a narrower wake.

Supercritical regime

When $Re \gtrsim 2 \cdot 10^6$ the boundary layer of the cylinder surface is completely turbulent. This regime is qualified as supercritical according to the definition originally given by [Roshko, 1961].

The regimes related to flow past a sphere (an other obstacle of interest in this study, besides the cylinder) are quite similar. They also have been the subject of many numerical and experimental analysis, and will be described in the sequel for the Reynolds numbers considered in our study. However, concerning the two geometries handled in this thesis for control application, namely the 2D semi-circular cylinder and the 3D hemisphere, very few numerical and experimental studies have been performed to our knowledge. A comparable description of the flow regimes past these obstacle is therefore non-existent in the literature. Another objective of this work will consist in drawing some comparisons between flows past circular obstacles and flows past square-back bluff bodies, at least for the Reynolds numbers considered in this study. We indeed expect the square back of these obstacles to have a significant influence on the general flow behavior (e.g. separation, recirculation at the rear back, vortex shedding). The flow regimes treated in this thesis through Direct Numerical Simulations (DNS) will be transitional ($100 \leq Re \leq 300$) and subcritical or rather "highly transitional" ($300 \leq Re \leq 9500$). We note here that our problem of interest, namely the passive flow control, cannot be treated at a realistic level using DNS. Indeed, the Reynolds number describing a realistic flow past a rear view mirror would rather reach values in the range of $10^4 - 10^5$, which, in the present state of the computational resources (access memory, data storage, running time), is not affordable.

3.1.3 Mechanism of vortex shedding

In order to conclude the first part of this chapter, we shortly explain the mechanism of vortex shedding. This phenomenon is indeed characteristic for most of the flows analyzed in the present work.

Flow representation	Regime	Reynolds number
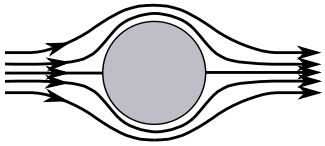	Creeping flow	$Re < 5$
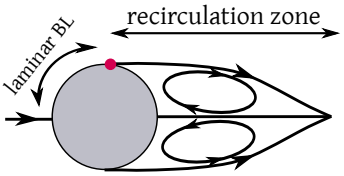	Steady separated flow	$5 < Re < 48$
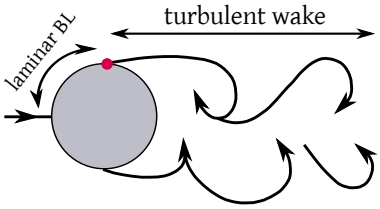	Unsteady laminar flow	$48 < Re < 180$
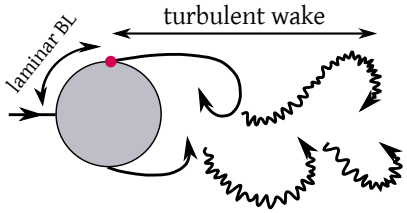	Transitional flow	$180 < Re < 300$
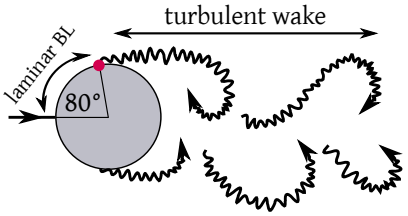	Subcritical	$300 < Re \lesssim 10^5$
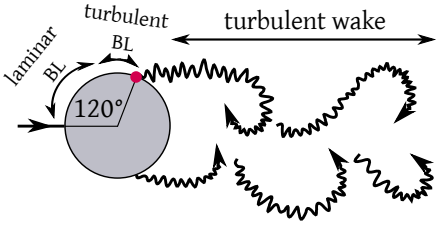	Critical	$10^5 \lesssim Re \lesssim 10^6$
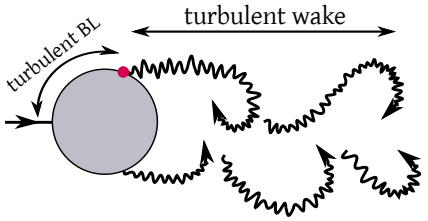	Supercritical	$Re \gtrsim 2 \cdot 10^6$

Table 3.1: The different regimes for flow past a circular cylinder

As explained in [Sumer and Fredsoe, 2006], when $Re \gtrsim 48$, one of two vortex of the downstream recirculation zone becomes larger than the other one, due to the flow instability. This situation is depicted in Figure 3.3a, where A denotes the larger vortex and B the second one. The vortex on top (here, vortex A) swirls in the clockwise direction with a negative vorticity, while the vortex formed on the bottom (here, vortex B) swirls in the anti-clockwise direction with a positive vorticity. While growing, the vortex A draws the opposing vortex B across the wake (Figure 3.3b). The approach of a vorticity of opposite sign finally leads to the disruption of vorticity supply to vortex A from its own boundary layer. At this moment, vortex A is shed, becoming a free vortex convected by the flow. The same process starts again with vortex B growing and giving rise to the formation of a new vortex (vortex C in Figure 3.3c). A shedding phenomenon develops alternatively on both sides of the bluff body.

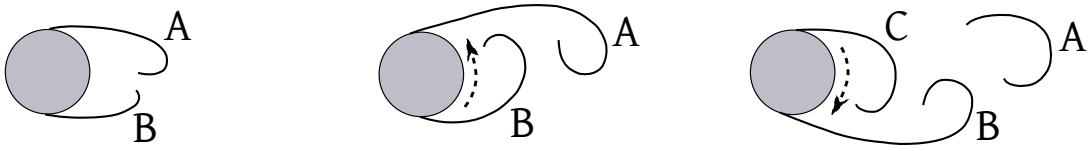

(a) (b) (c)

Figure 3.3: First steps in the vortex shedding mechanism.

When dealing with unsteady oscillating flows, an important dimensionless number to consider is the Strouhal number S_t (see Insert 4). In the following, this quantity will be used as a diagnostic allowing to characterize the flow under study and to validate the simulation results obtained with the present method.

Insert 4 – Strouhal number

The Strouhal number is a dimensionless quantity used to investigate the vibrations of a body immersed in a fluid. It is defined by:

$$S_t = \frac{fL}{\mathbf{u}_\infty}, \tag{3.2}$$

where f is the dominant frequency of vortex shedding, L is the characteristic length (e.g. the diameter in case of circular bluff bodies) and $\mathbf{u}_\infty$ is the unperturbed free stream velocity. Concerning the dominant frequency f:

- it is a function of the Reynolds number,
- it is equal to the frequency of the lift force oscillation and twice smaller than the one of drag force oscillation,
- it may be obtained in practice by running a Fast Fourier Transform and plotting the power spectrum of the lift force.

The Strouhal number is approximately constant and equal to 0.2 over a large Reynolds number interval ranging from 250 to $2 \cdot 10^5$. It this case, the vortex shedding frequency is thus proportional to the free stream velocity. At high Reynolds numbers one cannot identify a single dominant frequency: the vortex shedding rather occurs over a narrow band of frequencies and when the latter get close to the structural-vibration frequency of the body, then resonance may happen.

3.2 Numerical validations

The numerical validations presented in this section are based on DNS simulations performed for different types of flows. Two types of regimes will be considered, namely the transitional and the highly-transitional (subcritical) regime, as well as different obstacles: the circular-cylinder (2D) and the sphere (3D) on one hand, for which a lot of investigations exist in the literature, and the semi-circular cylinder (2D) and the hemisphere (3D) on the other hand, which constitute the obstacles of interest in the context of the flow control study we aim to carry out.

In all our simulations the size of the computational box was chosen large enough so that the presence of the artificial boundaries was found to be negligible. A careful convergence study with respect to the domain size has been performed in [Cottet and Poncet, 2003] for flow past a 2D circular cylinder using vortex methods. This study shows a first-order convergence for the lift coefficient and Strouhal number and third-order convergence for the drag coefficient. It demonstrates that a domain extending to about 6 cylinder diameters downstream is sufficient to provide reliable flow diagnostics. In the subsequent simulations, the size of the domain is set to $D = [-4,\ 8] \times [-5,\ 5]$ in 2D and to $D = [-2,\ 8.24] \times [-2.56,\ 2.56] \times [-2.56,\ 2.56]$ in 3D. The computational domains D and the geometrical setup are shown in Figure 3.4. A uniform free stream velocity $\mathbf{u}_\infty$ is imposed at the inlet with $u_\infty = 1$. The non-dimensional diameter d of each obstacle considered in this study is equal to 1 and the body is centered at the origin. The whole domain is covered by a uniform Cartesian grid.

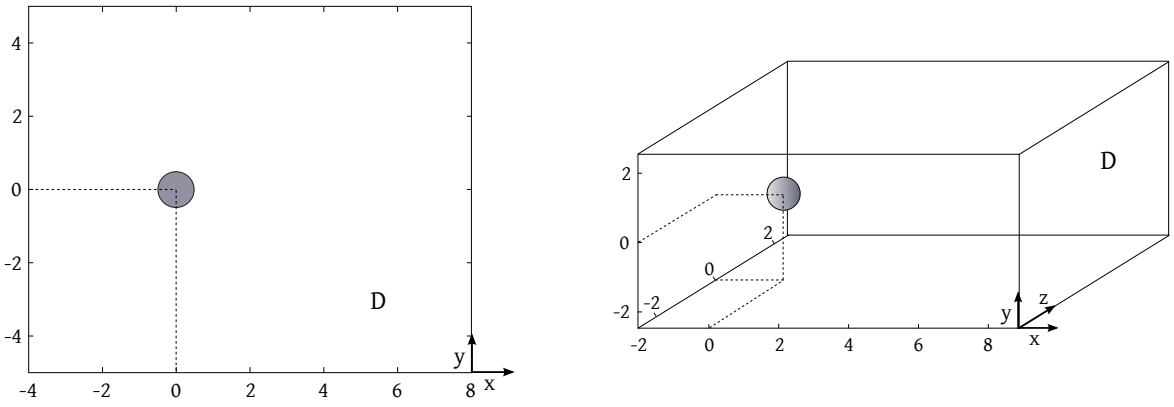

Figure 3.4: Computational domains: (a) in two dimensions, (b) in three dimensions.

In a first place we will present the validation results obtained in the two-dimensional case with the circular cylinder and the semi-circular cylinder. The second part of this section will be dedicated to the validation of the present method in the three-dimensional case. For that purpose we will consider flows past a sphere and a hemisphere. For each of these different flows, a convergence study will be carried out and comparisons of our results with respect to numerical and experimental references will be proposed.

3.2.1 The two-dimensional case

3.2.1.1 Flow past a 2D circular cylinder

Grid convergence study

A grid-convergence study is carried out for flow past a circular-cylinder at $Re = 550$ where the value of the grid step h ranges from 0.02 to 0.0025, with $h = 0.00125$ as reference case. We evaluate the L^1, L^2 and L^∞ norms of the error $e(\mathbf{x})$ of the drag coefficient and enstrophy time

evolution, with respect to the reference case:

$$e(\mathbf{x})_{L^1} = \int_D \mid q_{\text{ref}}(\mathbf{x}) - q(\mathbf{x}) \mid \mathrm{d}\mathbf{x} \tag{3.3}$$

$$e(\mathbf{x})_{L^2} = \left(\int_D \mid q_{\text{ref}}(\mathbf{x}) - q(\mathbf{x}) \mid^2 \mathrm{d}\mathbf{x} \right)^{1/2} \tag{3.4}$$

$$e(\mathbf{x})_{L^\infty} = \sup_{\mathbf{x}} \mid q_{\text{ref}}(\mathbf{x}) - q(\mathbf{x}) \mid \tag{3.5}$$

where the quantity q either denotes the drag coefficient C_D or the enstrophy Z. In this work all spatial operators were discretized in 2D with second order accurate schemes, the remeshing process is realized through the second order kernel M_4', the penalization discretization is of order 1 and exact FFT-based evaluations were performed to solve the diffusion and the Poisson equation. We therefore expect a space convergence order of approximately 2.

The numerical convergence results are reported in Figure 3.5a (drag coefficient) and 3.5b (enstrophy). In terms of drag coefficient history, the present method shows around second order convergence (2.41 for L^1, 2.65 for L^2 and 1.92 for L^∞). A slightly lower order of convergence is observed for the enstrophy (1.70 for L^1, 2.11 for L^2 and 1.71 for L^∞), but the final global order of convergence remains around 2. The convergence rates are thus in good agreement with our spatial discretization.

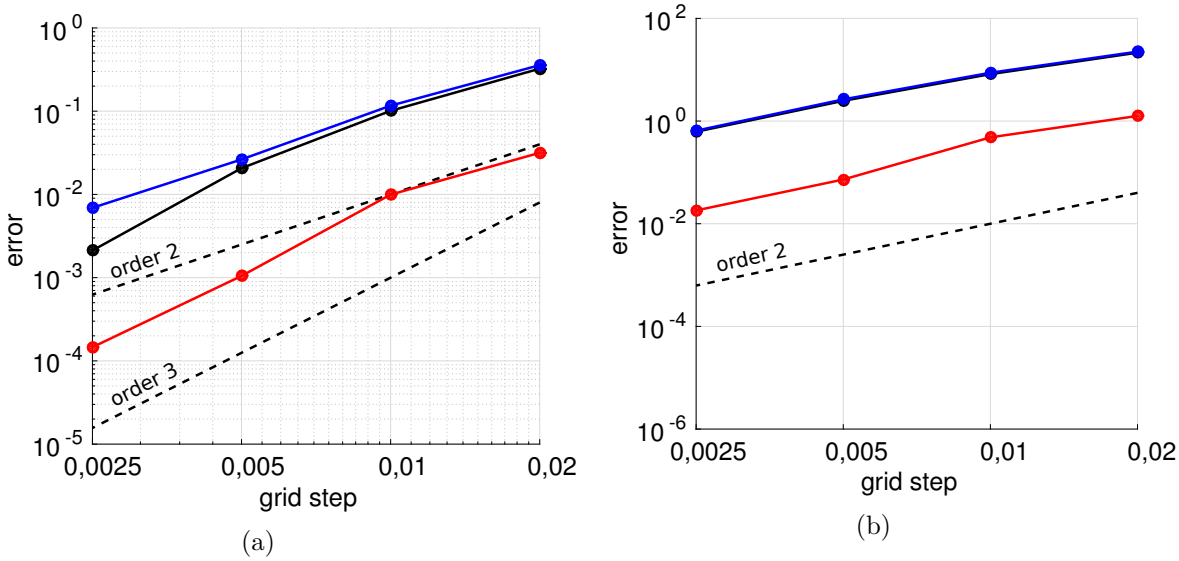

(a) (b)

Figure 3.5: Grid-convergence study for flow past a circular cylinder at $Re = 550$. The errors e_{L^1} (black), e_{L^2} (red) and e_{L^∞} (blue) are plotted against the grid step (a) Convergence of the drag coefficient. (b) Convergence of the enstrophy.

To complete this grid-convergence study, Table 3.2 gives the converged mean values of the drag coefficient and the enstrophy. These mean values are calculated on the time range $[\tilde{t},\ t_{\text{end}}]$, where $\tilde{t}$ denotes the time from which the flow regime is established. All the mean values considered in this thesis will be evaluated upon this principle. According to this table, one can consider that the grid convergence is achieved for $h = 0.005$, with values not varying more than 3% from those obtained with $h = 0.0025$.

λ-convergence study

We now perform a convergence study in terms of the penalization parameter λ in order to verify the ability of the present immersed body method to correctly model rigid motion inside a solid obstacle when increasing the value of λ. This λ-convergence study is carried out at

	$Re = 550$	
Grid	$\bar{c_D}$	$\bar{Z}$
$h = 0.02$	1.02	82
$h = 0.01$	1.31	121
$h = 0.005$	1.47	136
$h = 0.0025$	1.49	140

Table 3.2: Convergence study for flow past a circular cylinder at $Re = 550$. $\bar{c_D}$ and $\bar{Z}$ respectively denote the mean values of drag coefficient and enstrophy.

$Re = 550$ with $h = 0.005$ and $\Delta t = 0.0025$. The value of λ ranges from 1 to 10^6, with $\lambda = 10^8$ as reference case (solid case). We evaluate the L^1, L^2 and L^∞ norms of the error $e(y)$ in the mean velocity magnitude profile $|\bar{\mathbf{u}}|$ (at $x = 0$) with respect to the reference case:

$$e(y)_{L^\bullet} = \| \, |\bar{\mathbf{u}}|_{\lambda=10^8}(y) - |\bar{\mathbf{u}}|(y) \, \|_{L^\bullet} \quad , \qquad y \in [y_{\min}, y_{\max}]. \tag{3.6}$$

As Figure 3.6a shows, the numerical error decreases as $\mathcal{O}(\lambda^{-1/2})$ when $\lambda \leq 10^2$ and as $\mathcal{O}(\lambda^{-1})$ when $\lambda \geq 10^2$. The same study was performed at $Re = 100$ with smaller grid size and time step, respectively equal to $h = 0.0025$ and $\Delta t = 0.001$. This study may be considered as the numerical reference. The results are given by Figure 3.6b and show that the error behaves as $\mathcal{O}(\lambda^{-1/2})$ when $\lambda \leq 10^4$ and $\mathcal{O}(\lambda^{-1})$ when $\lambda \geq 10^4$. These convergence rates are in agreement with the numerical results found in [Angot et al., 1999] where it is stated that to increase λ to high values ($\lambda \geq 10^6$) a mesh refinement is necessary. Moreover, these numerical results are slightly better compared to the theoretical result given in [Angot et al., 1999], attesting that the upper bound on the global L^∞ error of the penalization is $\|\mathbf{u}_\lambda - \mathbf{u}\| \leq C\lambda^{-1/2}$. Furthermore, we can consider from this figure that the circular cylinder reaches the solid state from $\lambda = 10^4$, where $e(y) \leq 10^{-4}$. Thus, a permeable medium can be defined by setting the λ-values between 1 and 10^3, with very low permeability for the latter one.

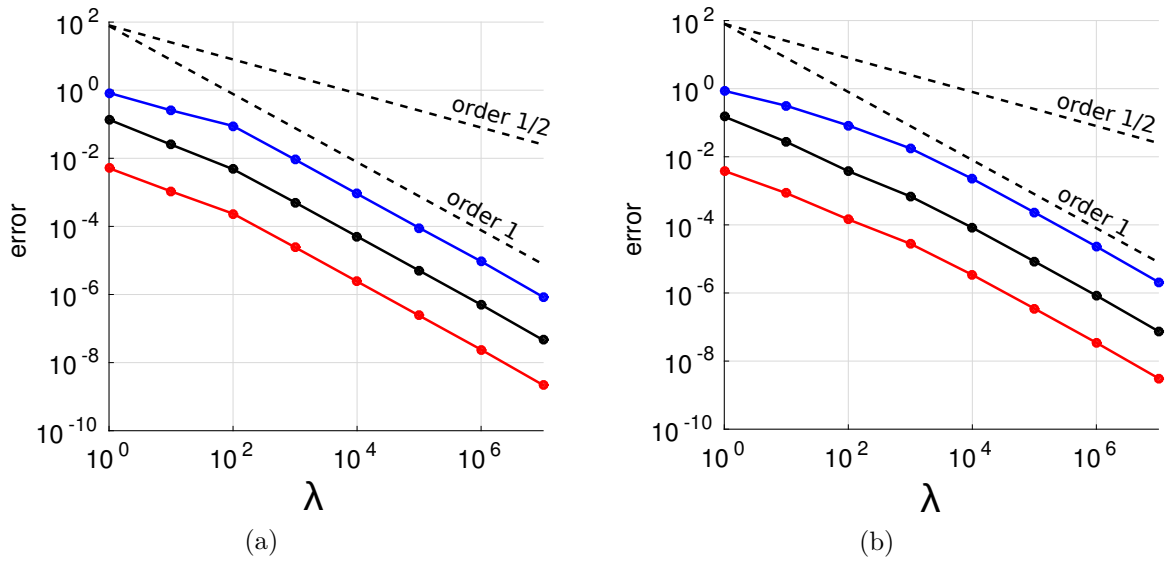

(a) (b)

Figure 3.6: λ-convergence study for flow past a circular cylinder. (a) $Re = 550$ with $h = 0.005$ and $\Delta t = 0.0025$. (b) $Re = 100$ with $h = 0.0025$ and $\Delta t = 0.001$. The errors e_{L^1} (black), e_{L^2} (red) and e_{L^∞} (blue) are plotted against λ values.

Flow analysis and validations

The first part of this flow analysis study is related to unsteady laminar flows, where the viscous effects are still predominant. The evaluation of forces has been carried out using the

momentum equation (2.33). The mean values and the amplitudes of the fluctuations of drag and lift coefficients for flows at $Re = 100$ and $Re = 200$ are computed and given in Table 3.3, as well as the value of the Strouhal number. As can be seen, these results are very close to experimental and numerical data collected by [Braza et al., 1986] and [Russell and Wang, 2003]. We note that, due to the symmetrical configuration of the cylinder, the mean value of the lift coefficient is zero.

	$Re = 100$			$Re = 200$		
Authors	$\bar{c_D}$	$\bar{c_L}$	S_t	$\bar{c_D}$	$\bar{c_L}$	S_t
Braza et al. (1986)	1.36 ± 0.015	0 ± 0.25	0.160	1.40 ± 0.050	0 ± 0.75	0.190
Russel and Wang (2003)	1.43 ± 0.009	0 ± 0.322	0.172	1.45 ± 0.036	0 ± 0.63	0.201
Present	1.40 ± 0.010	0 ± 0.32	0.165	1.44 ± 0.05	0 ± 0.75	0.200

Table 3.3: Comparison of mean drag and lift coefficients and Strouhal number for flow past a circular cylinder at $Re = 100$ and $Re = 200$.

Concerning the analysis of transitional flows, four Reynolds numbers are selected, namely Re = 550, 1000, 3000 and 9500. For the two last ones, the flow is unstable and characterized by complex vortex pairings in the wake; it is then often considered as *highly* transitional. The time evolution of the drag coefficient is reported in Figure 3.7 for each of these Reynolds numbers and is compared to the one numerically found by [Koumoutsakos and Leonard, 1995], [Ploumhans and Winckelmans, 2000] and [Rasmussen et al., 2011]. One can notice that the various results are in excellent agreement. For the particular case of $Re = 1000$, Table 3.4 shows the comparison of mean drag coefficient, amplitude fluctuation of lift coefficient and Strouhal number with other studies [Mittal and Kumar, 2001, Apte et al., 2008] for long time simulations. All these comparisons confirm an excellent agreement between our results and the reference results in the literature.

The set of numerical parameters chosen for each of these simulations, performed at Re = 550, 1000, 3000 and 9500, is given in Table 3.5. This table confirms that the choice of the grid resolution h at each flow regime is appropriate to capture the boundary layer thickness, expressed by $\delta \approx D/\sqrt{Re}$.

	Re=1000		
Authors	$\bar{c_D}$	$\bar{c_L}$	S_t
Mittal et al. (2001)	1.48 ± 0.21	0 ± 1.65	0.250
Apte et al. (2008)	1.50	0 ± 1.36	0.238
Present	1.51 ± 0.23	0 ± 1.54	0.245

Table 3.4: Comparison of mean drag coefficient, mean lift coefficient, and Strouhal number for flow past a circular cylinder at $Re = 1000$.

Re	Numerical parameters		δ	Nb of cells in boundary layer
	Δt	h		
550	0.005	0.005	~ 0.043	8.6
1000	0.003	0.0025	~ 0.032	12.8
3000	0.0025	0.0025	~ 0.018	7.2
9500	0.002	0.00125	~ 0.010	8

Table 3.5: Justification of the choice of mesh size h based on the boundary layer thickness δ, for the circular cylinder validation study.

More validations of the proposed method for flow past a circular cylinder can be found in the article [Mimeau et al., 2015] reported in Appendix (C).

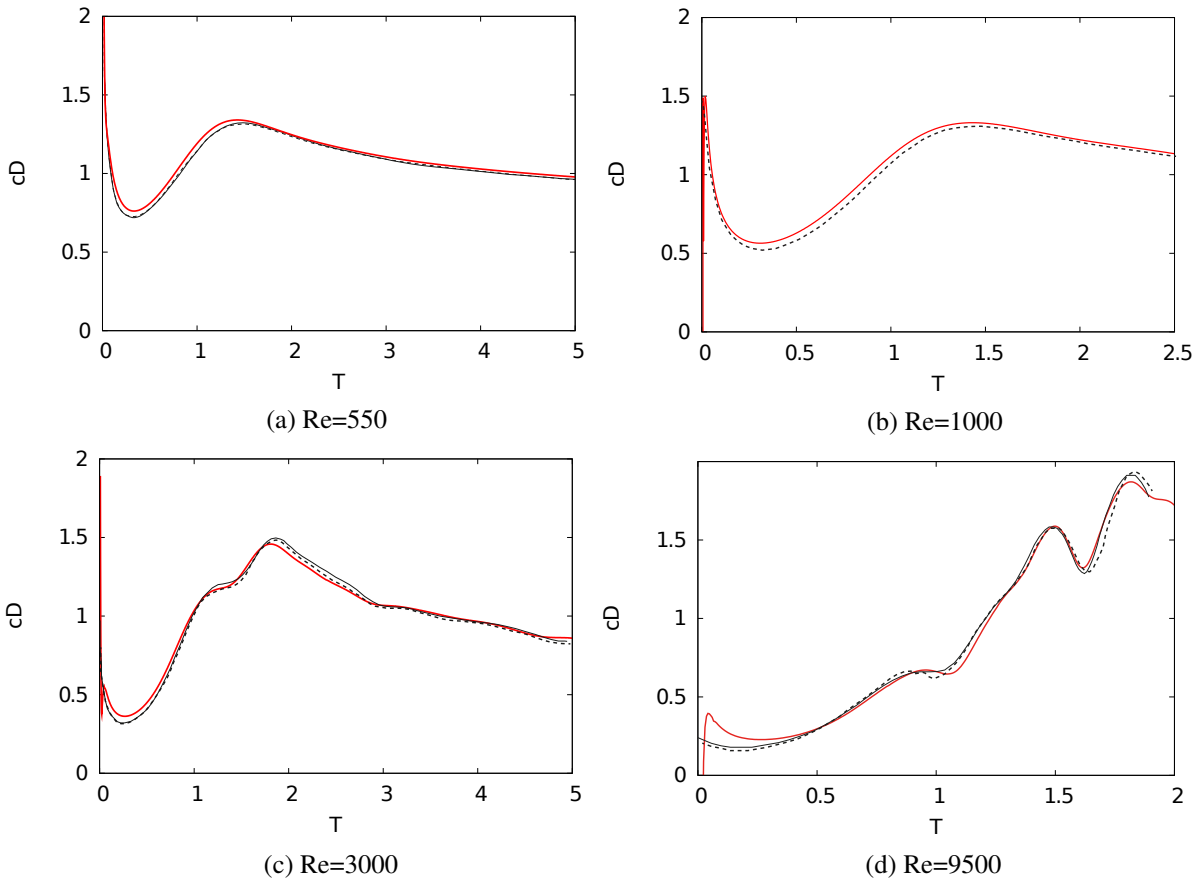

Figure 3.7: Drag evolution for (a) $Re = 550$, (b) $Re = 1000$, (c) $Re = 3000$ and (d) $Re = 9500$. Comparisons of present method (solid red line) with [Koumoutsakos and Leonard, 1995] (dashed line). Solid black line are results from [Ploumhans and Winckelmans, 2000] in (a), (b), (c) and from [Rasmussen et al., 2011] in (d).

3.2.1.2 Flow past a 2D semi-circular cylinder

In this section we consider flow past a semi-circular cylinder whose flat-surface is facing downstream. Compared to the circular cylinder, the semi-circular cylinder presents two singular points. The numerical studies presented in the sequel were carried out at $Re = 550$ and $Re = 3000$.

Grid convergence study

The grid convergence study is performed on three grid levels. For $Re = 550$ we consider three mesh sizes: $h = 0.01$, $h = 0.005$ and $h = 0.0025$ in the computational domain $D = [-4,\ 8] \times [-5,\ 5]$. For $Re = 3000$ as the boundary layer is thinner, we perform the convergence study with three finer mesh sizes, respectively $h = 0.005$, $h = 0.0025$ and $h = 0.00125$. The simulations are carried out in a smaller domain $D = [-2.5,\ 5] \times [-3,\ 3]$ in order to reduce the computational cost induced by the finest grid. We note that the drag coefficients we obtained with the two coarser grids ($h = 0.005$ and $h = 0.0025$) in the reduced domain only showed an error of 8% and 4% respectively compared to the one obtained in the large domain, which legitimates the results obtained with the reduced domain. The mean drag and enstrophy values are reported in Table 3.6. At $Re = 550$, on the basis of these results, one can consider that the grid convergence is achieved for $h = 0.005$, where the time step is equal to $\Delta t = 0.0025$. At $Re = 3000$ grid convergence is obtained with $h = 0.0025$ and $\Delta t = 0.002$. This study enables us

on one hand to prove the convergence of the method and provides on the other hand the optimal set of numerical parameters for the flow control application, allowing to achieve accurate results within a reasonable computational time. It is here important to emphasize the interest of the vortex methods which allow here to consider a highly transitional regime using a relatively large time step compared to classical Eulerian methods.

	$Re = 550$		$Re = 3000$	
Grid	$\bar{c_D}$	$\bar{Z}$	$\bar{c_D}$	$\bar{Z}$
$h = 0.01$	1.49	122	-	-
$h = 0.005$	1.91	158	1.89	313
$h = 0.0025$	1.98	161	1.94	292
$h = 0.00125$	-	-	1.96	280

Table 3.6: Convergence study for flow past a semi-circular cylinder at $Re = 550$ and $Re = 3000$. $\bar{c_D}$ and $\bar{Z}$ respectively denote the mean values of drag coefficient and enstrophy.

λ-convergence study

We now focus on the convergence of the present method with respect to the value of the penalization parameter λ inside the semi-circular cylinder, at $Re = 550$ and $Re = 3000$. The way this convergence study is carried out is exactly the same as presented previously in subsection (3.2.1.1). According to Figure 3.8, the numerical error is shown to decrease as $\mathcal{O}(\lambda^{-1/2})$ when $\lambda \leq 10^2$ and as $\mathcal{O}(\lambda^{-1})$ when $\lambda > 10^2$, like for the circular cylinder. Furthermore, the semi-circular cylinder reaches the solid state at $\lambda = 10^5$, where $e(y) \leq 10^{-4}$, for both regime. A permeable area can thus be defined with values of λ lower than 10^4. In the oncoming control study, we will increase the penalization parameter up to 10^3 inside the added porous layer in order to model a permeable medium.

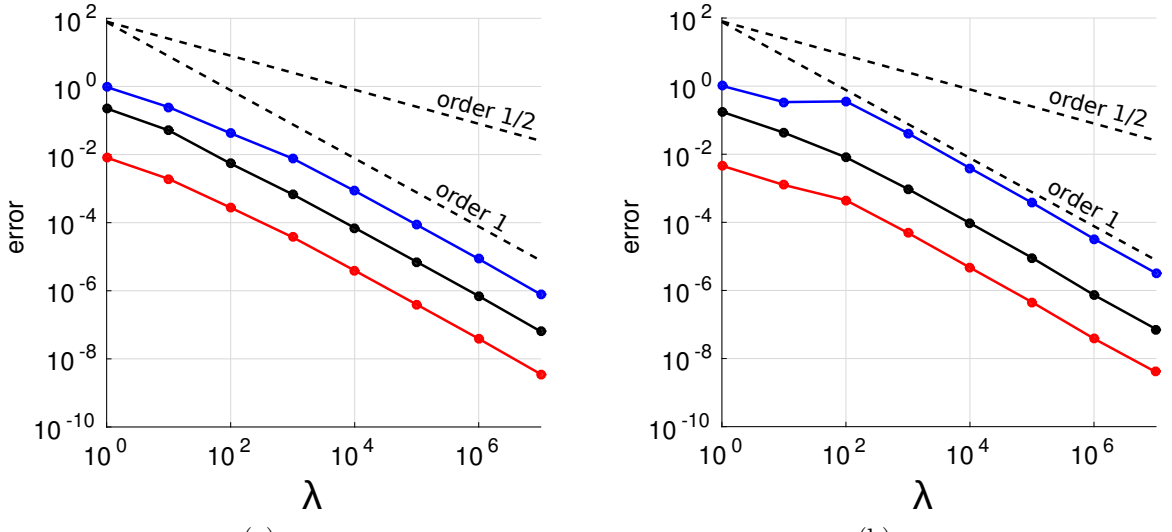

(a) (b)

Figure 3.8: λ-convergence study for flow past a semi-circular cylinder. (a) $Re = 550$ with $h = 0.005$ and $\Delta t = 0.0025$. (b) $Re = 3000$ with $h = 0.0025$ and $\Delta t = 0.002$ (b). The errors e_{L^1} (black), e_{L^2} (red) and e_{L^∞} (blue) are plotted against λ values.

Flow analysis and validations

The benchmark of incompressible flow past a semi-circular cylinder is not a classical one and, as far as we know, only few references already exist on this subject. Nevertheless, we aim at least to compare our results to numerical and experimental ones. To do so, we respectively consider the works of Farhadi et al. [Farhadi et al., 2010] and Boisaubert and Texier [Boisaubert and Texier, 1998].

As can be seen in Table 3.7, the results obtained at $Re = 100$ and $Re = 300$ show a good agreement with the numerical values given by [Farhadi et al., 2010]. A more detailed comparison is performed at $Re = 200$ and the related results are reported in Figure 3.9. As for drag and lift coefficients, one can say according to Figure 3.9a that our results coincide very well with those of [Farhadi et al., 2010] since we achieve $\bar{c_D} = 1.85 \pm 0.15$, $\bar{c_L} = 0 \pm 0.53$ and $S_t = 0.230$ against $\bar{c_D} = 1.85 \pm 0.12$, $\bar{c_L} = 0 \pm 0.50$ and $S_t = 0.215$ in [Farhadi et al., 2010]. Figure 3.9b gives a comparison of the normalized near-wake length L with the numerical results of [Farhadi et al., 2010] and the experimental data of [Boisaubert and Texier, 1998]. The near-wake length is defined as the x-coordinate of the point located on the centerline in the x-direction where the streamwise component of the velocity vanishes. As can be seen on the figure, the values obtained with the present method greatly coincide with the numerical and experimental reference results.

	$Re = 100$		$Re = 300$	
Authors	$\bar{c_D}$	S_t	$\bar{c_D}$	S_t
Farhadi et al. (2010)	1.73	0.180	1.955	0.22
Present	1.70	0.192	1.90	0.24

Table 3.7: Comparison of mean drag coefficient and Strouhal number for flow past a semi-circular cylinder at $Re = 100$ and $Re = 300$.

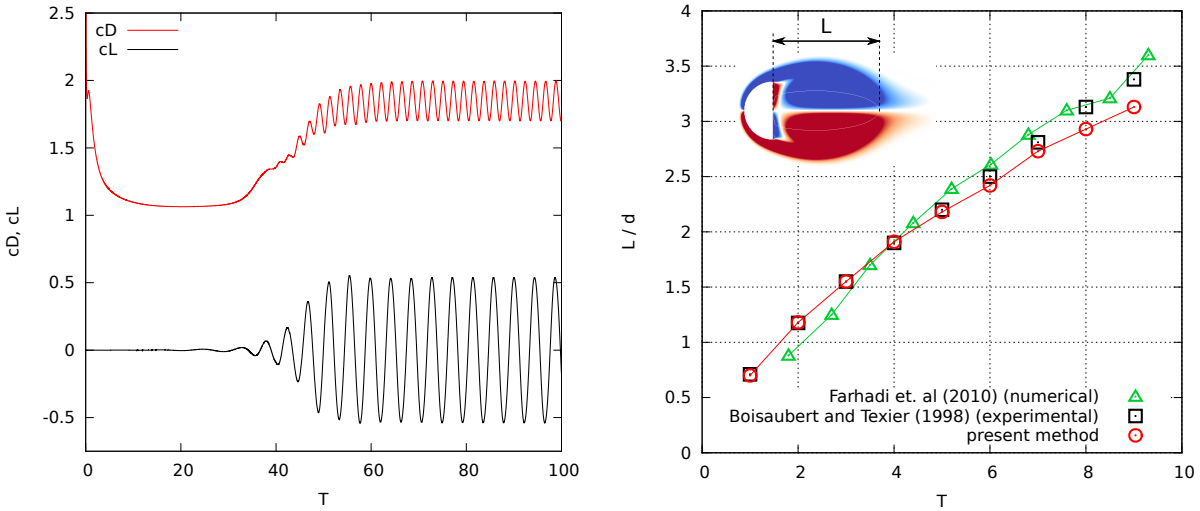

(a) (b)

Figure 3.9: (a) Drag and lift evolution for flow past a semi-circular cylinder at $Re = 200$. (b) Normalized near-wake length L/d of a semi-circular cylinder at $Re = 200$: comparison with numerical results [Farhadi et al., 2010] (green triangles) and experimental data [Boisaubert and Texier, 1998] (black squares).

3.2.2 The three-dimensional case

3.2.2.1 Flow past a 3D sphere

Grid convergence study

The convergence studies are performed in the context of flow past a 3D sphere at $Re = 300$. We first present the grid-convergence study, involving four mesh sizes: $h = 0.08$, $h = 0.04$, $h = 0.02$ and $h = 0.01$. Convergence orders are determined by computing the L^1, L^2 and L_∞ norms of the error of the drag coefficient and the enstrophy with respect to the best resolved case (see eqs. 3.3-3.5). In the particular context of this grid-convergence study, the adaptive time step is not defined by equation 2.72, which depends on the flow velocity gradient, but is instead set to:

$$\Delta t^n_{\text{adapt}} = \frac{\text{CFL} \cdot h}{\max\limits_{1 \leq i \leq 3} |u_i|}, \qquad \text{with CFL} = 0.5, \tag{3.7}$$

such that a CFL of 0.5 is ensured at any time for each simulation performed at each grid resolution. According to Figure 3.10, the method shows around second order convergence regarding drag coefficient (1.95 for L^1, 2.46 for L^2 and 1.98 for L_∞) and between first and second order convergence for the enstrophy (0.93 for L^1, 1.35 for L^2 and 1.06 for L_∞). The converged mean values of the drag coefficient and the enstrophy are given by Table 3.8 for each mesh size, and allow us to consider that the grid convergence is achieved for $h = 0.02$. The oncoming simulations involving incompressible flows past a 3D sphere at $Re = 300$ will therefore be performed fixing the mesh size to 0.02. As it will be outlined in the following, this mesh size involves a number of grid points within the boundary layer that may be considered sufficient to account for the expected flow dynamics.

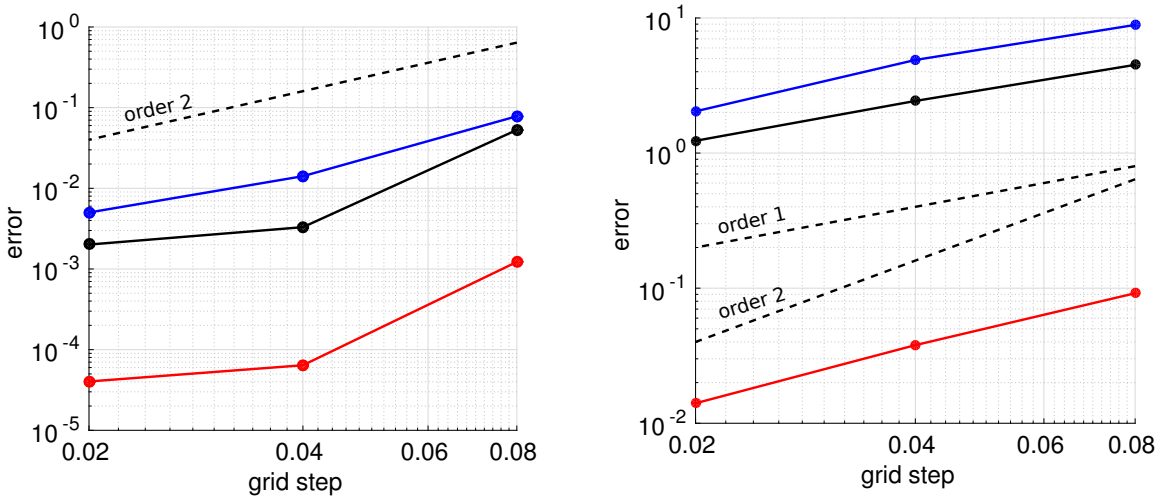

Figure 3.10: Grid-convergence study for flow past a sphere at $Re = 300$. The errors e_{L^1} (black), e_{L^2} (red) and e_{L^∞} (blue) are plotted against the grid step. (a) Convergence of the drag coefficient (b) Convergence of the enstrophy.

Flow analysis and validations

The capabilities of the HVP method are now analyzed in the context of flow past a 3D sphere. Like the circular cylinder, this type of flow has been widely studied numerically and experimentally which allowed us to precisely determine the different flow regimes. Following the

	$Re = 300$	
Grid	$\bar{c_D}$	$\bar{Z}$
$h = 0.08$	0.732	64.8
$h = 0.04$	0.679	66.5
$h = 0.02$	0.673	67.7
$h = 0.01$	0.676	68.9

Table 3.8: Convergence study for flow past a sphere at $Re = 300$. $\bar{c_D}$ and $\bar{Z}$ respectively denote the mean values of drag coefficient and enstrophy.

description given in [Ploumhans et al., 2002], we list the regimes related to Reynolds numbers ranging from 0 to several thousands and we represent them in Table 3.9:

- $Re <$ 210 - 212: the flow is steady and axisymmetric.
  An axisymmetric separation bubble exists at the back of the sphere with zero lift force.
- 210 - 212 $< Re <$ 270 - 290: the flow is steady and planar-symmetric.
  A pair of planar-symmetric vortical structures appears in the wake.
- 270 - 290 $< Re <$ 350 - 375: the flow is unsteady, time periodic and planar-symmetric.
  The wake is characterized by a cyclic shedding of ring vortices, with planar-symmetry.
- 350 - 375 $< Re <$ 800: the flow is unsteady, non-periodic and asymmetric.
- $Re >$ 800: the flow is unsteady, non-periodic, asymmetric and a Kelvin-Helmholtz instability occurs in the shear layer, propagating in the wake. The latter becomes fully turbulent, characterized by the emergence of small scales.

In the sequel, we propose validation studies for two Reynolds numbers corresponding to clearly distinct regimes: $Re = 300$ and $Re = 1000$.

We first present the results obtained at $Re = 300$. The simulation setup is the following: according to the grid convergence study presented previously (see Table 3.8), the 3D computational box $D = [-2,\ 8.24] \times [-2.56,\ 2.56] \times [-2.56,\ 2.56]$ is meshed by an uniform $512 \times 256 \times 256$ Cartesian grid ($h = 0.02$). As in [Ploumhans et al., 2002], a perturbation is addressed to the uniform upstream flow between the non-dimensional time $T = 3$ and $T = 4$, in order to trigger the instability. This perturbation is applied on the y component of the velocity and stands as $u_{y\infty} = \sin(\pi(T-3))$. The time step, initialized with the value $\Delta t = 0.0125$, is adaptive and is defined according to equation 2.72. As previously mentioned in chapter 2 with Figure 2.7, the time step actually shows to be approximately equal to 0.011 all along the simulation. Finally, the penalization parameter λ is set to 10^8 inside the sphere.

Table 3.10 provides the values of the drag and vertical lift coefficients obtained with the present method, as well as the Strouhal number for which the dominant shedding frequency is obtained from the power spectrum reported in Figure 3.12. These values are compared to results in literature [Roos and Willmarth, 1971, Johnson and Patel, 1999, Tomboulides and Orszag, 2000, Constantinescu and Squires, 2000, Kim and Choi, 2002, Ploumhans et al., 2002]. As the table shows, our results coincide well with these references. Figure 3.11 depicts the ω_z and ω_x isocontours for every quarter period of a shedding cycle. The contours obtained with the present method are compared with those published by [Ploumhans et al., 2002]. As can be observed on the figure, the vortical features are in very good agreement with the reference results. Moreover, one can notice that a true periodic regime is attained (the snapshots in Figures 3.11a and 3.11b depict the vorticity field at five equispaced times within one shedding period) and that the wake is perfectly symmetric in the XZ plane (see the ω_x isocontours in the XZ plane, Figure 3.11b). These observations confirm the description of the flow regime corresponding to Reynolds 300

Flow representation XY plane	Flow representation XZ plane	Reynolds number
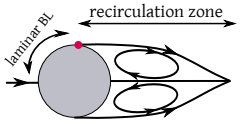	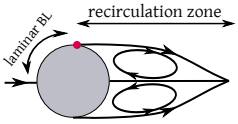	$Re < 210 - 212$
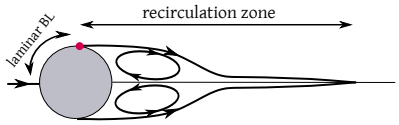	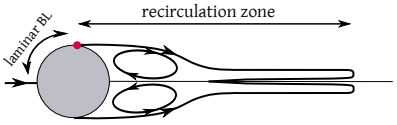	210-212$< Re <$270-290
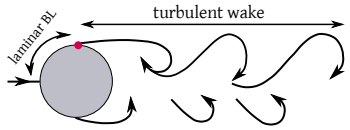	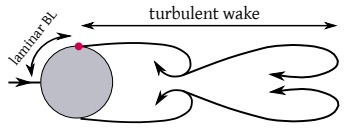	270-290$< Re <$350-375
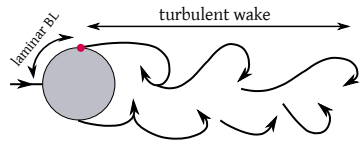	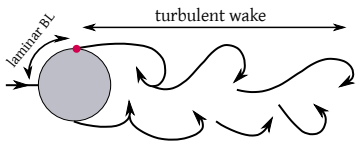	350-375$< Re <$800
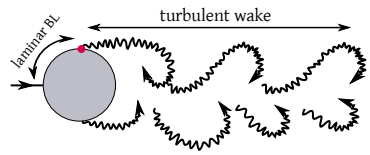	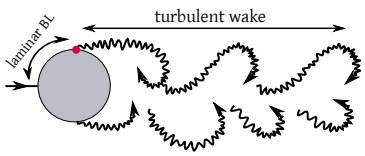	$Re > 800$

Table 3.9: Different transitional regimes for flow past a sphere.

thoroughly investigated by [Johnson and Patel, 1999, Tomboulides and Orszag, 2000] and given at the beginning of this subsection.

	$Re = 300$		
Authors	$\bar{c_D}$	$\bar{c_L}$	S_t
Roos & Willmarth * (1971)	0.629	-	-
Johnson & Patel (1999)	0.656	-0.069	0.137
Tomboulides & Orszag (2000)	0.671	-	0.136
Constantinescu & Squires (2000)	0.655	-0.065	0.136
Kim & Choi (2002)	0.657	-0.067	0.134
Ploumhans et al. (2002)	0.683	-0.061	0.135
Present	0.673	-0.066	0.133

Table 3.10: Comparison of drag and lift coefficients and Strouhal number for flow past a sphere at $Re = 300$. Star notation (*) refers to experimental results.

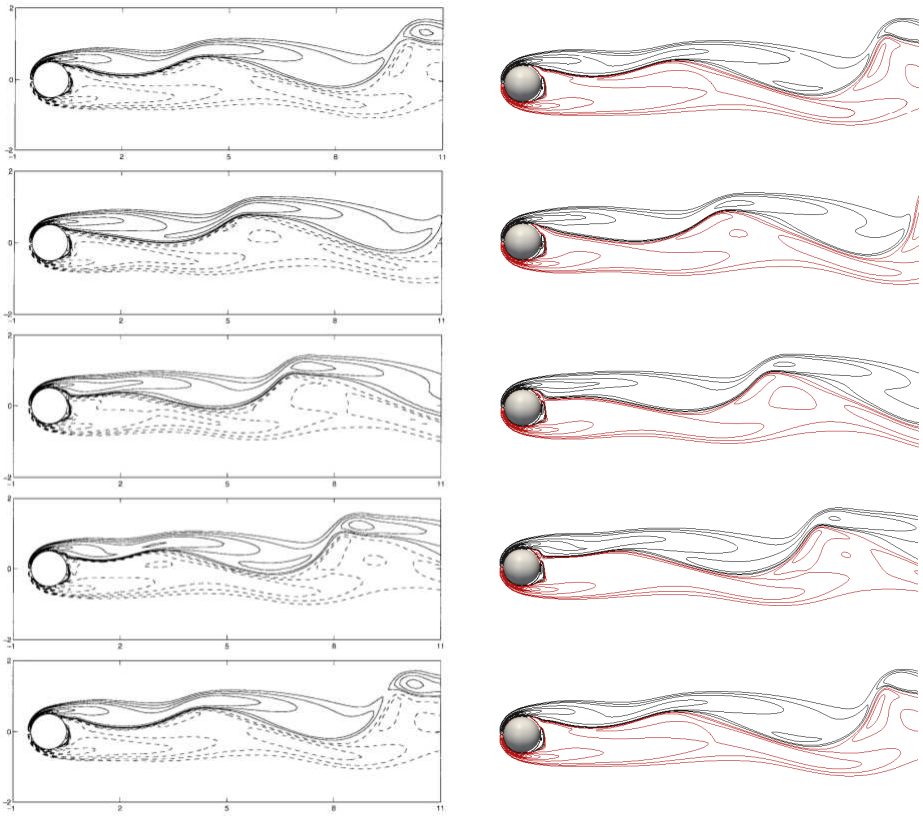

(a) Isocontours of ω_z in the XY plane

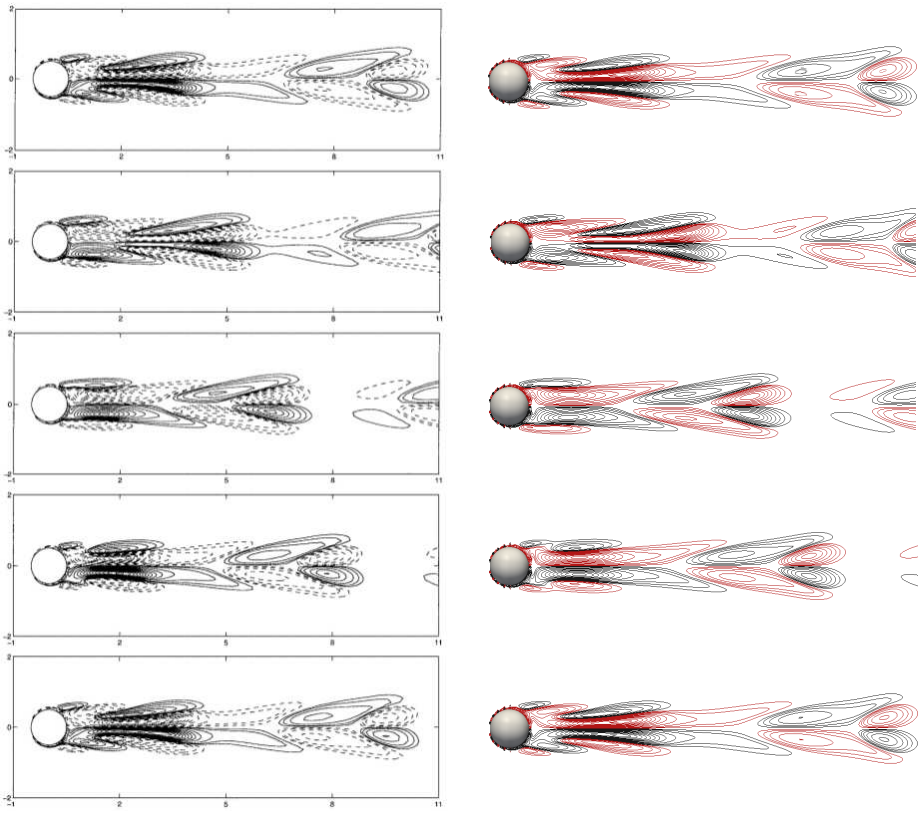

(b) Isocontours of ω_x in the XZ plane

Figure 3.11: Vorticity isocontours for flow past a sphere at $Re = 300$ for every quarter period of a shedding cycle. Comparison between [Ploumhans et al., 2002] (left columns) and present results (right columns).

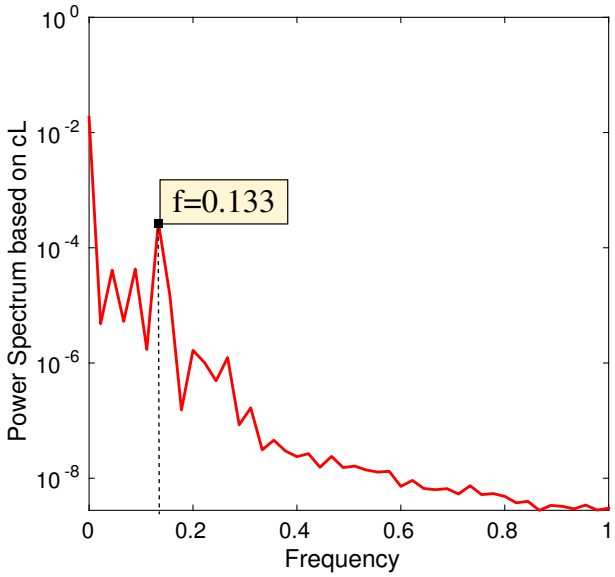

Figure 3.12: Power spectrum based on time evolution of the lift coefficient for flow past a sphere at $Re = 300$.

The flow analysis at $Re = 1000$ is now considered. The simulation is performed on an uniform $1024 \times 512 \times 512$ Cartesian grid ($h = 0.01$). Still following the setup of [Ploumhans et al., 2002], a perturbation is applied between $T = 3$ and $T = 4$ on the y component of the velocity, defined by $u_{y\infty} = 0.1 \sin(\pi(T-3))$. The adaptive time step is initialized with the value $\Delta t = 0.005$ and keeps approximately this value all along the simulation. The penalization parameter λ is fixed to 10^8 inside the sphere.

Figure 3.13 supplies several quantitative information about the flow quantities. First, a plot of the time average streamwise velocity u_x along the centerline is given in Figure 3.13a. The results obtained with the present method are compared to those of [Tomboulides and Orszag, 2000] together with the experimental data of [Wu and Faeth, 1993] at $Re = 960$, and show a good agreement. The same conclusion stands for the time evolution of force coefficients. Indeed, as shown in Figure 3.13b, the time evolution of the drag coefficient C_D and the vertical lift coefficient C_L coincide with the one found by [Ploumhans et al., 2002]. As emphasized in [Ploumhans et al., 2002], although the prescribed perturbation is symmetric, the flow is becoming fully three dimensional. This is confirmed by Figure 3.13c, giving the evolution of the force coefficients for a larger time range. We can especially notice that the side lift force coefficient C_S is non-zero, contrary to $Re = 300$ for instance, and shows significant variations which are actually in the same order of magnitude than the one of C_L. Concerning the drag coefficient C_D, the mean value obtained in the present study is 0.485, which coincide well with the numerical values reported by [Poon et al., 2009] and [Campregher et al., 2009], respectively equal to 0.46 and 0.478. Isocontours of $|\boldsymbol{\omega}|$ in the near wake are depicted in the XY and XZ plane for early times, respectively by Figure 3.14a and 3.14b. They are compared to those of [Ploumhans et al., 2002]. These figures, which show a good agreement, reveal that the flow is initially symmetric in the XZ plane. However, as highlighted by Figure 3.15, the near wake becomes asymmetric from $T = 18$. The same value of T is reported by [Ploumhans et al., 2002]. This loss in planar-symmetry intensifies in time and is perfectly clear at $T = 48$ (see Figure 3.15).

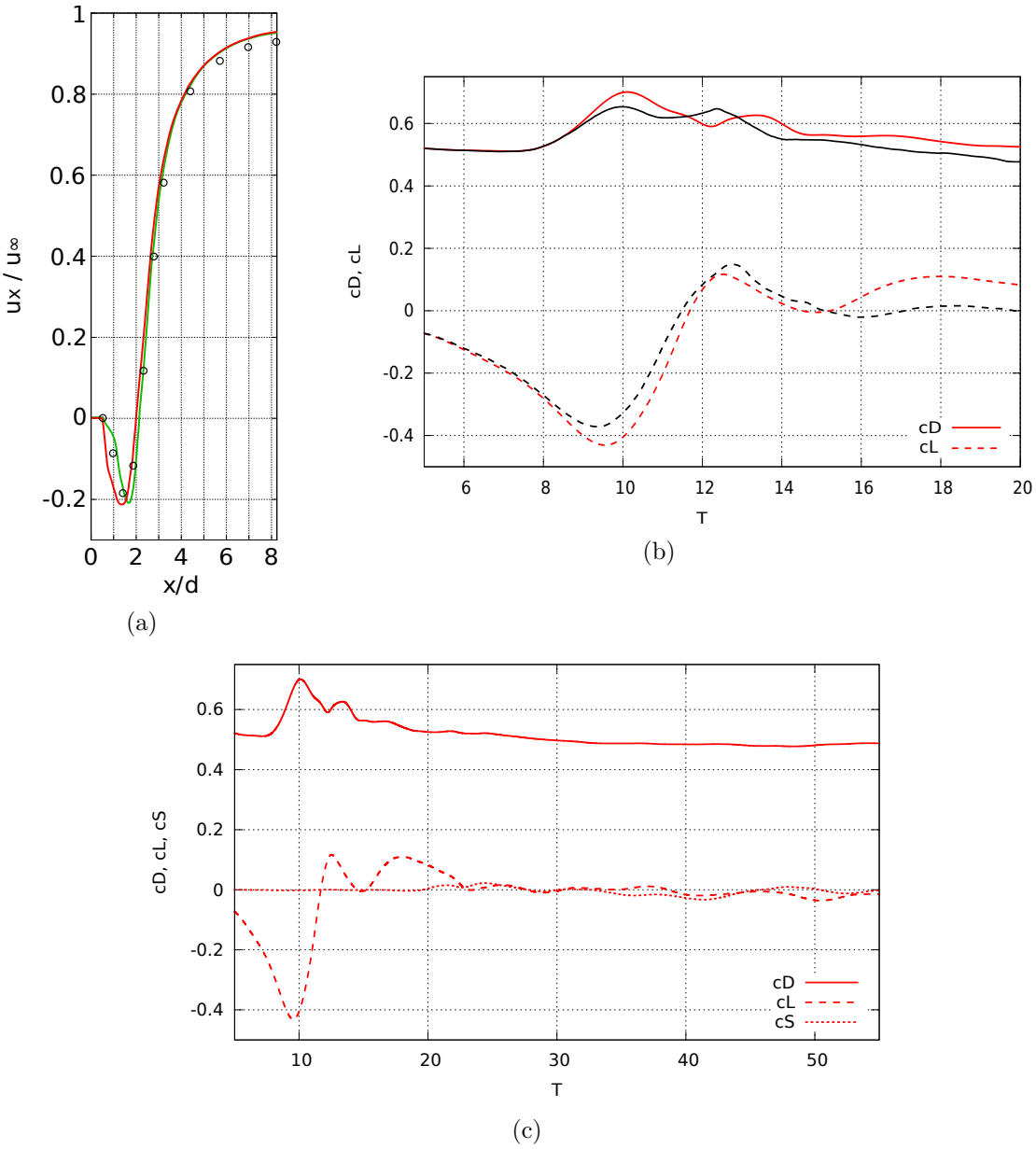

Figure 3.13: Sphere flow analysis at $Re = 1000$: (a) Average streamwise velocity u_x along the x-axis: comparison of the present results (red curve) with numerical results [Tomboulides and Orszag, 2000] (green curve) and experimental data [Wu and Faeth, 1993] at $Re = 960$ (black circles). (b) C_D (solid lines) and C_L (dashed lines) time evolution: comparison of the present results (red curves) with [Ploumhans et al., 2002] (black curves). (c) C_D (solid line), C_L (dashed line) and C_S (dotted line) time evolution.

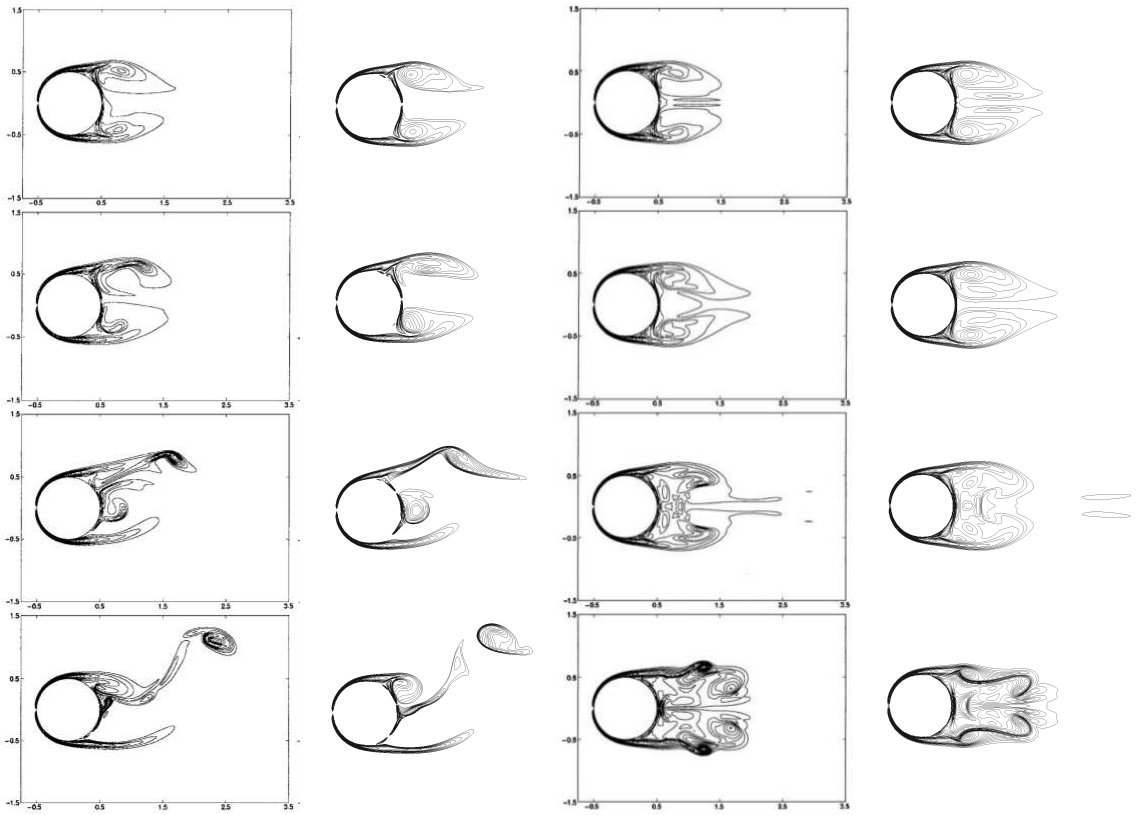

(a) Isocontours of $|\boldsymbol{\omega}|$ in the XY plane (b) Isocontours of $|\boldsymbol{\omega}|$ in the XZ plane

Figure 3.14: Isocontours of $|\boldsymbol{\omega}|$ for flow past a sphere at $Re = 1000$. Comparison between [Ploumhans et al., 2002] (left columns) and present results (right columns) at $T = 6$, 8, 10, 12.

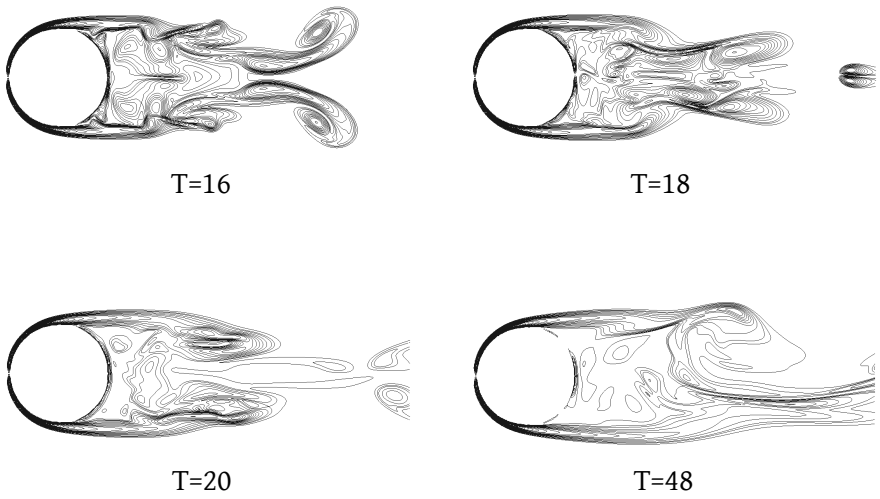

Figure 3.15: Isocontours of $|\boldsymbol{\omega}|$ in the XZ plane for flow past a sphere at $Re = 1000$. The near wake becomes asymmetric from $T = 18$.

3.2.2.2 Flow past a 3D hemisphere

Grid convergence study

The last validation study of this work is performed for flow past a 3D hemisphere at $Re = 300$. In the same way as for the sphere, four different mesh sizes are considered for the grid convergence study and the time step is defined according to equation 3.7. The order of convergence for the drag coefficient was found to be 1.80 for L^1, 2.23 for L^2, 1.48 for L_∞ and 0.95 for L^1, 1.49 for L^2, 1.23 for L_∞ concerning the enstrophy. These convergence orders are very similar to those found for the sphere. They are complemented by Table 3.11, giving the converged mean values of the two flow quantities at $Re = 300$. Here again, one may consider that the grid convergence is obtained by setting $h = 0.02$.

	$Re = 300$	
Grid	$\bar{c_D}$	$\bar{Z}$
$h = 0.08$	0.787	73.4
$h = 0.04$	0.725	73.0
$h = 0.02$	0.721	73.3
$h = 0.01$	0.725	74.0

Table 3.11: Convergence study for flow past a hemisphere at $Re = 300$. $\bar{c_D}$ and $\bar{Z}$ respectively denote the mean values of drag coefficient and enstrophy.

λ-convergence study

Like in 2D, we verify the convergence of the method with respect to the penalization parameter λ. This study is performed at $Re = 300$ with $h = 0.02$, following the same process as in 2D. The results are reported by Figure 3.16.

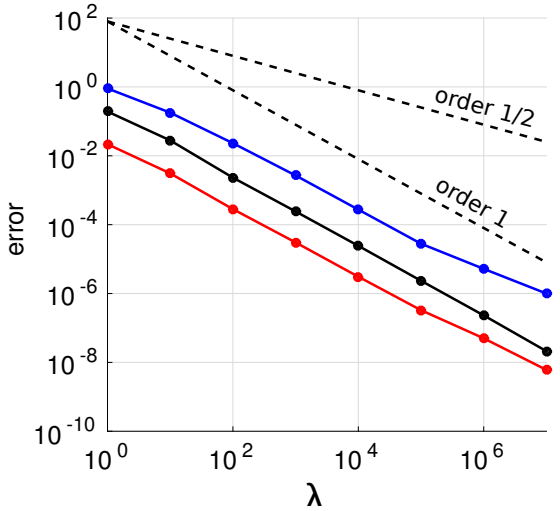

Figure 3.16: λ-convergence study for flow past a hemisphere at $Re = 300$ with $h = 0.02$. The errors e_{L^1} (black), e_{L^2} (red) and e_{L^∞} (blue) are plotted against λ values.

The numerical error is shown to decrease as $\mathcal{O}(\lambda^{-1/2})$ when $\lambda \leq 10^2$ and $\lambda \geq 10^5$, and as as $\mathcal{O}(\lambda^{-1})$ when $10^2 \leq \lambda \leq 10^5$. The fact that the error is shown to decrease as $\mathcal{O}(\lambda^{-1/2})$ for $\lambda \geq 10^5$ perfectly coincides with the already mentioned remark made in [Angot et al., 1999], stating that to increase λ to high values a mesh refinement is necessary. This can be explained by the fact that high values of λ model bodies of almost zero permeability, thus implying steep

solid-fluid interfaces and high velocity gradients in this region. The results reported in Figure 3.16 therefore mean that the simulations carried out here with a mesh size equal to $h = 0.02$ are on the edge of under-resolution in the region of the boundary layer. Nevertheless, as it will be presented in the following, this mesh size is enough to capture the global flow characteristics needed to perform the flow control study.

Flow analysis and validations

As we aim to perform passive flow control past a hemisphere, it is important to validate the present method in the context of such geometry. Similarly to the semi-circular cylinder, we expect the hemisphere's rear back to have an influence on the flow behavior. However, as already mentioned at the beginning of this chapter, experimental and numerical results related to this problem are very few to our knowledge. The main study on which this section is based is the one carried out by [Kim and Choi, 2003], who investigated in details the behavior of flows past a hemisphere at different Reynolds numbers, ranging from 100 to 300. In their study, the authors report the following flow regimes:

- $Re = 100$, 130, 150, 170: the flow is steady and axisymmetric.
- $Re = 180$, 190: the flow is steady and planar-symmetric.
- $Re = 200$, 210: the flow is unsteady, time periodic and asymmetric.
- $Re = 220$, 250, 270: the flow is unsteady, time periodic and planar-symmetric.
- $Re = 280$, 300: the flow is unsteady, non-periodic and asymmetric.

Let us first draw some comparisons between these flow regimes and the ones of the sphere, listed in the previous section. One can notice that steady flows over a hemisphere are very similar to those over a sphere, even if the transitions between the different flow regimes occur at lower Reynolds numbers in the hemisphere case. Indeed, as explained in [Kim and Choi, 2003], the steady axisymmetric flow is characterized by an axisymmetric recirculation zone behind the hemisphere, while for the steady planar-symmetric flow two streamwise vortical structures are formed in the wake. However, according to the authors, an important difference exists between the unsteady flows past a hemisphere and those past a sphere. We indeed notice that when $220 \leq Re \leq 270$, the flow past a hemisphere recovers planar-symmetry while for lower Reynolds number ($Re = 200$, 210), it was totally asymmetric. This behavior is not observed in the sphere case.

As we only aim for dealing with unsteady flows, we will focus this validation study on three Reynolds numbers, each corresponding to a different unsteady flow behavior: $Re = 200$, 250, and 300. These Reynolds numbers are also studied in details in [Kim and Choi, 2003], which supplies a great support for validation and comparisons. For each simulations, we consider a $512 \times 256 \times 256$ Cartesian grid ($h = 0.02$), the time step is defined according to equation 2.72 and initialized with $\Delta t = 0.0125$, and λ equals 10^8 within the hemisphere.

The flow at $Re = 200$ is first considered. Figure 3.17a shows the time evolution of the drag and lift coefficients, which are compared to those obtained by [Kim and Choi, 2003]. First, one can notice a very good agreement between the different results, which is confirmed by the first lines of Table 3.12 giving the mean values of the force coefficients at $Re = 200$. Concerning the Strouhal number, one can see in our case and in the reference results that the Strouhal based on the lift is half the one based on the drag. Finally, we focus on the side lift coefficient C_S. At $Re = 200$ the time average of this coefficient is not zero, which corroborates the fact that the flow does not maintain the planar-symmetry. This statement is confirmed by Figure 3.18 depicting the vorticity norm $|\boldsymbol{\omega}|$ at two different times, where one can see that the wake is not

symmetric in the plane XZ at this Reynolds number.

Let us now focus on flow past a hemisphere at $Re = 250$. Figure 3.17b and Table 3.12 show that the present outcomes coincide well with the reference results. As for the flow at $Re = 200$, the shedding frequency is equal to the frequency of the lift ($St_{\text{lift}} = 0.128$) and half the frequency of the drag ($St_{\text{drag}} = 0.256$). Finally, Figure 3.18 confirms that the flow at $Re = 250$ recovers the symmetry in the XZ plane. This observation explains the zero time average side lift coefficient ($\bar{C_S} = 0$) read in Table 3.12.

The last simulation is performed at $Re = 300$. According to Figure 3.17c the flow has a more complex behavior, showing drag and lift coefficients with complicated variations in time. The vorticity norm reported in Figure 3.18 also highlights the absence of any planar-symmetry, as expected. On the other hand, Table 3.12 and Figure 3.20 reveal that, at this regime, there co-exist two distinct values of the Strouhal number based on the power spectrum of the drag. The lower frequency ($St_{\text{drag1}} = 0.04$) is due to the large-scale instability of the wake, while the higher frequency ($St_{\text{drag2}} = 0.270$) is attributed to the small-scale instabilities caused by the separation of the shear layer. The St_{drag2} value is still approximately equal to twice the dominant frequency of the lift ($St_{\text{lift}} = 0.138$). One can also remark in Table 3.12 that the time average lift coefficient $\bar{C_L}$ is zero (like for $Re = 200$ and $Re = 250$), which is not the case for flow past a sphere at $Re = 300$ (see $\bar{C_L}$ in Table 3.10). This difference can be explained by the discrepancy in the process of vortex shedding. Indeed, as can be seen in Figure 3.18, in the case of a hemisphere the vortices shed alternatively with the same strength in the XY plane, leading to $\bar{C_L} = 0$. On the contrary, at the same Reynolds number, the vortex shedding from a sphere does not symmetrically alternate. This phenomenon is depicted in Figure 3.19 and also in Figure 3.11a, where one can clearly see, in the XY plane, that the top eddies are much stronger than the bottom ones. It confirms the observations made by [Kim and Choi, 2002].

$Re = 200$	$\bar{c_D}$	$\bar{c_L}$	$\bar{c_S}$	St_{lift}	St_{drag}	
Kim & Choi (2003)	0.790	0.0 ± 0.024	0.049	0.128	0.256	
Present	0.805	0.003 ± 0.025	0.043	0.129	0.257	
$Re = 250$	$\bar{c_D}$	$\bar{c_L}$	$\bar{c_S}$	St_{lift}	St_{drag}	
Kim & Choi (2003)	0.742	0.0 ± 0.05	0.0	0.127	0.254	
Present	0.757	0.0 ± 0.05	0.0	0.128	0.256	
$Re = 300$	$\bar{c_D}$	$\bar{c_L}$	$\bar{c_S}$	St_{lift}	St_{drag1}	St_{drag2}
Kim & Choi (2003)	0.715	0.0 ± 0.062	0.0	0.135	0.04	0.270
Present	0.729	-0.002 ± 0.063	-0.0016	0.134	0.04	0.270

Table 3.12: Comparison of mean drag and lift coefficients as well as Strouhal numbers for flow past a hemisphere at $Re = 200$, 250 and 300.

Conclusion 3.1

This validation study presented in this chapter showed that the HVP method was able to model the correct behavior of a transitional or highly transitional 3D flow. We also noticed that this correct behavior was obtained with relatively reduced computational domains, which shows the limitation of blockage effects due to the boundaries on the solution, and with large time step values compared to classical Eulerian schemes. These outcomes thus allow to save computational efforts. Finally, the present convergence and validation studies enabled us to determine the appropriate numerical parameters (in the sense of grid size, penalization parameter λ and time steps) needed to obtain accurate results in the more challenging application that will be considered in the following chapter.

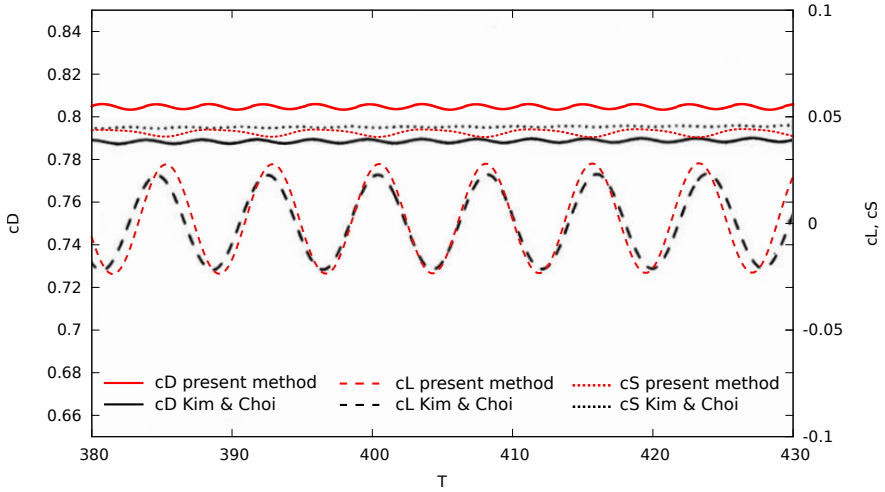

(a) $Re = 200$

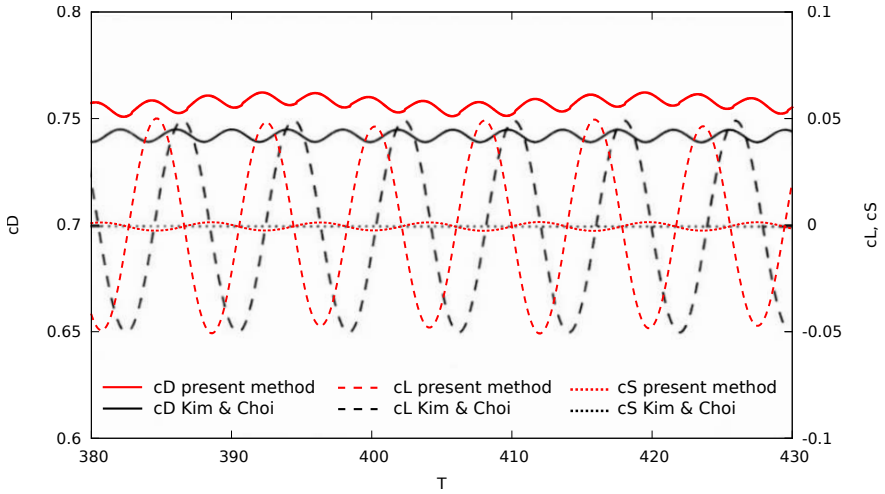

(b) $Re = 250$

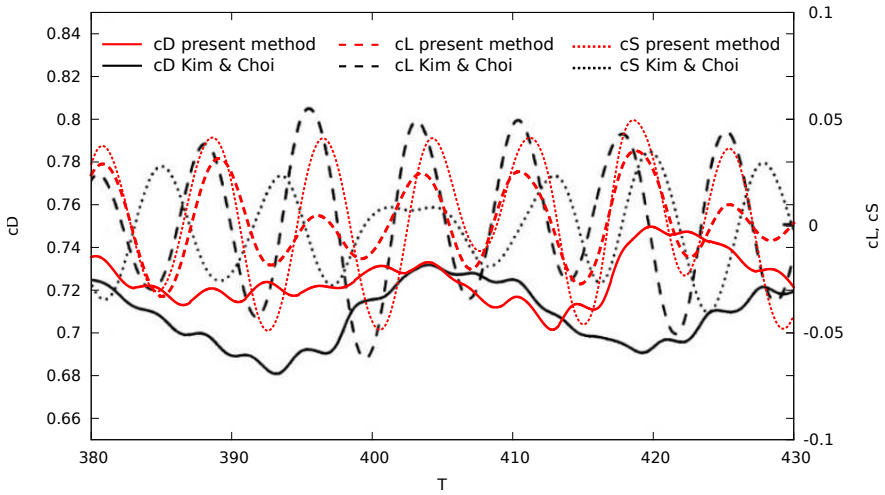

(c) $Re = 300$

Figure 3.17: Time evolution of the force coefficients for flow past a hemisphere. Comparison with the numerical results of [Kim and Choi, 2003].

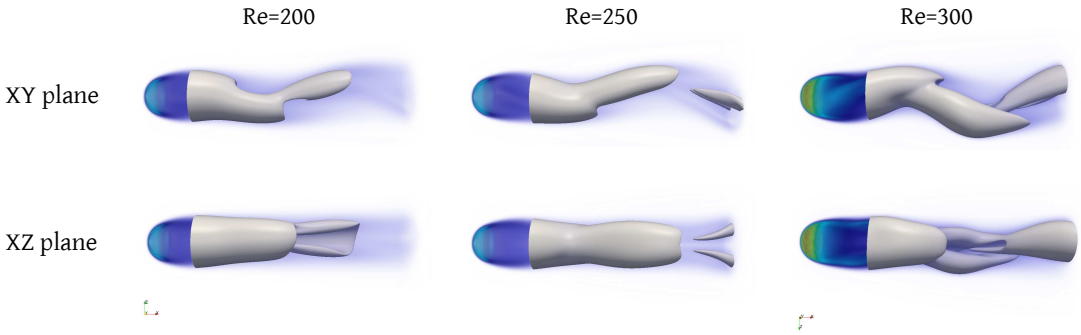

(a) $T = 100$

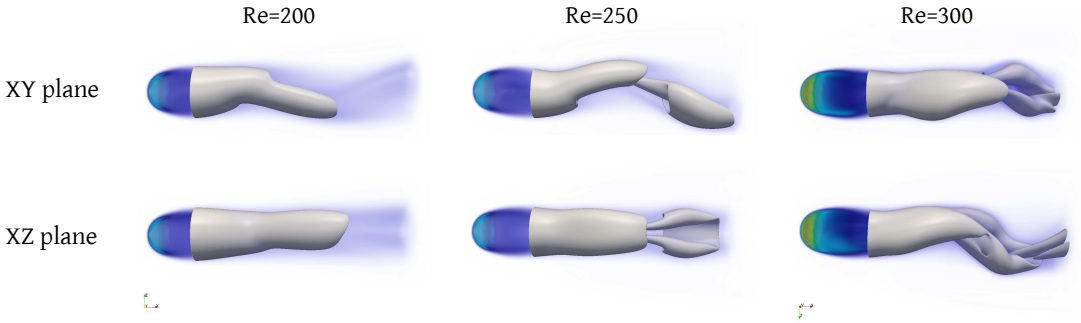

(b) $T = 200$

Figure 3.18: Flow past a hemisphere at $Re = 200$, 250 and 300: instantaneous 3D vortical structures with isocontour $|\boldsymbol{\omega}| = 0.8$ at (a) $T = 100$ and (b) $T = 200$.

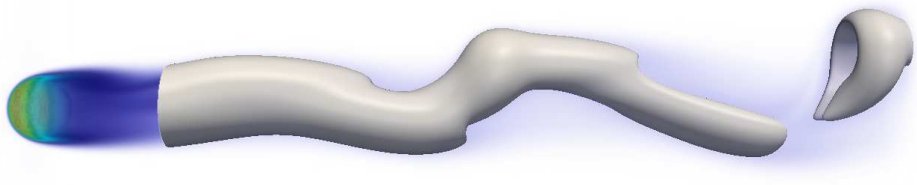

Figure 3.19: Flow past a sphere at $Re = 300$: instantaneous 3D vortical structures with isocontour $|\boldsymbol{\omega}| = 0.45$ in a longer computational domain $D = [-2,\ 18.48] \times [-2.56,\ 2.56] \times [-2.56,\ 2.56]$.

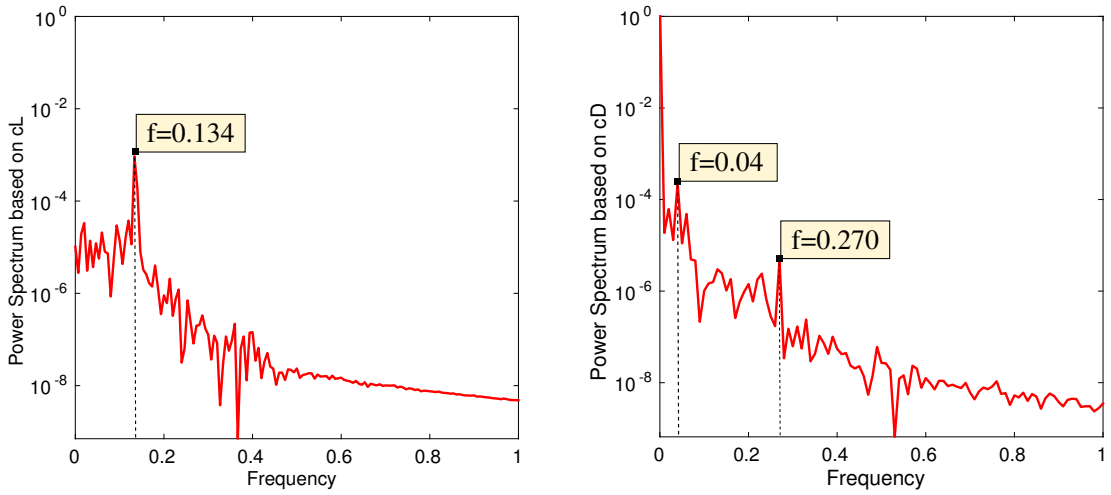

Figure 3.20: Power spectrum based on time evolution of the lift coefficient (left) and on the drag coefficient (right) for flow past a hemisphere at $Re = 300$.

4

Application to passive flow control using porous media

Contents

Résumé 4

Dans ce chapitre, la méthode HVP présentée et validée précédemment est appliquée à l'étude d'écoulements à travers des milieux solides-fluides-poreux. Cette étude peut-être considérée comme une extension des premiers travaux proposés par Bruneau & Mortazavi, dans lesquels la méthode de pénalisation est utilisée dans un contexte purement eulérien et bidimensionnel afin de modéliser ce type de problèmes. A travers ce chapitre nous illustrons l'efficacité de la méthode vortex hybride pénalisée dans le traitement de problèmes physiques 2D et 3D où les propriétés intrinsèques du corps considéré ainsi que les conditions à la frontière varient. Plus précisément, nous nous focalisons sur une étude de contrôle passif d'écoulements visant à recouvrir d'un revêtement poreux l'obstacle immergé afin d'en améliorer les performances aérodynamiques. Pour mener à bien cette étude, nous nous intéressons au contrôle d'écoulements autour d'une représentation très simplifiée de rétroviseur automobile (un hémisphère), le but étant de comprendre les mécanismes mis en jeu par la présence du revêtement poreux régularisant afin de proposer des dispositifs viables et abordables. Pour cela plusieurs configurations géométriques de revêtement poreux sont analysées en considérant différentes épaisseurs et perméabilités. Les études de contrôle passif de ce chapitre permettent de mettre en évidence l'efficacité des obstacles contrôlés où les parties poreuses sont insérées au niveau des points de séparation de l'écoulement. Il s'avère également que, dans certains cas, de faibles épaisseurs de revêtement poreux suffisent à diminuer de façon significative la production de traînée ou d'enstrophie. Ces dispositifs se révèlent d'autre part plus performants que ceux incluant une couche poreuse homogène sur la totalité de la surface de l'obstacle. Ils constituent ainsi un bon compromis entre efficacité et facilité de production.

This chapter is devoted to the study of passive flow control past bluff bodies with a rear wall, using porous media. It illustrates the efficiency of the vortex penalization method to handle problems where the physical properties or boundary conditions vary in the body.

The penalization method has already been used to model the solid-fluid-porous problem in 2D with pressure-velocity formulations [Bruneau and Mortazavi, 2004, Bruneau and Mortazavi, 2006, Bruneau et al., 2008]. In this work, the problem is handled through a velocity-vorticity formulation of the governing equations. The resulting hybrid vortex penalization model, described in details in chapter 2, is presently used to simulate two- and three-dimensional flows around obstacles which are totally or partially covered with a porous coating. This passive flow control study is performed in order to find out viable and affordable solutions that would allow to improve the aerodynamic performances of the side-view mirrors on a ground vehicle. In this work, the study will be focused on a very simplified version of the mirrors geometry which corresponds to a hemisphere configuration. Let us precise that the simulations performed in this flow control study are Direct Numerical Simulations, which imposes to consider a range of Reynolds numbers below the realistic values. Nevertheless, a clear understanding of the physical mechanisms involved in the vicinity of the porous interfaces is necessary in order to consider further studies at a realistic level. For that purpose, it seems important to first perform studies that take into account all the physical scales.

This chapter will be introduced giving the motivations of the present flow control study as well as an overview of the existing solutions in order to perform it. The passive control results obtained in the present work in 2D and in 3D through the HVP method will then be presented.

4.1 Motivations and solutions

When the speed of a ground vehicle is greater than 80 km/h, most of the energy supplied by the engine is dedicated to struggle against air resistance. This resistance is directly linked to the vehicle aerodynamic drag. Consequently, the lower is the drag, the lower will be the fuel consumption of the vehicle and thus, the carbon dioxide emissions. Nowadays, reducing the CO_2 emissions is a crucial issue and the automotive industry has a responsibility to find solutions to ensure this reduction. In particular, the side-view mirrors have a significant influence on the drag production. Indeed, due to their spanwise position, they generate a non-negligible wake which interferes with the flow past car sides. Although they only represent 0.5% of the total projected surface, the mirrors are responsible for up to 10% of the total vehicle drag. This observation provides a good motivation to find solutions leading to the regularization of the flow past side-view mirrors and to the reduction of their drag.

Side-view mirrors have been subject to extensive investigations in order to reduce the vibration of their surface [Watkins and Oswald, 1999] as well as the intrinsic acoustic noise they produce [Ono et al., 1999, Dolek et al., 2004, Lounsberry et al., 2007, Chen et al., 2009]. These aspects will not be considered in the present study.

This work instead focuses on a strategy allowing to reduce the drag production. For that purpose, a natural and common solution is shape optimization. Recently, [Othmer, 2014] and [Hojjat et al., 2014] independently used morphing routines in order to optimize the shape of the side-view mirrors of a car. With a drag reduction of 7% for the mirrors, the first author achieved a 1% drag reduction of the entire car by simply optimizing the mirror shapes and leaving the rest of the car unchanged. Considering an additional constraint on the mirror shape, the second authors reached a global drag reduction of 0.6% with the same drag reduction of 7% for the mirrors themselves. In the same class of techniques, we can also cite the one consisting in varying some parameters related to the mirror setup in order to reduce the drag. This problem was for instance addressed recently by [Olsson, 2011] who proposed to numerically and experimentally perform small variations in the height of the foot, the gap from the car sides and the inclination of the mirror. All these approaches lead to significant improvements, nevertheless the

drag reduction remains limited by the numerous regulations and legal demands related to safety aspects, which impose strong constraints on the mirrors' shape. Therefore, a complementary issue would be to consider a drag reduction technique that do not change the geometry or the position of the mirrors. This objective may be achieved through flow control.

Among the flow control techniques one can distinguish the *active* and the *passive* ones. Active flow control devices have been thoroughly used to reduce the drag generated at the rear back of a ground vehicle, which accounts for about 30% of the total vehicle drag. One can for instance cite the use of synthetic jets (produced by a periodic ejection and suction of fluid from a small opening) [Leclerc, 2008, Pasquetti and Peres, 2015], pulsed jets (device cyclically injecting momentum in the flow) [Bruneau et al., 2010, Bideaux et al., 2011] or deflectors (power-operated device allowing to modify the flow direction) [Aider et al., 2009]. This type of flow control is very efficient and may lead to local drag reduction of about 20% [Bruneau et al., 2010, Bideaux et al., 2011]. Nevertheless, active flow control devices have a non-negligible production cost and require maintenance. Moreover, they are practically impossible to implement on side-view mirrors.

The solution therefore retained in the present work is the passive flow control technique. The latter is becoming more and more used in automotive industry since it involves devices that are easy to set up and low cost, like for example splitter plates (separating plates modifying the wake dimension)[Gilliéron, 2001, Khalighi et al., 2001] or vortex generators (trapezoidal obstacles settled on the car roof allowing to break the large vortical structures into smaller ones) [Park et al., 2007, Aider et al., 2009]. In the case of a side-view mirror, a suitable solution would be the one initially proposed by [Bruneau and Mortazavi, 2004, Bruneau and Mortazavi, 2006, Bruneau et al., 2008]. It consists in adding a porous sheath on the obstacle surface in order to reduce the vorticity generation of the boundary layer. The presence of a porous medium at the solid-fluid interface indeed imposes a kind of mixed boundary condition intermediate between the no-slip and the slip one on the solid boundary [Carbou, 2008]. As a result, the shear forces are decreased and the flow dynamics is smoothed.

As a first step, this work aims to perform such passive flow control past a three dimensional hemisphere, which can be considered as a very simplified geometry of a side-view mirror. As shown in [Rouméas et al., 2009, Bruneau et al., 2010], a flow past a square back obstacle is not dominated by longitudinal three-dimensional vortical structures. In [Bruneau et al., 2010], the authors affirm that this flow characteristic ensures comparable tendencies between two- and three-dimensional flow control studies. Therefore a preliminary two-dimensional control study on flow past a two-dimensional semi-circular cylinder can be useful in our case to supply information and general trends for a further control study in three dimensions around a hemisphere. In the sequel we will first carry out a detailed flow control study in the 2D case. We will then take advantages of the outcomes of this study to handle the more realistic 3D problem of flow past a hemisphere.

4.2 Passive flow control past a 2D semi-circular cylinder

As explained in chapter 2, the method presented here, based on the vortex-penalization technique, involves a unique equation in the whole domain and enables one to accurately model each of the different solid, fluid and porous regions by varying the value of the dimensionless penalization factor λ. In two dimensions, the penalized vorticity equation reads:

$$\frac{\partial \omega}{\partial t} + (\mathbf{u}.\nabla)\omega = \frac{1}{\mathrm{Re}}\Delta\omega + \nabla \times [\lambda\ \chi_S(\mathbf{u}_s - \mathbf{u})]. \tag{4.1}$$

We recall that $\lambda = \nu\Phi H/k\bar{\mathbf{u}}$ essentially depends, in the inverse proportion, on the physical intrinsic permeability of the medium k which directly derives from the Darcy law $\mathbf{u} = -\frac{k}{\mu\Phi}\nabla p$.

Varying the value of λ thus directly characterizes the different media.

In this section, the vortex penalization method is applied to passive flow control around a 2D semi-circular cylinder. The control is achieved covering this obstacle with a porous coating. The expected effect of a porous medium at the solid-fluid interface is to modify the vorticity generation of the boundary layer as well as the vortex shedding, and therefore to reduce the drag force improving the aerodynamic properties of the obstacle. The Direct Numerical Simulations (DNS) are performed in the computational domain $D = [-4,\ 8] \times [-5,\ 5]$. The semi-circular cylinder has a total dimensionless diameter of $d = 1$. The backward face of the obstacle is centered at the point $(0, 0)$ (see Figure 4.1a). The total diameter of the semi-circular cylinder includes a porous layer of thickness τ, constituting the passive control device (see Figure 4.1b). According to the Brinkman's equation on which our model is based, the porosity Φ of the added layer has to be close to 1. In practice, one can consider materials like wire crimps ($\Phi \sim 0.72$), fiberglass ($\Phi \sim 0.9$), steel wool ($\Phi \sim 0.9$) or hair like texture ($\Phi \sim 0.97$).

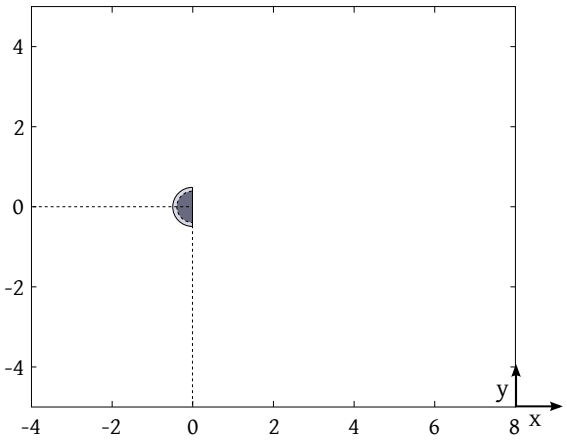

(a) Semi-circular cylinder within the computational domain.

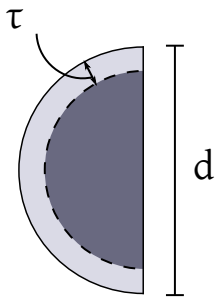

(b) Porous coating of thickness τ at the surface of the semi-circular cylinder of total diameter d.

Figure 4.1: Computational domain for flow control past a semi-circular cylinder.

4.2.1 Impacts of the porous layer on the flow

In this first part we aim to investigate the influence of the added porous layer on the flow in a natural and simple case. For this purpose we consider the following flow control device: an homogeneous porous layer of thickness $\tau = 10\%d = 0.1$ is inserted at the surface of the semi-circular cylinder, following the pattern depicted in Figure 4.1b. The λ parameter is set to 1 within this layer, which, according to the λ-convergence studies reported in Figure 3.8, represents a high permeability. The control study is realized at $Re = 550$. Based on the grid convergence study carried out in the previous chapter at this flow regime (Table 3.6), the numerical simulations are performed on a 2400×2000 grid (corresponding to $h = 0.005$).

In order to analyze the effects of our control approach, a comparison between the controlled device and the uncontrolled obstacle (that is to say the solid semi-circular cylinder with $\lambda = 10^8$), is needed. For this purpose we will systematically analyze the following diagnostics in both cases:

- Global flow quantities :
  - mean drag force ($\bar{F_x}$): we consider drag force instead of drag coefficient since the C_D formula (2.40) involves the diameter d of the obstacle which is not clearly defined because of the porous coating

  - mean enstrophy ($\bar{Z}$): the enstrophy measures the dissipation effects in the flow (see equation 2.121). A decrease of enstrophy may lead in this context to a delay of transition to turbulence.
  - Strouhal number (S_t) (see insert 4)

- Time averaged flow fields [2]:
  - mean velocity field (in the whole computational domain)
  - mean vorticity field (in the near wake)
  - mean pressure field (in the near wake)
- Instantaneous vorticity field
- Time averaged profiles:
  - mean pressure profile
  - mean velocity profile

Let us first focus on the drag production. In the uncontrolled case, the mean drag force is equal to 0.957 whereas it equals 0.695 with the added porous layer, which corresponds to a decrease of 27%. As emphasized in the literature [Bruneau et al., 2010, Bruneau et al., 2008], the main source of drag force for bluff bodies with square back is the low pressure recirculation zone in the near wake of the vertical wall. In Figure 4.2 are plotted the mean pressure profiles at the rear end of the two obstacles. One can see on this figure that the back wall pressure significantly rises in the case of the controlled obstacle compared to the uncontrolled one, thus explaining the important drag reduction.

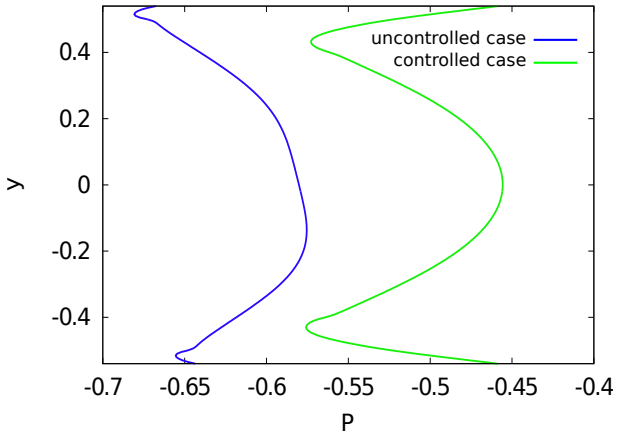

Figure 4.2: Mean pressure profiles at the rear end of the uncontrolled and the controlled semi-circular cylinder at $Re = 550$.

This drag reduction may also be qualitatively confirmed by analyzing the time averaged flow fields reported in Figure 4.3. Figure 4.3a precisely shows an increase of downstream pressure at the rear back of the controlled body. Moreover, as can be seen in Figure 4.3b, the near wake vortical structures of the controlled device are smaller, the back recirculation zone is strongly reduced and the wake dimension $\mathcal{L}$ in the crosswise direction is thinner. These features therefore explain the important drag reduction achieved with the controlled obstacle. Finally, the mean velocity of the wake clearly diminishes, leading to lower vorticity gradients (Figure 4.3c).

[2] All the mean values considered in this chapter are calculated on the time range $[\tilde{t},\ t_{\text{end}}]$, where $\tilde{t}$ denotes the time from which the flow regime is established.

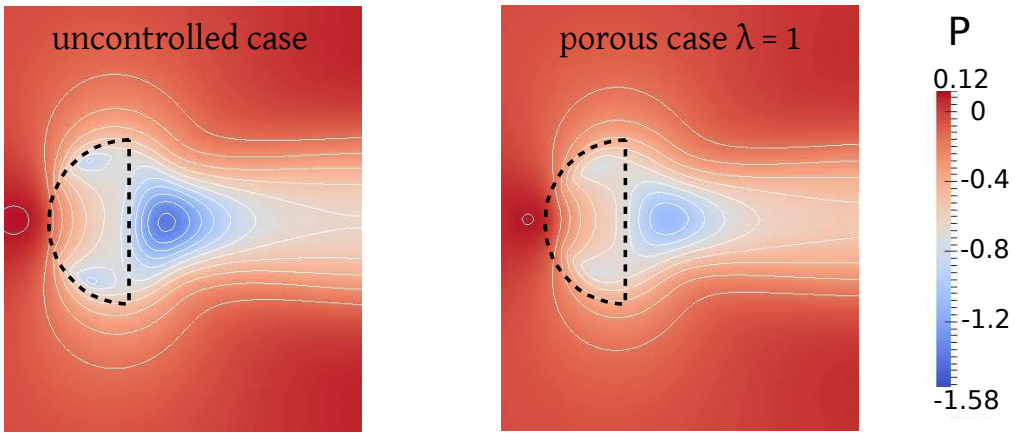

(a) Mean pressure field in the near wake

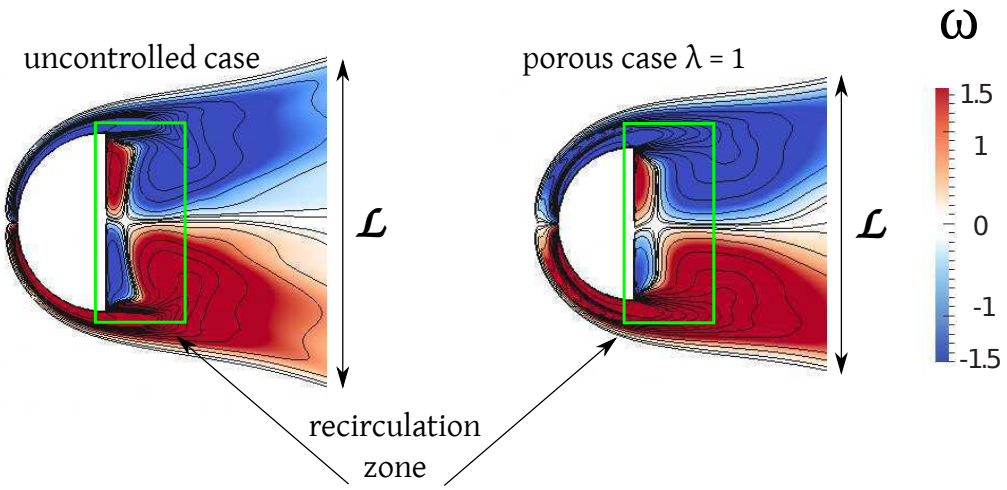

(b) Mean vorticity field in the near wake

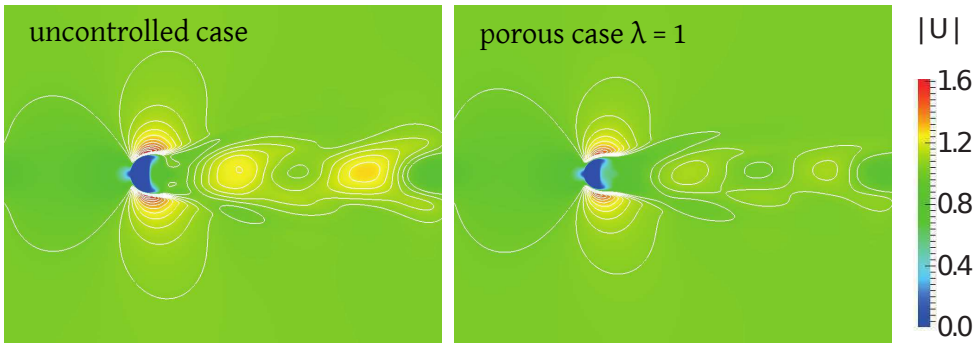

(c) Mean velocity magnitude

Figure 4.3: Different fields for flow past the uncontrolled and the controlled semi-circular cylinder at $Re = 550$.

This reduction of velocity gradients observed in the whole wake is also related to the enstrophy, that is defined in the entire computational domain. With the controlled semi-circular cylinder, we found the mean enstrophy to be reduced of 38% ($\bar{Z} = 97.5$) compared to the uncontrolled one ($\bar{Z} = 158.4$), which corresponds to a drastic diminution of the energy dissipation in the flow. Concerning the Strouhal number related to the controlled case we found a raise of 15% ($S_t = 0.284$) compared to the solid case ($S_t = 0.248$), which implies an increase of the vortex shedding frequency. This quantitative result is supported by Figure 4.4 showing the Von Kármán alleys of the two cases under study. Indeed, these instantaneous wakes indicate that the eddies are shed more frequently from the body in the controlled case. The vortex shedding is then characterized by a larger number of eddies of smaller size and lower intensity compared to the solid case.

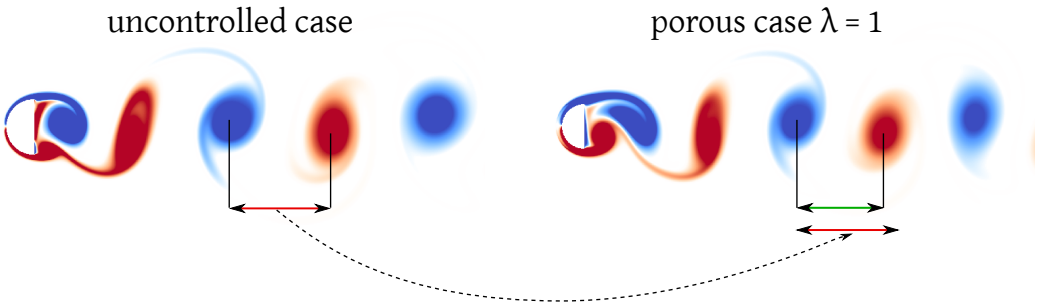

Figure 4.4: Instantaneous vorticity fields for flow past the uncontrolled and the controlled semi-circular cylinder at $Re = 550$. The frequency of the vortex shedding is higher for the controlled case than for the uncontrolled case (diminution of the inter-eddies distance).

In order to better understand the driving mechanisms of such flow control, a focus has to be made inside the porous layer. Figure 4.5 (left) reports mean velocity profiles at $x = -0.05$ (see the right hand-side of the figure to visualize the profile position). These profiles are given for three different cases: the uncontrolled case (solid case), the controlled case (porous case) and the "fluid" case. The fluid case means a semi-cylinder including a porous layer of infinite permeability ($\lambda = 0$): it actually corresponds to a smaller semi-circular cylinder of diameter $d - 2\tau$ and thus to a diminution of the Reynolds number. Here, the "fluid" case corresponds to flow past a semi-circular cylinder of diameter $d = 0.8$ at $Re = 440$.

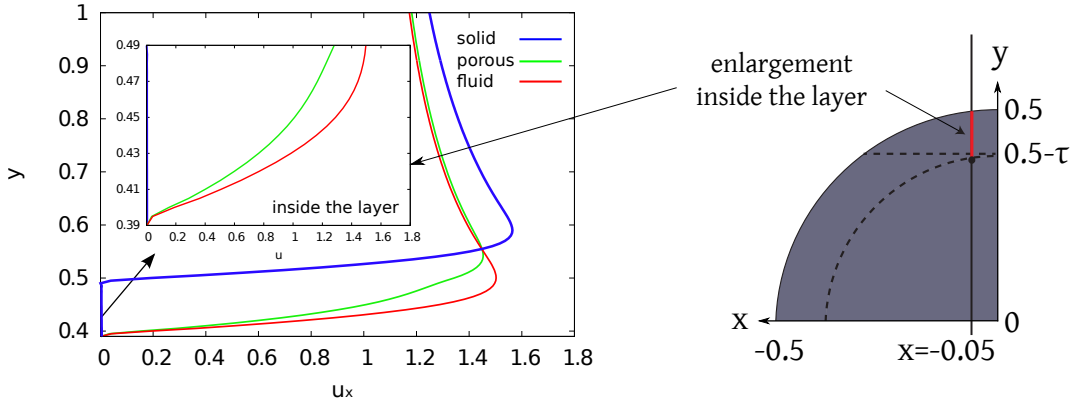

Figure 4.5: (Left) Mean profiles of the streamwise component of the velocity u_x at $x = -0.05$ for the uncontrolled case, the controlled case and the fluid case at $Re = 550$. (Right) Representation of the profiles location.

On the figure one can see that the flow has a non-zero velocity within the porous medium (green curve). It corresponds to the Darcy velocity described in Figure 2.1 in chapter 2. This velocity is bounded by the one of the uncontrolled case (blue curve), equal to 0 inside the layer, and the one of the fluid case (red curve). The regularization effects observed previously are precisely due to the establishment of a Darcy velocity inside the porous coating allowing to reduce the velocity gradients at the interface with the fluid medium.

This section offered a first insight into the type of influence that an added porous layer may have on the flow. In order to extend our control application and to analyze the performances of such passive device in a more systematic way, we will perform in the following several parametric studies based on the variation of the value of λ in the porous coating, the thickness τ and the positioning of porous material at the surface of the semi-circular cylinder. These parametric control studies will be performed for flows at transitional ($Re = 550$) and highly transitional ($Re = 3000$) regimes.

4.2.2 Parametric study with respect to the penalization parameter λ

In this section we study the influence of the porous layer permeability, in other words the value of λ, on the flow behavior and the efficiency of such a passive control. This parametric study is performed at $Re = 550$ and $Re = 3000$ with different values of the penalization factor, ranging from $\lambda = 0.125$ (very high permeability) to 10^3 (very low permeability). These values were chosen according to the outcomes of the λ-convergence study presented in Figure 3.8. The results are compared to the one corresponding to the solid ($\lambda = 10^8$) and fluid ($\lambda = 0$) cases. As in the previous part, the thickness of the coating is set in a first place to ten percent of the diameter, $\tau = 0.1$, for all the cases (see Figure 4.6). The numerical simulations are performed in the computational domain D represented in Figure 4.1 on a 2400×2000 grid ($h = 0.005$) for $Re = 550$ and on a 4800×4000 grid ($h = 0.0025$) for $Re = 3000$, according to the results of the grid convergence study presented in chapter 3 and reported in Table 3.6.

In order to analyze the effects of our control approach we take into account the same diagnostics and global flow quantities as the ones considered in the previous section.

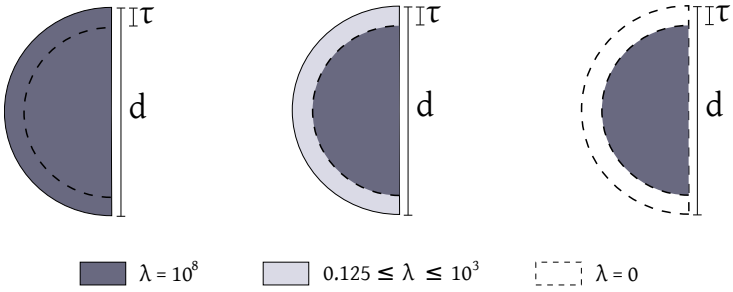

Figure 4.6: (left) Solid/uncontrolled case, (center) Porous case, (right) Fluid case.

The results of the parametric study performed at $Re = 550$ are given in Table 4.1. Concerning the Strouhal number S_t, one can notice that it continuously increases as the λ value decreases. As highlighted in our preliminary control study, the presence of a permeable layer around the obstacle induces a raise of the shedding frequency, and in the limit $\lambda \to 0$ one tends to the flow dynamics of the fluid case which is characterized by smaller vortices swirling at higher frequency (Figure 4.7). Regarding $\bar{F}_x$, Table 4.1 shows that, as expected, the drag reduces as the controlled case tends to the fluid case. Nevertheless, one can observe a slight increase of the drag force for intermediate values of λ, namely $\lambda = 100$ and $\lambda = 10$. Figure 4.8 summarizes this observation showing the evolution of the mean drag force (red curve) with respect to the λ parameter. In fact, this range of permeability values ($10 \leq \lambda \leq 100$) is responsible for a high resistance of the flow inside the layer inducing higher friction forces at the interface, and thus a higher total drag.

	$Re = 550$		
Cases	$\bar{F_x}$	$\bar{Z}$	S_t
uncontrolled case	0.957	158.4	0.248
porous case $\lambda = 1000$	0.957 (-0%)	154.0 (-3%)	0.248 (+0%)
porous case $\lambda = 100$	0.968 (+1.1%)	143.3 (-10%)	0.248 (+0%)
porous case $\lambda = 10$	0.970 (+1.4%)	114.4 (-28%)	0.252 (+1.6%)
porous case $\lambda = 5$	0.893 (-7%)	100.6 (-36%)	0.257 (+4%)
porous case $\lambda = 2.5$	0.788 (-19%)	93.7 (-41%)	0.268 (+8%)
porous case $\lambda = 1$	0.695 (-27%)	97.5 (-38%)	0.284 (+15%)
porous case $\lambda = 0.5$	0.664 (-31%)	101.9 (-36%)	0.291 (+17%)
porous case $\lambda = 0.25$	0.648 (-32%)	105.5 (-33%)	0.296 (+19%)
porous case $\lambda = 0.125$	0.643 (-33%)	107.7 (-32%)	0.298 (+20%)
fluid case	0.640	110.9	0.300

Table 4.1: Reduction effects in terms of mean drag force, mean enstrophy and Strouhal number brought by the different layer permeabilities in comparison to the uncontrolled case at $Re = 550$.

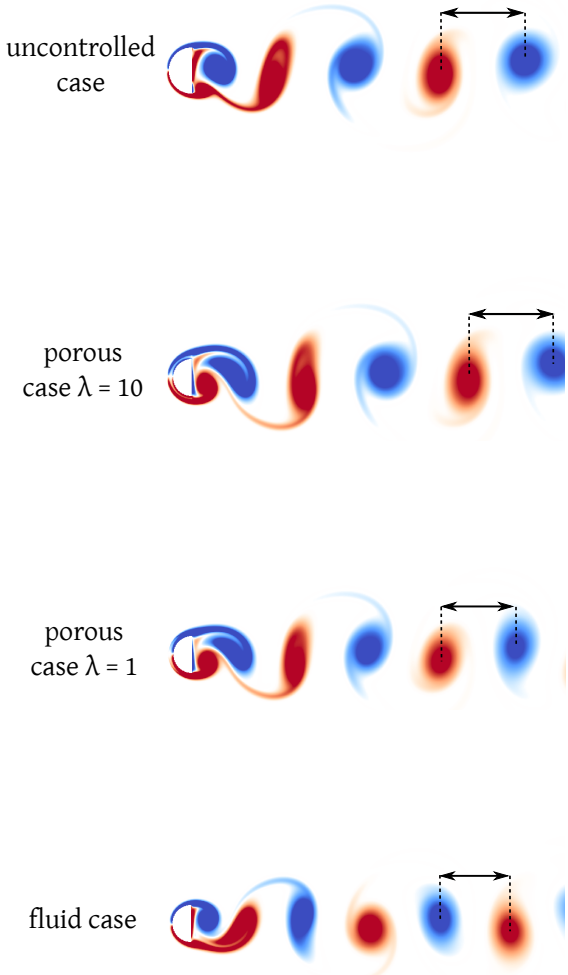

Figure 4.7: Instantaneous vorticity fields for flow past a semi-circular cylinder. The vortex shedding of the two controlled cases ($\lambda = 10$ and $\lambda = 1$, with $\tau = 0.1$) are compared to the one of the uncontrolled case and the fluid case (reduced obstacle) at $Re = 550$

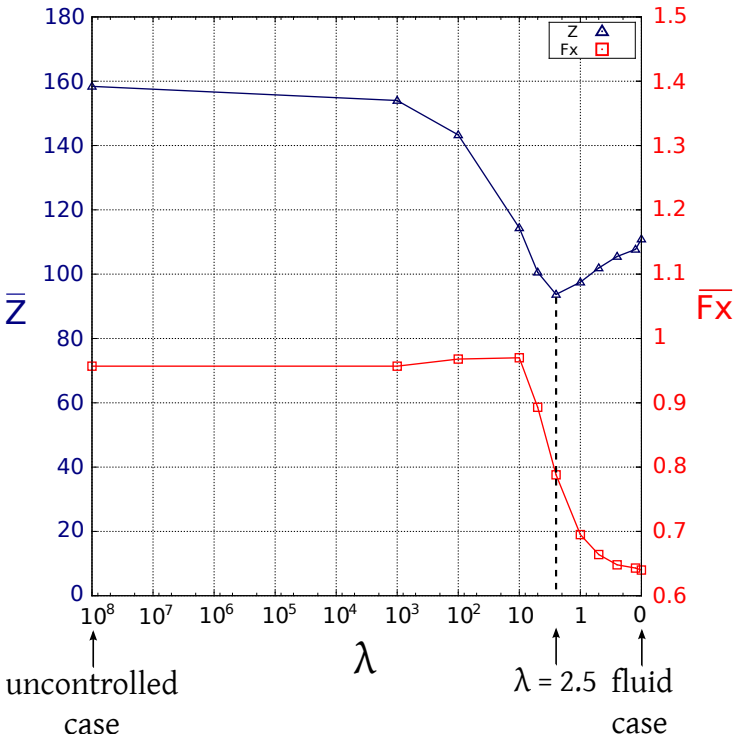

Figure 4.8: Effects of various layer permeabilities on the mean drag force $\bar{F}_x$ (red curves) and the mean enstrophy $\bar{Z}$ (blue curves) for flow past a semi-circular cylinder with $\tau = 0.1$ at $Re = 550$.

The quantitative results reported in Table 4.1 are also highlighted in Figures 4.9 and 4.10 respectively depicting the mean velocity and mean vorticity fields.

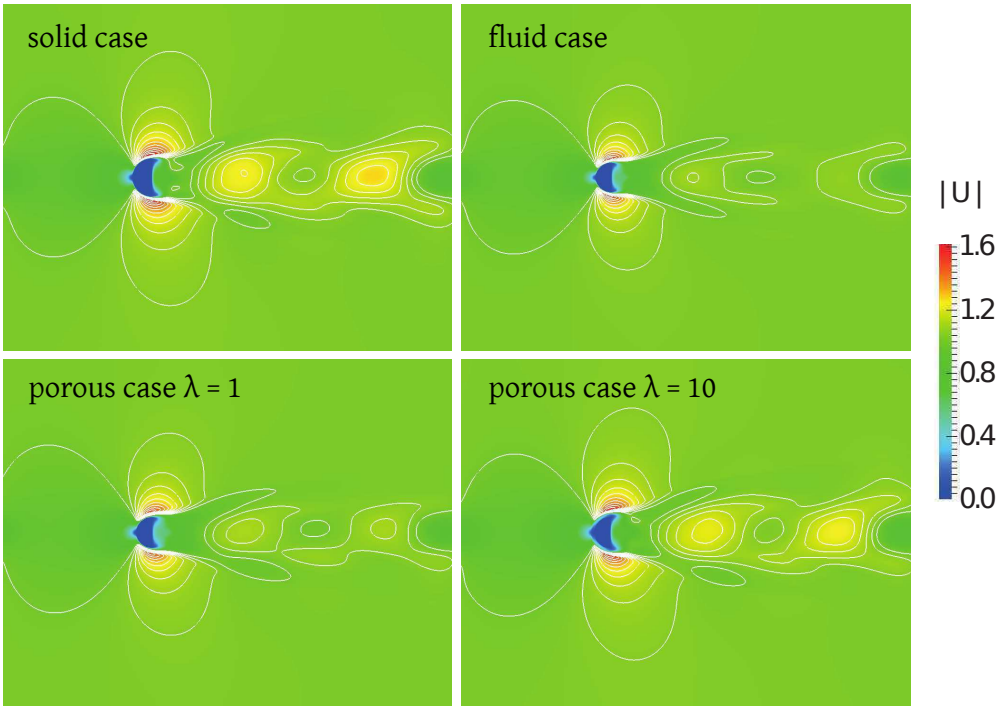

Figure 4.9: Isolines of mean velocity magnitude for the flow past a semi-circular cylinder at $Re = 550$ with $\tau = 0.1$.

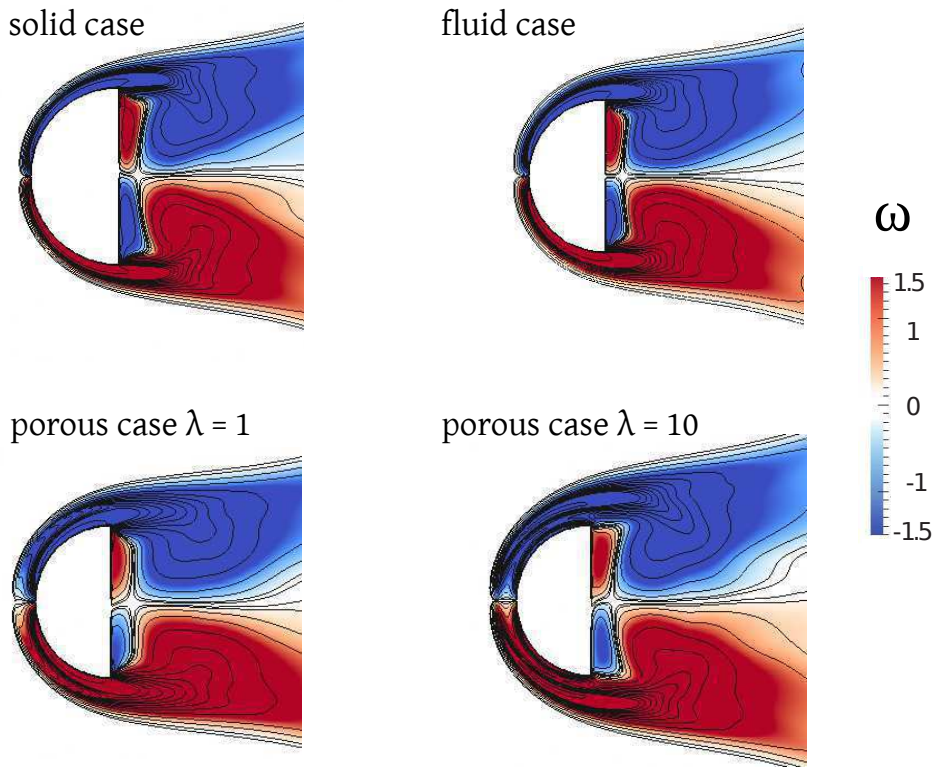

Figure 4.10: Mean vorticity fields and isolines in the near wake for the flow past a semi-circular cylinder at $Re = 550$ with $\tau = 0.1$.

Contrary to the case $\lambda = 1$ investigated in the previous part and also reported in these figures, the flow behavior obtained with $\lambda = 10$ looks very similar to the one of the uncontrolled case with an important crosswise extent of the wake (Figure 4.10) and high velocities in the flow, comparable to those of the uncontrolled case (Figure 4.9). This confirms the results given in Table 4.1 and allows us to conclude that this value of λ is not suitable at this regime to achieve drag reduction. However, with $\lambda = 10$ we obtain an important reduction of the enstrophy (-28%) which implies a delay in flow transition. This observation leads us to the analysis of control efficiency in terms of enstrophy, for which we observe a more complex behavior. Indeed, as can be seen in Table 4.1 and Figure 4.8 (blue curve), the enstrophy decreases with λ to reach an optimal value, for $lambda = 2.5$ (-41% compared to uncontrolled case). Below this λ value, the enstrophy increases again to finally reach the value corresponding to the reduced obstacle (fluid case). Furthermore, when $\lambda < 10$ then $\bar{Z}_\lambda < \bar{Z}_{\text{fluid}}$, where $\bar{Z}_\lambda$ and $\bar{Z}_{\text{fluid}}$ respectively denote the mean value of enstrophy in the controlled case and in the fluid case. It demonstrates the non-monotonic behavior of the enstrophy in the range of permeabilities taken into account in this parametric study (for all values of λ in $\{0.125, 1000\}$, $\bar{Z}_\lambda < \bar{Z}_{\text{solid}}$).

At $Re = 3000$, the evolution of the Strouhal number as a function of λ is similar to the one observed at $Re = 550$: the more permeable is the added layer, the higher is the shedding frequency (Table 4.2). This behavior is represented by the vorticity fields of Figure 4.11, where one can clearly see the benefits of the porous coating which allows to go from a chaotic wake with large eddies of strong intensity (uncontrolled case) to a time-periodic Von Kármán street composed of numerous small vortices (controlled case with $\lambda = 1$), similar to the one of the fluid case.

	$Re = 3000$		
Cases	$\bar{F_x}$	$\bar{Z}$	S_t
uncontrolled case	0.926	334.2	0.238
porous case $\lambda = 1000$	0.936 (+1%)	325.8 (-2.5%)	0.236 (-0.84%)
porous case $\lambda = 100$	0.873 (-6%)	270.0 (-19%)	0.211 (-11%)
porous case $\lambda = 10$	1.054 (+14%)	248.8 (-26%)	0.246 (+4%)
porous case $\lambda = 5$	1.048 (+13%)	211.9 (-37%)	0.282 (+19.5%)
porous case $\lambda = 2.5$	0.933 (+0.76%)	187.7 (-44%)	0.295 (+25%)
porous case $\lambda = 1$	0.870 (-6%)	236.7 (-29%)	0.313 (+33%)
porous case $\lambda = 0.5$	0.869 (-6%)	261.6 (-22%)	0.323 (+37%)
porous case $\lambda = 0.25$	0.838 (-9.5%)	302.3 (-9.5%)	0.321 (+36%)
porous case $\lambda = 0.125$	0.869 (-6%)	300.9 (-10%)	0.328 (+39%)
fluid case	0.880	319.3	0.331

Table 4.2: Reduction effects in terms of mean drag force, mean enstrophy and Strouhal number brought by the different layer permeabilities in comparison to the uncontrolled case at $Re = 3000$.

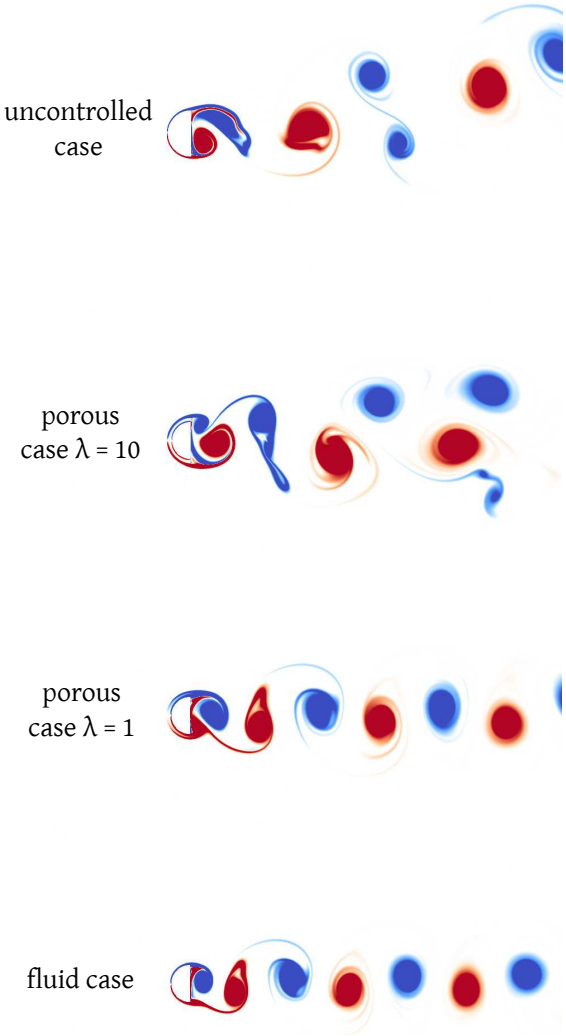

Figure 4.11: Instantaneous vorticity fields for flow past a semi-circular cylinder. The vortex shedding of the two controlled cases ($\lambda = 10$ and $\lambda = 1$, with $\tau = 0.1$) are compared to the one of the uncontrolled case and the fluid case (reduced obstacle) at $Re = 3000$.

On the other hand, the results obtained in terms of mean drag force and mean enstrophy are also comparable to those obtained at $Re = 550$, with a more pronounced behavior. Concerning the drag force, we indeed notice in Table 4.2 and Figure 4.12 that intermediate permeabilities ($\lambda \approx 10$) completely deteriorate the performances. On the contrary, below $\lambda = 5$, the drag reduction is enhanced.

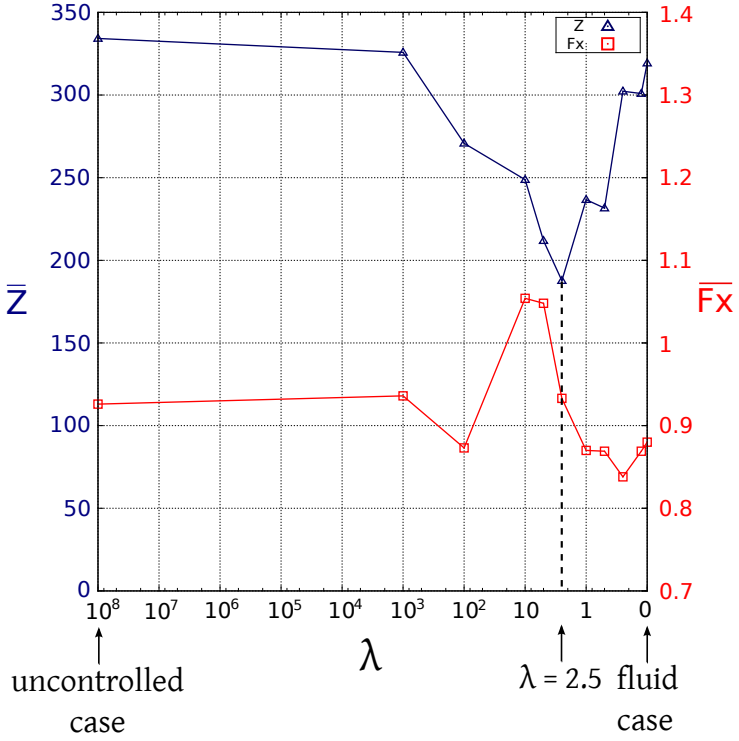

Figure 4.12: Effects of various layer permeabilities on the mean drag force $\bar{F_x}$ (red curves) and the mean enstrophy $\bar{Z}$ (blue curves) for flow past a semi-circular cylinder with $\tau = 0.1$ at $Re = 3000$.

This assessment is confirmed by Figures 4.13 and 4.14 showing on one hand low velocity gradients and a symmetric, thin and regular wake as well as small recirculation zone with the case $\lambda = 1$, whereas the case $\lambda = 10$ is responsible for a strong increase of the crosswise dimension of the wake and of the recirculation region. However, the drag reductions obtained with $\lambda < 5$ at this regime remain largely smaller than the one achieved with the same λ values at $Re = 550$. Regarding enstrophy, similarly as in the $Re = 550$ study, we identify an optimum λ value, still equal to 2.5, for which the enstrophy reaches a global minimum value leading to a reduction of 44% (Table 4.2 and Figure 4.12). In a general way, this non-monotonic behavior of the enstrophy proves that the regularization effects reported here are not due to a change of the Reynolds number, since we have for instance $\bar{Z}_{\lambda=2.5} < \bar{Z}_{\lambda=1} < \bar{Z}_{\text{fluid}}$, whereas $Re_{\lambda=2.5} > Re_{\lambda=1} > Re_{\text{fluid}}$. In fact, the introduction of a porous layer generates Kelvin-Helmoltz instabilities at the solid-porous interface. These instabilities, depicted in Figure 4.15 at $Re = 3000$ for the $\lambda = 1$ test case, change the shear forces at the interface and therefore modify the vortex shedding mechanism and the global flow dynamics. The presence of such instabilities explains in particular the qualitative and quantitative differences between the fluid case and the very permeable cases.

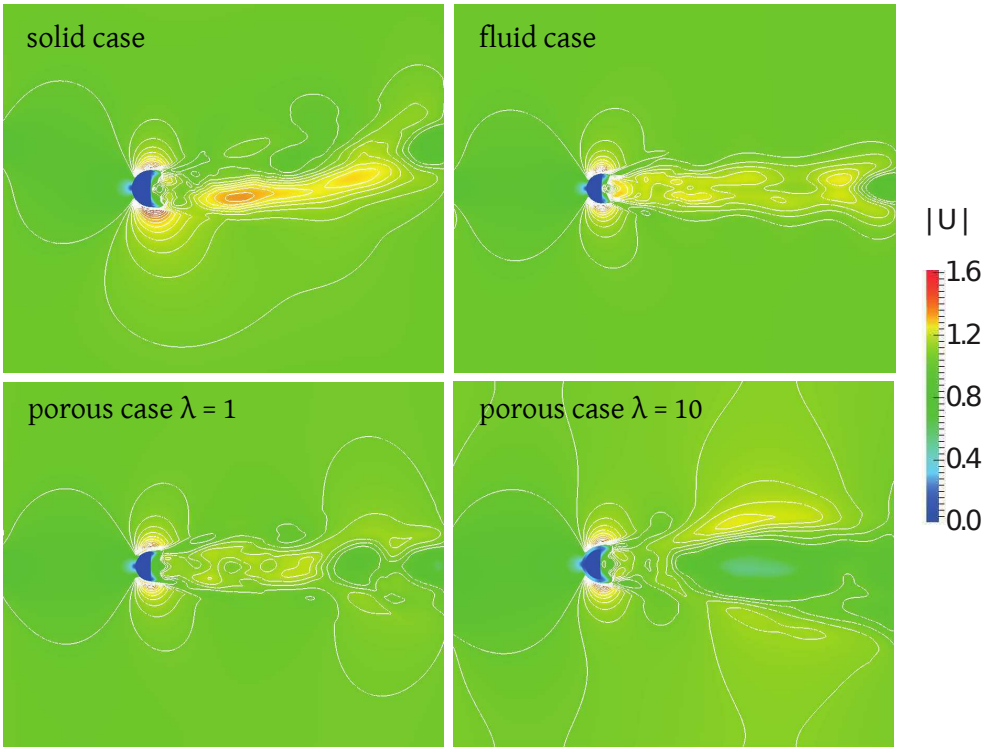

Figure 4.13: Isolines of mean velocity magnitude for the flow past a semi-circular cylinder at $Re = 3000$ with $\tau = 0.1$.

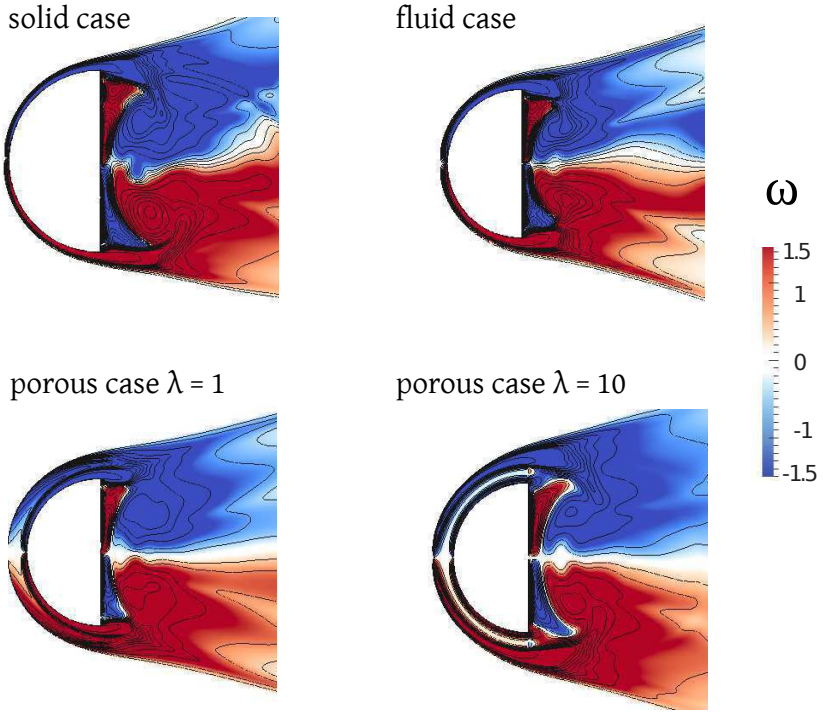

Figure 4.14: Mean vorticity fields and isolines in the near wake for the flow past a semi-circular cylinder at $Re = 3000$ with $\tau = 0.1$.

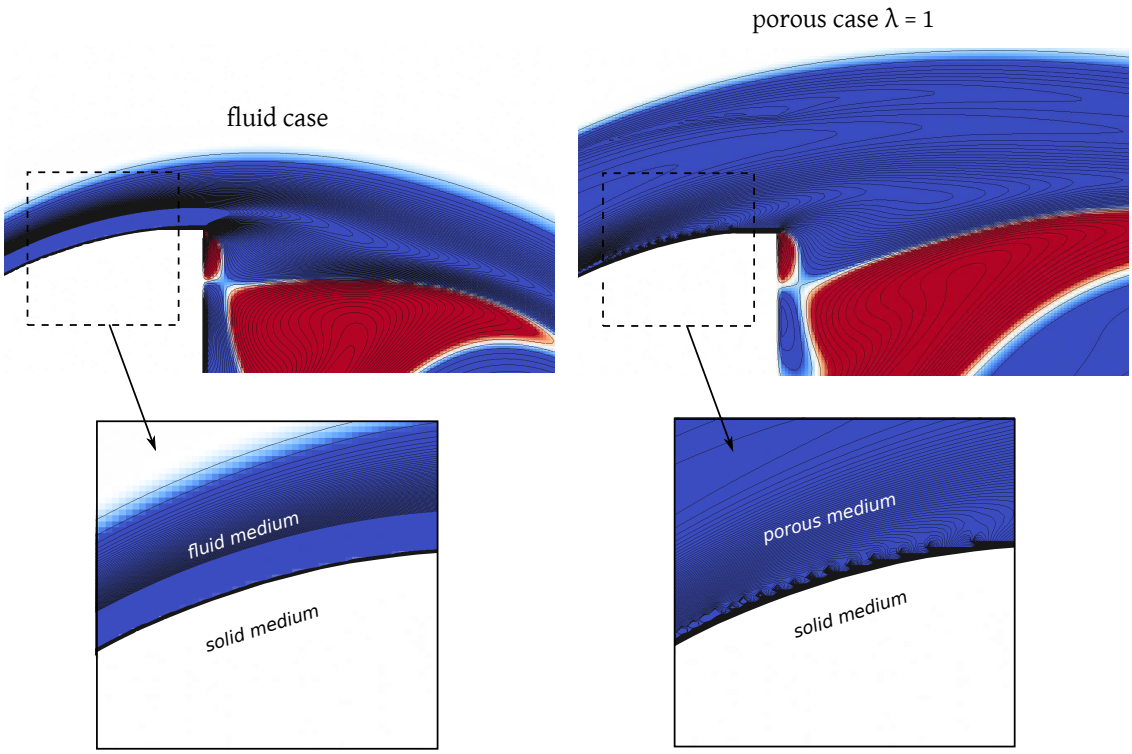

Figure 4.15: Zoom of the instantaneous vorticity fields and isolines in the vicinity of the solid interface at $Re = 3000$ for the two following cases: the fluid case (left) and the controlled case with $\lambda = 1$ and $\tau = 0.1$ (right).

Finally, an other important observation which emerges from this parametric study is the difference of behavior between the enstrophy and the drag evolution. In the presence of a porous coating, we indeed highlighted a systematic enstrophy reduction compared to the solid case, regardless of the permeability, whereas some values of λ were found to be responsible for a non negligible drag increase, especially at $Re = 3000$. This is directly due to the way these two quantities are evaluated. The enstrophy quantifies the energy dissipation of the whole system, it is therefore evaluated in the entire domain. Thus, the laminar velocities caused by the presence of the permeable layer and appearing in the vicinity of the separation points, lead to a delay in transition to turbulence and directly impact the transport of the vorticity which is regularized. On the contrary, the drag force is evaluated on the walls of the obstacle or in the vicinity of the body and is directly linked to the vorticity generation. Therefore, the high friction phenomenon caused by some permeabilities (namely intermediate permeabilities) and implying a resistance of the flow in the front part of the obstacle, is directly reported in the drag diagnostic and in the very near-wake analysis. The $\lambda = 10$ test case at $Re = 3000$ clearly illustrates these statements: one can indeed notice the beneficial effects of the permeable coating on the wake, which tends to become time-periodic and centered around the x-axis (Figure 4.11) and does not show high velocity gradients anymore (Figure 4.13). As a consequence, we achieve a reduction of enstrophy (Table 4.2). On the opposite, the effects on the very near-wake and on the drag in particular are clearly not beneficial (Table 4.2). As can be seen on Figure 4.14, the case $\lambda = 10$ shows important recirculation zones in the rear back of the solid, responsible for a pressure decrease and thus for a drag growth. Therefore, the drag forces are more sensitive to the permeability values.

To conclude this λ-parametric study we can assert that, when considering an homogeneous porous layer device, the control should be performed with high permeability coefficients ($\lambda \leq 2.5$)

in order to combine both a significant drag reduction and a regularization of the wake. However, we noticed in this analysis that even with very low values of λ, the drag and enstrophy reductions were moderate at $Re = 3000$ which was not the case at $Re = 550$. As mentioned in this section, these moderate results can be explained by the resistance experienced by the flow in the porous front part of the obstacle. This phenomenon prevents the Darcy velocity from properly settling within the porous medium before reaching the separation point, which therefore implies rather poor drag reductions. It is even more enhanced with intermediate permeabilities, for which the drag is increased compared to the uncontrolled case. A solution allowing to bypass this problem would then consist in concentrating the porous zones in the vicinity of the separation points. This point is addressed in the following section.

4.2.3 Influence of the porous layer configuration on flow control efficiency

According to the parametric study and to the final remarks of the previous section, we will study different configurations of porous coating at the surface of the semi-circular cylinder. We propose to compare the six test cases depicted in Figure 4.16. Case 0 refers to the uncontrolled case, cases 1 and 2 correspond to the homogeneous layer cases already investigated in the previous section where λ respectively equals 1 and 10, and cases 3 to 5 refer to heterogeneous cases where the porous layer is split into two regions with different permeabilities. In case 3, high permeable regions ($\lambda = 1$) are inserted at the top and bottom of the semi-circular cylinder and the front part of the porous layer is characterized by an intermediate permeability ($\lambda = 10$). In a control efficiency point of view, we expect this mixed configuration to be better than case 2 since the separation points region is treated with a high permeability. The cases 4 and 5 first appear as very interesting in terms of industrial applications. Indeed, compared to cases 1 and 2 they involve less permeable material and are much easier to industrially build than case 3 which mixes high and intermediate permeabilities. For these cases, the front part of the coating is no more permeable, but completely solid and porous layers are only placed in the two edge parts of the obstacle, which makes the practical implementation much more easier. Beyond this non negligible practical aspect, cases 4 and 5 will enable us to verify our hypothesis stating that the adding of a porous coating might be more beneficial when inserted in the region of the separation points. Their geometrical configuration will be called the "poles" configuration in the sequel.

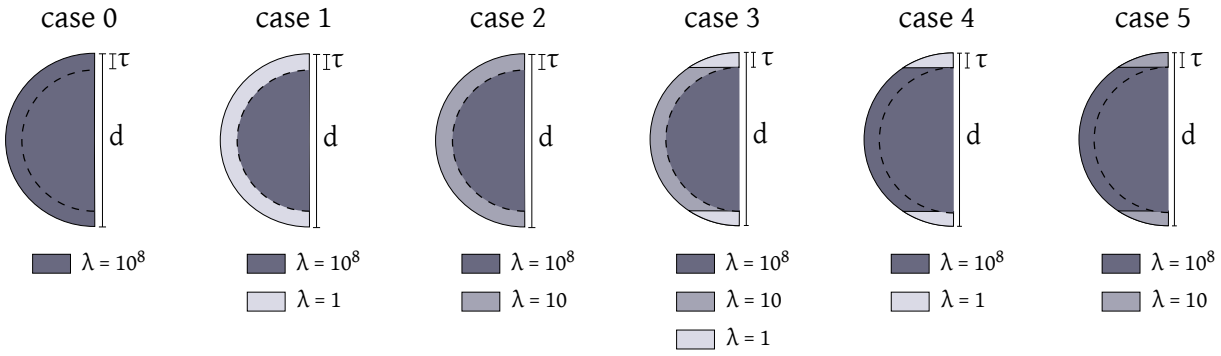

Figure 4.16: Cases 1 to 5 corresponding to different porous layer configurations. Case 0 depicts the uncontrolled case.

In a first place, the thickness of the layer is kept to $\tau = 0.1$. The asymptotic mean values of global flow quantities and the time averaged vorticity, velocity and pressure fields will be analyzed for each of the six considered devices at $Re = 550$ and $Re = 3000$.

First of all, the results reported here give further information concerning cases 1 and 2 already discussed in detail in the previous section. Indeed, Figures 4.17 and 4.18 clearly show that, contrary to case 1, a low pressure still exists at the body's back wall for case 2. These observations

on the pressure field confirm the results obtained in the previous section and reported here in Table 4.3, where we observe a drag reduction with case 1 ($\lambda = 1$) and a drag increase for case 2 ($\lambda = 10$).

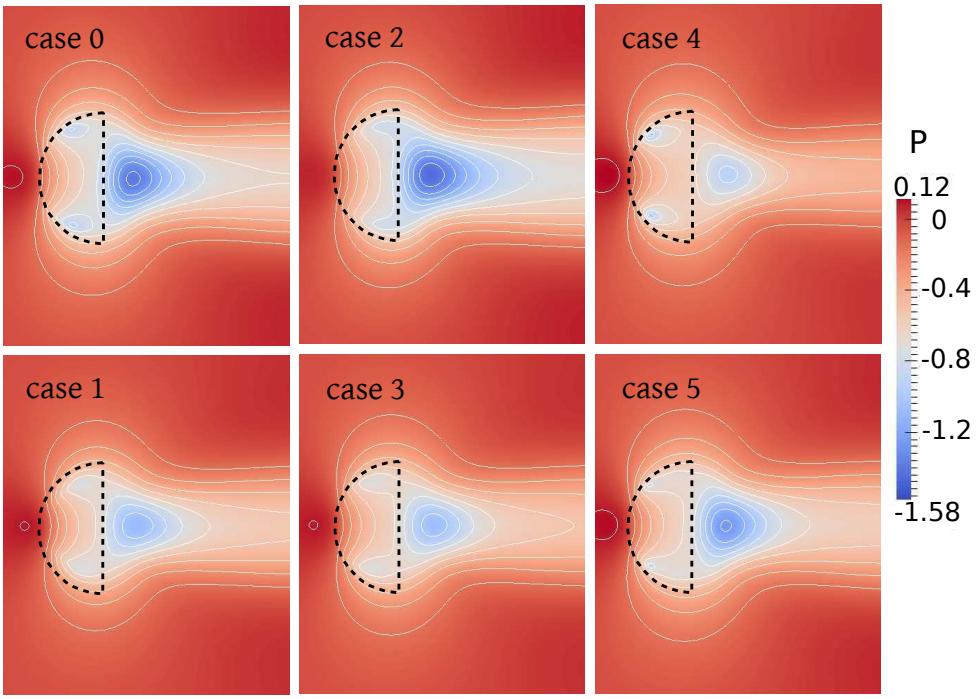

Figure 4.17: Mean pressure fields and isolines in the near wake for the flow past a semi-circular cylinder at $Re = 550$ with $\tau = 0.1$.

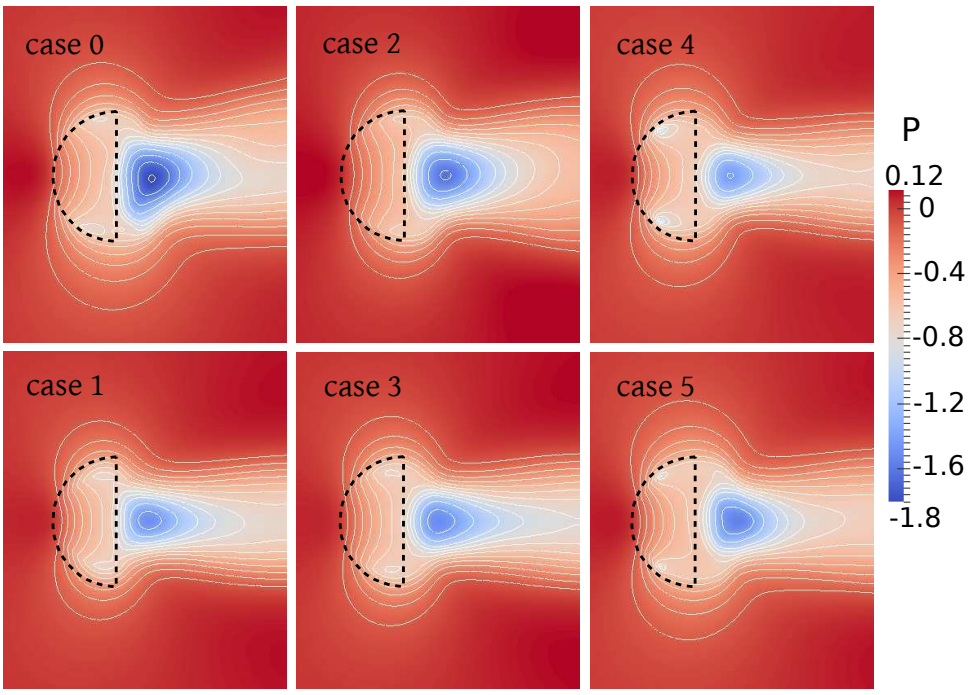

Figure 4.18: Mean pressure fields and isolines in the near wake for the flow past a semi-circular cylinder at $Re = 3000$ with $\tau = 0.1$.

Let us now focus on the heterogeneous devices. For both regime, the case 3 shows benefits

	$Re = 550$		$Re = 3000$	
$\tau = 0.1$	$\bar{F}_x$	$\bar{Z}$	$\bar{F}_x$	$\bar{Z}$
case 0 (uncontrolled case)	0.957	158.4	0.926	334.2
case 1	0.695 (-27%)	97.5 (-38%)	0.870 (-6%)	236.7 (-29%)
case 2	0.970 (+1.4%)	114.4 (-28%)	1.054 (+14%)	248.8 (-26%)
case 3	0.668 (-30%)	87.4 (-45%)	0.922 (-0.4%)	223.2 (-33%)
case 4	0.551 (-40%)	110.2 (-30%)	0.737 (-20%)	270.6 (-19%)
case 5	0.738 (-23%)	125.2 (-21%)	0.860 (-7%)	281.3 (-16%)

Table 4.3: Reduction effects brought by the different porous layer configurations in comparison to the uncontrolled case at $Re = 550$ and $Re = 3000$ with $\tau = 0.1$.

which are very comparable to those of case 1. We note that its only geometrical difference with case 2 is the presence of highly permeable poles in the layer. This change allows a diminution of the back wall recirculation zone (Figures. 4.19 and 4.20) and a noticeable increase of downstream near wall pressure (Figures 4.17 and 4.18).

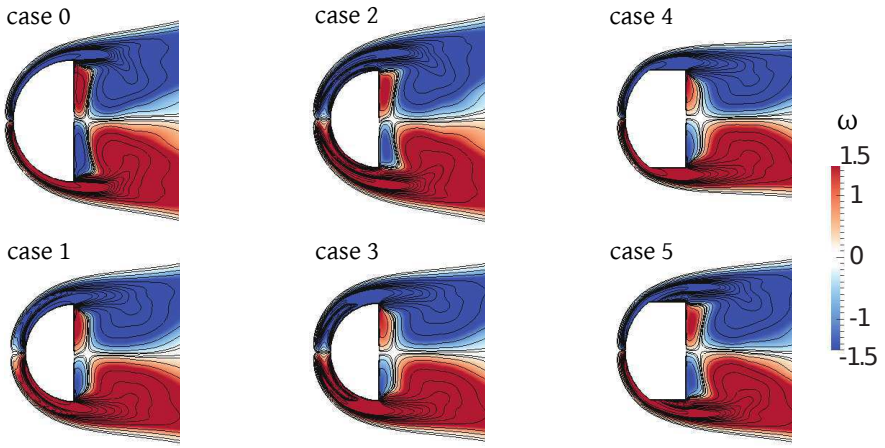

Figure 4.19: Mean vorticity fields and isolines in the near wake for the flow past a semi-circular cylinder at $Re = 550$ with $\tau = 0.1$.

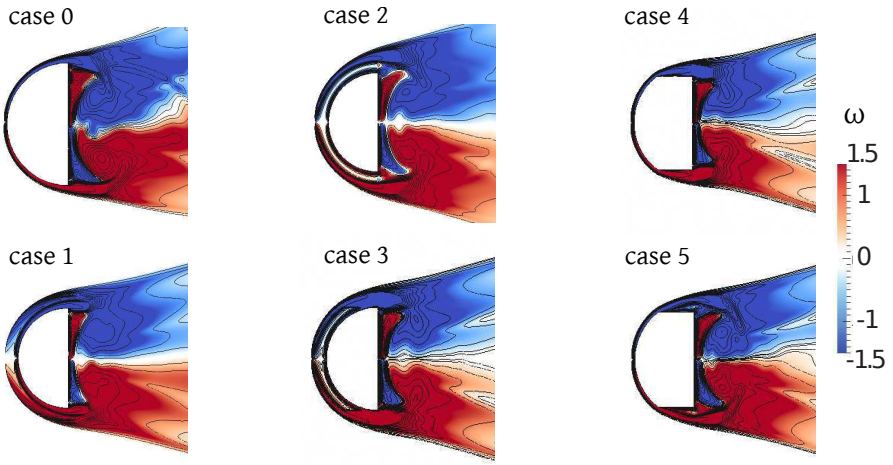

Figure 4.20: Mean vorticity fields and isolines in the near wake for the flow past a semi-circular cylinder at $Re = 3000$ with $\tau = 0.1$.

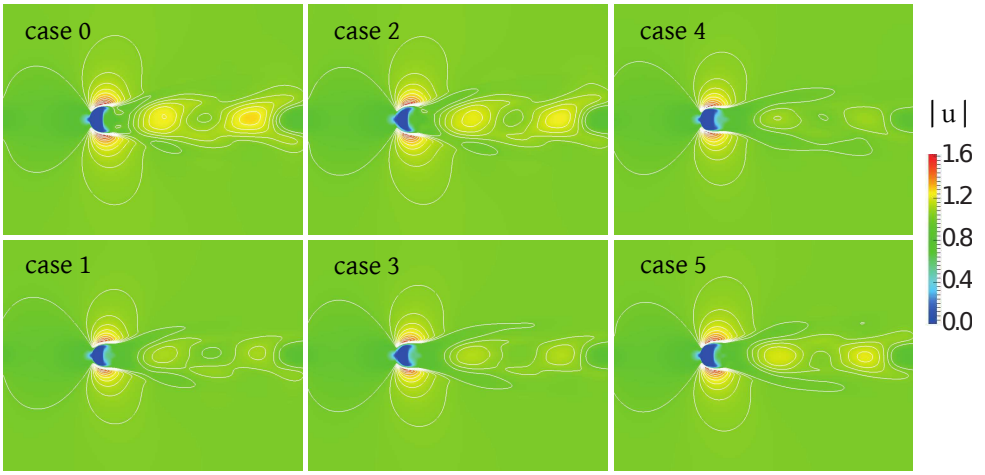

Figure 4.21: Fields and isolines of mean velocity magnitude for the flow past a semi-circular cylinder at $Re = 550$ with $\tau = 0.1$.

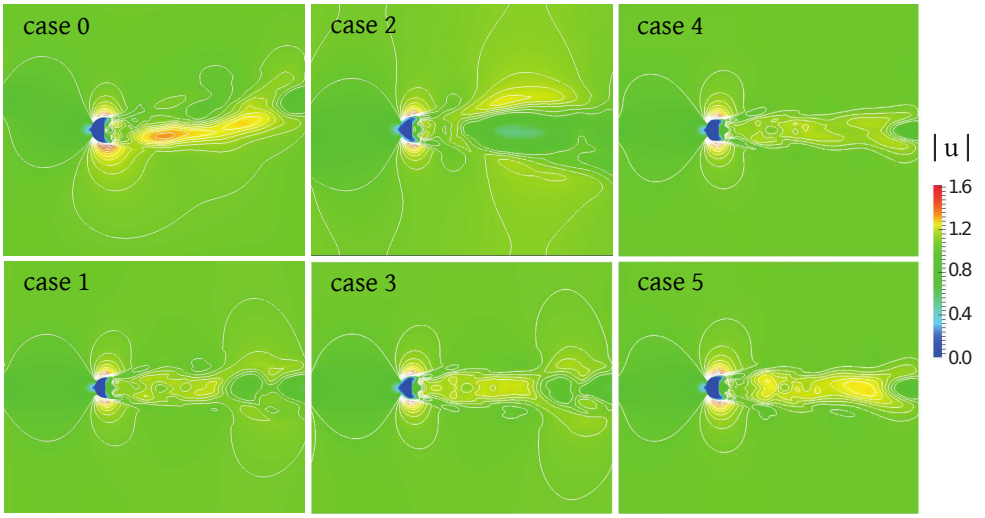

Figure 4.22: Fields and isolines of mean velocity magnitude for the flow past a semi-circular cylinder at $Re = 3000$ with $\tau = 0.1$.

The case 3 also leads to a significant regularization of the wake, showing lower velocities (Figures 4.21 and 4.22). It emerges from these observations that the reduction effects mainly come from the permeable parts located in both edges of the body, corresponding to the region where the flow separation occurs. In order to make sure of this statement, we should therefore look at devices where the permeable zone is only positioned in the vicinity of the separation points. This lead us to the study of cases 4 and 5.

For cases 4 and 5 and at both Reynolds numbers 550 and 3000, the enstrophy and the drag force undergo a tremendous decrease except for the case 5 at $Re = 3000$ where the drop of the drag force is limited to 7% because of the lower permeability of the porous layer (Table 4.3). Figures 4.17 to 4.22 confirm these results. They show a reduction of the mean velocity in the wake which becomes almost symmetrical with respect to the x-axis (Figures 4.21 and 4.22) as well as a decrease of the crosswise dimension of the two counter-rotating vortical structures at the back of the obstacle (Figures 4.19 and 4.20). Also, the near wall pressure values (Figures 4.17 and 4.18), especially for the case 4, are sensibly diminished which is in agreement with drag results.

These results emphasize the importance of the position of the permeable zones and confirm the hypothesis made from the previous λ-parametric study: the beneficial effects obtained in this study essentially come from the fact that a porous medium is inserted in the vicinity of the separation points. Moreover, its presence in the front part of the obstacle may turn to deteriorate the control performances due to the resistance effects experienced by the flow in this region. The case 4 thus definitely appears as the most efficient device to regularize the flow dynamics and more especially to reduce the drag. On the other hand, test case 5, made of intermediate permeabilities on both edges of the body, may correspond to a more realistic device compared to the very permeable poles of case 4.

4.2.4 Influence of the porous layer thickness τ on flow control efficiency

In the previous sections, the control effects were studied for different configurations using a constant porous layer thickness $\tau = 10\%d = 0.1$. In this section, the effect of the thickness for different configurations will be investigated, and a special focus will be made on thin layers in order to reduce the use of porous materials and to find out a compromise between practical constraints and control efficiency. The same test cases (see Figure 4.16) are now considered setting the thickness of the layer to $\tau = 5\%d = 0.05$ and to $\tau = 2.5\%d = 0.025$.

	$Re = 550$		$Re = 3000$	
$\tau = 0.1$	$\bar{F}_x$	$\bar{Z}$	$\bar{F}_x$	$\bar{Z}$
case 0 (uncontrolled case)	0.957	158.4	0.926	334.2
case 1	0.695 (-27%)	97.5 (-38%)	0.870 (-6%)	236.7 (-29%)
case 2	0.970 (+1.4%)	114.4 (-28%)	1.054 (+14%)	248.8 (-26%)
case 3	0.668 (-30%)	87.4 (-45%)	0.922 (-0.4%)	223.2 (-33%)
case 4	0.551 (-40%)	110.2 (-30%)	0.737 (-20%)	270.6 (-19%)
case 5	0.738 (-23%)	125.2 (-21%)	0.860 (-7%)	281.3 (-16%)

Table 4.4: Reduction effects brought by the different porous layer configurations in comparison to the uncontrolled case at $Re = 550$ and $Re = 3000$ with $\tau = 0.1$.

	$Re = 550$		$Re = 3000$	
$\tau = 0.05$	$\bar{F}_x$	$\bar{Z}$	$\bar{F}_x$	$\bar{Z}$
case 0 (uncontrolled case)	0.957	158.4	0.926	334.2
case 1	0.774 (-19%)	123.7 (-22%)	0.999 (+8%)	285.2 (-15%)
case 2	0.914 (-4%)	123.5 (-22%)	0.979 (+6%)	253.7 (-24%)
case 3	0.751 (-22%)	110.4 (-30%)	0.947 (+2%)	247.6 (-26%)
case 4	0.618 (-35%)	127.6 (-19%)	0.819 (-12%)	326.2 (-2%)
case 5	0.753 (-21%)	135.4 (-15%)	0.847 (-8.5%)	312.3 (-6.5%)

Table 4.5: Reduction effects brought by the different porous layer configurations in comparison to the uncontrolled case at $Re = 550$ and $Re = 3000$ with $\tau = 0.05$.

Tables 4.4, 4.5 and 4.6 respectively report the control performances in terms of mean global flow quantities, obtained for each case with $\tau = 0.1$, $\tau = 0.05$ and $\tau = 0.025$. Table 4.4 is actually a copy of Table 4.3. It is duplicated here to facilitate the comparisons between the different cases. For both regimes $Re = 550$ and $Re = 3000$, when comparing Tables 4.4, 4.5 and 4.6, a slight decrease of control effects is observed when diminishing the thickness of the porous coating. This can be explained looking at the mean profiles of the streamwise component of the velocity, u_x at $x = -0.05$ plotted in Figures 4.23 and 4.24.

These profiles show higher acceleration of the flow field inside the layer when its thickness drops, inducing higher velocity gradients in the vicinity of the solid-porous-fluid interface and

	$Re = 550$		$Re = 3000$	
$\tau = 0.025$	$\bar{F_x}$	$\bar{Z}$	$\bar{F_x}$	$\bar{Z}$
case 0 (uncontrolled case)	0.957	158.4	0.926	334.2
case 1	0.821 (-14%)	139.3 (-12%)	1.011 (+9%)	318.4 (-5%)
case 2	0.879 (-8%)	134.5 (-15%)	1.018 (+10%)	283.7 (-15%)
case 3	0.824 (-14%)	129.6 (-18%)	0.929 (+0.4%)	271.1 (-19%)
case 4	0.768 (-20%)	140.2 (-11%)	0.806 (-13%)	331.4 (-0.8%)
case 5	0.810 (-15%)	143.4 (-10%)	0.828 (-10.5%)	320.6 (-4%)

Table 4.6: Reduction effects brought by the different porous layer configurations in comparison to the uncontrolled case at $Re = 550$ and $Re = 3000$ with $\tau = 0.025$.

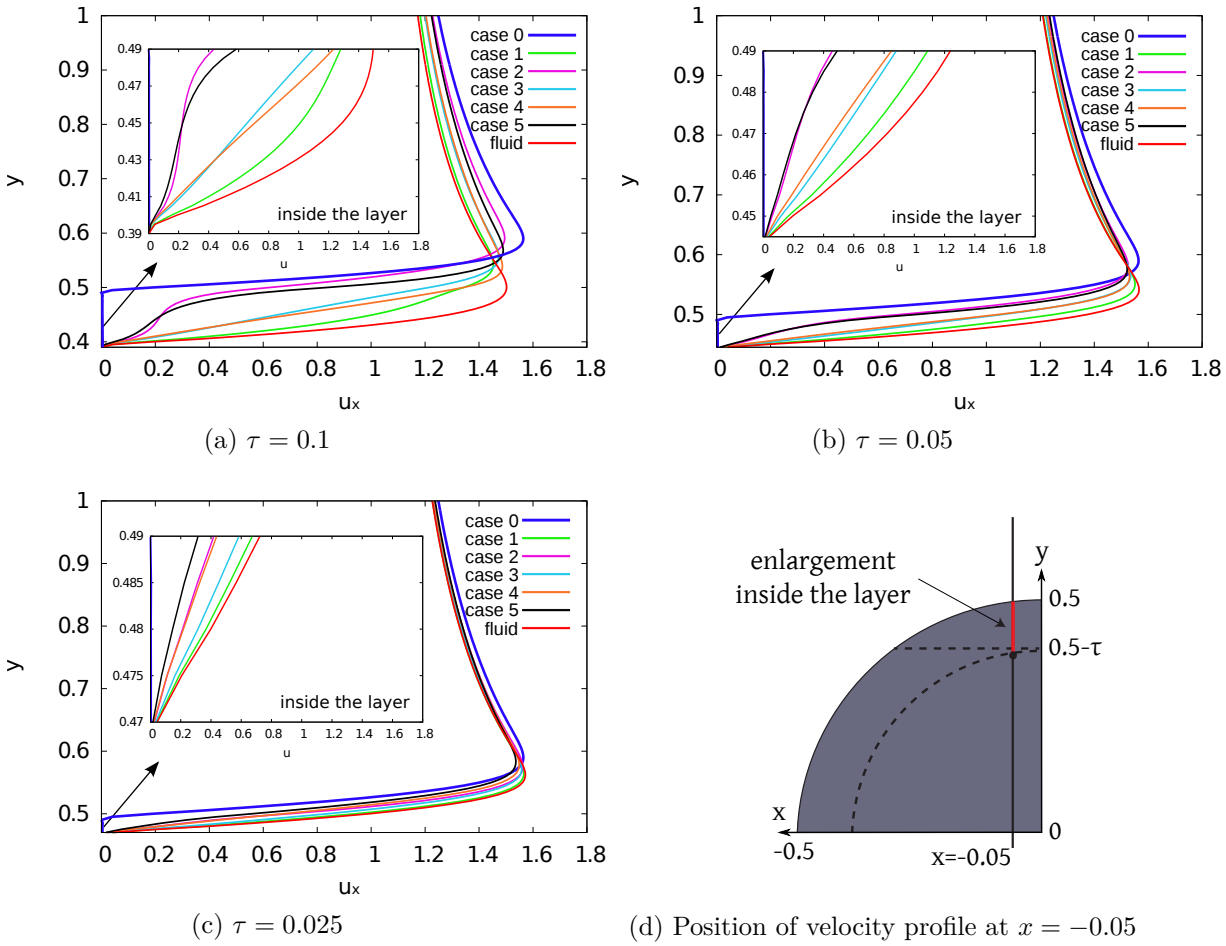

(a) $\tau = 0.1$

(b) $\tau = 0.05$

(c) $\tau = 0.025$

(d) Position of velocity profile at $x = -0.05$

Figure 4.23: Mean profiles of the streamwise component of the velocity u_x at $x = -0.05$ for different porous layer thicknesses τ at $Re = 550$. Picture (d) gives the pattern of profile configuration at $x = -0.05$ showing the location of the profiles enlargement inside the layer proposed in (a), (b) and (c).

make the vortex shedding occurring earlier, resulting in a little reduction of beneficial effects. Also, Figure 4.25 shows a direct correlation at $Re = 550$ between the drag reduction achieved with the different cases and the related back wall pressure forces: when the drag drops, the back wall pressure rises. This fact is more unstable for the $Re = 3000$ as the flow is highly transitional (Figure 4.26). Furthermore, for the later flow regime, decreasing the layer thickness in cases 1, 2 and 3 deteriorates the drag performances. This can be explained by the fact that the flow velocity significantly slows down inside the thin layer compared to the thick one (Figure 4.24) thus increasing the skin friction effects and so the drag forces.

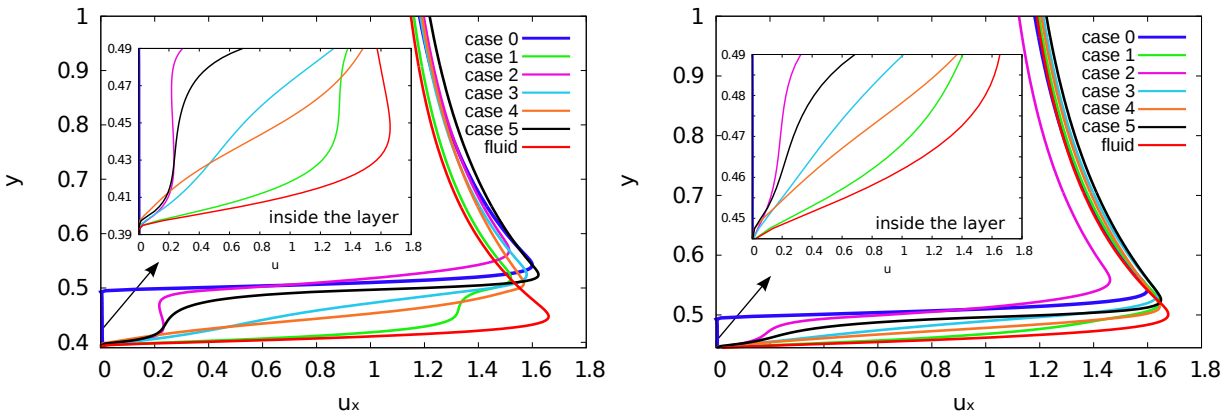

(a) $\tau = 0.1$ (b) $\tau = 0.05$

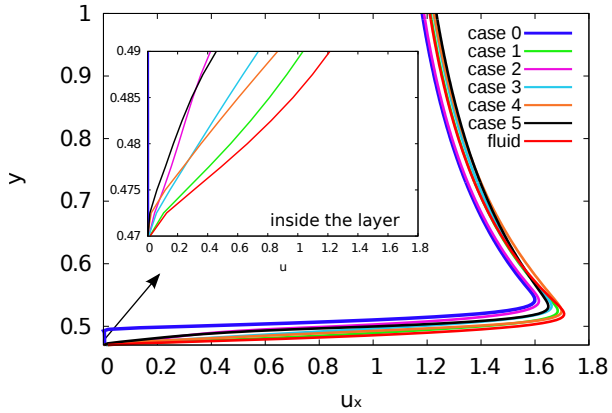

(c) $\tau = 0.025$

Figure 4.24: Mean profiles of the streamwise component of the velocity u_x at $x = -0.05$ for different porous layer thicknesses τ at $Re = 3000$ (see Figure 4.23d for profiles location.)

Now let us focus on cases 4 and 5. One can observe in Tables 4.4, 4.5, 4.6 that case 4 remains the best control device in terms of drag reduction, regardless of the coating thickness and Reynolds number. As discussed in the previous section, this is due to the fact that the front part of the obstacle is completely solid and that highly permeable zones are precisely located in the vicinity of the boundary layer separation points where the shedding starts. For both cases 4 and 5, Figures 4.23 and 4.24 show a uniform and relatively low acceleration of the flow field inside the layer, which does not change very much between the three different thicknesses. This explains why for cases 4 and 5 the decrease of drag and enstrophy remains important for thinner porous layers. As the case 5 is maybe the most practical benchmark (more than all other cases since the porous materials with moderate permeability and edge locations are easier to handle for the manufacturing of a real device), its control efficiency has to be studied attentively. Table 4.6 shows that at $Re = 550$ the drag reduction achieved with case 5 and $\tau = 0.025$ is equal to -15% which represents a strong diminution. The most interesting phenomenon arises at $Re = 3000$. At this regime, the control efficiency of case 5 is inversely proportional to the porous layer thickness τ. Indeed, Tables 4.4, **??** and 4.6 respectively report drag reductions of -7%, -8.5% and -10.5%. This promising assessment seems to be due to the fact that the flow resistance inside a thin porous layer is less important than in a thicker layer but the shedding is still well tuned thanks to the position of porous coatings in the body corners.

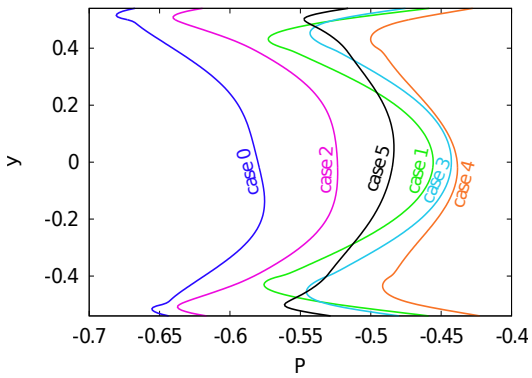

(a) $\tau = 0.1$

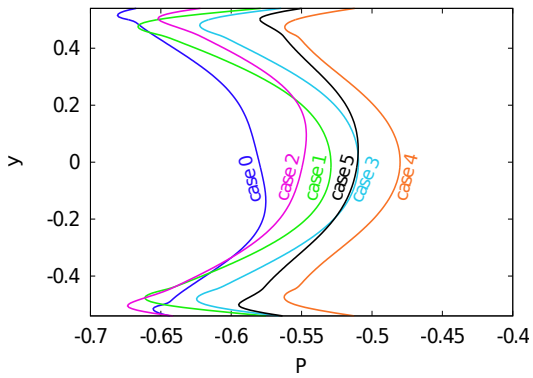

(b) $\tau = 0.05$

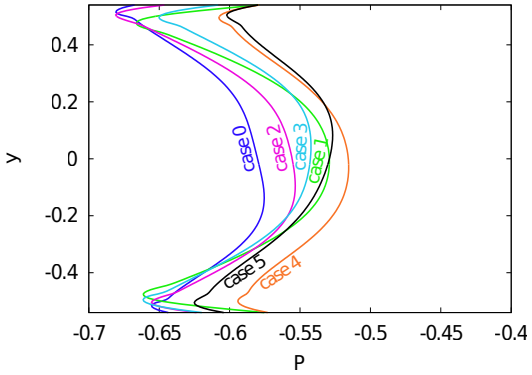

(c) $\tau = 0.025$

Figure 4.25: Mean pressure profiles at the rear end of the body at $Re = 550$.

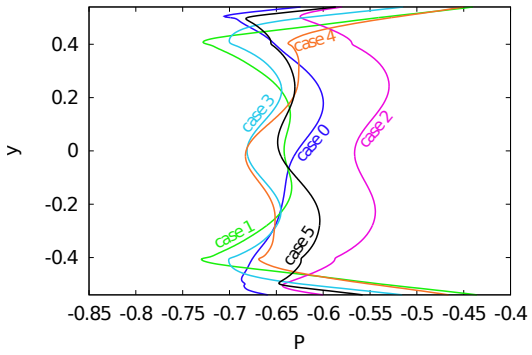

(a) $\tau = 0.1$

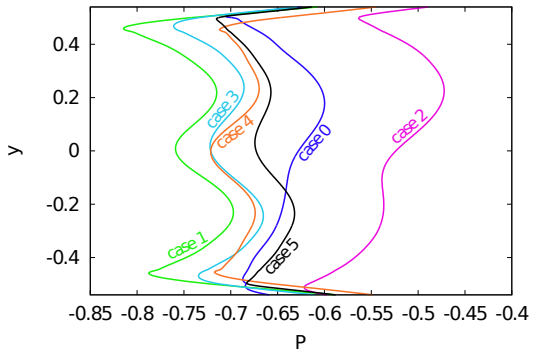

(b) $\tau = 0.05$

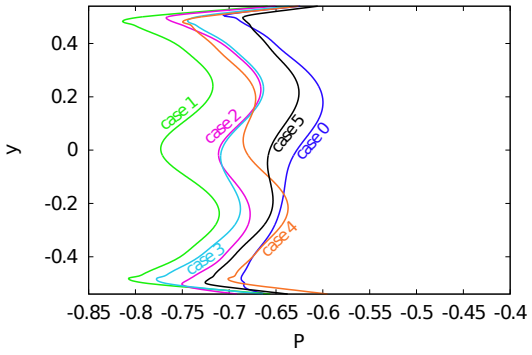

(c) $\tau = 0.025$

Figure 4.26: Mean pressure profiles at the rear end of the body at $Re = 3000$.

The results obtained throughout this preliminary two-dimensional study are recapitulated in the following list. They stand for the transitional and the highly transitional regime:

- ✓ When considering an homogeneous porous layer device covering the whole surface of the semi-circular cylinder, the permeability should be set to high values ($\lambda \leq 2.5$) in order to combine significant drag and enstrophy reduction.
- ✓ The best porous layer configuration in terms of global flow regularization is the "porous poles" configuration. Such passive flow control device concentrates the porous parts in the vicinity of the separation points, thus preventing the flow-resistance effects in the front part of the body.
- ✓ In general, reducing the thickness of the porous coating softens the control performances, or even deteriorates them (in the case of the homogeneous porous layer for example). Nevertheless, the "porous poles" configuration still provides significant drag reductions with small thicknesses.

Taking into account these observations, a more realistic study is now carried out in the three-dimensional case.

4.3 Passive flow control past a 3D hemisphere

The vortex penalization method is now used to discretize the three-dimensional penalized Navier-Stokes equations 2.21-2.22 and is applied to passive flow control around a 3D hemisphere. The two different Reynolds numbers carried out in the present study are $Re = 300$ and $Re = 1000$. These choices are based on the available reference results about flows past a sphere or a hemisphere from which we could perform validations in chapter 3. These validations indeed enabled us to identify the mesh sizes allowing to account for the correct flow behaviors at these two Reynolds numbers, corresponding to two different flow regimes.

The direct numerical simulations are performed in a computational domain $D = [-2,\ 8.24] \times [-2.56,\ 2.56] \times [-2.56,\ 2.56]$. The hemisphere has a diameter d equal to 1 and its rear back surface is centered at the point $(0, 0, 0)$. According to the convergence study and the validation results reported in section (3.2.2), the simulations at $Re = 300$ and $Re = 1000$ are carried out setting the grid resolution to $512 \times 256 \times 256$ ($h = 0.02$) and $1024 \times 512 \times 512$ ($h = 0.01$) respectively. The time step is adaptive and defined according to equation 2.72. As in the validation simulations, a perturbation is applied to the flow between $T = 3$ and $T = 4$ in order to trigger the instability (see section (3.2.2)).

4.3.1 Influence of the porous layer configuration and permeability on flow control efficiency

Following the same process as in 2D, the control around the hemisphere is achieved covering the obstacle with a porous coating for which different geometrical configurations are considered. These configurations are depicted in Figure 4.27, where case 0 refers to the uncontrolled case, case 1 contains a porous layer on the whole hemisphere surface, case 2 involves two porous poles on top and bottom of the body, case 3 contains a porous zone corresponding to the revolution of the previous poles in the z-direction, case 4 implements a thin porous ring and finally the "fluid case" corresponds to the hemisphere of diameter $d - 2\tau$. We note that case 1 and case 3 respectively represent the three-dimensional counterpart of the "homogeneous layer" (cases 1-2 in Figure 4.16) and "poles" configuration (cases 4-5 in Figure 4.16) handled in 2D . In the present simulations, the porous areas of cases 1, 2, 3 and 4 will be modeled setting λ to 1 or 10. In a first place, the thickness of the coating is set to $\tau = 0.1$ for all the cases.

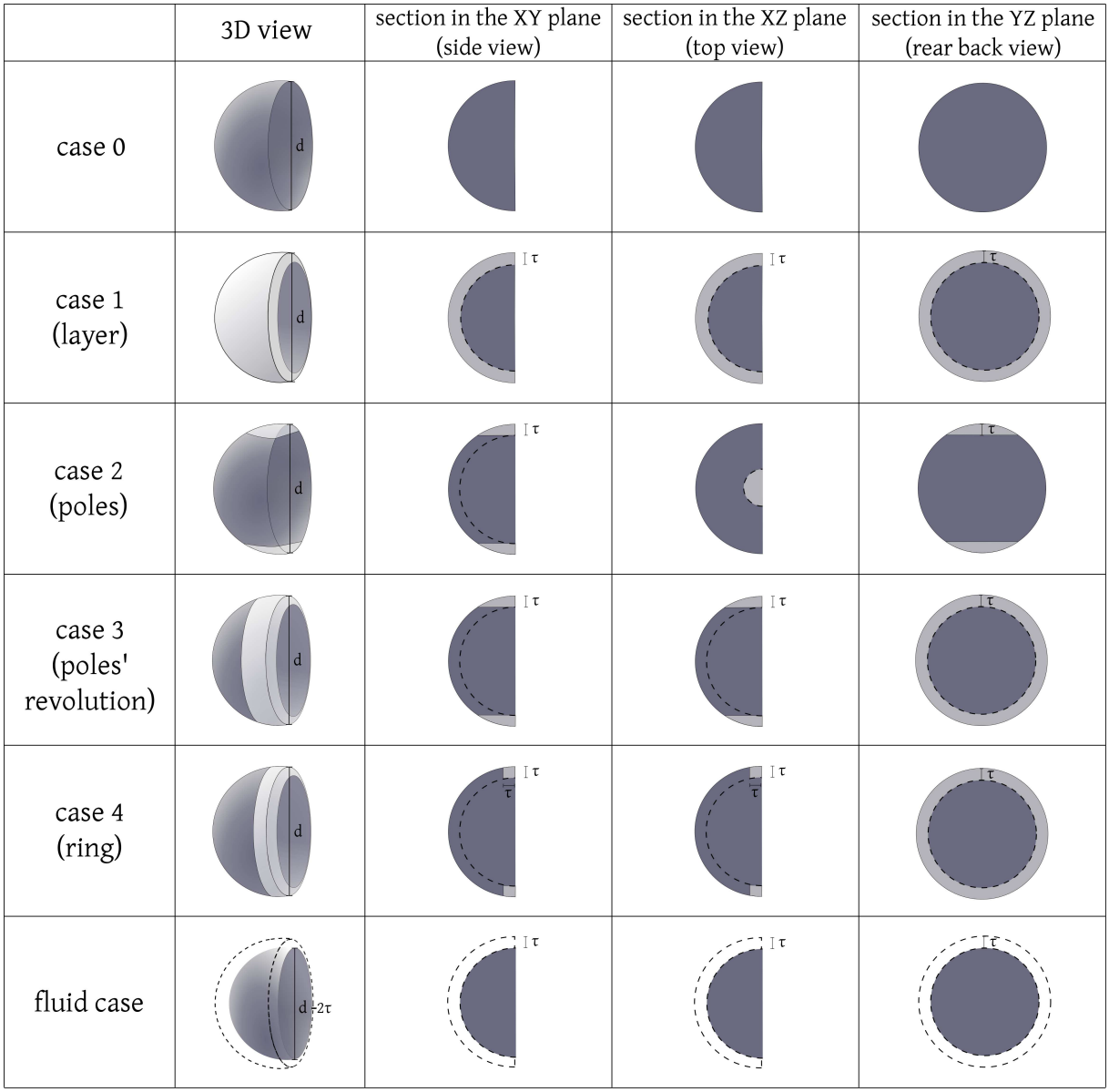

Figure 4.27: Cases 1 to 4 corresponding to different porous layer configurations. Case 0 depicts the uncontrolled case and "fluid case" corresponds to the case of a smaller hemisphere of diameter $d - 2\tau$.

4.3.1.1 Numerical results for $Re = 300$

The flow control results are first analyzed for $Re = 300$, fixing $\lambda = 1$ within the porous areas. At this regime, the less efficient passive control device is the case 4. Indeed, as reported in Table 4.7 and Figure 4.28, the drag reduction induced by the ring configuration is particularly moderated (-1.4%) and concerning the enstrophy, one can notice a slight increase compared to the uncontrolled case (+0.4%).

$\lambda = 1,\ \tau = 0.1$	$\bar{F_x}$	$\bar{Z}$	S_t
case 0	0.285	73.0	0.134
case 1	0.246 (-14%)	49.6 (-32%)	0.140 (+4.5%)
case 2	0.269 (-7%)	69.0 (-5.5%)	0.087 (-35%)
case 3	0.224 (-21%)	55.0 (-25%)	0.140 (+4.5%)
case 4	0.281 (-1.4%)	73.3 (+0.4%)	0.140 (+4.5%)
fluid case	0.189	49.8	0.158

Table 4.7: Reduction effects brought by the different porous layer configurations in comparison to the uncontrolled case at $Re = 300$ with $\lambda = 1$ within the permeable regions and $\tau = 0.1$.

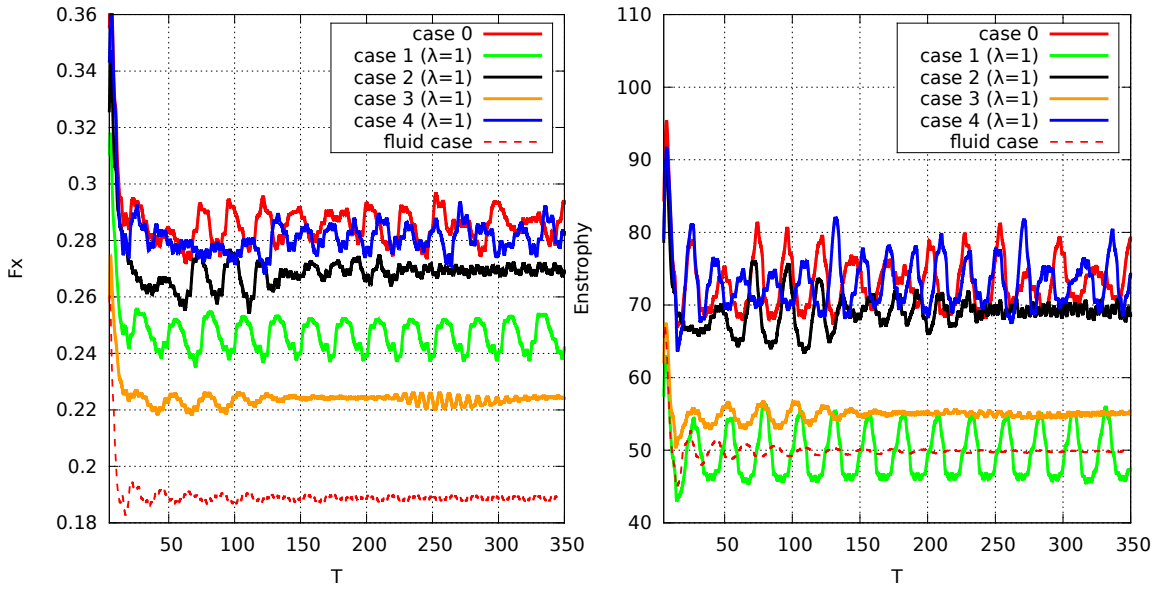

(a) History of drag force

(b) History of enstrophy

Figure 4.28: Effects of various layer configurations on drag force (a) and enstrophy (b) for flow past a hemisphere at $Re = 300$, with $\lambda = 1$ within the permeable regions and $\tau = 0.1$.

The poor performance of this device is corroborated by Figure 4.29, showing the time-averaged vorticity magnitude in the domain. On this figure one can indeed see that the mean wake obtained with case 4 is very similar to the one obtained with case 0. The phase diagram $(F_y,\ F_z)$ plotted in Figure 4.30 also confirms that even with a porous ring the flow remains chaotic and do not turn to become time-periodic. This statement is also verifiable with Figure 4.28. The phase diagram related to case 4 is moreover very comparable to the one of the uncontrolled case. Finally, the instantaneous 3D vorticity field $|\boldsymbol{\omega}|$ of case 4, presented in Figure 4.31, shows that the wake is thick and not planar symmetric. The lack of efficiency of the porous ring can be explained by the fact that it is too close to the back wall edge and does not offer a clear entrance area for the upstream flow inside the porous part (see the side view and top view of case 4 in Figure 4.27). This makes the adding of such device almost useless.

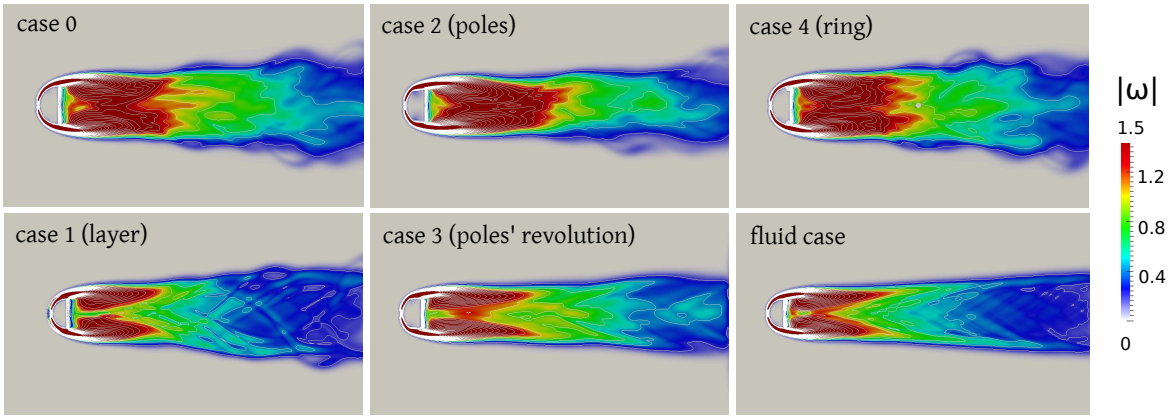

(a) XY plane

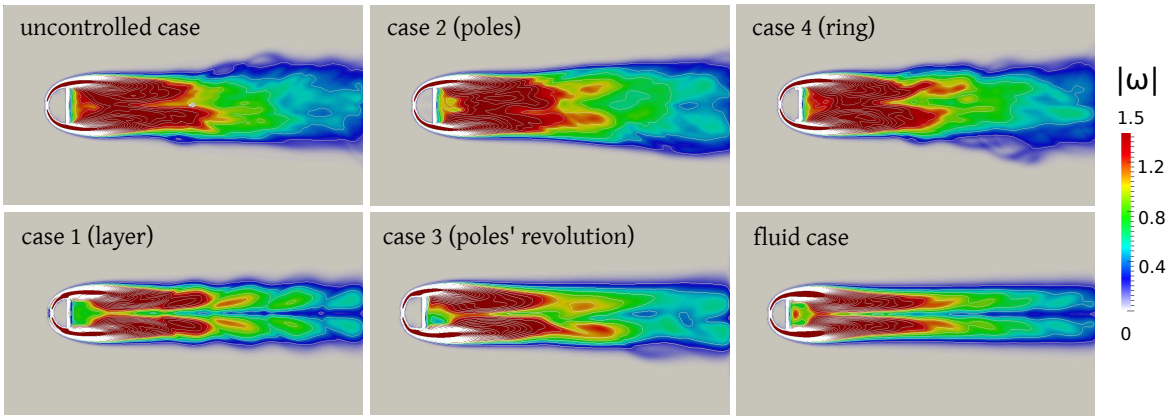

(b) XZ plane

Figure 4.29: Effects of various layer configurations on mean vorticity magnitude for flow past a hemisphere at $Re = 300$, with $\lambda = 1$ within the permeable regions and $\tau = 0.1$.

According to Table 4.7 and Figure 4.28, the case 1 is an efficient device to reduce drag (-14%) and more especially enstrophy (-32%). The mean wake related to this type of controlled hemisphere is still relatively thick in the XY plane (although the vorticity intensity of the eddies is strongly decreased compared to case 0) but it shows a perfect symmetry in the XZ plane (Figure 4.29). This planar symmetry is confirmed by Figure 4.30 showing for case 1 a phase diagram centered around $F_z = 0$. This diagram also indicates an emerging time-periodicity in the solution which is indeed confirmed by Figure 4.28. The representation of the 3D vorticity field in Figure 4.31 clearly highlights the capability of the homogeneous porous layer to regularize the flow. We can notice that the result is very close to the one obtained with the fluid case, that is to say with the hemisphere of diameter $d - 2\tau = 0.8$, for which the actual Reynolds number is equal to 240. Let us recall that in the validation study performed in the case of flow past a hemisphere at $Re = 250$, the flow was indeed shown to be periodic and planar symmetric (see section (3.2.2.2)). The efficiency of case 1 can be explained by the fact that the whole porous layer acts as a damper and regularizes the flow.

The results obtained with the case 2 are much more moderated. Indeed, although the presence of porous poles tends to make the wake periodic (Figure 4.30) and planar symmetric (Figure 4.29b), high vorticity values can still be observed (Figure 4.29), and finally the drag force and the enstrophy only reduce respectively of 7% and 5.5% compared to the uncontrolled case (Table 4.7 and Figure 4.28). The case 2 therefore has a positive effect but its action area remains too small compared to the whole separation zone.

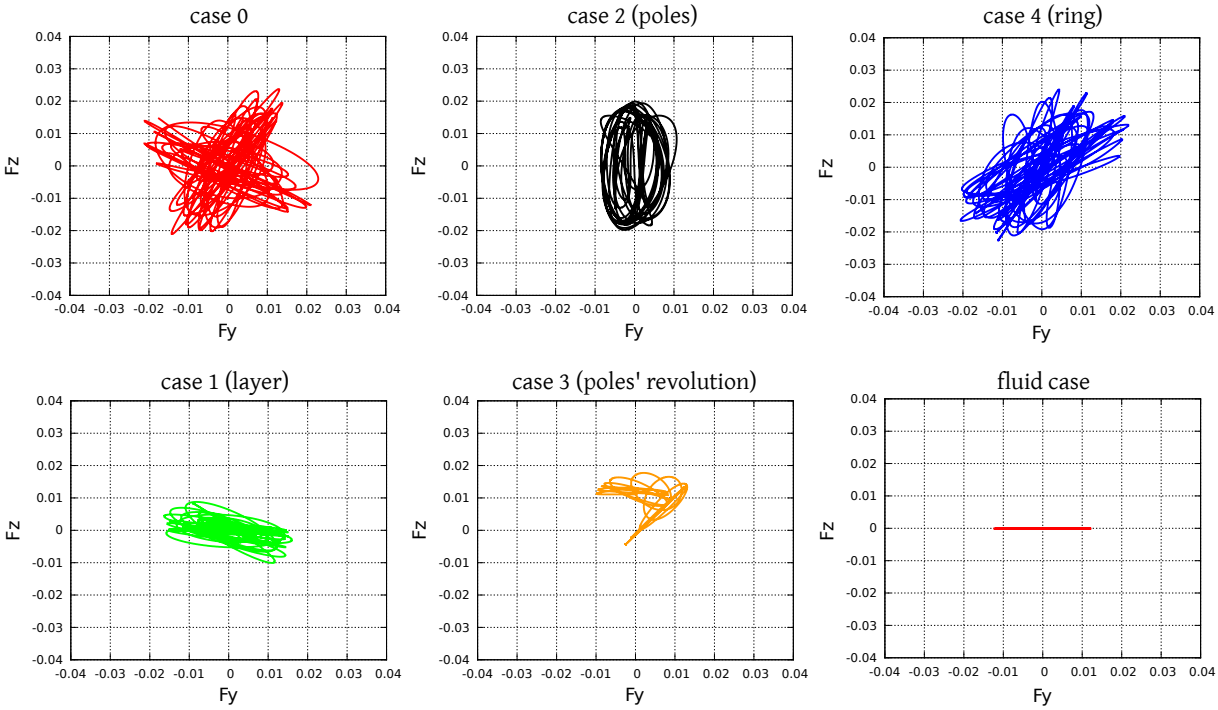

Figure 4.30: Effects of various layer configurations on the phase diagram (F_y, F_z) for flow past a hemisphere at $Re = 300$, with $\lambda = 1$ within the permeable regions and $\tau = 0.1$.

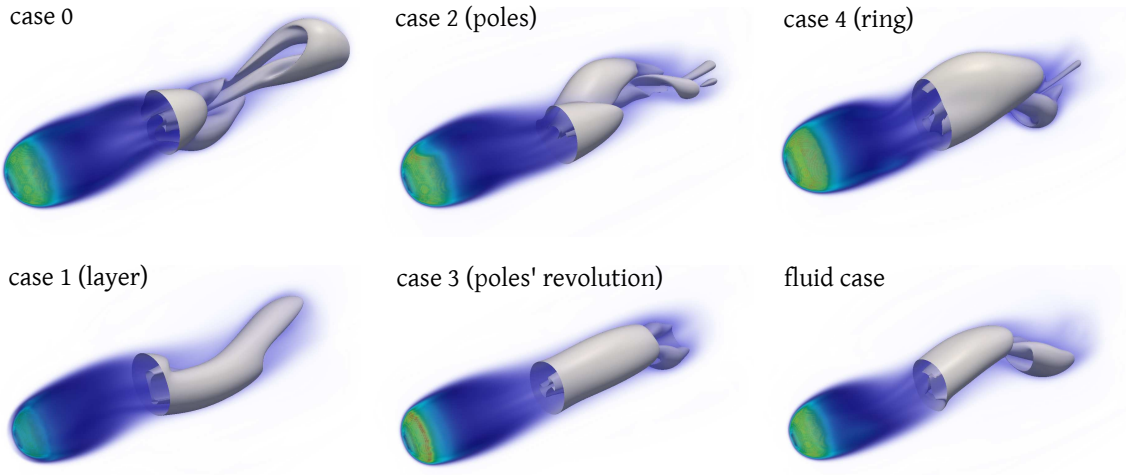

Figure 4.31: Effects of various layer configurations on instantaneous vorticity magnitude 3D field and isocontour $|\boldsymbol{\omega}| = 1$ for flow past a hemisphere at $Re = 300$, with $\lambda = 1$ within the permeable regions and $\tau = 0.1$.

Let us consequently focus on the actual three-dimensional counterpart of the "poles" configuration discussed in 2D. It corresponds to the case 3. The drag reduction induced by this type of device is the best one among all the considered configurations. It indeed reaches -21%. As regards enstrophy, a decrease of 25% is observed with such a device (Table 4.7 and Figure 4.28). These significant reductions are related to the global flow regularization, evidenced by the wake in Figure 4.29 as well as the instantaneous vorticity in Figure 4.31. Nevertheless, one can notice in Figure 4.29b that with case 3 the wake is not planar symmetric, contrary to case 1. Indeed, the phase diagram $(F_y,\ F_z)$ is not vertically centered at the point $F_z = 0$. Furthermore,

no clear periodic pattern emerges from the solution (see Figure 4.28). Despite this absence of periodicity, we can however remark the low amplitude of the drag and enstrophy solution, which confirms the regularizing effects brought by this device. Unlike the case 4, this case allows the flow to easily penetrate within the porous layer which greatly enhances the flow regularization.

The same devices are now analyzed, at the same flow regime, considering an intermediate permeability within the porous areas, materialized by $\lambda = 10$. According to the previous discussion, the case 4 will not be taken into consideration in this study and in the sequel.

In general, the control performances obtained fixing $\lambda = 10$ in the porous areas are quite reduced compared to the one achieved with devices containing high permeable zones ($\lambda = 1$). Considering the case 1 in a first place, one can even notice non-beneficial effects in terms of drag production. Indeed, as shown by Table 4.8 and Figure 4.32, case 1 is responsible for an increase of 7.4% of the drag force compared to the uncontrolled case. The reduction of enstrophy allowed with such device is quite limited and only reaches -7%.

$\lambda = 10,\ \tau = 0.1$	$\bar{F}_x$	$\bar{Z}$	S_t
case 0	0.285	73.0	0.134
case 1	0.306 (+7.4%)	67.7 (-7%)	0.140 (+4.5%)
case 2	0.280 (-2%)	71.5 (-2%)	0.153 (+14%)
case 3	0.273 (-4%)	67.9 (-7%)	0.140 (+4.5%)
fluid case	0.189	49.8	0.158

Table 4.8: Reduction effects brought by the different porous layer configurations in comparison to the uncontrolled case at $Re = 300$ with $\lambda = 10$ within the permeable regions and $\tau = 0.1$.

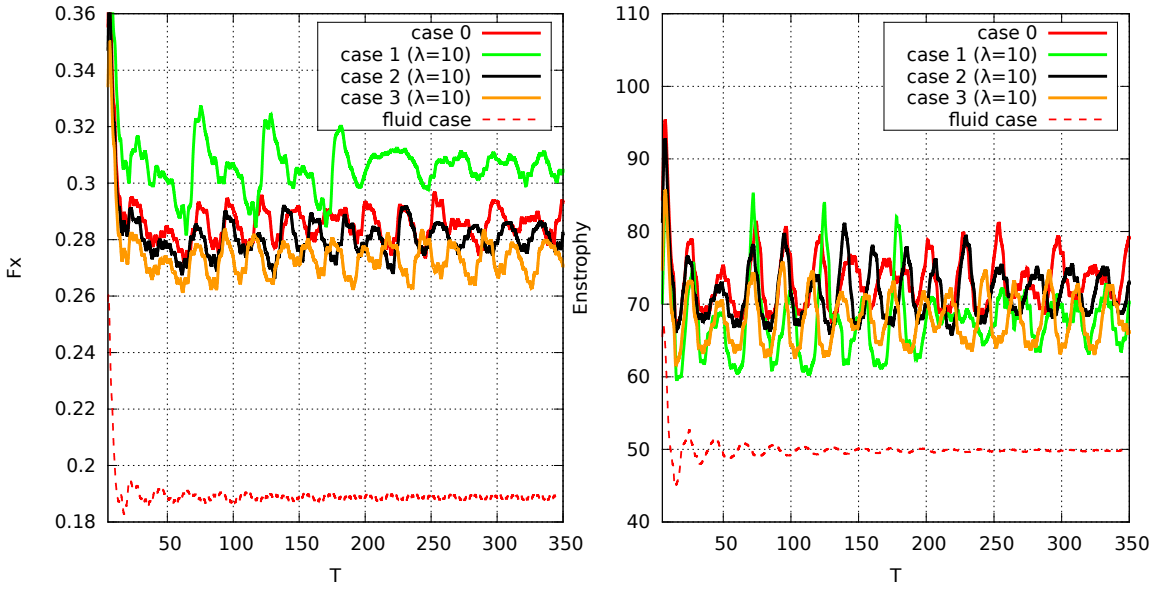

(a) History of drag force

(b) History of enstrophy

Figure 4.32: Effects of various layer configurations on drag force (a) and enstrophy (b) for flow past a hemisphere at $Re = 300$, with $\lambda = 10$ within the permeable regions and $\tau = 0.1$.

Contrary to the case where $\lambda = 1$ inside the porous layer, the mean wake do not present here planar symmetry (Figure 4.33b) and is still rather perturbed (Figure 4.33a). The phase diagram of case 1 plotted in Figure 4.34 is more regular that the one of case 0 but shows however non negligible amplitudes for the lift forces F_y and F_z. In fact, as highlighted in the 2D study, decreasing the permeability makes the fluid displacement more difficult inside the porous layer

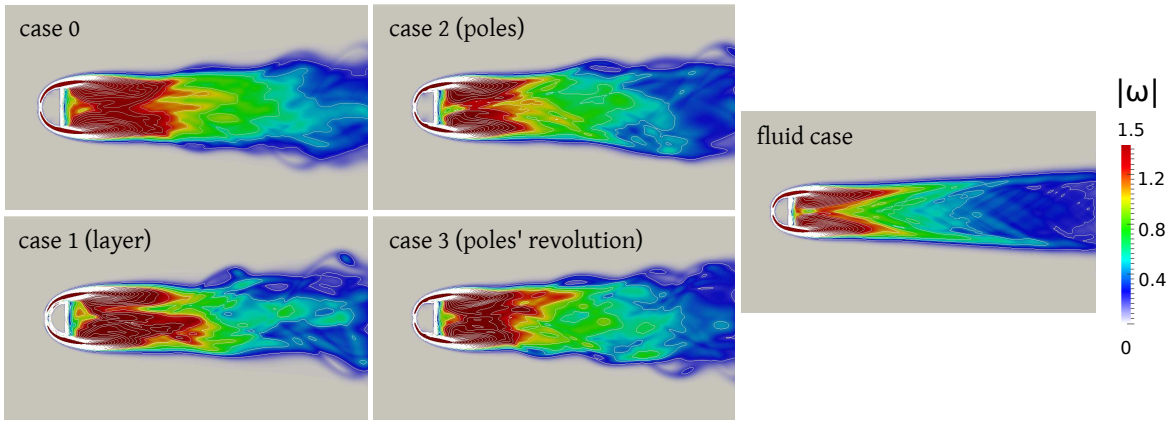

(a) XY plane

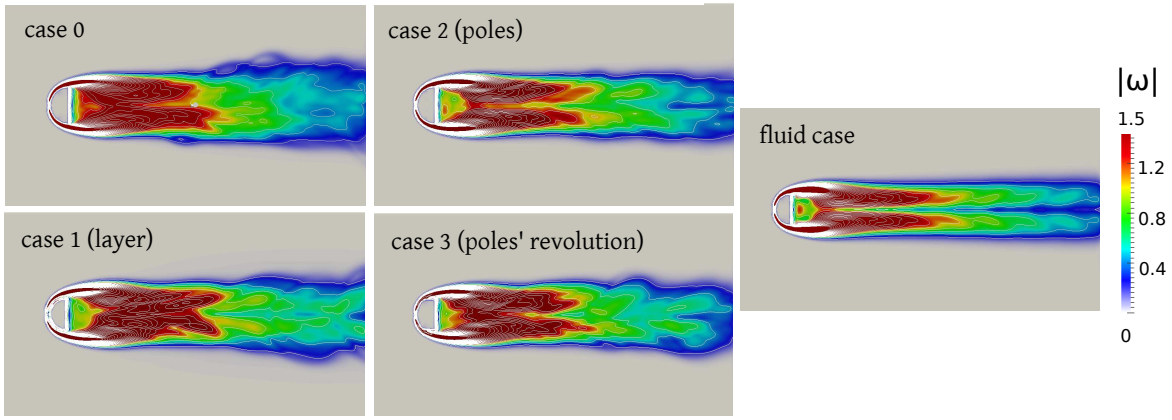

(b) XZ plane

Figure 4.33: Effects of various layer configurations on mean vorticity magnitude for flow past a hemisphere at $Re = 300$, with $\lambda = 10$ within the permeable regions and $\tau = 0.1$.

and increases the resistance to its movement. All these observations highlight the importance of the location of the porous parts on the obstacle. Once again it appears that these areas should be concentrated in the vicinity of the flow separation points. The results obtained with case 2 confirm this statement. Even if the control effects achieved with such device are really moderated (Table 4.8 and Figure 4.32), the performances are not deteriorated. From a qualitative point of view, the phase diagram (F_y, F_z) and the mean wake in the XY plane remain very similar to the one of case 0 (Figure 4.34 and Figure 4.33a), but a symmetry emerges in the XZ plane (Figure 4.33a), confirming the beneficial effects brought by the two porous poles.

In the end, the case 2 cannot be qualified as efficient but its comparison with case 1 enables us to enhance the importance of the position of the porous parts when their permeability is increased. The best flow control device considered here is the case 3, allowing for a drag reduction of 4% and a decrease of the enstrophy of 7% (Table 4.8 and Figure 4.32). Figure 4.33b shows that compared to case 0 the flow better attaches to the obstacle with case 3, leading to a thinner wake. The 3D instantaneous vorticity fields depicted in Figure 4.35 clearly show the benefits obtained with case 3 compared to cases 1 and 2 since its wake is the only one showing a clear regularization compared to case 0.

Finally, concerning the Strouhal number, one can see in Tables 4.7 and 4.8 that for cases 1, 2 and 4 the presence of a porous coating at the hemisphere surface is responsible for a small and constant increase of the shedding frequency compared to case 0, while we notice sharp fluctuations with case 2. In the 3D case, the evolution of the Strouhal number therefore seems to be significantly influenced by the position and the permeability of the porous coating.

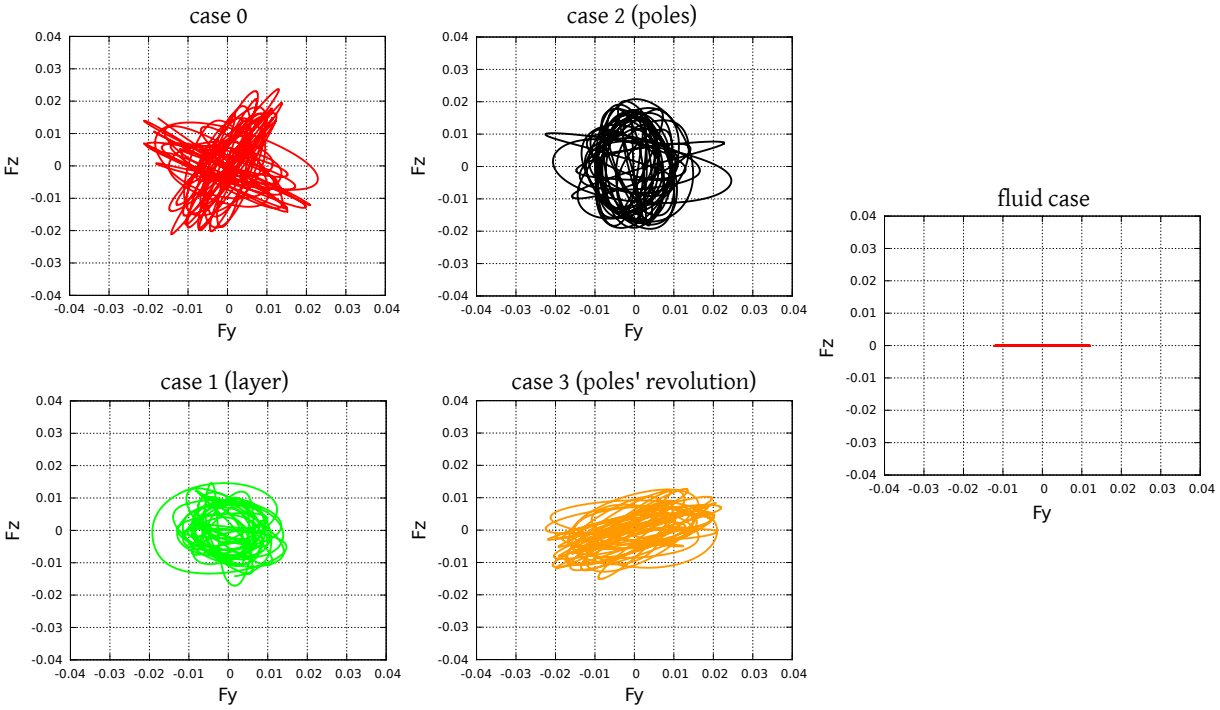

Figure 4.34: Effects of various layer configurations on the phase diagram (F_y, F_z) for flow past a hemisphere at $Re = 300$, with $\lambda = 10$ within the permeable regions and $\tau = 0.1$.

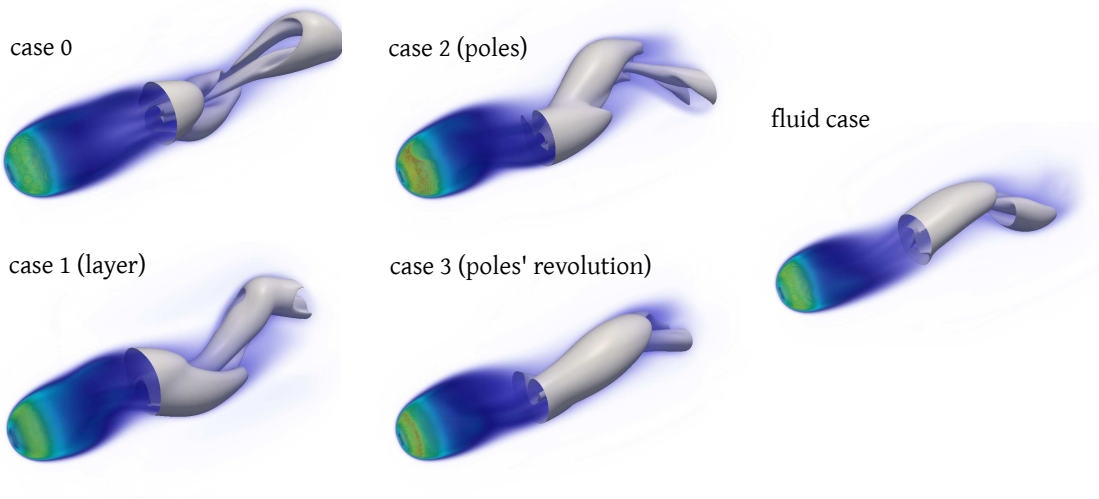

Figure 4.35: Effects of various layer configurations on instantaneous vorticity magnitude 3D field and isocontour $|\boldsymbol{\omega}| = 1$ for flow past a hemisphere at $Re = 300$, with $\lambda = 10$ within the permeable regions and $\tau = 0.1$.

4.3.1.2 Numerical results for $Re = 1000$

Let us now focus on the flow control results at $Re = 1000$. At this regime, we only take into consideration the best configurations outlined in the previous section, namely the case 1 (homogenous layer) and the case 3 (poles' revolution). For the latter, two different permeabilities are handled within the porous part: $\lambda = 1$ and $\lambda = 10$. The reduction effects in terms of drag force and enstrophy are given by Table 4.9 and Figure 4.36. As can be seen, the case 3 with $\lambda = 1$ is the only device providing a drag decrease (-16%). In particular, case 1 with $\lambda = 1$ is responsible for a drag increase of 3% while it ensures a reduction of enstrophy of 30%, which

is more than the reduction achieved with case 3 and $\lambda = 1$ (-19%). In this context, the case 1 is therefore better suited to regularize the wake. Indeed, as can be noticed on Figure 4.37, the homogeneous layer of permeability $\lambda = 1$ significantly impacts the wake that tends to present the same characteristics that the one of the fluid case. It allows in particular to recover a planar symmetric wake (Figure 4.37b), which is not the case for the case 3 with $\lambda = 1$. However, the latter represents the best device in terms of global regularization. Besides the important reductions reported in Table 4.9, the mean wake obtained from case 3 with $\lambda = 1$ is smoother than the one of case 0, with lower vorticity values and a thinner dimension in the crosswise direction (Figure 4.37a) and in the spanwise direction (Figure 4.37b). The instantaneous 3D vorticity field depicted in Figure 4.38 also shows the same effects on the wake and enhances the regularization capabilities of such device. On the contrary, setting $\lambda = 10$ within the porous area of case 3 deteriorates the performances. The wake indeed thickens, showing higher vorticity values (Figures 4.37 and 4.38), and the drag force as well as the enstrophy raise of 5% and 2% respectively (Table 4.9 and Figure 4.36). In conclusion, among the configurations handled in this flow control study at $Re = 1000$ with the high layer thickness $\tau = 0.1$, the most competitive device is clearly the case 3 with a high permeability ($\lambda = 1$) settled within the porous coating.

$\tau = 0.1$	$\bar{F}_x$	$\bar{Z}$
case 0	0.210	175.8
case 1, $\lambda = 1$	0.217 (+3%)	123.1 (-30%)
case 3, $\lambda = 1$	0.177 (-16%)	141.8 (-19%)
case 3, $\lambda = 10$	0.221 (+5%)	179.6 (+2%)
fluid case	0.143	126.5

Table 4.9: Reduction effects brought by different porous layer configurations in comparison to the uncontrolled case at $Re = 1000$ with $\tau = 0.1$.

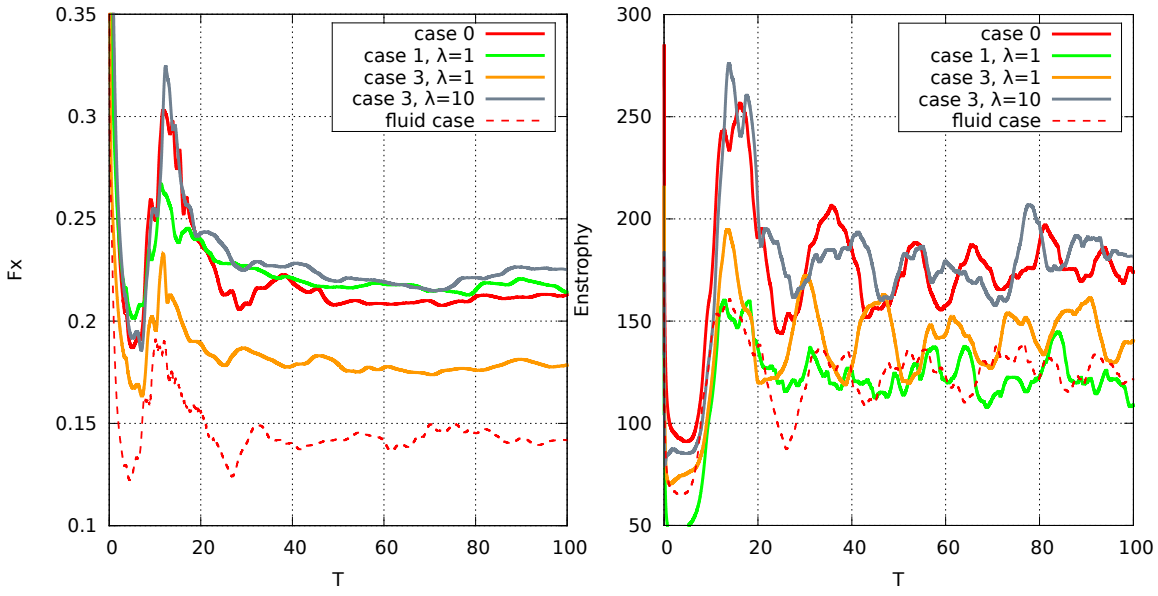

(a) History of drag force

(b) History of enstrophy

Figure 4.36: Effects of various layer configurations on drag force (a) and enstrophy (b) for flow past a hemisphere at $Re = 1000$, with $\tau = 0.1$.

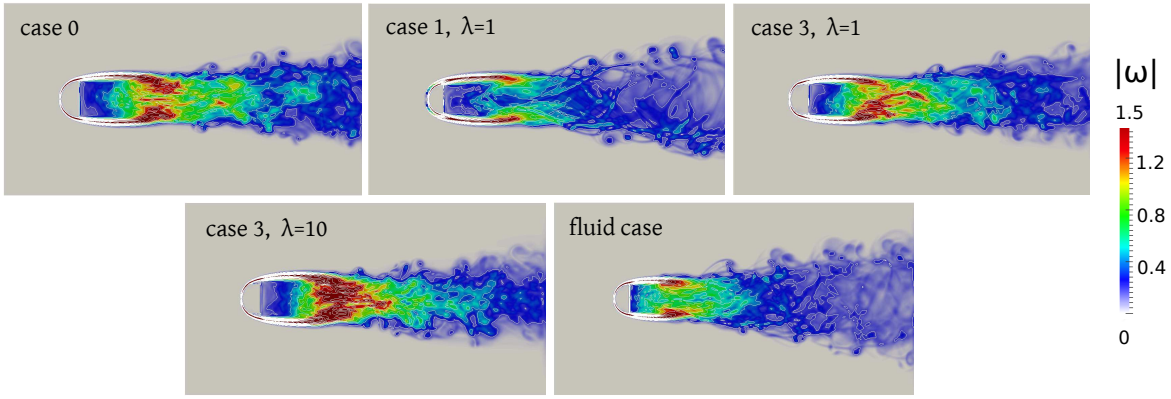

(a) XY plane

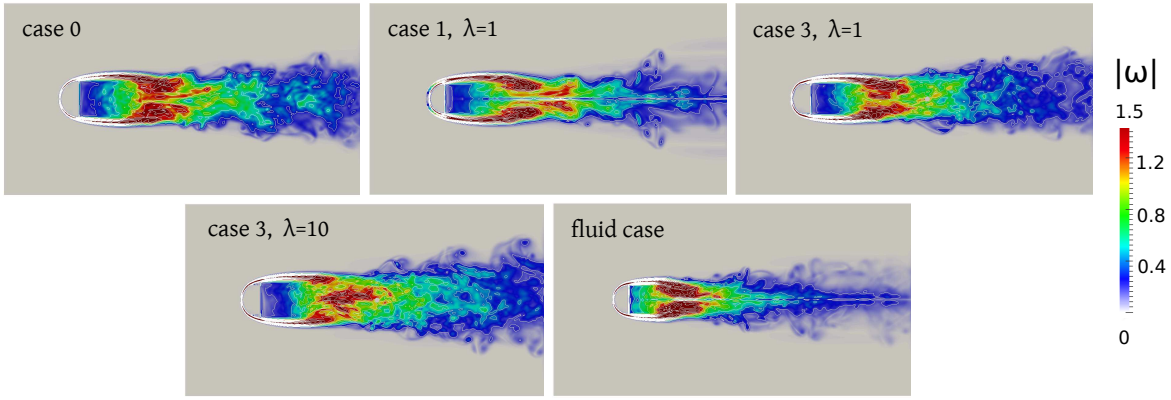

(b) XZ plane

Figure 4.37: Effects of various layer configurations on mean vorticity magnitude for flow past a hemisphere at $Re = 1000$, with $\tau = 0.1$.

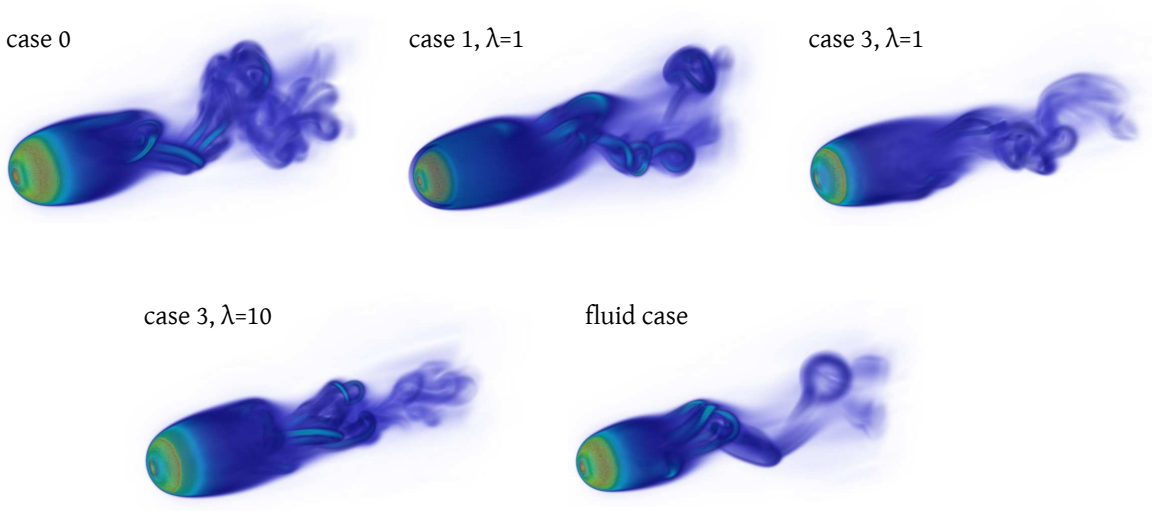

Figure 4.38: Effects of various layer configurations on instantaneous vorticity magnitude 3D field for flow past a hemisphere at $Re = 1000$, with $\tau = 0.1$.

4.3.2 Influence of the porous layer thickness τ on flow control efficiency

4.3.2.1 Numerical results for $Re = 300$

In this section we focus on the influence of the porous coating thickness τ on the flow control efficiency. At the flow regime considered here, namely $Re = 300$, we will only perform this τ-parametric study with the "poles' revolution" device (case 3) where $\lambda = 10$ within the porous part. Indeed, according to the above discussion, this device appears as a good compromise between flow control efficiency and manufacturing constraints since it involves intermediate permeability. In order to facilitate the manufacturing of such obstacle, it would be interesting to investigate the performance of such device with a thickness lower than $\tau = 0.1$. Like in the 2D study, we consider for that purpose two other values of τ, namely $\tau = 0.05$ and $\tau = 0.025$. The 3D representation of the poles' revolution device with the different values of τ is given by Figure 4.39.

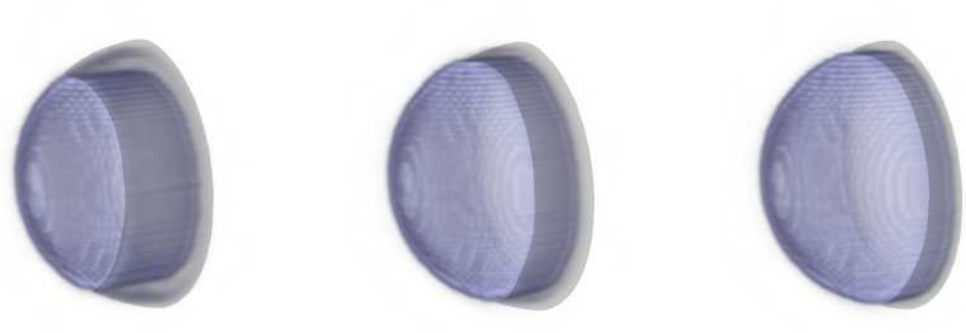

(a) $\tau = 0.1$ (b) $\tau = 0.05$ (c) $\tau = 0.025$

Figure 4.39: Graphical representation of the control device corresponding to case 3 (poles' revolution) with the resolution used for simulations at $Re = 300$ (i.e. $h = 0.02$). Three different thicknesses τ are considered. The shaded areas depict the permeable part of the hemisphere.

The reduction effects brought by the case 3 with respect to the thickness are reported in Table 4.10 and Figure 4.40.

$\lambda = 10$	$\bar{F}_x$	$\bar{Z}$	S_t
case 0	0.285	73.0	0.134
case 3, $\tau = 0.1$	0.273 (-4%)	67.9 (-7%)	0.140 (+4.5%)
case 3, $\tau = 0.05$	0.268 (-6%)	68.4 (-6%)	0.133 (-1%)
case 3, $\tau = 0.025$	0.273 (-4%)	69.9 (-4%)	0.140 (+4.5%)
fluid case	0.189	49.8	0.158

Table 4.10: Reduction effects brought by the case 3 configuration for various layer thicknesses τ with $\lambda = 10$ within the permeable region, in comparison to the uncontrolled case at $Re = 300$.

Surprisingly, the solutions obtained with $\tau = 0.05$ and $\tau = 0.025$ are quite similar to the one obtained with $\tau = 0.1$. In particular one can even notice an improvement in terms of drag reduction with $\tau = 0.05$ (-6%) compared to $\tau = 0.1$ (-4%). The good performances of case 3 with $\tau = 0.05$ are indeed enhanced by Figure 4.41 showing a strong decrease of the vorticity intensity in the mean wake, which tends to become very thin and planar symmetric 4.41b. The regularization effects caused by such device are also clearly shown on Figure 4.42. When decreasing τ to 0.025, the drag and enstrophy decrease are both equal to 4%. All these observations attest that the case 3 handled with a thickness equal to 0.05 corresponds to the best candidate in terms of flow control, at this regime. However, we would like to temper the results obtained with $\tau = 0.025$ since the space resolution considered in our simulations ($h = 0.02$)

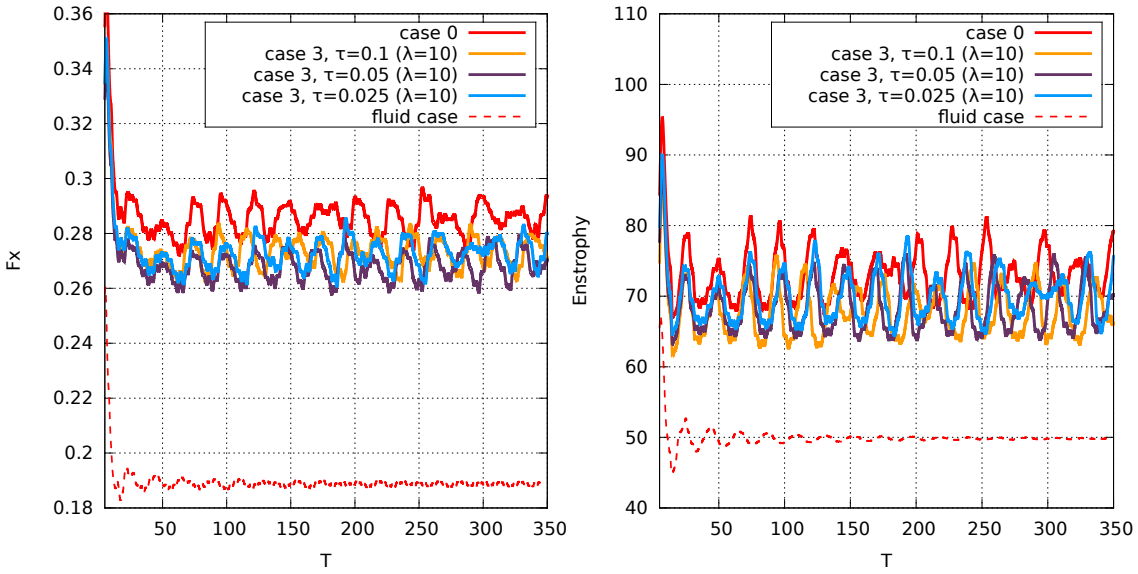

(a) History of drag force (b) History of enstrophy

Figure 4.40: Effects of various layer thicknesses τ for case 3 on drag force (a) and enstrophy (b) for flow past a hemisphere at $Re = 300$, with $\lambda = 10$ within the permeable region.

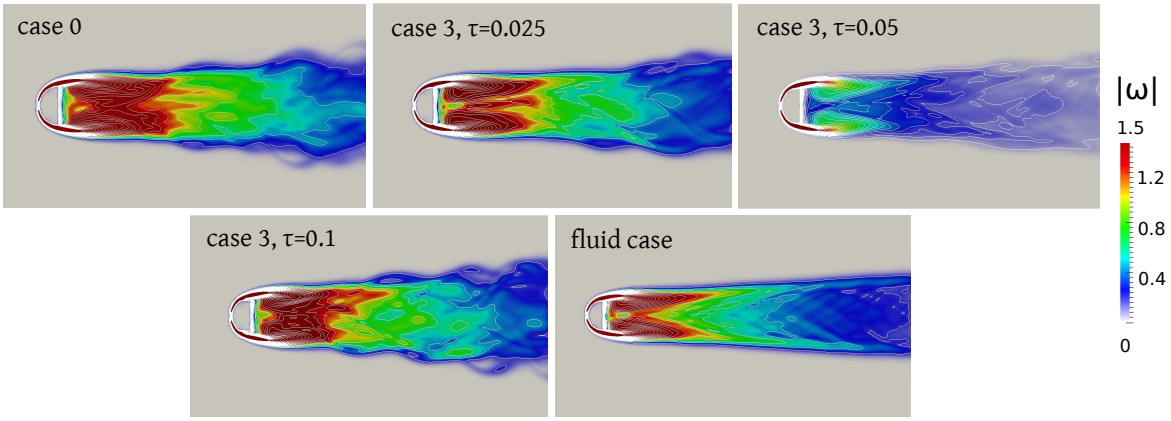

(a) XY plane

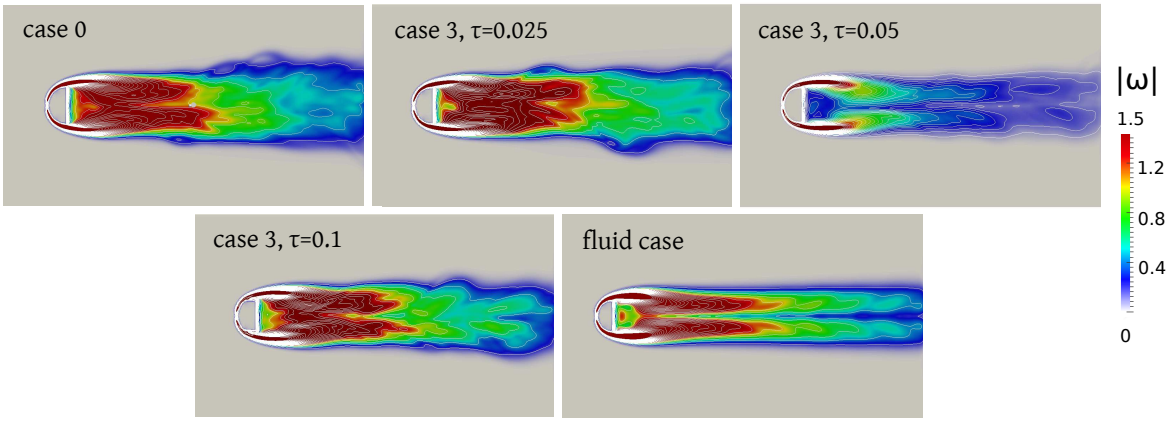

(b) XZ plane

Figure 4.41: Effects of various layer thicknesses τ for case 3 on mean vorticity magnitude for flow past a hemisphere at $Re = 300$, with $\lambda = 10$ within the permeable region.

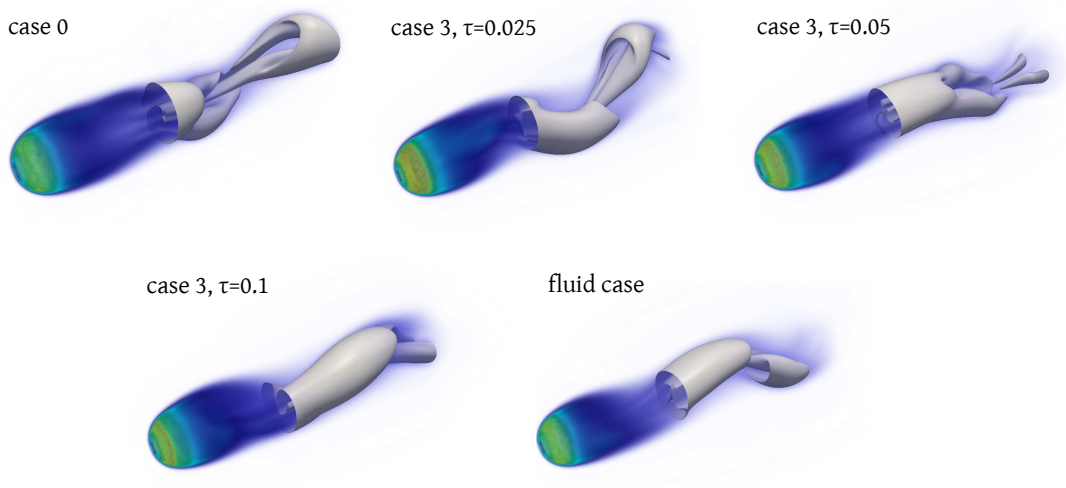

Figure 4.42: Effects of various layer thicknesses τ for case 3 on instantaneous vorticity magnitude 3D field and isocontour $|\boldsymbol{\omega}| = 1$ for flow past a hemisphere at $Re = 300$, with $\lambda = 10$ within the permeable region.

might be too large to perfectly capture the effects caused by this really thin porous part.

4.3.2.2 Numerical results for $Re = 1000$

A similar τ-parametric study is also performed at $Re = 1000$ considering the same three values of τ, namely 0.1, 0.05 and 0.025. The controlled device under consideration here is the case 3 ("poles' revolution") setting $\lambda = 1$ within the porous region. As this device allowed to achieve by far the best drag reduction in the study carried out at the same Reynolds number in subsection (4.3.1.2) (see Table 4.9), we aim to investigate its performances with thinner porous layers, in a search of manufacturing savings.

Table 4.11 and Figure 4.43 indicate that the drag and enstrophy reductions obtained with $\tau = 0.05$ and 0.025 are noticeably tempered compared to the case where $\tau = 0.1$. Furthermore, the results obtained with the lower value $\tau = 0.025$ are quite similar to the one obtained with $\tau = 0.05$. The regularization effects brought by the cases $\tau = 0.05$ and $\tau = 0.025$ are also qualitatively reported in Figure 4.44 and Figure 4.45. They show that the mean and instantaneous wakes obtained with $\tau = 0.025$ in case 3 resemble to the one obtained with the uncontrolled case. A smoothing tendency is then observed from this lower value of τ to the higher one. At this flow regime, the "poles' revolution" configuration with $\tau = 0.1$ therefore appears as the most suitable control device.

$\lambda = 1$	$\bar{F}_x$	$\bar{Z}$
case 0	0.210	175.8
case 3, $\tau = 0.1$	0.177 (-16%)	141.8 (-19%)
case 3, $\tau = 0.05$	0.198 (-6%)	170.6 (-3%)
case 3, $\tau = 0.025$	0.201 (-4%)	170.4 (-3%)
fluid case	0.143	126.5

Table 4.11: Reduction effects brought by the case 3 configuration with $\lambda = 1$ within the permeable region, in comparison to the uncontrolled case at $Re = 1000$.

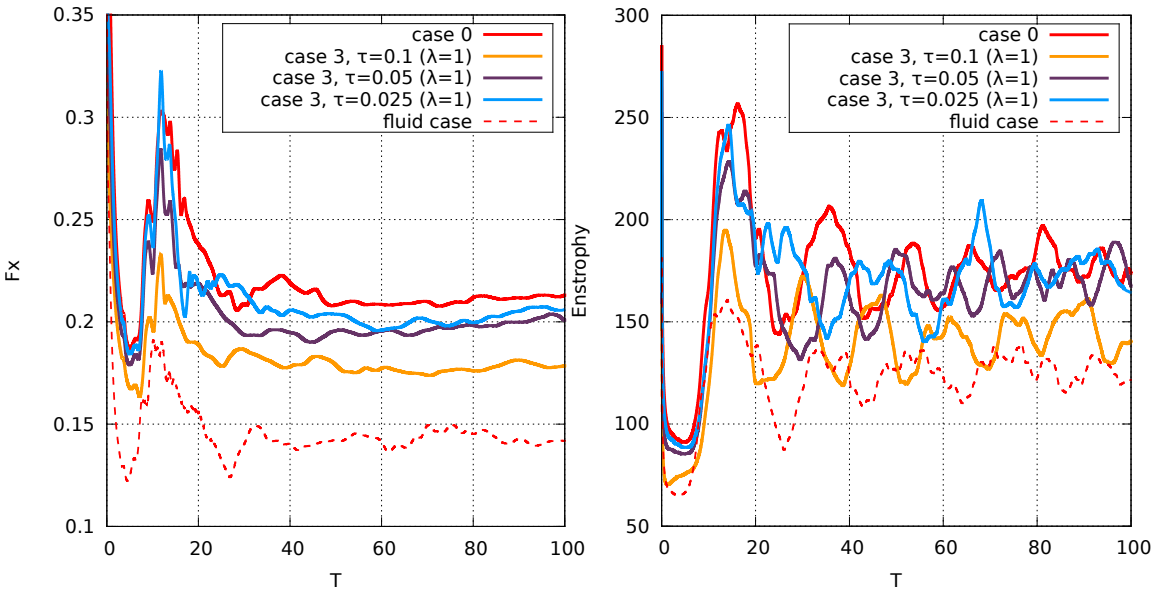

(a) History of drag force (b) History of enstrophy

Figure 4.43: Effects of various layer thicknesses τ for case 3 on drag force (a) and enstrophy (b) for flow past a hemisphere at $Re = 1000$, with $\lambda = 1$ within the permeable region.

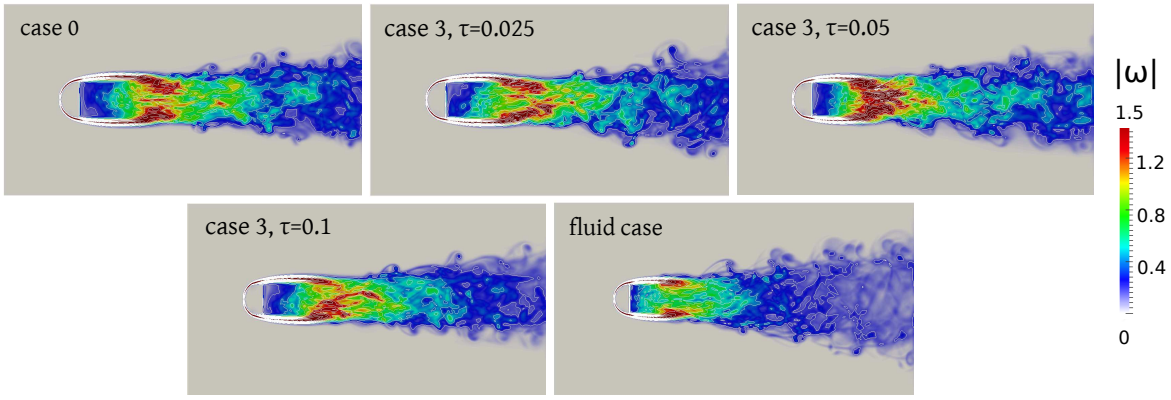

(a) XY plane

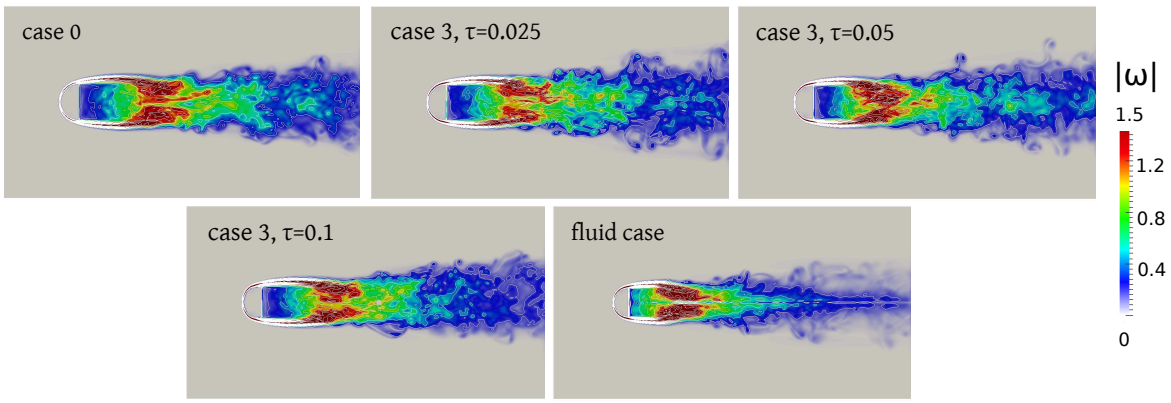

(b) XZ plane

Figure 4.44: Effects of various layer thicknesses τ for case 3 on mean vorticity magnitude for flow past a hemisphere at $Re = 1000$, with $\lambda = 1$ within the permeable region.

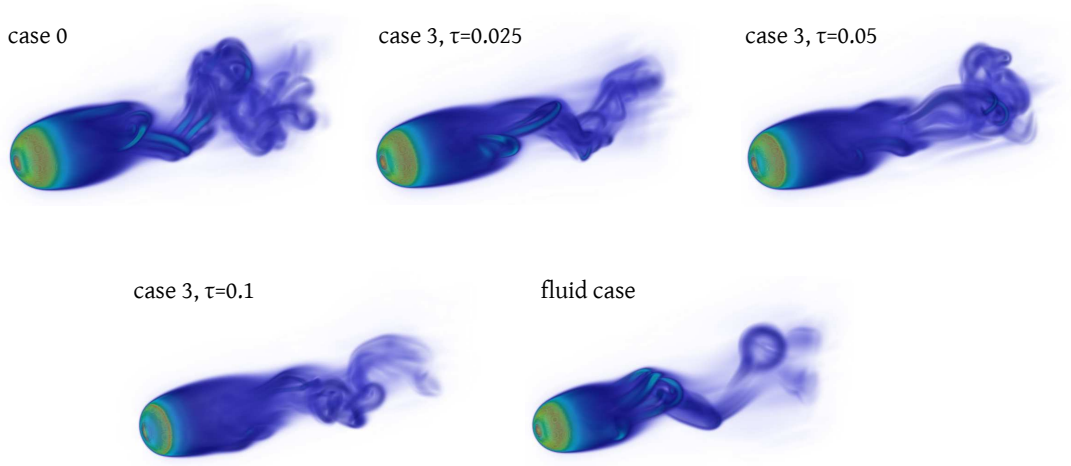

Figure 4.45: Effects of various thicknesses τ for case 3 on instantaneous vorticity magnitude 3D field for flow past a hemisphere at $Re = 1000$, with $\lambda = 1$ within the permeable region.

4.3.3 Comparable tendencies between the 2D and the 3D studies

Although a straight comparison between the flow control outcomes obtained in 2D and in 3D would be inappropriate because of the major discrepancies existing between 2D and 3D flows, it can be however interesting to enhance the common tendencies observed in both cases.

Let us first of all focus on the results obtained in transitional flow regime (i.e. $Re = 550$ in 2D and $Re = 300$ in 3D). When the permeability inside the porous areas is really high (typically $\lambda = 1$) and the thickness is set to 10% of the diameter ($\tau = 0.1$), we observed both in the 2D and the 3D case that the best device in terms of drag reduction was the "poles' revolution" device (case 4 in 2D and case 3 in 3D). In terms of enstrophy reduction, we found that the best candidate was the "homogeneous layer" device (case 1 in 2D and in 3D). We note that the same conclusion holds for the highly transitional regime ($Re = 3000$ in 2D and $Re = 1000$ in 3D).

When the permeability of the porous coating is intermediate (typically $\lambda = 10$) and $\tau = 0.1$, we systematically noticed at a transitional regime that the "homogeneous layer" device was responsible for an increase of the drag production, even if it ensured a reduction of enstrophy (case 2 in 2D and case 1 in 3D). We can therefore conclude that this type of device is not viable for passive flow control past a hemisphere. From these observations, the 2D and 3D studies finally came to the conclusion that it was essential to carefully choose the position of the porous zones, and in both case it turned out that a good location was the vicinity of the flow separation points. The devices built on this principle indeed showed very satisfactory results.

Finally, some similar tendencies may be observed in terms of flow response to the thickness variation, especially at highly transitional regime (i.e. $Re = 3000$ in 2D and $Re = 1000$ in 3D) when considering the "poles's revolution" device with high permeability (case 4 in 2D and case 3 in 3D). A summary overview is given by Table 4.12 and clearly shows that, in that case, the best control results are obtained fixing $\tau = 0.1$ and that the results achieved with $\tau = 0.05$ and $\tau = 0.025$ are very comparable, both in 2D and in 3D.

	F_x		Enstrophy	
Thickness τ	2D	3D	2D	3D
$\tau = 0.1$	-20%	-16%	-19%	-19%
$\tau = 0.05$	-12%	-6%	-2%	-3%
$\tau = 0.025$	-13%	-5%	-0.8%	-3%

Table 4.12: Drag force and enstrophy reductions brought by the "poles' revolution" configuration with $\lambda = 1$, compared to the uncontrolled case in 2D (at $Re = 3000$) and in 3D (at $Re = 1000$)

Conclusion 4.1

The control application performed in this chapter illustrated the capability of the present method to successively handle flows in solid-fluid-porous media. A passive flow control study around a semi-circular cylinder in 2D and around a hemisphere in 3D was performed at transitional and highly transitional regimes, consisting in adding a porous coating on the obstacle surface in order to smooth the flow dynamics. The distinction between the three different media was performed by varying the value of the penalization parameter without prescribing a boundary condition at the solid boundary or at the porous-fluid interface. The presence of a porous layer at the solid-fluid interface is responsible for a decrease of the shear forces and the vorticity generation of the boundary layer, leading to significant wake stabilization and drag reduction. Among the control devices investigated in this chapter, one can retain the "poles' revolution" configuration (respectively "porous poles" in 2D) which only includes porous parts in the region of the flow separation. With an appropriate choice of the permeability and the thickness, this porous device represents a good compromise between control efficiency and manufacturing constraints. It is believed to be challenging in an industrial point of view.

5

Perspectives

Contents

Résumé 5

Dans la dernière partie de cette thèse nous proposons plusieurs pistes d'études afin de compléter le travail exposé et rendre certains aspects plus performants. Tout d'abord, nous soulevons un problème majeur lié à la performance numérique. En effet, avec des simulations directes (DNS en anglais), les limites en termes de capacité de calcul de notre librairie scientifique semblent clairement être atteintes. Une première solution pourrait donc consister à discrétiser le domaine avec des maillages cartésiens non-uniformes, permettant ainsi de concentrer les efforts de calcul dans les régions comportant de l'information sur l'écoulement (typiquement les bords de l'obstacle et le sillage). L'alternative plutôt priviligée dans notre cas, du moins dans un premier temps, est celle de la mise en oeuvre d'un modèle de turbulence, de type LES (Large Eddy Simulations), permettant de s'épargner la résolution des plus petites échelles de l'écoulement. Quelques pistes de réflexion ont déjà été menées à ce sujet et des résultats préliminaires sont exposés dans ce chapitre. Une deuxième perspective de travail porte sur la montée en ordre globale de la méthode numérique. Cette dernière est en effet limitée par la méthode de pénalisation, qui n'est discrétisée qu'avec un schéma d'ordre 1. La possibilité d'une montée en ordre de la méthode de pénalisation sera alors évoquée dans ce chapitre. La dernière perspective proposée dans cette partie concerne la partie applicative de cette étude, à savoir le contrôle passif d'écoulement autour de l'hémisphère. La méthode proposée dans cette thèse ne permet pas d'identifier clairement l'apparition des instabilités dans les écoulements autour d'une hémisphère non contrôlée et d'une hémisphère équipée d'un dispositif poreux. Une étude d'instabilité apparaît alors essentielle afin de comprendre les mécanismes physiques à l'origine des effets régularisants du revêtement poreux et donc d'optimiser les dispositifs de contrôle passif.

This last part aims to outline possible future work directions related to the present study. These perspectives respectively concern the computational performances, the improvement of the numerical approach and the physical interpretations of flow control results.

5.1 An artificial viscosity model for Large Eddy Simulations

As evoked throughout the two last chapters of this thesis, one of the main limitation experienced by the present numerical method is related to the computational resources needed to deal with large problems. When increasing the Reynolds number in the present direct numerical simulations, the handling of a uniform Cartesian grid finally requires to consider prohibitive mesh sizes in order to correctly capture the boundary layer, which makes the computation unaffordable. In order to overcome this problem, a good solution relies in multiresolution [Bergdorf et al., 2005, Rasmussen et al., 2011] and grid adaptivity [Rossinelli et al., 2015]. However all these approaches require major modifications in the computational solver. A more straightforward technique that could be considered in a first attempt relies in Large Eddy Simulations (LES), that is to say in the construction of a eddy viscosity model. LES models are based on the resolution of the Navier-Stokes equations where a low-pass filtering is performed on the flow quantities. The small scales of the solution are therefore discarded, allowing to reduce the computational cost. Contrary to the Reynolds-Averaged Navier-Stokes turbulence model (RANS) based on time-averaged Navier-Stokes equations, the LES resolves the large scales of the flow, thus providing more accurate and realistic solutions. As regards the smallest scales, they are not directly solved like in Direct Numerical Simulations, but modeled. The filtered Navier-Stokes equations for Large Eddy Simulations are given in their velocity-pressure formulation by:

$$\frac{\partial \overline{u}_i}{\partial t} + (\overline{\mathbf{u}} \cdot \nabla)\overline{u}_i + \frac{\partial \overline{p}_i}{\partial x_i} - \nu \Delta \overline{u}_i = -\frac{\partial \tau_{ij}}{\partial x_j} \tag{5.1}$$

$$\text{div } \overline{\mathbf{u}} = 0, \tag{5.2}$$

where $\overline{\mathbf{u}}$ and $\overline{p}$ denote the resolved (i.e. filtered) velocity and pressure fields and τ_{ij} corresponds to the subgrid-scale stress tensor. This tensor models the small scales of the advection term $\partial_j(\overline{u_i u_j})$, which are not resolved. It is defined as follows [Leonard, 1974]:

$$\tau_{ij} = \overline{u_i u_j} - \overline{u}_i \overline{u}_j. \tag{5.3}$$

The aim of LES models based on the filtered Navier-Stokes relies in the estimation of τ_{ij}, which is usually modeled by a dissipation term, allowing the energy to cascade from the large scales to the smallest one.

In the context of vortex methods, the derivation of a eddy viscosity model can be done in a different way. When considering purely Lagrangian vortex methods, one obtains an exact weak solution of convection equations. Therefore, the truncation error of these methods only comes from the regularization used to compute the velocity of the particles (see subsection (1.1.1)). Nevertheless, the studies of [Henshaw et al., 1991] highlighted the fact that vortex methods experienced difficulties in modeling the merging of small eddies into larger ones. These difficulties may be explained by dissipative mechanisms embedded in the truncation error. The model derived in [Cottet, 1996] is based on a correction of the equations satisfied by vortex schemes in order to recover the expected large eddy dynamics. We give hereafter the main steps of this model derivation.

5.1.1 Model description

The vorticity field $\boldsymbol{\omega}$ is the solution of the following convection equation, using vortex blob method (see subsection (1.1.1)):

$$\frac{\partial \boldsymbol{\omega}}{\partial t} + \mathrm{div}(\mathbf{u}_\varepsilon \boldsymbol{\omega}) = 0, \tag{5.4}$$

$$\mathbf{u}_\varepsilon = K_\varepsilon \star \boldsymbol{\omega}, \tag{5.5}$$

with

$$K_\varepsilon = K \star \zeta_\varepsilon, \tag{5.6}$$

and where the function ζ_ε results from a cutoff function ζ:

$$\zeta_\varepsilon = \frac{\zeta(\mathbf{x}/\varepsilon)}{\varepsilon^2}. \tag{5.7}$$

We assume the particular case of a positive cutoff function ζ, decaying at infinity, of mean value 1 and with radial symmetry. The approximation of the exact vorticity field $\boldsymbol{\omega}$ is then naturally defined by:

$$\boldsymbol{\omega}_\varepsilon = \boldsymbol{\omega} \star \zeta_\varepsilon, \tag{5.8}$$

Therefore, performing the convolution of 5.4 with ζ_ε one gets:

$$\frac{\partial \boldsymbol{\omega}_\varepsilon}{\partial t} + \mathrm{div}(\mathbf{u}_\varepsilon \boldsymbol{\omega}_\varepsilon) = E, \tag{5.9}$$

where E represents the truncation error resulting from the fact that the convolution was only applied on $\boldsymbol{\omega}$ in the advection term $\mathrm{div}(\mathbf{u}_\varepsilon \boldsymbol{\omega})$. When omitting the variable t for the sake of clarity, the expression of this truncation error is given by:

$$E(\mathbf{x}) = \mathrm{div}_x \int \boldsymbol{\omega}(\mathbf{y})[\mathbf{u}_\varepsilon(\mathbf{x}) - \mathbf{u}_\varepsilon(\mathbf{y})]\zeta_\varepsilon(\mathbf{x}-\mathbf{y})\ d\mathbf{y}. \tag{5.10}$$

In order to identify the antidiffusive mechanisms carried by the error E, we evaluate the enstrophy production based on equation 5.10. Replacing $\boldsymbol{\omega}$ by $\boldsymbol{\omega}_\varepsilon$ in 5.10, multiplying the equation by $\boldsymbol{\omega}_\varepsilon$ and integrating by parts, one obtains:

$$\frac{1}{2}\frac{d}{dt}\int \boldsymbol{\omega}^2\ d\mathbf{x} = \iint \boldsymbol{\omega}(\mathbf{x})\boldsymbol{\omega}(\mathbf{y})[\mathbf{u}(\mathbf{x}) - \mathbf{u}(\mathbf{y})] \cdot \nabla\zeta(\mathbf{x}-\mathbf{y})\ d\mathbf{x}d\mathbf{y}. \tag{5.11}$$

where the subscript ε has been dropped for clarity. Then, rewriting $\boldsymbol{\omega}(\mathbf{x})$ like follows:

$$\boldsymbol{\omega}(\mathbf{x}) = \boldsymbol{\omega}(\mathbf{y}) + \boldsymbol{\omega}(\mathbf{x}) - \boldsymbol{\omega}(\mathbf{y}), \tag{5.12}$$

on gets:

$$\begin{aligned}\frac{1}{2}\frac{d}{dt}\int \boldsymbol{\omega}^2\ d\mathbf{x} = &\iint \boldsymbol{\omega}^2(\mathbf{y})[\mathbf{u}(\mathbf{x}) - \mathbf{u}(\mathbf{y})] \cdot \nabla\zeta(\mathbf{x}-\mathbf{y})\ d\mathbf{x}d\mathbf{y} \\ &+ \iint [\boldsymbol{\omega}(\mathbf{x}) - \boldsymbol{\omega}(\mathbf{y})]\boldsymbol{\omega}(\mathbf{y})[\mathbf{u}(\mathbf{x}) - \mathbf{u}(\mathbf{y})] \cdot \nabla\zeta(\mathbf{x}-\mathbf{y})\ d\mathbf{x}d\mathbf{y}.\end{aligned} \tag{5.13}$$

Putting out $\boldsymbol{\omega}(\mathbf{y})$ of the first integral with respect to $\mathbf{x}$ in the right-hand side and using the incompressibility condition, this first integral vanishes. So, upon writing $2\boldsymbol{\omega}(\mathbf{y}) = [\boldsymbol{\omega}(\mathbf{x}) + \boldsymbol{\omega}(\mathbf{y})] - [\boldsymbol{\omega}(\mathbf{x}) - \boldsymbol{\omega}(\mathbf{y})]$, and using the radial symmetry of ζ, one obtains the following expression of the enstrophy rate:

$$\frac{d}{dt}\int \boldsymbol{\omega}^2\ d\mathbf{x} = -\iint [\boldsymbol{\omega}(\mathbf{x}) - \boldsymbol{\omega}(\mathbf{y})]^2\ [\mathbf{u}(\mathbf{x}) - \mathbf{u}(\mathbf{y})] \cdot \nabla\zeta(\mathbf{x}-\mathbf{y})\ d\mathbf{x}d\mathbf{y}. \tag{5.14}$$

From this expression it is therefore clear that the enstrophy will increase because of the exchange of vorticity between point $\mathbf{x}$ and $\mathbf{y}$ when they will satisfy:

$$[\mathbf{u}(\mathbf{x}) - \mathbf{u}(\mathbf{y})] \cdot \nabla\zeta(\mathbf{x} - \mathbf{y}) < 0. \tag{5.15}$$

Considering the assumptions made on ζ, one can rewrite $\nabla\zeta$ as follows, with $f' \leq 0$:

$$\nabla\zeta(\mathbf{z}) = \frac{\mathbf{z} f'(|\mathbf{z}|)}{|\mathbf{z}|}. \tag{5.16}$$

Therefore, equation 5.15 is equivalent to:

$$[\mathbf{u}(\mathbf{x}) - \mathbf{u}(\mathbf{y})] \cdot (\mathbf{x} - \mathbf{y}) > 0. \tag{5.17}$$

To cancel positive contribution to the enstrophy budget, one can consequently use the following advection scheme:

$$\frac{d\boldsymbol{\omega}_p}{dt} = \sum_q \mathbf{v}_q \left\{ [\mathbf{u}(\mathbf{x}_p) - \mathbf{u}(\mathbf{x}_q)] \cdot [\mathbf{x}_p - \mathbf{x}_q] \frac{f'(|\mathbf{x}_p - \mathbf{x}_q|)}{|\mathbf{x}_p - \mathbf{x}_q|} \right\}_- (\boldsymbol{\omega}_p - \boldsymbol{\omega}_q) \tag{5.18}$$

where $a_- = \min(0, a)$ and where $\boldsymbol{\omega}_p$ and $\mathbf{v}_p$ respectively refer to the vorticity value and the volume of particle located at position $\mathbf{x}_p$. This defines a minimal artificial viscosity model, which allows to cancel the enstrophy only under condition 5.15, thus preserving the anisotropy of the model.

5.1.2 Preliminary numerical results

In our case, we aim to transport the vorticity field on a fine grid with a regularized velocity, resolved on a coarse mesh, and to counterbalance the enstrophy production with the diffusion model 5.18. In three dimensions, this model stands as follows:

$$\frac{d\boldsymbol{\omega}_p}{dt} = (\boldsymbol{\omega}_p \cdot \nabla)\mathbf{u}(\mathbf{x}_p, t) + C \sum_q \mathbf{v}_q \Big\{ [\mathbf{u}(\mathbf{x}_p) - \mathbf{u}(\mathbf{x}_q)] \cdot [\mathbf{x}_p - \mathbf{x}_q] g(|\mathbf{x}_p - \mathbf{x}_q|) \Big\}_+ (\boldsymbol{\omega}_p - \boldsymbol{\omega}_q), \tag{5.19}$$

where $(\boldsymbol{\omega}_p \cdot \nabla)\mathbf{u}(\mathbf{x}_p, t)$ is the stretching term and where $\nabla\zeta(\mathbf{x}_p - \mathbf{x}_q)$ is defined in this case by:

$$\nabla\zeta(\mathbf{x}_p - \mathbf{x}_q) = C\ [\mathbf{x}_p - \mathbf{x}_q]\ g(|\mathbf{x}_p - \mathbf{x}_q|), \tag{5.20}$$

with g a function decaying at infinity and C a constant to adjust in the model. The model 5.19 has been implemented in the present hybrid vortex scheme and has been applied to the Taylor-Green vortex benchmark, which constitutes a relevant three-dimensional test case to investigate the generation of small-scale vorticity. The simulations are handled in a periodic cubic box of side length $L = 2\pi$ and initialized with the following smooth condition:

$$\begin{aligned} u_x(\mathbf{x}, t = 0) &= \sin(x)\cos(y)\cos(z) \\ u_y(\mathbf{x}, t = 0) &= -\cos(x)\sin(y)\cos(z) \\ u_z(\mathbf{x}, t = 0) &= 0 \end{aligned} \tag{5.21}$$

The Reynolds number of the flow is set to $Re = 1600$. First of all, we are eager to validate the results obtained with our method in the context of direct numerical simulations. The mesh resolution is set to 256^3. Figure 5.1a shows the curve of enstrophy as a function of time compared to the one obtained with the same remeshed vortex method by [van Rees et al., 2011] with a 256^3 resolution. One can see that these DNS results coincide very well.

Let us now consider a 64^3 mesh size for the velocity calculations and a 256^3 particle mesh. The vorticity field is thus fully resolved on the fine 256^3 mesh while the small scales of the

velocity field are filtered so that we only consider the velocity values on a coarse 64^3 grid. The velocity filtering is performed through the following cutoff filter, defined in the Fourier space:

$$f_{k_\Delta}(|\mathbf{k}|) = \begin{cases} 1 & \text{if } |\mathbf{k}| \leq k_\Delta = \dfrac{\pi}{\Delta} \\ 0 & \text{otherwise,} \end{cases}$$

where $\Delta = 4h$ is the filter size, with $h = L/256$ denoting the fine grid step. Figure 5.1b reports the evolution of enstrophy when no artificial viscosity is added in the model (black curve). It is compared to the DNS result (blue curve). This figure clearly confirms the enstrophy production induced by the original equations and justifies the use of an artificial viscosity model, namely the model 5.19, able to provide artificial diffusion. Figure 5.1c shows enstrophy evolution curves obtained with model 5.19 for different values of the constant C. It emerges from these results

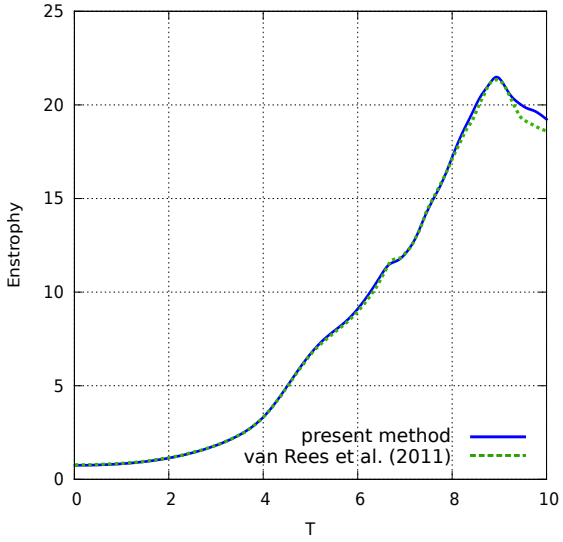

(a) DNS results with a 256^3 resolution

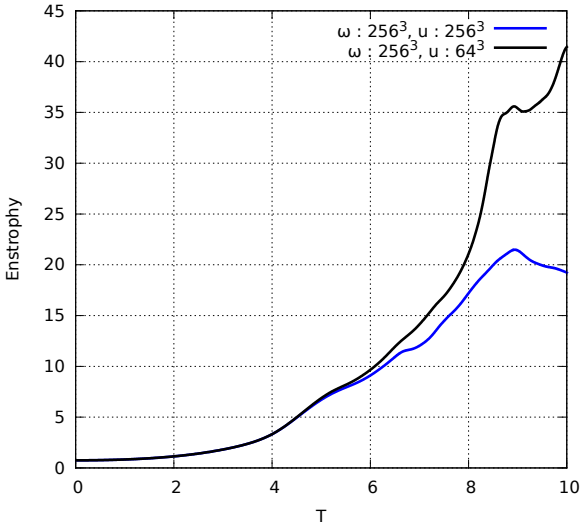

(b) DNS vs model 5.19 with $C = 0$

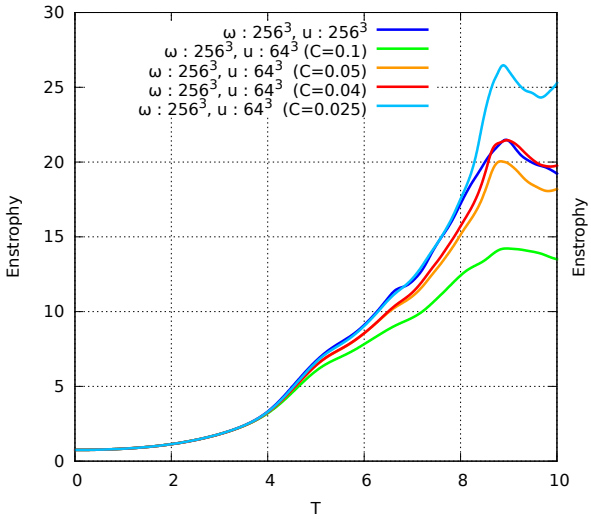

(c) DNS vs model 5.19 with different values of C

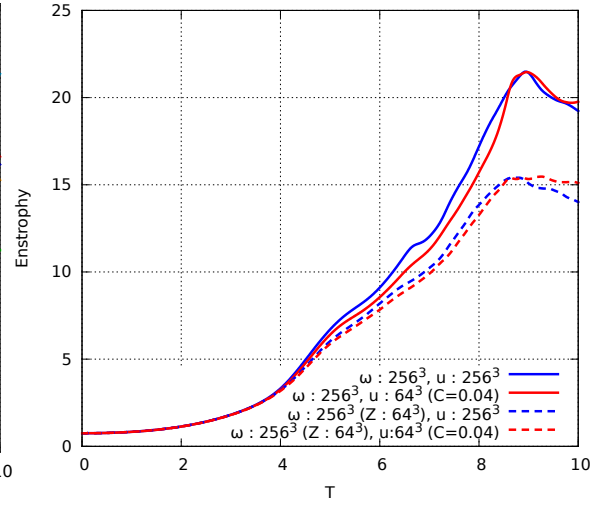

(d) DNS vs model 5.19 with $C = 0.04$

Figure 5.1: Enstrophy of Taylor-Green vortex as a function of time, at $Re = 1600$.

that the artificial viscosity model 5.19 with $C = 0.04$ manages to capture the correct behavior of the flow, especially between $T = 8$ and $T = 10$ when small-scale vortical structures start to appear. The enstrophy evolution obtained with 5.19 and $C = 0.04$ is reported in a clearer way in Figure 5.1d and compared to the DNS result (red and blue solid lines). We also plotted in this figure the curves corresponding to the same simulations where the enstrophy (denoted "Z"

in the figure caption) has been evaluated on the coarse 64^3 grid (red and blue dashed lines). Figure 5.1d thus clearly highlights the fact that the model 5.19, represented by the solid red curve, is halfway between DNS (blue solid curve) and LES (red dashed curve) since it allows to directly take into account some small-scales. The vorticity field representation is also given at $T = 8$ (Figure 5.2) and $T = 9$ (Figure 5.3), comparing the results obtained from DNS with a 256^3 resolution and the ones obtained with model 5.19 and $C = 0.04$ with a 256^3 resolution for the vorticity field and a 64^3 resolution for the velocity field, denoted $256^3 - 64^3$ resolution. The good qualitative agreement observed between the two models confirms the capability of the proposed artificial viscosity model to capture the large scales of the flow and thus to account for the global behavior of the flow.

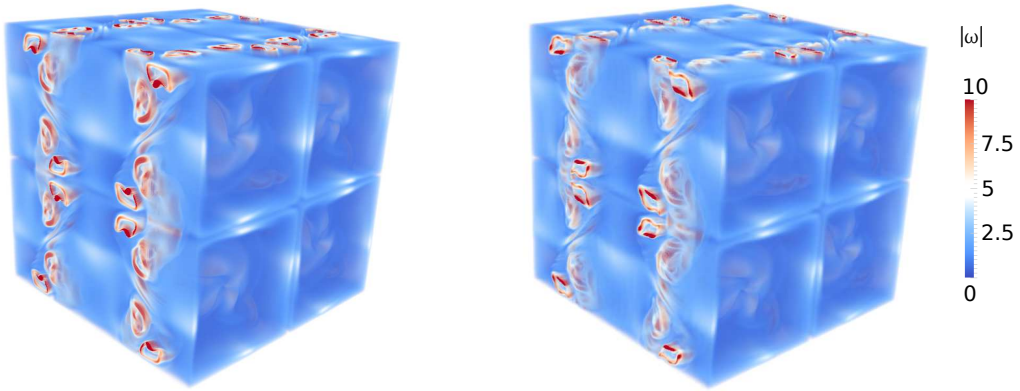

(a) 3D vorticity magnitude with DNS (left) and model 5.19 ($C = 0.04$) (right)

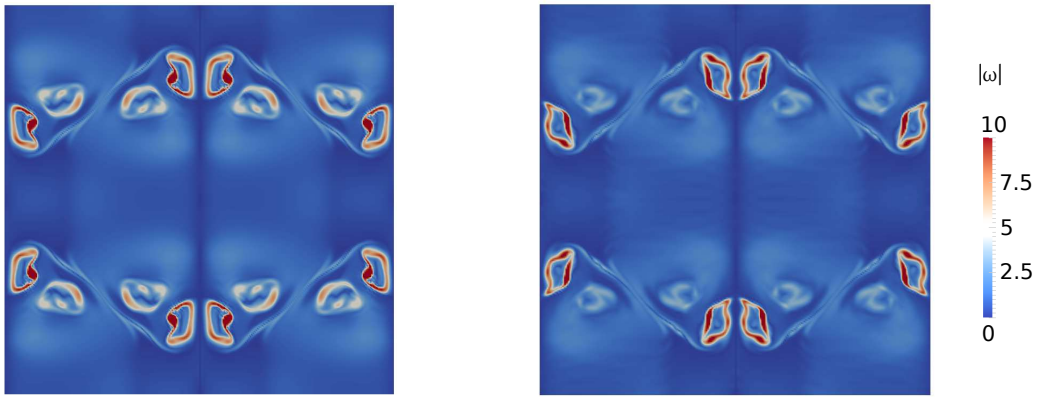

(b) $|\boldsymbol{\omega}|$ in the YZ plane at $x = 0$ with DNS (left) and model 5.19 ($C = 0.04$) (right)

Figure 5.2: Taylor-Green vorticity field at $T = 8$. Comparison between DNS results obtained with a 256^3 resolution and results obtained with model 5.19 and a $256^3 - 64^3$ resolution.

Simulations based on model 5.19 were also performed with a $512^3 - 128^3$ resolution, setting $C = 0.04$. Figures 5.4a and 5.4b compare the contours of $|\boldsymbol{\omega}|$ obtained respectively at $T = 8$ and $T = 9$ with a $256^3 - 64^3$ and a $512^3 - 128^3$ resolution to the contours reported in [van Rees et al., 2011] obtained with DNS based on a 512^3 resolution. These figures show that the contours obtained with model 5.19 and a $512^3 - 128^3$ resolution are very close in a qualitative point of view to the one given by the Direct Numerical Simulations of [van Rees et al., 2011], which confirms the capability of the proposed model to correctly take into account the physics of the problem.

These results constitute preliminary studies. Among the next tasks to consider, the main one would consist in dealing with multi-scale problems on hybrid CPU-GPU architecture in order to significantly enhance the computational performances. In practice, we aim to dedicate the

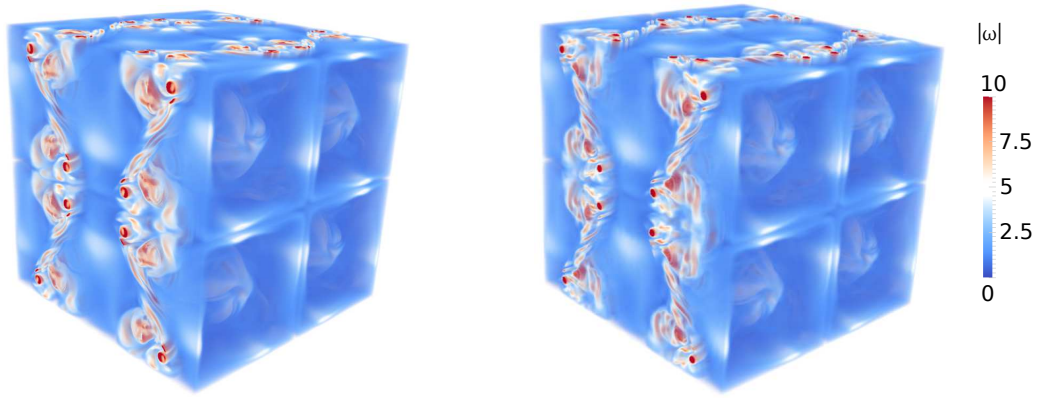

(a) 3D vorticity magnitude with DNS (left) and model 5.19 ($C = 0.04$) (right)

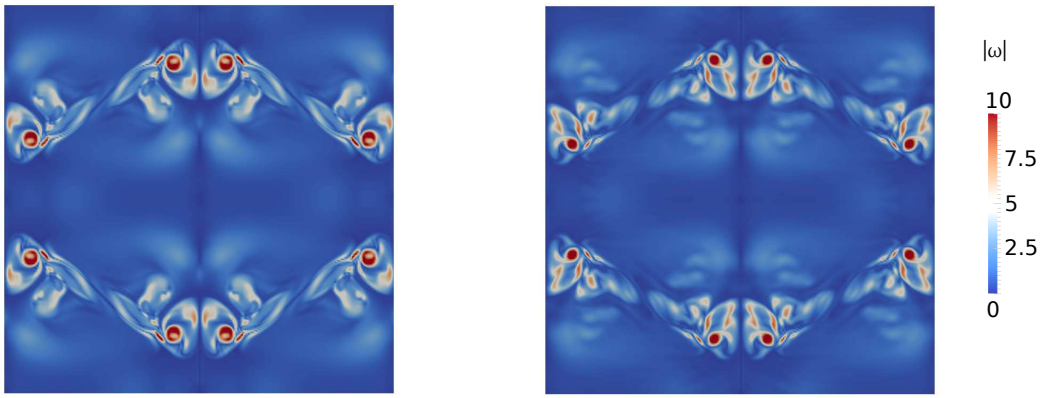

(b) $|\boldsymbol{\omega}|$ in the YZ plane at $x = 0$ with DNS (left) and model 5.19 ($C = 0.04$) (right)

Figure 5.3: Taylor-Green vorticity field at $T = 9$. Comparison between DNS results obtained with a 256^3 resolution and results obtained with model 5.19 and a $256^3 - 64^3$ resolution.

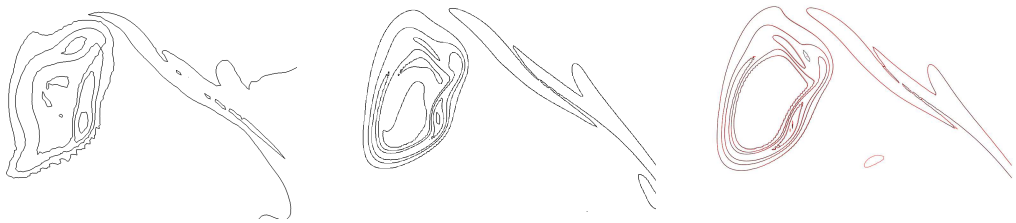

(a) $T = 8$

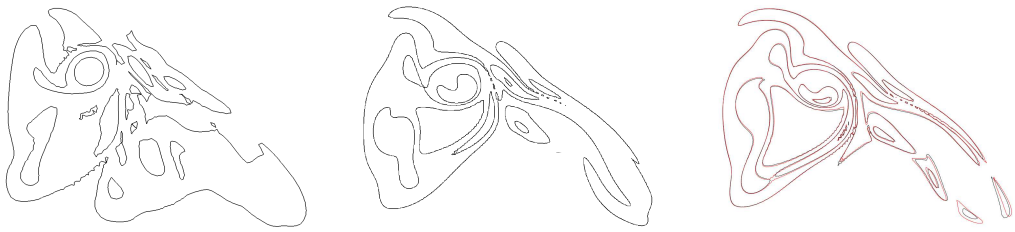

(b) $T = 9$

Figure 5.4: Contours of $|\boldsymbol{\omega}|$ in YZ plane at $x = 0$ obtained through the present model 5.19 ($C = 0.04$) with a $256^3 - 64^3$ resolution (left) and a $512^3 - 128^3$ resolution (center). They are compared to the DNS results obtained by [van Rees et al., 2011] with a 512^3 resolution (right).

high resolution vorticity transport/stretching sub-problems on multi-GPU's while solving the diffusion and Poisson equations on multi-CPU's with a velocity field defined on a coarse grid. This strategy would therefore require interpolation operations between the two interacting flow quantities. Interesting multi-scales results have already been obtained with the HySoP library in the context of passive scalar transport [Etancelin, 2014].

5.2 A second order penalization method

Another perspective related to the present work concerns the penalization method. Indeed, the global convergence order of our algorithm is limited by this technique which is only handled through a first-order discretization method (see section (2.5)).

Among the few studies that have been carried out on this subject, we can first refer to the method proposed by [Bergmann et al., 2014], called the Image Point Correction method (IPC). This approach, designed through a $(\mathbf{u}, p)$ formulation of the Navier-Stokes equations, lies on a simple principle: a correction of the penalized velocity is performed at the solid points having at least one neighboring point in the fluid part. Let us denote these points $\mathbf{x}_S$. The classical first-order penalization method is applied to all the remaining nodes in the body. The correction step in the IPC method is done using a ghost-cell technique consisting in updating the penalized velocity at the grid points $\mathbf{x}_S$ such that the velocity gradient at the solid-fluid interface remains the same on both sides. This method ensures a second-order accuracy in velocity and has been successfully used to treat three-dimensional problems involving fluid-structure interactions with moving and deforming bodies.

We can also cite the recent work proposed by [Hejlesen et al., 2015] based on an iterative vortex-Brinkman penalization method. This approach allows to achieve more accurate results thanks to the iterative process. It also prevents from considering very small time steps, which are often required by the penalization method. However, even if the number of penalization-iterations may be controlled, this algorithm remains quite costly since a Poisson equation has to be solved at each iteration. Moreover, the existence of a fixed-point in the iterative algorithm is not evident. Finally, this penalization method remains of order 1. This approach may be consequently considered as a way to improve the accuracy of the overall method, but not its order of convergence.

5.3 Flow instability analysis

The perspectives considered in this last section are related to the passive flow control application presented in this thesis. Although we managed to enhance significant control performances induced by the presence of a porous coating, the present direct numerical simulations did not allow to clearly identify the physical causes of the observed behaviors. One may indeed wonder for instance what are the physical mechanisms proper to solid-fluid-porous media responsible for the delay in transition. A solution to answer that type of questions would be to carry out a flow stability analysis. As discussed in the Chapter 3 of this thesis, stability analysis have been widely performed in the case of flow past a cylinder or a sphere. They are nevertheless almost non-existent concerning flow past a hemisphere or past a bluff body covered with a porous coating. Concerning this last case, one can cite the stability analysis performed by [Pluvinage et al., 2014] in the boundary layer of a permeable and compliant wall. This study highlights in particular the capability of the permeable wall to destabilize the Tollmien-Schlichting (TS) modes, which are related to the major streamwise instability arising in a viscous boundary layer and from which a laminar boundary layer transitions to turbulence. The modification of the TS modes is shown in this study to delay the transition. Flow instability analysis therefore plays a preponderant role in the identification of the mechanisms that actually drive the flow control performances.

The future work that is considered in the framework of this thesis is the implementation of a linear global stability analysis. This type of approach is based on the investigation of the asymptotic time evolution of infinitesimally small perturbations leading a steady flow to become unstable. In this case, the perturbations are small enough to consider the analysis as linear. More precisely, and as explained in [Loiseau et al., 2014], a linear global stability analysis is decomposed in two distinct steps:

1. **The base flow computation**
   The aim of this sub-step is to find a stationary solution of the Navier-Stokes equations,

from which the linear stability will be carry out afterward. This equilibrium solution may be calculated using a selective frequency damping (SFD) technique, which consists in using a low-pass filter to soften the oscillations carried by the unsteady part of the solution.

2. **The global stability analysis**
   Based on the stationary solution computed previously, the dynamics of the infinitesimal perturbations present in the vicinity of the equilibrium point of the original system may be expressed. Their governing equations may then be recast into a linear dynamical system.

When starting the simulation from the base flow, the resolution of this linear problem allows to enhance the so-called linear global mode, corresponding to a perturbation growing faster than the others. Under the influence of the nonlinear effects, the growth of the linear global mode becomes more and more limited and it finally saturates to a periodic state. This phenomenon is called a Hopf bifurcation.

Based on the fully 3D linear global stability analysis performed in [Loiseau et al., 2014], the same type of approach is aimed to be adopted in the context of the present hybrid vortex penalization method.

Conclusion

The main objective of this thesis was to demonstrate the capability of particle methods to handle complex and challenging incompressible flow problems. For this purpose it was applied to two- and three-dimensional passive flow control using porous media.

Chapter 1 went through the history of vortex methods. This state of art enabled us to better understand the development of these particle methods and their insertion in the CFD community from their first appearance in 1928 until nowadays. In spite of the strong advantages they intrinsically had over Eulerian methods, vortex methods experienced during several years some difficulties in dealing with major problems like the treatment of boundary conditions or the diffusion effects. With the emergence of hybrid vortex methods in the 1990's, characterized by the introduction of an underlying grid and a periodic remeshing of the particles on this grid in order to prevent from distortion phenomena, vortex methods got more visibility. Since then, the performance and algorithmic issues related to these methods became a keypoint and a lot of works have been dedicated to improve their accuracy and implement them in an efficient way. The present thesis was defined in this context and aimed in particular for highlighting the competitiveness of these methods compared to purely grid-based ones.

In this work, a hybrid particle penalization technique has been employed in order to benefit from the advantages of immersed boundary methods - through the penalization technique - and remeshed particle methods. On one hand the latter maintain the efficiency and the robustness of vortex methods, solving the flow equations in a fast Lagrangian way. Indeed, remeshed vortex methods do not need classical CFL condition to ensure the stability, which enables the use of greater time steps. On the other hand the penalization technique eases numerical implementation since it allows to consider the governing equations in the whole computational domain allowing the use of structural grids and avoiding the overhead and the complexity typical of body fitted grids. This immersed-boundary method is also of particular interest to consider multi-scales problems: the underlying Cartesian mesh indeed greatly simplifies the handling of flow fields resolved on different grid sizes. The hybrid vortex penalization method was described in chapter 2 as well as its implementation within a new parallel scientific library dedicated to flow simulations, called HySoP. This common framework, written using an object-oriented paradigm, has been designed paying a strong attention to flexibility, portability and modularity. HySoP will be soon distributed under a GPLv3 license [3].

The validation studies reported in chapter 3 were systematically carried out at different flow regimes in the case of a cylinder and a semi-cylinder in 2D and a sphere and a hemisphere in 3D. Grid-refinement studies enabled us to identify the global order of convergence of the method. This order was shown to be approximately equal to 2. Convergence studies on the penalization parameter λ also allowed to validate the modeling of rigid motion inside a solid obstacle through the penalization approach. It furthermore permitted to determine the range of λ values modeling a porous medium, namely $1 \lesssim \lambda \lesssim 10^3$. Finally, a careful flow analysis was performed for the different obstacles considered in this study and the results were compared to a large number of reference works in the literature. The two- and three-dimensional numerical results reported in this chapter eventually prove the ability of the present method to correctly

[3] hysop.imag.fr

account for the expected flows' behaviors at transitional and highly transitional regimes.

In chapter 4, we applied the present hybrid vortex penalization method to passive flow control using porous media. The modeling of flows in solid-fluid-porous media was performed through the variation of the λ penalization factor, corresponding to a non-dimensional quantity inversely proportional to the intrinsic permeability of the considered medium. The control studies were performed at different flow regimes around a semi-circular cylinder (in 2D) and a hemisphere (in 3D) containing a porous coating. Several parameter studies were carried out in order to determine efficient devices able to regularize the global flow and to decrease the drag. For this purpose, the parameters considered in these studies were the permeability, identified by the λ value, the thickness and the position of the added porous coating. Similar control trends were obtained in 2D and in 3D, highlighting first of all the fact that better performances were achieved with highly permeable and rather thick porous layers. Interestingly, it moreover turned out that the efficiency of the controlled device was highly correlated to the location of the porous coating: the control devices for which the porous area is only located in the vicinity of the detachment points indeed show much better results than the ones containing a whole porous layer at the surface. It was also noticed that, in some cases, thin porous coatings are sufficient to achieve satisfactory control performances. The confirmation of such assessments would need a comparison with experimental results. This point is actually under consideration and some partnership are being created with the experimental community in order to reproduce similar controlled devices and validate the results obtained with the proposed numerical study.

Bibliography

[Adams et al., 2007] Adams, B., Pauly, M., Keiser, R., and Guibas, L. (2007). Adaptively sampled particle fluids. *SIGGRAPH '07: ACM SIGGRAPH 2007 papers*, page 48.

[Adams et al., 1980] Adams, J. C., Swarztrauber, P., and Sweet, R. (1980). Fishpack: A package of fortran subprograms for the solution of separable elliptic PDE's. `https://www2.cisl.ucar.edu/resources/legacy/fishpack`.

[Aider et al., 2009] Aider, J.-L., Lasserre, J.-J., Beaudouin, J.-F., Herbert, V., and Wesfreid, J. E. (2009). Controle d'écoulement en aérodynamique automobile. In *19ème Congrès Francais de Mécanique, Marseille, 24-28 aout.*

[Anderson, 1989] Anderson, C. (1989). Vorticity boundary conditions and boundary vorticity generation for two-dimensional viscous incompressible flows. *J. Comput. Phys.*, 80:72–97.

[Anderson and Greengard, 1985] Anderson, C. and Greengard, C. (1985). On vortex methods. *SIAM J. Num. Anal.*, 22:413–440.

[Anderson and Reider, 1994] Anderson, C. and Reider, M. (1994). Investigation of the use of Prandtl/Navier-Stokes equation procedures for two-dimensional incompressible flows. *Physics of fluids*, 6(7):2380–2389.

[Angelidis and Neyret, 2005] Angelidis, A. and Neyret, F. (2005). Simulation of smoke based on vortex filament primitives. In *ACM-SIGGRAPH/EG Symposium on Computer Animation (SCA).*

[Angot et al., 1999] Angot, P., Bruneau, C.-H., and Fabrie, P. (1999). A penalization method to take into account obstacles in incompressible viscous flows. *Numer. Math.*, 81:497–520.

[Apte et al., 2008] Apte, S. V., Martin, M., and Patankar, N. A. (2008). A numerical method for Fully Resolved Simulation (FRS) of rigid particle-flow interactions in complex flows. *J. Comput. Phys.*, 228:2712–2738.

[Balaras, 2004] Balaras, E. (2004). Modeling complex boundaries using an external force field on fixed cartesian grids in large-eddy simulations. *Computers & Fluids*, 33(3):375–404.

[Bandringa, 2010] Bandringa, H. (2010). Immersed boundary methods. Master's thesis, University of Groningen, Faculty of mathematics and natural sciences.

[Batchelor, 1967] Batchelor, G. (1967). *An Introduction to Fluid Dynamics*. Cambridge University Press.

[Beale and Majda, 1982] Beale, J. and Majda, A. (1982). Vortex methods II: high order accuracy in 2 and 3 dimensions. *Math. Comput.*, 32:29–52.

[Beale and Majda, 1985] Beale, J. and Majda, A. (1985). High order accurate vortex methods with explicit velocity kernels. *J. Comput. Phys.*, 58:188–208.

[Beale, 1988] Beale, J. T. (1988). On the accuracy of vortex methods at large times. *Computational Fluid Dynamics and Reacting Gas Flows, B. Engquist et al., ed., Springer-Verlag, New York*, pages 19–32.

[Beale et al., 1991] Beale, J. T., Eydeland, A., and Turkington, B. (1991). Numerical tests of 3-D vortex methods using a vortex ring with swirl. *Vortex Dynamics and Vortex Methods, C. Anderson and C. Greengard, ed.*, A.M.S.:1–9.

[Beale and Majda, 1981] Beale, J. T. and Majda, A. (1981). Rates of convergence for viscous splitting of the Navier-Stokes equations. *Math. Comput.*, 37:243–259.

[Beavers and Joseph, 1967] Beavers, G. D. and Joseph, D. D. (1967). Boundary conditons at a naturally permeable wall. *J. Fluid Mech.*, 30:197–207.

[Benfatto and Pulvirenti, 1986] Benfatto, G. and Pulvirenti, M. (1986). Convergence of Chorin-Marsden product formula in the half-plane. *Commun. Math. Phys.*, 106:427–458.

[Bergdorf et al., 2005] Bergdorf, M., Cottet, G.-H., and Koumoutsakos, P. (2005). Multilevel adaptive particle methods for convection-diffusion equations. *Multiscale Modeling and Simulation: A SIAM Interdisciplinary Journal*, 4(1):328–357.

[Bergdorf and Koumoutsakos, 2006] Bergdorf, M. and Koumoutsakos, P. (2006). A Lagrangian particle-wavelet method. *SIAM Multiscale Model. Simul.*, 5:980–995.

[Bergmann et al., 2014] Bergmann, M., Hovnanian, J., and Iollo, A. (2014). An accurate cartesian method for incompressible flows with moving boundaries. *Commun. Comput. Phys.*, 15(5):1266–1290.

[Bideaux et al., 2011] Bideaux, E., Bobillier, P., Fournier, E., Gillieron, P., El Hajem, M., Champagne, J., Gilotte, P., and Kourta, A. (2011). Drag reduction by pulsed jets on strongly unstructured wake: towards the square back control. *Int. J. of Aerodynamics*, 1(3):282–298.

[Boisaubert and Texier, 1998] Boisaubert, N. and Texier, A. (1998). Effect of a splitter plate on the near-wake development of a semi-circular cylinder. *Experimental Thermal and Fluid Science*, 16:100–111.

[Borgers and Peskin, 1987] Borgers, C. and Peskin, C. (1987). A Lagrangian fractional step method for the incompressible Navier-Stokes equations on a periodic domain. *J. Comput. Phys.*, 70:397–438.

[Brandt, 1977] Brandt, A. (1977). Multi-level adaptive solutions to boundary-value problems. *Math. Comp.*, 31:333–390.

[Braza et al., 1986] Braza, M., Chassaing, P., and Minh, H. H. (1986). Numerical study and physical analysis of the pressure and velocity fields in the near wake of a circular cylinder. *J. Fluid Mech.*, 165:79–130.

[Breugem et al., 2005] Breugem, W. P., Boersma, B. J., and Uittenbogaard, R. E. (2005). The laminar boundary layer over a permeable wall. *Transp. Porous Med.*, 59:267–300.

[Bruneau et al., 2010] Bruneau, C.-H., Creusé, E., Depeyras, D., Gilliéron, P., and Mortazavi, I. (2010). Coupling active and passive techniques to control the flow past the square back ahmed body. *Comput. Fluids*, 38:1875–1892.

[Bruneau et al., 2008] Bruneau, C.-H., Gilliéron, P., and Mortazavi, I. (2008). Passive control around a two-dimensional square back ahmed body using porous media. *J. Fluids Engineering*, 130(6).

[Bruneau and Mortazavi, 2004] Bruneau, C.-H. and Mortazavi, I. (2004). Passive control of the flow around a square cylinder using porous media. *Int. J. Numer. Meth. Fluids*, 46:415–433.

[Bruneau and Mortazavi, 2006] Bruneau, C.-H. and Mortazavi, I. (2006). Control of vortex shedding around a pipe section using a porous sheat. *J. Offshore and Polar Eng.*, 16.

[Bruneau and Mortazavi, 2008] Bruneau, C.-H. and Mortazavi, I. (2008). Numerical modelling and passive flow control using porous media. *Comput. Fluids*, 37:488–498.

[Buzbee et al., 1970] Buzbee, B. L., Golub, G. H., and Nielson, C. W. (1970). On direct methods for solving Poisson's equations. *SIAM J. Numer. Anal.*, 7:627–656.

[Caltagirone, 1994] Caltagirone, J. P. (1994). Sur l'intéraction fluide-milieu poreux : Application au calcul des efforts exercés sur un obstacle par un fluide visqueux. *C. R. Acad. Sci. Paris*, 318.

[Campregher et al., 2009] Campregher, R., Militzer, J., Mansur, S., and da Silveira Neto, A. (2009). Computations of the flow past a still sphere at moderate Reynolds numbers using an immersed boundary method. *J. of the Braz. Soc. of Mech. Sci. & Eng.*, 31(4):344–352.

[Carbou, 2008] Carbou, G. (2008). Brinkmann model and double penalization method for the flow around a porous thin layer. *J. Math. Fluid Mech.*, 10:126–158.

[Casciola et al., 1996] Casciola, C.-M., Piva, R., and Bassanini, P. (1996). Vorticity generation on a flat surface in 3D flows. *J. Comput. Phys.*, 129:345–356.

[Chatelain et al., 2008] Chatelain, P., Curioni, A., Bergdorf, M., Rossinelli, D., Andreoni, W., and Koumoutsakos, P. (2008). Billion vortex particle direct numerical simulations of aircraft wakes. *Computer Methods in Applied Mechanics and Engineering*, 197:13–16:1296–1304.

[Cheer, 1983] Cheer, A. J. (1983). Numerical study of incompressible slightly viscous flow past blunt bodies and airfoils. *SIAM J. Sc. Stat. Comp.*, 4:685–705.

[Chen et al., 2009] Chen, K., Johnson, J., Dietschi, U., and Khalighi, B. (2009). Wind noise measurements for automotive mirrors. *SAE Paper*, 2009–01–0184.

[Choquin and Huberson, 1989] Choquin, J. and Huberson, S. (1989). Particle simulation of viscous flow. *Comput. Fluids*, 17:397–410.

[Choquin and Cottet, 1988] Choquin, J.-P. and Cottet, G.-H. (1988). Sur l'analyse d'une classe de methodes de vortex tridimensionnelles. *C. R. Acad. Sci., Paris*, Ser. I 306:739–742.

[Choquin and Lucquin-Desreux, 1988] Choquin, J.-P. and Lucquin-Desreux, B. (1988). Accuracy of a deterministic particle method for the Navier-Stokes equations. *Int. J. Num. Fluids*, 8:1439–1458.

[Chorin, 1973] Chorin, A. J. (1973). Numerical study of slighly viscous flow. *J. Fluid Mech.*, 57:785–796.

[Chorin, 1978] Chorin, A. J. (1978). Vortex sheet approximation of boundary layers. *J. Comput. Phys.*, 27:428–442.

[Chorin, 1980] Chorin, A. J. (1980). Vortex models and boundary layer instability. *SIAM J. Sc. Stat. Comp.*, 1:1–21.

[Chorin, 1989] Chorin, A. J. (1989). Computational fluid mechanics. *Academic Press, New York.*

[Chorin and Bernard, 1973] Chorin, A. J. and Bernard, P. S. (1973). Discretization of a vortex sheet, with an example of roll-up. *J. Comput. Phys.*, 13:423–429.

[Chorin et al., 1978] Chorin, A. J., Hughes, T. J. R., McCracken, M., and Marsden, J. E. (1978). Product formulas and numerical algorithms. *Commun. Pure and Appl. Math.*, 31:205.

[Christiansen, 1973] Christiansen, J. (1973). Numerical solution of hydrodynamics by the method of point vortices. *J. Comput. Phys.*, 13:363–379.

[Constantinescu and Squires, 2000] Constantinescu, G. S. and Squires, K. D. (2000). LES and DES investigations of turbulent flow over a sphere. *AIAA Paper 2000-0540*.

[Coquerelle and Cottet, 2008] Coquerelle, M. and Cottet, G.-H. (2008). A vortex level-set method for the two-way coupling of an incompressible fluid with colliding rigid bodies. *J. Comput. Phys.*, 227:9121–9137.

[Cottet, 1982] Cottet, G.-H. (1982). PhD thesis, Université Paris 6, Paris, France.

[Cottet, 1988a] Cottet, G.-H. (1988a). A new approach for the analysis of vortex methods in two and three dimensions. *Annales de l'I. H. P., Analyse non linéaire*, section C, tome 5 (3):227–285.

[Cottet, 1988b] Cottet, G.-H. (1988b). Vorticity boundary conditions and the deterministic vortex method for the Navier-Stokes equation. *Mathematical Aspects of Vortex Dynamic, Leesburg, Virginia, april 25-27*, pages 128–143.

[Cottet, 1991] Cottet, G.-H. (1991). Particle-grid domain decomposition methods for the Navier-Stokes equations in exterior domains. *Vol. 28 of Lectures in Applied Mathematics Series, American Mathematical Society, New York*, pages 100–118.

[Cottet, 1994] Cottet, G.-H. (1994). A vorticity creation algorithm for the Navier-Stokes equations in arbitrary domain. *Navier-Stokes equations and related non-linear problems, A. Sequeira (ed), Plenum Press.*

[Cottet, 1996] Cottet, G.-H. (1996). Artificial viscosity models for vortex and particle methods. *J. Comput. Phys.*, 127:199–208.

[Cottet et al., 2014] Cottet, G.-H., Etancelin, J.-M., Perignon, F., and Picard, C. (2014). High order semi-lagrangian particles for transport equations: numerical analysis and implementation issues. *ESAIM: Mathematical Modelling and Numerical Analysis*, 48:1029–1064.

[Cottet and Koumoutsakos, 2000] Cottet, G.-H. and Koumoutsakos, P. (2000). *Vortex Methods - Theory and Practice*. Cambridge University Press.

[Cottet et al., 2000] Cottet, G.-H., Koumoutsakos, P., and Ould-Salihi, M. (2000). Vortex methods with spatially varying cores. *J. Comput. Phys.*, 162 (1):164–185.

[Cottet and Magni, 2009] Cottet, G.-H. and Magni, A. (2009). TVD remeshing schemes for particle methods. *C. R. Acad. Sci. Paris*, Ser. I, 347:1367–1372.

[Cottet and Mas-Gallic, 1983] Cottet, G.-H. and Mas-Gallic, S. (1983). Une méthode de décomposition pour une équation de type convection-diffusion combinant résolution explicite et méthode particulaire. *C. R. Acad. Sci. Paris*, 297:133–136.

[Cottet and Mas-Gallic, 1990] Cottet, G.-H. and Mas-Gallic, S. (1990). A particle method to solve the Navier-Stokes system. *Num. Math.*, 57:1–23.

[Cottet and Poncet, 2003] Cottet, G.-H. and Poncet, P. (2003). Advances in direct numerical simulation of 3D wall-bounded flows by Vortex-In-Cell methods. *J. Comput. Phys.*, 193:136–158.

[Cottet and Weynans, 2006] Cottet, G.-H. and Weynans, L. (2006). Particle methods revisited: a class of high-order finite-difference schemes. *C. R. Acad. Sci. Paris*, 343:51–56.

[Cottet and Wray, 1997] Cottet, G.-H. and Wray, A. (1997). Anisotropic grid-based formulas for subgrid-scale models. *Annual Research Briefs, Center for Turbulence Research, Stanford.*

[Degond and Mas-Gallic, 1989] Degond, P. and Mas-Gallic, S. (1989). The weighted particle method for convection-diffusion equations. *Math. Comput.*, 53:485–526.

[Dolek et al., 2004] Dolek, O., Ozkan, G., and Ozdemir, I. (2004). Structures of flow around a full scale side mirror of a car with relevance to aerodynamic noise. *Journal of Automobile Engineering*, 218:1085–1097.

[Dongli and Hong, 2012] Dongli, Z. and Hong, Q. (2012). Energy-centric adaptive particle fluid simulation based on wavelet analysis. Technical report, Stony Brook University, USA.

[E and Liu, 1996] E, W. and Liu, J. (1996). Finite-difference schemes for incompressible flows in vorticity formulation. *Vortex Flows and Related Numerical Methods II, ESAIM Proc*, pages 181–195.

[Eldredge et al., 2002] Eldredge, J., Colonius, T., and Leonard, A. (2002). A general deterministic treatment of derivatives in particle methods. *J. Comput. Phys.*, 180:686–709,.

[Etancelin, 2014] Etancelin, J.-M. (2014). *Couplage de modèles, algorithmes multi-échelles et calcul hybride.* PhD thesis, Université de Grenoble.

[Fadlun et al., 2000] Fadlun, E., Verzicco, R., Orlandi, P., and Mohd-Yusof, J. (2000). Combined immersed-boundary finite-difference methods for three-dimensional complex flow simulations. *J. Comput. Phys.*, 161(1):35–60.

[Farhadi et al., 2010] Farhadi, M., Sedighi, K., and Fattahi, E. (2010). Effect of a splitter plate on flow over a semi-circular cylinder. In *Proceedings of the Institution of Mechanical Engineers, Part G: Journal of Aerospace Engineering*, pages 224–321.

[Farjoun and Seibold, 2009] Farjoun, Y. and Seibold, B. (2009). An exactly conservative particle method for one dimensional scalar conservation laws. *J. Comput. Phys.*, 228:5298–5315.

[Fishelov, 1990a] Fishelov, D. (1990a). A new vortex scheme for viscous flows. *J. Comput. Phys.*, 86:211–224.

[Fishelov, 1990b] Fishelov, D. (1990b). Vortex methods for slightly viscous three dimensional flow. *SIAM J. Sc. Stat. Comp.*, 3:399–424.

[Frigo and Johnson, 2005] Frigo, M. and Johnson, S. G. (2005). The design and implementation of FFTW3. *Proceedings of the IEEE, Invited paper, Special Issue on Program Generation, Optimization, and Platform Adaptation*, 93(2):216–231.

[Fronteau and Combis, 1984] Fronteau, J. and Combis, P. (1984). A lie admissible method of integration of Folkler-Plank equations with non linear coefficients (exact and numerical solutions),. *Hadronic J.*, 7:911–930.

[Gallizio, 2009] Gallizio, F. (2009). *Analytical and numerical vortex methods to model separated flows.* PhD thesis, Politecnico di Torino.

[Gazzola, 2013] Gazzola, M. (2013). *Simulation, optimization and learning of artificial swimmers*. PhD thesis, ETH Zurich, Switzerland.

[Gazzola et al., 2011] Gazzola, M., Chatelain, P., van Rees, W. M., and Koumoutsakos, P. (2011). Simulations of single and multiple swimmers with non-divergence free deforming geometries. *J. Comput. Phys.*, 230:7093–7114.

[Gazzola et al., 2014] Gazzola, M., Hejazialhosseini, B., and Koumoutsakos, P. (2014). Reinforcement learning and wavelet adapted vortex methods for simulations of self-propelled swimmers. *SIAM J. Sci. Comput.*, 36(3):B622–B639.

[Gazzola et al., 2012] Gazzola, M., van Rees, W. M., and Koumoutsakos, P. (2012). C-start: optimal start of larval fish. *J. Fluid Mech.*, 698:5–18.

[Gerrard, 1978] Gerrard, J. (1978). The wakes of cylindrical bluff bodies at low Reynolds number. *Transactions of the Royal Soc., London*, Series A, 288 (A1354):351–382.

[Gharakhani and Ghoniem, 1998] Gharakhani, A. and Ghoniem, A. (1998). Simulation of the piston driven flow inside a cylinder with an eccentric port. *J. Fluids Eng.*, 120:319–326.

[Gilliéron, 2001] Gilliéron, P. (2001). Analyse de la contribution des plaques séparatrices à la réduction de la trainée aérodynamique. Technical report, Note interne RENAULT n0455/64260/2001.

[Goodman, 1987] Goodman, J. (1987). Convergence of the random vortex method. *Comm. Pure Appl. Math.*, 40(2):189–220.

[Goodman et al., 1990] Goodman, J., Hou, T., and Lowengrub, J. (1990). Convergence of the point vortex method for the 2-D Euler equations. *Commun. Pure Appl. Math.*, 43:415–430.

[Gosselin, 2009] Gosselin, F. (2009). *Mécanismes d'intéractions fluide-structure entre écoulements et végétation*. PhD thesis, Ecole Polytechnique, Palaiseau, France.

[Gottlieb and Shu, 1998] Gottlieb, S. and Shu, C. W. (1998). Total variation diminishing Runge-Kutta schemes. *Mathematics of Computation*, 67:73–85.

[Greengard and Rokhlin, 1987] Greengard, L. and Rokhlin, V. (1987). A fast algorithm for particle simulations. *J. Comput. Phys.*, 73(2):325–348.

[Guermond et al., 1993] Guermond, J.-L., Huberson, S., and Shen, W.-Z. (1993). Simulation of 2D external viscous flows by means of a domain decomposition method. *J. Comput. Phys.*, 108:343–352.

[Gustafasson and Sethian, 1991] Gustafasson, K. and Sethian, J. (1991). ed., Vortex Methods and Vortex Motion. *SIAM, Philadelphia*.

[Hahn et al., 2002] Hahn, S., Je, J., and Choi, H. (2002). Direct numerical simulation of turbulent channel flow with permeable walls. *J. Fluid Mech.*, 450:259–285.

[Hald, 1979] Hald, O. (1979). Convergence of vortex methods II. *SIAM J. Num. Anal*, 16:726–755.

[Hanspal et al., 2006] Hanspal, N., Waghode, A., Nassehi, V., and Wakeman, R. (2006). Numerical analysis of coupled Stokes/Darcy flows in industrial filtrations. *Transp. Porous Med.*, 64:73–101.

[Hejlesen et al., 2015] Hejlesen, M., Koumoutsakos, P., Leonard, A., and Walther, J. (2015). Iterative Brinkman penalization for remeshed vortex methods. *J. Comput. Phys.*, 280:547–562.

[Henshaw et al., 1989] Henshaw, W., Kreiss, H.-O., and Reyna, L. (1989). On the smallest scale for the compressible Navier-Stokes equations. *Theor. Comput. Fluid Dyn.*, 1:65–95.

[Henshaw et al., 1991] Henshaw, W., Kreiss, H.-O., and Reyna, L. (1991). On the smallest scale estimates and a comparison of the vortex method to the Pseudo-Spectral method. *Lectures in Appl. Math.*, 28:303.

[Hojjat et al., 2014] Hojjat, M., Stavropoulou, E., and Bletzinger, K.-U. (2014). The vertex morphing method for node-based shape optimization. *Comput. Methods Appl. Mech. Engrg.*, 268:494–513.

[Hou et al., 1991] Hou, T., Lowengrub, J., and Krasny, R. (1991). Convergence of a point vortex method for vortex sheets. *SIAM J. Num. Anal.*, 28:308–320.

[Huberson and Jollès, 1990] Huberson, S. and Jollès, A. (1990). Correction de l'erreur de projection dans les méthodes particules/maillage. *La recherche aérospatiale*, 4:1–6.

[Iaccarino and Verzicco, 2003] Iaccarino, G. and Verzicco, R. (2003). Immersed boundary technique for turbulent flow simulations. *Applied Mechanics Reviews*, 56(3):331–347.

[Jimenez et al., 2001] Jimenez, J., Uhlmann, M., Pinelli, A., and Kawahara, G. (2001). Turbulent shear flow over active and passive porous surfaces. *J. Fluid Mech.*, 442:89–117.

[Johnson and Patel, 1999] Johnson, T. A. and Patel, V. C. (1999). Flow past a sphere up to a Reynolds number of 300. *J. Fluid Mech.*, 378:19–70.

[Kevlahan and Ghidaglia, 2001] Kevlahan, N. and Ghidaglia, J. M. (2001). Computation of turbulent flow past an array of cylinders using a spectral method with Brinkman penalization. *Eur. J. Mech.*, B 20:333–350.

[Khalighi et al., 2001] Khalighi, B., Zhang, S., Koromilas, C., Balkanyi, S., Bernal, L., Iaccarino, G., and Moin, P. (2001). Experimental and computational study of unsteady wake flow behind a bluff body with a drag reduction device. *SAE SP-1600, Detroit, Michigan.*

[Kim and Choi, 2002] Kim, D. and Choi, H. (2002). Laminar flow past a sphere rotating in the streamwise direction. *J. Fluid Mech.*, 461:365–386.

[Kim and Choi, 2003] Kim, D. and Choi, H. (2003). Laminar flow past a hemisphere. *Physics of Fluids*, 15(8):2457–2460.

[Kornev et al., 2013] Kornev, N., Jacobi, G., and Zhdanov, V. (2013). Development of a hybrid approach using coupled grid-based and grid-free methods. *V International Conference on Computational Methods in Marine Engineering.*

[Koumoutsakos, 1997] Koumoutsakos, P. (1997). Inviscid axisymmetrization of an elliptical vortex. *J. Comput. Phys.*, 138:821–857.

[Koumoutsakos, 2005] Koumoutsakos, P. (2005). Multiscale flow simulations using particles. *Ann. Rev. Fluid Mechanics*, 37:457–487.

[Koumoutsakos and Leonard, 1995] Koumoutsakos, P. and Leonard, A. (1995). High-resolution simulations of the flow around an impulsively started cylinder using vortex methods. *J. Fluid Mech.*, 296:1–38.

[Koumoutsakos et al., 1994] Koumoutsakos, P., Leonard, A., and Pépin, F. (1994). Boundary conditions for viscous vortex methods. *J. Comput. Phys.*, 113(1):52–61.

[Krasny, 1986] Krasny, R. (1986). A study of singularity formation in a vortex sheet by the point vortex approximation. *J. Fluid Mech.*, 167:65–93.

[Kudela and Kozlowski, 2009] Kudela, H. and Kozlowski, T. (2009). Vortex-in-cell method for exterior problems. *Journal of theoretical and applied mechanics*, 47(4):779–796.

[Labbé et al., 2003] Labbé, S., Laminie, J., and Louvet, V. (2003). Méthodologie et environnement de développement orientés objets : de l'analyse mathématique à la programmation. *MATAPLI*, 70.

[Lagaert et al., 2014] Lagaert, J.-B., Balarac, G., and Cottet, G.-H. (2014). Hybrid spectral particle method for the turbulent transport of a passive scalar. *J. Comput. Phys.*, 260:127–142.

[Leclerc, 2008] Leclerc, C. (2008). *Réduction de la trainée d'un véhicule automobile à l'aide du controle actif par jet synthétique*. PhD thesis, Insitut Mécanique des Fluides de Toulouse.

[Leonard, 1974] Leonard, A. (1974). Energy cascade in large-eddy simulations of turbulent fluid flows. *Advances in Geophysics A*, 18:237–248.

[Leonard, 1975] Leonard, A. (1975). Numerical simulation of interacting vortex filaments. In *Proceedings of the IV Intl. Conference on Numerical Methods of Fluid Dynamics, Springer-Verlag, New York.*

[Leonard, 1980] Leonard, A. (1980). Vortex methods for flow simulation. *J. Comput. Phys.*, 37:289–335.

[Leonard, 1985] Leonard, A. (1985). Computing three-dimensional incompressible flows with vortex elements. *Ann. Rev. Fluid Mech.*, 17:523–559.

[Lewis, 1990] Lewis, R. I. (1990). *Vortex Element Methods for Fluid Dynamic Analysis of Engineering Systems*. Cambridge.

[Lifschitz et al., 1996] Lifschitz, A., Suters, H., and Beale, T. (1996). A numerical and analytical study of vortex rings with swirl. *ESAIM: Proceedings*, 1:565–575.

[Lighthill, 1963] Lighthill, M. J. (1963). Introduction. boundary layer theory. *J. Rosenhead, ed., Oxford U. Press, New York*, pages 54–61.

[Liu, 2001] Liu, C. H. (2001). A three-dimensional vortex particle-in-cell method for vortex motions in the vicinity of a wall. *International Journal for Numerical Methods in Fluids*, 37 (5):501–523.

[Liu and Masliyah, 2005] Liu, S. and Masliyah, J. (2005). *Handbook of Porous Media*, chapter Dispersion in porous media, pages 81–140. Ed. K. Vafai, second edition, Taylor and Francis, Boca, Raton, FL.

[Loiseau et al., 2014] Loiseau, J.-C., Robinet, J.-C., Cherubini, S., and Leriche, E. (2014). Investigation of the roughness-induced transition: global stability analyses and direct numerical simulations. *J. Fluid Mech.*, 760:175–211.

[Long, 1988] Long, D.-G. (1988). Convergence of the random vortex method in two dimensions. *J. Amer. Math. Soc*, 1:779–804.

[Lounsberry et al., 2007] Lounsberry, T., Gleason, M., and Puskarz, M. (2007). Laminar flow whistle on a vehicle side mirror. *SAE Paper*, 2007–01–1549.

[Magni, 2011] Magni, A. (2011). *Méthodes particulaires avec remaillage : analyse numérique, nouveaux schémas et applications pour la simulation d'équations de transport*. PhD thesis, Université de Grenoble, France.

[Magni and Cottet, 2012] Magni, A. and Cottet, G.-H. (2012). Accurate, non-oscillatory remeshing schemes for particle methods. *J. Comput. Phys.*, 231(1):152–172.

[Manickathan, 2014] Manickathan, L. B. (2014). Hybrid Eulerian-Lagrangian vortex particle method : A fast and accurate numerical method for 2D vertical-axis wind turbine. Master's thesis, Delft University of Technology, Department Of Aerodynamics and Wind Energy.

[Marchioro and Pulvirenti, 1982] Marchioro, C. and Pulvirenti, M. (1982). Hydrodynamics in two dimensions and vortex theory. *Commun. Math. Phys.*, 84:483–503.

[Marzouk and Ghoniem, 2005] Marzouk, Y. M. and Ghoniem, A. F. (2005). K-means clustering for optimal partitioning and dynamic load balancing of parallel hierarchical N-body simulations. *J. Comput. Phys.*, 207(2):493–528.

[Mehta and Pallis, 2001] Mehta, R. and Pallis, J. M. (2001). The aerodynamics of a tennis ball. *Sports Engineering*, 4(4):177–189.

[Milinazzo and Saffman, 1977] Milinazzo, F. and Saffman, P. G. (1977). The calculation of large reynolds number two-dimensional flow using discrete vortices with random walk. *J. Comput. Phys.*, 23:380–392.

[Mimeau et al., 2015] Mimeau, C., Gallizio, F., Cottet, G.-H., and Mortazavi, I. (2015). Vortex penalization method for bluff body flows. *Int. J. Numer. Meth. Fluids*, DOI: 10.1002/fld.4038.

[Mittal and Iaccarino, 2005] Mittal, R. and Iaccarino, G. (2005). Immersed boundary methods. *Annu. Rev. Fluid Mech.*, 37:239–61.

[Mittal and Kumar, 2001] Mittal, S. and Kumar, V. (2001). Flow-induced vibrations of a light circular cylinder at reynolds numbers 1000 to 10000. *Journal of Sound and Vibration*, 245:923–946.

[Mohamed-Kassim and Filippone, 2010] Mohamed-Kassim, Z. and Filippone, A. (2010). Fuel savings on a heavy vehicle via aerodynamic drag reduction. *Transportation Research Part D*, 15:275–284.

[Mohd-Yusof, 1997] Mohd-Yusof, J. (1997). Combined immersed-boundary/B-spline methods for simulations of flow in complex geometries. *Center for Turbulence Research Annual Research Briefs*, 161(1):317–327.

[Monaghan, 1985] Monaghan, J. (1985). Extrapolating B-splines for interpolation. *J. Comput. Phys.*, 60:253–262.

[Morency et al., 2012] Morency, F., Beaugendre, H., and Gallizio, F. (2012). Aerodynamic force evaluation for ice shedding phenomenon using vortex in cell scheme, penalisation and level set approaches. *International Journal of Computational Fluid Dynamics*, 26(9–10):435–450.

[Morgenthal and Walther, 2007] Morgenthal, G. and Walther, J. H. (2007). An immersed interface method for the Vortex-In-Cell algorithm. *Computers and Structures*, 85:712–726.

[Nield and Bejan, 1999] Nield, D. A. and Bejan, A. (1999). *Convection in Porous Media*. Springer.

[Noca et al., 1999] Noca, F., Shiels, D., and Jeon, D. (1999). A comparison of methods for evaluating time-dependent fluid dynamic forces on bodies, using only velocity fields and their derivatives. *J. Fluids Struct.*, 13:551–578.

[Olsson, 2011] Olsson, M. (2011). Designing and optimizing side-view mirrors. Master's thesis, Chalmers University of Technology, Department of Applied Mechanics.

[Ono et al., 1999] Ono, K., Himeno, R., and Fukushima, T. (1999). Prediction of wind noise radiated from passenger cars and its evaluation based on auralization. *Journal of Wind Engineering and Industrial Aerodynamics*, 81:403–419.

[Orszag and Israeli, 1974] Orszag, S. and Israeli, M. (1974). Numerical simulation of viscous incompressible flows. *Annu. Rev. Fluid. Mech.*, 6:281–318.

[Othmer, 2014] Othmer, C. (2014). Adjoint methods for car aerodynamics. *Journal of Mathematics in Industry*, 4:6.

[Ould-Sahili, 1998] Ould-Sahili, M. L. (1998). *Couplage de méthodes numériques en simulation directe d'écoulements incompressibles*. PhD thesis, Université Joseph Fourier - Grenoble I.

[Ould-Salihi et al., 2000] Ould-Salihi, M., Cottet, G.-H., and El Hamraoui, M. (2000). Blending finite-difference and vortex methods for incompressible flow computations. *SIAM J. Sci. Comp.*, 22:1655–1674.

[Pan and Chew, 2002] Pan, L. S. and Chew, Y. T. (2002). A general formula for calculating forces on a 2-D arbitrary body in incompressible flow. *J. Fluids Struct.*, 16(1):71–82.

[Park et al., 2007] Park, P., Jeon, W.-P., Choi, H., and Yoo, J. Y. (2007). Mixing enhancement behind a backward-facing step using tabs. *Phys. Fluids*, 19-105103.

[Parker and Balachandar, 2001] Parker, S. J. and Balachandar, S. (2001). Stability and vortex shedding of bluff body arrays. Technical report, Air Conditioning and Refrigeration Center. College of Engineering. University of Illinois at Urbana-Champaign.

[Pasquetti et al., 2008] Pasquetti, R., Bwemba, R., and Cousin, L. (2008). A pseudo-penalization method for high Reynolds number unsteady flows. *Applied Numerical Mathematics*, 58:946–954.

[Pasquetti and Peres, 2015] Pasquetti, R. and Peres, N. (2015). A penalty model of synthetic micro-jet actuator with application to the control of wake flows. *Computers & Fluids,*, 114:203–217.

[Peskin, 1972] Peskin, C. (1972). Flow patterns around heart valves: A numerical method. *J. Comput. Phys.*, 10(2):252–271.

[Peskin, 1977] Peskin, C. (1977). Numerical analysis of blood flow in the heart. *J. Comput. Phys.*, 25:220–252.

[Peyret and Taylor, 1983] Peyret, R. and Taylor, T. D. (1983). Computational methods for fluid flow. *Springer-Verlag, New York*.

[Ploumhans and Winckelmans, 2000] Ploumhans, P. and Winckelmans, G. S. (2000). Vortex methods for high-resolution simulations of viscous flow past bluff bodies of general geometry. *J. Comput. Phys.*, 165:354–406.

[Ploumhans et al., 2002] Ploumhans, P., Winckelmans, G. S., Salmon, J. K., Leonard, A., and Warren, M. S. (2002). Vortex methods for direct numerical simulation of three-dimensional bluff body flows: Applications to the sphere at $Re = 300$, 500 and 1000. *J. Comput. Phys.*, 178:427–463.

[Pluvinage et al., 2014] Pluvinage, F., Kourta, A., and Bottaro, A. (2014). Instabilities in the boundary layer over a permeable, compliant wall. *Physics of Fluids*, 26.

[Poncet, 2001] Poncet, P. (2001). *Méthodes particulaires pour la simulation des sillages tridimensionnels*. PhD thesis, Université Joseph-Fourier - Grenoble I.

[Poon et al., 2009] Poon, E., Iaccarino, G., Ooi, A., and Giacobello, M. (2009). Numerical studies of high Reynolds number flow past a stationary and rotating sphere. *Seventh International Conference on CFD in the Minerals and Process Industries CSIRO, Melbourne, Australia*.

[Prager, 1928] Prager, W. (1928). Die druckverteilung an korpern in ebener potentialstromung. *Physikalische Zeitschrift*, 29:865–869.

[Prandtl, 1904] Prandtl, W. (1904). Uber flussigkeitbewegung bei sehr kleiner reibung,. In *Proceedings of the Fourth Mathematics Congress, Heidelberg, 484–491*.

[Protas, 2007] Protas, P. (2007). On an attempt to simplify the Quartapelle-Napolitano approach to computation of hydrodynamic forces in open flows. *J. Fluids Struct.*, 23:1207–1214.

[Quartapelle, 1981] Quartapelle, L. (1981). Vorticity conditioning in the computation of two-dimensional viscous flows. *J. Comput. Phys.*, 40:453–477.

[Quartapelle and Napolitano, 1982] Quartapelle, L. and Napolitano, M. (1982). Force and moment in incompressible flows. *AIAA J.*, 21:911–913.

[Rasmussen et al., 2011] Rasmussen, J. T., Cottet, G.-H., and Walther, J. H. (2011). A multiresolution remeshed vortex-in-cell algorithm using patches. *J. Comput. Phys.*, 230:6742–6755.

[Rees and Morton, 1991] Rees, M. D. and Morton, K. W. (1991). Moving point, particle, and free-Lagrange methods for convection-diffusion equations. *SIAM J. Sci. and Stat. Comput.*, 12(3):547–572.

[Rehbach, 1978] Rehbach, C. (1978). Numerical calculation of three-dimensional unsteady flows with vortex sheets. *AIAA Paper*, 111.

[Rivoalen et al., 1997] Rivoalen, E., Huberson, S., and Hauville, F. (1997). Simulation numérique des équations de Navier-Stokes 3D par une méthode particulaire. *Comptes Rendus de l'Académie des Sciences - Series IIB - Mechanics-Physics-Chemistry-Astronomy*, 324:543–549.

[Roache, 1972] Roache, P. J. (1972). Computational fluid dynamics. *Hermosa Publishers, Albuquerque*.

[Roos and Willmarth, 1971] Roos, F. W. and Willmarth, W. W. (1971). Some experimental results on sphere and disk drag. *AIAA J.*, 9:285–291.

[Rosenhead, 1931] Rosenhead, L. (1931). The formation of vortices from a surface of discontinuity. *Proc. R. Soc. London Ser. A*, 134(823):170–192.

[Roshko, 1961] Roshko, A. (1961). Experiments on the flow past a circular cylinder at very high Reynolds number. *J. Fluid Mech.*, 10(3):345–356.

[Rossinelli, 2011] Rossinelli, D. (2011). *Multiresolution flow simulations on multi/many-core architectures*. PhD thesis, ETH Zurich.

[Rossinelli et al., 2015] Rossinelli, D., Hejazialhosseini, B., van Rees, W. M., Gazzola, M., Bergdorf, M., and Koumoutsakos, P. (2015). MRAG-I2D: Multi-resolution adapted grids for remeshed vortex methods on multicore architectures. *J. Comput. Phys.*, 288:1–18.

[Rouméas et al., 2009] Rouméas, M., Gilliéron, P., and Kourta, A. (2009). Analysis and control of the near-wake flow over a square-back geometry. *Computers & Fluids*, 38:60–70.

[Russell and Wang, 2003] Russell, D. and Wang, Z. J. (2003). A cartesian grid method for modeling multiple moving objects in 2D incompressible viscous flow. *J. Comput. Phys.*, 191:177–205.

[Russo and Strain, 1994] Russo, G. and Strain, J. (1994). Fast triangulated vortex methods for the 2D Euler equations. *J. Comput. Phys.*, 111:291–323.

[Saffman, 1992] Saffman, P. G. (1992). *Vortex Dynamics*. Cambridge University Press.

[Sbalzarini et al., 2006] Sbalzarini, I., Walther, J., Bergdorf, M., Hieber, S., Kotsalis, E., and Koumoutsakos, P. (2006). PPM - a highly efficient parallel particle-mesh library for the simulation of continuum systems. *J. Comput. Phys.*, 215:566–588.

[Schoenberg, 1946] Schoenberg, I. J. (1946). Contributions to the problem of approximation of equidistant data by analytic functions. *Quarterly of Applied Mathematics*, 4.2.

[Schrader et al., 2010] Schrader, B., Sbalzarini, I., and Redoux, S. (2010). Discretization correction of general integral PSE operators for particle methods. *J. Comput. Phys.*, 229:4159–4182.

[Secomb et al., 2001] Secomb, T., Hsu, R., and Pries, A. (2001). Effect of the endothelial surface layer on transmission of fluid shear stress to endothelial cells. *Biorheology*, 38:143–150.

[Sethian and Ghoniem, 1988] Sethian, J. A. and Ghoniem, A. F. (1988). Validation study of vortex methods. *J. Comput. Phys.*, 74:283–317.

[Shankar and van Dommelen, 1996] Shankar, S. and van Dommelen, L. (1996). A new diffusion procedure for vortex methods. *J. Comput. Phys.*, 127:88–109.

[Smith and Stansby, 1988] Smith, P. and Stansby, P. (1988). Impulsively started flow around a circular cylinder by the vortex method. *J. Fluid Mech.*, 194:45–77.

[Smith and Stansby, 1989] Smith, P. and Stansby, P. (1989). An efficient surface algorithm for random-particle simulation of vorticity and heat transport. *J. Comput. Phys.*, 81:349–371.

[Sterenborg et al., 2014] Sterenborg, J., van Zuijlen, A., and Bijl, H. (2014). Experimental benchmark of a free plunging wing with imposed flap oscillations. *Journal of Fluids and Structures*, 49:338–359.

[Strain, 1997] Strain, J. (1997). Fast adaptive 2D vortex methods. *J. Comput. Phys.*, 132:108–122.

[Sumer and Fredsoe, 2006] Sumer, B. and Fredsoe, J. (2006). *Hydrodynamics Around Cylindrical Structures*. World Scientific.

[Tomboulides and Orszag, 2000] Tomboulides, A. and Orszag, A. (2000). Numerical investigation of transitional and weak turbulent flow past a sphere. *J. Fluid Mech.*, 416:45–73.

[Udaykumar et al., 2001] Udaykumar, H., Mittal, R., Rampunggoon, P., and Khanna, A. (2001). A sharp interface cartesian grid method for simulating flows with complex moving boundaries. *J. Comput. Phys.*, 174(1):345–380.

[Udaykumar et al., 1999] Udaykumar, H., Mittal, R., and Shyy, W. (1999). Computation of solid-liquid phase fronts in the sharp interface limit on fixed grids. *J. Comput. Phys.*, 153 (2):535–574.

[van Dommelen, 1986] van Dommelen, L. L. (1986). Computation of unsteady separation using lagrangian procedures. In *IUTAM Symposium on boundary layer separation, London, England*, pages 73–87.

[van Rees, 2014] van Rees, W. M. (2014). Personal communication, July 14, 2014.

[van Rees et al., 2013] van Rees, W. M., Gazzola, M., and Koumoutsakos, P. (2013). Optimal shapes for anguilliform swimmers at intermediate reynolds numbers. *J. Fluid Mech.*, 722.

[van Rees et al., 2011] van Rees, W. M., Leonard, A., Pullin, D., and Koumoutsakos, P. (2011). A comparison of vortex and pseudo-spectral methods for the simulation of periodic vortical flows at high reynolds numbers. *J. Comput. Phys.*, 230(8):2794–2805.

[Vaseashta and Dimova-Malinovska, 2005] Vaseashta, A. and Dimova-Malinovska, D. (2005). Nanostructured and nanoscale devices, sensors and detectors. *Science and Technology of Advanced Materials*, 6:312–318.

[Venkataraman and Bottaro, 2012] Venkataraman, D. and Bottaro, A. (2012). Numerical modeling of flow control on a symmetric aerofoil via a porous, compliant coating. *Phys. Fluids*, 24:093601.

[Verzicco et al., 2000] Verzicco, R., Mohd-Yusof, J., Orlandi, P., and Haworth, D. (2000). LES in complex geometries using boundary body forces. *AIAA J.*, 38:427–433.

[von Kármán, 1912] von Kármán, T. (1912). Nachr. ges. wissenschaft. *Gottingen*, pages 547–556.

[Wang, 1995] Wang, S.-C. (1995). *Control of dynamic stall.* PhD thesis, FAMU-FSU, College of Engineering, Tallahassee, Florida, USA.

[Watkins and Oswald, 1999] Watkins, S. and Oswald, G. (1999). The flow field of automobile add-ons-with particular reference to the vibration of external mirrors. *Journal of Wind Engineering and Industrial Aerodynamics*, 83:54–554.

[Whitaker, 1999] Whitaker, S. (1999). *The Method of Volume Averaging.* Kluwer: Dordercht.

[Williamson, 1988] Williamson, C. (1988). The existence of two stages in the transition of three-dimensionality of a cylinder wake. *Phys. Fluids*, 31(11):3165–3168.

[Wu and Faeth, 1993] Wu, J. and Faeth, G. (1993). Sphere wakes in still surroundings at intermediate Reynolds numbers. *AIAA J.*, 31(8):1448–1455.

[Ye et al., 1999] Ye, T., Mittal, R., Udaykumar, H., and Shyy, W. (1999). An accurate cartesian grid method for viscous incompressible flows with complex immersed boundaries. *J. Comput. Phys.*, 156(2):209–240.

[Yokota et al., 2009] Yokota, R., Narumi, T., Sakamaki, R., Kameoka, S., Obi, S., and Yasuoka, K. (2009). Fast multipole methods on a cluster of GPUs for the meshless simulation of turbulence. *Comp. Physics Comm.*, 180(11):2066–2078.

A

Calculation of the dimensionless terms of the Brinkman Navier-Stokes equation

From the following relations:

$$\omega = \omega' \frac{\bar{\mathbf{u}}}{H} \qquad \mathbf{u} = \mathbf{u}'\bar{\mathbf{u}} \qquad x = x'H \qquad t = t'\bar{t} = t'\frac{H}{\bar{\mathbf{u}}} \qquad \lambda = \lambda'\frac{1}{\bar{t}}, \tag{A.1}$$

one evaluates the dimensionless formulation of each term of the following dimensional penalized Vortex-Transport-Equation :

$$\frac{\partial \omega}{\partial t} + (\mathbf{u}\cdot\nabla)\omega - (\omega\cdot\nabla)\mathbf{u} = \nabla \times \Big(\lambda\ \chi_b(\mathbf{u}_b - \mathbf{u})\Big) + \nu\Delta\omega. \tag{A.2}$$

Vorticity time derivative

$$\frac{\partial \omega}{\partial t} = \frac{\bar{\mathbf{u}}}{H}\frac{\partial \omega'}{\partial t} = \frac{\bar{\mathbf{u}}}{H}\left(\frac{\partial \omega'}{\partial t'}\frac{\partial t'}{\partial t}\right) \tag{A.3}$$

since $\quad t = t'\dfrac{H}{\bar{\mathbf{u}}} \quad$ then $\quad \dfrac{\partial t'}{\partial t} = \dfrac{\bar{\mathbf{u}}}{H} \quad$ and :

$$\frac{\partial \omega}{\partial t} = \frac{\bar{\mathbf{u}}^2}{H^2}\frac{\partial \omega'}{\partial t'} \tag{A.4}$$

Convection term

$$(\mathbf{u}\cdot\nabla)\omega = \mathbf{u}'\bar{\mathbf{u}}\cdot(\nabla\omega) = \mathbf{u}'\bar{\mathbf{u}}\cdot\left(\nabla\left(\omega'\frac{\bar{\mathbf{u}}}{H}\right)\right) \tag{A.5}$$

since $\quad \nabla(\cdot) = \nabla'(\cdot)\dfrac{1}{H} \quad$ then $\quad \nabla\left(\omega'\dfrac{\bar{\mathbf{u}}}{H}\right) = \dfrac{\bar{\mathbf{u}}}{H}\dfrac{1}{H}\nabla'\omega' \quad$ and :

$$(\mathbf{u}\cdot\nabla)\omega = \frac{\bar{\mathbf{u}}^2}{H^2}(\mathbf{u}'\cdot\nabla')\omega' \tag{A.6}$$

Stretching term

Processing similarly as for the convection term, one has :

$$(\omega\cdot\nabla)\mathbf{u} = \left(\omega'\frac{\bar{\mathbf{u}}}{H}\right)\cdot\nabla(\mathbf{u}'\bar{\mathbf{u}}) = \frac{\bar{\mathbf{u}}}{H}\frac{\bar{\mathbf{u}}}{H}(\omega'\cdot\nabla')\mathbf{u}' = \frac{\bar{\mathbf{u}}^2}{H^2}(\omega'\cdot\nabla')\mathbf{u}' \tag{A.7}$$

Penalization term

$$\nabla \times \Big(\lambda\ \chi_b(\mathbf{u}_b - \mathbf{u})\Big) = \nabla \times \left(\frac{\mu\Phi}{\rho k}\ \chi_b(\mathbf{u}_b - \mathbf{u})\right) = \nabla' \times \left(\frac{\mu\Phi}{\rho k}\frac{\bar{\mathbf{u}}}{H}\ \chi_b(\mathbf{u}_b' - \mathbf{u}')\right) \tag{A.8}$$

because $\nabla(\cdot) = \nabla'(\cdot)\dfrac{1}{H}$ and $\mathbf{u} = \mathbf{u}'\bar{\mathbf{u}}$. Therefore :

$$\nabla \times \Big(\lambda\ \chi_b(\mathbf{u}_b - \mathbf{u})\Big) = \nabla' \times \left(\frac{\mu\Phi\bar{\mathbf{u}}}{\rho k H}\ \chi_b(\mathbf{u}_b' - \mathbf{u}')\right) \tag{A.9}$$

Diffusion term

$$\frac{\mu}{\rho}\ \Delta\omega = \frac{\mu}{\rho}\ \left(\Delta\left(\omega'\frac{\bar{\mathbf{u}}}{H}\right)\right) \tag{A.10}$$

since $\left(\Delta\left(\omega'\dfrac{\bar{\mathbf{u}}}{H}\right)\right) = \dfrac{\bar{\mathbf{u}}}{H}\Delta(\omega') = \dfrac{\bar{\mathbf{u}}}{H}\dfrac{1}{H^2}\Delta'\omega'$ then :

$$\frac{\mu}{\rho}\ \Delta\omega = \frac{\mu\bar{\mathbf{u}}}{\rho H^3}\ \Delta'\omega' \tag{A.11}$$

Replacing these dimensionless terms in equation A.2 gives :

$$\frac{\bar{\mathbf{u}}^2}{H^2}\frac{\partial\omega'}{\partial t'} + \frac{\bar{\mathbf{u}}^2}{H^2}(\mathbf{u}'\cdot\nabla')\omega' - \frac{\bar{\mathbf{u}}^2}{H^2}(\omega'\cdot\nabla')\mathbf{u}' = \nabla' \times \left(\frac{\mu\Phi\bar{\mathbf{u}}}{\rho k H}\ \chi_b(\mathbf{u}_b' - \mathbf{u}')\right) + \frac{\mu\bar{\mathbf{u}}}{\rho H^3}\ \Delta'\omega', \tag{A.12}$$

which, after multiplying by $\dfrac{H^2}{\bar{\mathbf{u}}^2}$ and omitting the $(\cdot)'$ notation, yields :

$$\frac{\partial\omega}{\partial t} + (\mathbf{u}\cdot\nabla)\omega - (\omega\cdot\nabla)\mathbf{u} = \nabla \times \left(\underbrace{\frac{\mu\Phi H}{\rho k\bar{\mathbf{u}}}}_{\lambda}\ \chi_b(\mathbf{u}_b - \mathbf{u})\right) + \underbrace{\frac{\mu}{\rho H\bar{\mathbf{u}}}}_{Re}\Delta\omega \tag{A.13}$$

B

Stability analysis for the stretching equation

The stability analysis is performed from the following formulation of the stretching equation :

$$\frac{\partial \boldsymbol{\omega}}{\partial t} = [\nabla \mathbf{u}] \cdot \boldsymbol{\omega} \tag{B.1}$$

In order to solve equation B.1 one can consider the following linear system, where $A = [\nabla \mathbf{u}]$:

$$\boldsymbol{\omega}' = A\boldsymbol{\omega} \tag{B.2}$$

If A is diagonalizable, this problem can be reduced to the study of the eigenvalues of matrix A :

$$\boldsymbol{\omega}' = \lambda_i \boldsymbol{\omega} \qquad \text{with} \quad i \in \{1, 2, 3\} \tag{B.3}$$

For the system to converge, λ has to satisfy $\mathrm{Re}(\lambda) < 1$ (we only focus here on the real part of λ since the complex part is a function oscillating between 1 and -1, that is to say bounded).

We want the equation to converge in time. In other words, if one considers a scheme involving two different time steps:

$$\boldsymbol{\omega}^{n+1} = B\boldsymbol{\omega}^n, \tag{B.4}$$

we want the absolute value of B to be bounded by 1, such that :

$$\left| \frac{\boldsymbol{\omega}^{n+1}}{\boldsymbol{\omega}^n} \right| < 1 \tag{B.5}$$

The conditions to be satisfied for the Euler scheme and the RKα schemes, with $\alpha = 2, 3, 4$, are given in the following :

The Euler scheme (1^{st} order)

The discretization of equation B.1 using an Euler scheme is given by:

$$\frac{\boldsymbol{\omega}^{n+1} - \boldsymbol{\omega}^n}{\Delta t} = [\nabla \mathbf{u}] \cdot \boldsymbol{\omega}^n \tag{B.6}$$

which yields:

$$\boldsymbol{\omega}^{n+1} = [1 + \nabla \mathbf{u}.\Delta t] \cdot \boldsymbol{\omega}^n \tag{B.7}$$

The condition for the Euler scheme is thus : $|B| = |1 + X| < 1$, where $X = \nabla \mathbf{u}.\Delta t$. Therefore, X has to be greater than -2, that is to say:

$$-\nabla \mathbf{u}.\Delta t < 2 \tag{B.8}$$

If the matrix $[-\nabla \mathbf{u}]$ is diagonalizable, one has :

$$-\lambda_i \Delta t < 2 \qquad \forall\, i \in \{1,2,3\}, \tag{B.9}$$

and knowing that :

$$-\lambda_i < \max_i |-\lambda_i| \qquad \forall\, i \in \{1,2,3\}, \tag{B.10}$$

the inequality B.9 may be reduced to the following one :

$$\Delta t < \frac{2}{\max_i |-\lambda_i|} \Longleftrightarrow \Delta t < \frac{2}{\max_i |\lambda_i|} \qquad \forall\, i \in \{1,2,3\}. \tag{B.11}$$

The use of the Gershgorin circle theorem now enables us to upper-bound the spectral radius $\max_i |\lambda_i|$ with respect to the coefficients of $A = [\nabla \mathbf{u}]$. This will allow to supply a general condition on Δt only depending on $\nabla \mathbf{u}$ (a quantity that is easily available in the computational solver).

Theorem B.1 (*Gershgorin circle theorem*)

Let A be a complex $n \times n$ matrix with coefficients a_{ij}. Every eigenvalue of A lies within at least one of the Gershgorin discs : $D_i = \{z \in \mathbb{C}, |a_{ii} - z| \leq \sum_{i \neq j} |a_{ij}|\}$.

According to this theorem, one therefore gets the following inequality :

$$\max_i |\lambda_i| \leq \max_i \left(\sum_j \left| \frac{\partial u_i}{\partial x_j} \right| \right), \tag{B.12}$$

and the stability condition for the Euler scheme is finally given by:

$$\Delta t < \frac{2}{\max_i \left(\sum_j \left| \frac{\partial u_i}{\partial x_j} \right| \right)}. \tag{B.13}$$

The Runge Kutta 2 scheme (2^{nd} order)

With the RK2 scheme, the time discretization of equation B.1 gives:

$$\boldsymbol{\omega}^{n+1} = \left[1 + \nabla \mathbf{u}.\Delta t + \frac{1}{2} (\nabla \mathbf{u}.\Delta t)^2 \right] \cdot \boldsymbol{\omega}^n. \tag{B.14}$$

Applying again the theorem B.1, one eventually gets the following stability condition :

$$\Delta t < \frac{2}{\max_i \left(\sum_j \left| \frac{\partial u_i}{\partial x_j} \right| \right)}, \tag{B.15}$$

where the coefficient 2 is obtained from the non-zero solution given by figure B.1b.

The Runge Kutta 3 scheme (3^{rd} order)

Using the RK3 scheme one gets :

$$\boldsymbol{\omega}^{n+1} = \left[1 + \nabla \mathbf{u}.\Delta t + \frac{1}{2} (\nabla \mathbf{u}.\Delta t)^2 + \frac{1}{6} (\nabla \mathbf{u}.\Delta t)^3 \right] \cdot \boldsymbol{\omega}^n \tag{B.16}$$

According to the non-zero solution given by figure B.1c and using theorem B.1, one gets :

$$\Delta t < \frac{2.5127}{\max_i \left(\sum_j \left| \frac{\partial u_i}{\partial x_j} \right| \right)}. \tag{B.17}$$

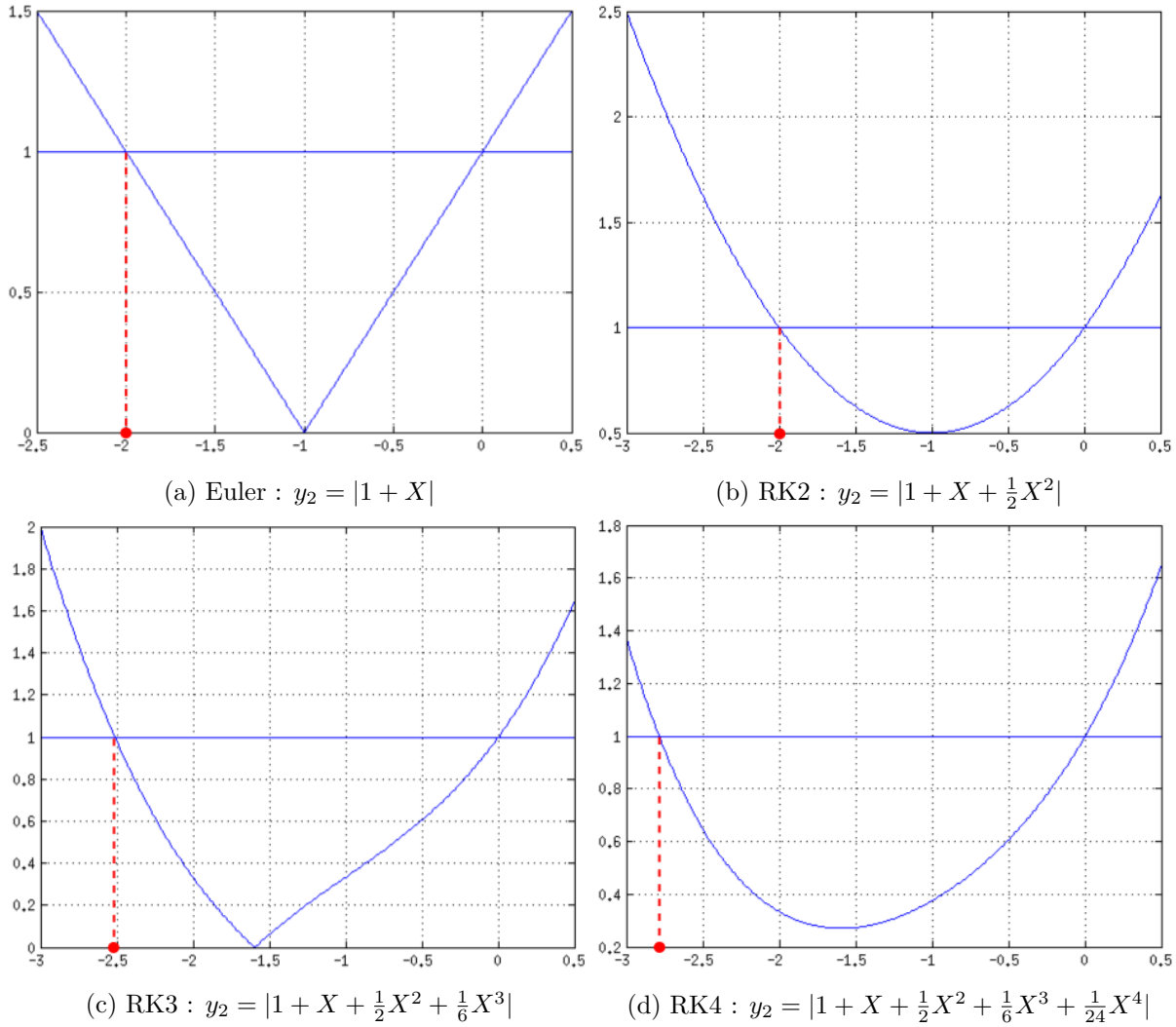

(a) Euler : $y_2 = |1 + X|$

(b) RK2 : $y_2 = |1 + X + \frac{1}{2}X^2|$

(c) RK3 : $y_2 = |1 + X + \frac{1}{2}X^2 + \frac{1}{6}X^3|$

(d) RK4 : $y_2 = |1 + X + \frac{1}{2}X^2 + \frac{1}{6}X^3 + \frac{1}{24}X^4|$

Figure B.1: Graphical representation of the solutions of equation $y_1 = y_2$, where $y_1 = 1$ and $y_2 = f(X)$, for the estimation of the time step condition when using (a) Euler scheme, (b) RK2 scheme, (c) RK3 scheme and (d) RK4 scheme.

The Runge Kutta 4 scheme (4^{th} order)

With the RK4 scheme, the time discretization of the stretching equation B.1 gives:

$$\boldsymbol{\omega}^{n+1} = \left[1 + \nabla\mathbf{u}.\Delta t + \frac{1}{2}(\nabla\mathbf{u}.\Delta t)^2 + \frac{1}{6}(\nabla\mathbf{u}.\Delta t)^3 + \frac{1}{24}(\nabla\mathbf{u}.\Delta t)^4\right] \cdot \boldsymbol{\omega}^n \tag{B.18}$$

According to the non-zero solution read on figure B.1d and applying theorem B.1, one obtains:

$$\Delta t < \frac{2.7853}{\max\limits_i\left(\sum\limits_j \left|\frac{\partial u_i}{\partial x_j}\right|\right)} \tag{B.19}$$

C

Publications

INTERNATIONAL JOURNAL FOR NUMERICAL METHODS IN FLUIDS
Int. J. Numer. Meth. Fluids (2015)
Published online in Wiley Online Library (wileyonlinelibrary.com). DOI: 10.1002/fld.4038

Vortex penalization method for bluff body flows

Chloe Mimeau[1], Federico Gallizio[2], Georges-Henri Cottet[1] and Iraj Mortazavi[3,*,†]

[1]*Université Grenoble-Alpes, LJK, 51 rue des Mathématiques, F-38041 Grenoble, France*
[2]*Optimad Engineering Srl, 18 via Giacinto Collegno, 10143 Torino Italia*
[3]*EA-7340-M2N-Modélisation Mathématique et Numérique, Case 2D5000 Conservatoire National des Arts et Métiers, 292 Rue St Martin, 75003 Paris, France*

SUMMARY

In this work, a penalization method is discussed in the context of vortex methods for incompressible flows around complex geometries. In particular, we illustrate the method in two cases: the flow around a rotating blade for Reynolds numbers 1000 and 10,000 and the flow past a semi-circular body consisting of a porous layer surrounding a rigid body at Reynolds numbers 550 and 3000. In the latter example, the results are interpreted in terms of control strategy. Copyright © 2015 John Wiley & Sons, Ltd.

Received 3 February 2014; Revised 5 February 2015; Accepted 24 March 2015

KEY WORDS: vortex methods; penalization technique; moving obstacles; porous medium

1. INTRODUCTION

Vorticity is an important characteristic of flows in many applications. It is a signature of wakes in bluff body flows and, as such, is related to aerodynamic performance of moving or fixed obstacles [1]. The vorticity formulation of the Navier–Stokes equations is therefore a natural framework to address questions related to flow control. In these equations, for moderate and high Reynolds numbers, the vorticity advection is predominant, which motivates the use of Lagrangian or semi-Lagrangian schemes to discretize these equations. Particle methods belong to this category. They have long been used for the simulation of vortex flows, and in particular for bluff body flows, since the pioneering simulation of flows past a two-dimensional (2D) cylinder in [2]. Three-dimensional (3D) simulations followed this work [3–5]. In all these works, the no-slip condition at the body surface is imposed through vorticity fluxes. This method relies on an analysis of the relationship between vorticity fluxes and velocity boundary conditions [4, 6]. Vorticity fluxes are implemented in vortex methods by means of integral equations [7]. This method is physically appealing but relies on a delicate tuning of several parameters and remains delicate to implement. Immersed boundary conditions have been proposed in [4, 8] to simplify the treatment of complex geometry and the computation of velocity from vorticity. Later on, following the work of Angot *et al.* [9] and Kevlahan and Ghidaglia [10], a penalization method coupled to the vorticity formulation of the Navier–Stokes equation was proposed and extended to the two-way interaction of a rigid body and a 3D incompressible fluid in [11]. The method was validated in 3D flows at low Reynolds numbers and was extended to deforming bodies and applied to find optimal swimming modes of fishes [12–14]. The work in [15] provides additional 2D validations of the method and illustrates its efficiency in the context of Graphics Processing Unit (GPU) computing.

*Correspondence to: Iraj Mortazavi, EA-7340-M2N-Modélisation Mathématique et Numérique, Case 2D5000 Conservatoire National des Arts et Métiers, 292 Rue St Martin, 75003 Paris France.
†E-mail: iraj.mortazavi@cnam.fr

The purpose of this work is to further illustrate its flexibility by focusing on the case of two bi-dimensional complex flows where the combined use of vortex and penalization proves to be efficient: the flow around a vertical axis turbine (VAT), on the one hand, and the flow past a semi-circular obstacle made of a porous layer surrounding a rigid core, on the second hand. In the first case, we discuss the different flow patterns and frequencies corresponding to moderate and high Reynolds numbers. In the second case, we study the influence of the porous layer on the wake strength and on the drag value. We also provide validation studies, which allow to determine the numerical parameters needed to provide the desired accuracy on these applications.

This paper is organized as follows. In Section 2, we describe the vortex penalization model and its implementation in a vortex particle method. In particular, we indicate how the body forces are computed in such a model. In Section 3, we provide convergence studies of the method with respect to the penalization parameter and the grid size, and we validate the method on the benchmark test of the flow past a 2D circular cylinder at various Reynolds numbers. In Section 4, we apply the method to the case of a rotating turbine blade, and Section 5 is devoted to the analysis of the flow around a semi-circular cylinder with a porous coating, where the characteristics of the flows are analyzed from the point of view of flow control. Finally, Section 6 summarizes our results and draws some conclusions.

2. NUMERICAL ALGORITHM

2.1. Vorticity formulation and remeshed particle method

The dynamics of an incompressible flow without external force fields is governed by the incompressible Navier–Stokes equations

$$\nabla \cdot \mathbf{u} = 0 \quad \text{in } D, \tag{1}$$

$$\frac{\partial \mathbf{u}}{\partial t} + (\mathbf{u} \cdot \nabla)\mathbf{u} = -\nabla p + \frac{1}{\mathrm{Re}} \Delta \mathbf{u} \quad \text{in } D, \tag{2}$$

where D is the computational domain, and Re is the Reynolds number.

Taking the curl of Equation (2) and using Equation (1), we obtain the Helmholtz or the vorticity transport equation for the vorticity $\boldsymbol{\omega} = \nabla \times \mathbf{u}$

$$\frac{\partial \boldsymbol{\omega}}{\partial t} + (\mathbf{u} \cdot \nabla)\boldsymbol{\omega} - (\boldsymbol{\omega} \cdot \nabla)\mathbf{u} = \frac{1}{\mathrm{Re}} \Delta \boldsymbol{\omega} \quad \text{in } D. \tag{3}$$

This equation has to be coupled to the system giving the velocity in terms of the vorticity. It is convenient to use the Helmholtz decomposition

$$\mathbf{u} = \nabla \times \boldsymbol{\psi} + \nabla \varphi. \tag{4}$$

The stream function $\boldsymbol{\psi}$ and potential φ satisfy the following systems in D

$$-\Delta \boldsymbol{\psi} = \boldsymbol{\omega}, \ \nabla \cdot \boldsymbol{\psi} = 0, \ \Delta \varphi = 0, \tag{5}$$

complemented with appropriate boundary conditions. The vorticity transport equation does not explicitly contain the pressure term, but the pressure can be recovered from the velocity field by integrating the following Poisson equation:

$$\Delta p = -\nabla \cdot (\mathbf{u} \cdot \nabla)\mathbf{u}, \quad \text{in } D, \tag{6}$$

which is derived as the divergence of Equation (2).

The previous equations are approximated using a remeshed vortex particle method [2, 6, 16]. In this approach, the vorticity is carried by particles. Particles follow the trajectories associated with the velocity field. Simultaneously, the vorticity carried by the particles is updated to account for vortex stretching and diffusion. Particle remeshing is used to overcome accuracy loss due to local

DOI: 10.1002/fld

distortion of the flow map [2]. In that case, particles are remeshed through interpolation on a regular mesh at each time step. This grid is used to compute the velocity through a Poisson solver. Details of the algorithm are given in the sequel.

In incompressible flows, the unique sources of the vorticity are boundaries. It is therefore important to capture in an accurate way vorticity boundary conditions. In classical implementations of vortex methods, the no-slip boundary condition is satisfied through the creation of vortex elements [16–18] or by updating particle strength to account for vorticity fluxes at the boundary [2, 4, 7]. The no-through flow boundary conditions are implemented together with the Poisson equation to determine stream functions and potential in (5).

These methods involve several parameters to enforce the no-slip conditions at the boundaries: a more straightforward alternative to these techniques can be derived from the penalization method.

2.2. Vortex penalization method

2.2.1. Penalization in velocity formulation. In this section, we show how the penalization method can be used successfully to model the flow of an incompressible fluid around an obstacle. In the penalization technique, the system is considered as a single flow, subject to the Navier–Stokes equation with a penalization term that enforces continuity at the solid–fluid interface and rigid motion inside the solid. The main advantage of this method is that it needs the mesh neither to fit the boundaries nor to specify no-slip boundary conditions. In addition, it allows to compute the pressure as a continuous field on the whole domain including the solids and the lift and drag coefficients by integrating the penalization term inside the solid bodies [19].

In a porous medium, the velocity $\mathbf{u}$ is given by the Darcy law

$$\mathbf{u} = -\frac{k}{\mu\Phi}\nabla p, \tag{7}$$

where p is the pressure, k is the intrinsic permeability, μ is the dynamic viscosity of the fluid, and Φ is the porosity of the medium. On the other hand, assuming that the Boussinesq hypothesis is satisfied for the fluid saturating the porous medium, we obtain the Brinkman equation that includes the diffusion inside the solid and is only valid when the porosity coefficient is close to 1. Here, we set this coefficient equal to 1 and take the hypothesis of the viscosity equivalence for both Darcy and diffusive terms [20, 21]

$$\nabla p = -\frac{\mu}{k}\mathbf{u} + \mu\Delta\mathbf{u}. \tag{8}$$

Complementing the Brinkman equation with the inertial terms and the Dupuit–Forchheimer relation [21], we finally obtain the modified Forchheimer–Navier–Stokes equation [22, 23]

$$\rho\,\partial_t\mathbf{u} + \rho\,(\mathbf{u}\cdot\nabla)\,\mathbf{u} + \nabla p = -\frac{\mu}{k}\mathbf{u} + \mu\Delta\mathbf{u}, \tag{9}$$

where ρ is the density of the fluid.

Then, using the following usual substitutions including the mean velocity of the fluid $\overline{\mathbf{u}}$ and the size of the body H

$$\mathbf{u} = \mathbf{u}'\,\overline{\mathbf{u}}\ ;\ \ x = x'\,H\ ;\ \ t = t'\frac{H}{\overline{\mathbf{u}}}\ ;\ \ p = p'\rho|\overline{\mathbf{u}}|^2, \tag{10}$$

we obtain the penalized non-dimensional Navier–Stokes equations or Brinkman–Navier–Stokes equations for the unknowns $(\mathbf{u}', p')$ denoted $(\mathbf{u}, p)$ for the sake of simplicity

$$\partial_t\mathbf{u} + (\mathbf{u}\cdot\nabla)\mathbf{u} - \frac{1}{\mathrm{Re}}\Delta\mathbf{u} + \frac{\mathbf{u}}{K} + \nabla p = 0 \text{ in } D_T = D\times(0,T), \tag{11}$$

$$\nabla\cdot\mathbf{u} = 0 \text{ in } D_T. \tag{12}$$

DOI: 10.1002/fld

This system of equations exactly corresponds to the penalization of Equations (1) and (2), where $K = \frac{\rho k \bar{\mathbf{u}}}{\mu H \Phi}$ represents the non-dimensional coefficient of permeability of the medium, and $\mathrm{Re} = \frac{\rho \bar{\mathbf{u}} H}{\mu}$ is the Reynolds number based on H, the height of the body, and D, the full domain including the solid body. This model is able to represent the two media as follows. The zone variation is realized changing the penalization coefficient that defines the permeability of each region. In the fluid, the permeability coefficient goes to infinity, the penalization term vanishes, and we solve the non-dimensional Navier–Stokes equations. In the solid body, the permeability coefficient goes to 0, and it has been shown in [9] that solving these equations corresponds to solve Darcy's law in the solid, and that the velocity is proportional to K. One can thus write $K = \frac{1}{\lambda}\chi_S$, where χ_S denotes the characteristic function of S, and λ is a penalization parameter satisfying $\lambda \gg 1$. For numerical simulations, we typically set $\lambda \geqslant 10^8$. If the full domain including the solid body is defined as $D = F \cup S$, one finally obtains the following penalized Navier–Stokes equations:

$$\partial_t \mathbf{u} + (\mathbf{u}\cdot\boldsymbol{\nabla})\mathbf{u} - \frac{1}{\mathrm{Re}}\boldsymbol{\Delta}\mathbf{u} + \lambda\chi_S\mathbf{u} + \boldsymbol{\nabla} p = 0 \ \text{ in } \ D, \tag{13}$$

$$\boldsymbol{\nabla}\cdot\mathbf{u} = 0 \ \text{ in } \ D. \tag{14}$$

In addition, as the pressure is computed inside the solid body, it is shown in [19] that one can compute the drag and lift forces by integrating the penalization term on the volume of the body

$$\mathbf{F} = \frac{1}{\mathrm{Re}}\int_S \boldsymbol{\Delta}\mathbf{u}\, d\mathbf{x} - \int_S \boldsymbol{\nabla} p\, d\mathbf{x} \approx \int_D \lambda\, \chi_S\, \mathbf{u}\, d\mathbf{x}. \tag{15}$$

2.2.2. Penalization in vorticity formulation and implementation with a vortex method. We first show how to extend the penalization method to the vorticity formulation of the Navier-Stokes equations.

By differentiation of the velocity-based penalization Equation (13), we obtain the following non-dimensional [10, 11] vorticity–penalization equation:

$$\frac{\partial\boldsymbol{\omega}}{\partial t} + (\mathbf{u}\cdot\boldsymbol{\nabla})\boldsymbol{\omega} - (\boldsymbol{\omega}\cdot\boldsymbol{\nabla})\mathbf{u} = \frac{1}{\mathrm{Re}}\boldsymbol{\Delta}\boldsymbol{\omega} + \boldsymbol{\nabla}\times[\lambda\ \chi_S(\mathbf{u}_s - \mathbf{u})]. \tag{16}$$

In the aforementioned equation, we have generalized the boundary value problem to allow for a rigid body motion of the obstacle S with velocity $\mathbf{u}_s$, where $\mathbf{u}_s$ is the rigid body velocity, and χ_S is the characteristic function of the solid. This system has to be complemented by the usual system giving the velocity in terms of the vorticity

$$\boldsymbol{\nabla}\cdot\mathbf{u} = 0 \text{ in } D, \qquad \boldsymbol{\nabla}\times\mathbf{u} = \boldsymbol{\omega} \text{ in } D, \tag{17}$$

and appropriate boundary conditions on the walls Γ_D.

We describe here how the vorticity Equation (16) is discretized in a vortex method. For simplicity, we assume that the computational domain, including the solid body, is covered by a uniform Cartesian grid with mesh size h.

Equation (16) is split in two sub-steps. At each time step, one successively solves the following equations:

$$\frac{\partial\boldsymbol{\omega}}{\partial t} = \boldsymbol{\nabla}\times(\lambda\ \chi_S(\mathbf{u}_s - \mathbf{u}))\,, \tag{18}$$

$$\frac{\partial\boldsymbol{\omega}}{\partial t} + (\mathbf{u}\cdot\boldsymbol{\nabla})\,\boldsymbol{\omega} - (\boldsymbol{\omega}\cdot\boldsymbol{\nabla})\mathbf{u} = \frac{1}{\mathrm{Re}}\boldsymbol{\Delta}\boldsymbol{\omega}. \tag{19}$$

We set $t_n = n\Delta t$, where Δt is the time step. If $\mathbf{u}^n, \boldsymbol{\omega}^n$ denote the velocity and vorticity values on the grid at time t_n, following [11], the resolution of Equation (18) is performed using a Euler implicit scheme, which yields

DOI: 10.1002/fld

$$\tilde{\boldsymbol{\omega}}^{n+1} = \boldsymbol{\nabla} \times \left[\frac{\mathbf{u}^n + \lambda \Delta t \chi_S \mathbf{u}_s^n}{1 + \lambda \Delta t \chi_S} \right]. \tag{20}$$

The right-hand side mentioned earlier is evaluated by centered finite differences on the grid.

To solve the advection–stretching–diffusion Equation (19), we proceed as follows. Particles are initialized on grid points where vorticity value is above a given threshold (typically 10^{-5}). If $\mathbf{x}_p^n, \boldsymbol{\omega}_p^n$ denote the locations (grid points) and vorticity of particles ($\boldsymbol{\omega}_p^n = \tilde{\boldsymbol{\omega}}^{n+1}(\mathbf{x}_p)$), Equation (19) is firstly handled by solving the following system of Ordinary Differential Equation (ODEs) [6]

$$\begin{cases} d\mathbf{x}_p/dt &= \mathbf{u}_p, \\ d\boldsymbol{\omega}_p/dt &= [\boldsymbol{\nabla} \mathbf{u}_p]\boldsymbol{\omega}_p. \end{cases} \tag{21}$$

This system is typically solved using a second-order Runge–Kutta time stepping. Let us denote by $\mathbf{x}_p^{n+1}, \tilde{\boldsymbol{\omega}}_p^{n+1}$ the locations and strengths of the particle at the end of the time step. Particles are then remeshed on the original grid points by interpolation, with the formula

$$\boldsymbol{\omega}_p^{n+1} = \sum_p \tilde{\boldsymbol{\omega}}_p^{n+1} \Lambda \left(\frac{\mathbf{x}_p^n - \mathbf{x}_p^{n+1}}{h} \right). \tag{22}$$

In this study, the function Λ in the aforementioned formula is obtained by tensor product of a piecewise cubic third-order interpolation kernel, the so-called M_4' kernel originally proposed in [24] is as follows:

$$\Lambda(x) = \begin{cases} 0 & \text{if } |x| > 2 \\ \frac{1}{2}(2 - |x|)^2(1 - |x|) & \text{if } 1 \leqslant |x| \leqslant 2 \\ 1 - \frac{5x^2}{2} + \frac{3|x|^3}{2} & \text{if} |x| \leqslant 1 \end{cases} \tag{23}$$

We would like to point out here that remeshing schemes based on linear interpolation kernels are in general not consistent for unsteady flow velocities. This is demonstrated in [25]. On the contrary, the M_4' scheme is shown in [26] to have the minimal smoothness required for consistency.

The same kernel is also used to interpolate grid velocity values onto particles in the time-stepping scheme to solve (21).

After remeshing, vorticity values are known on the grid, and the remaining diffusion equation is implicitly solved either with a grid-based Poisson solver or with a Fourier method. Grid values for the vorticity are now available at time t_{n+1}. Velocity values are in turn obtained from vorticity grid values by solving systems (4) and (5) with a classical grid-based Poisson solver or using a Fourier method, and a new cycle of iterations can start.

One of the main features of particle methods is that it does not have a Courant Friedrichs Lewy (CFL) restriction on the time step Δt. It is indeed shown in [26] that a remeshed particle method for a transport equation with velocity $\mathbf{u}$ is stable under the condition

$$\Delta t \leqslant \frac{C}{\|\nabla \mathbf{u}\|_\infty}, \tag{24}$$

where C is a constant that only needs to be smaller than 1.

2.3. Force calculation

Assume a flow in $\mathbb{R}^N$ around a bounded body S with velocity and vorticity vanishing at infinity and having a prescribed value $\mathbf{u}_b$ on the body. The formula (15) is based on the velocity–pressure formulation of the penalization method. It assumes that the velocity is of the order of K inside the body. In a vorticity formulation, however, there is no direct control of the velocity in the body. In practice, one observes that the velocity in the body is small but larger than K. This can be seen in Figure 2 (left). In that case, we found that accurate computations of forces could not be achieved

DOI: 10.1002/fld

using the formula (15) and we instead used force evaluations in terms of vorticity distributions around the body.

The force $\mathcal{F}$ exerted by this flow on the body is given by the following formula:

$$\mathcal{F} = -\frac{d}{dt}\int_{S'} \mathbf{u}\, d\mathbf{x}, \tag{25}$$

where S' denotes the domain outside S. Integration by parts allows to express this force in terms of the vorticity, with N denoting the space dimension

$$\mathcal{F} = -\frac{1}{N-1}\frac{d}{dt}\int_{S'} \mathbf{x}\times\boldsymbol{\omega}\, d\mathbf{x} - \frac{1}{N-1}\frac{d}{dt}\oint_{\partial S} \mathbf{x}\times(\mathbf{n}\times\mathbf{u}) d\mathbf{s}, \tag{26}$$

where the first integral is the linear hydrodynamical impulse, and the second integral is the bound vorticity [27]. For an impulsively started obstacle at early times, the vorticity remains essentially attached to the body, and this formula can be used by taking a computational domain large enough to contain the vorticity support. When vorticity shedding occurs, this is no longer possible. Alternatively, one may use the Navier–Stokes equations and the expression (25) to obtain

$$\mathcal{F} = -\nu\int_{\partial S} \boldsymbol{\omega}\times\mathbf{n}\, d\mathbf{s} + \int_{\partial S} p\mathbf{n}\; d\mathbf{s}. \tag{27}$$

In the case of a 2D circular cylinder of radius R, this yields the following formula [2]:

$$\mathcal{F} = \nu R\left(\int_0^{2\pi} \omega\overrightarrow{\mathbf{e}_\theta}\, d\theta - \int_0^{2\pi} \frac{\partial\omega}{\partial n}\overrightarrow{\mathbf{e}_\theta}\, d\theta\right). \tag{28}$$

This expression assumes that vorticity vanishes at infinity, which in practice is always the case, and allows to distinguish friction (in the first integral) and pressure drag (in the second integral).

For a detached bluff body flow, this formula can be used as long as vorticity and its normal derivatives are accurately captured at the boundary. However, the penalization method just described is derived from a method, which is only first order for the velocity. It therefore does not capture vorticity values and fluxes at the boundary with enough accuracy to give reliable force evaluation through (28) with reasonable grid sizes. It is therefore necessary to use a method that does not involve integrals of the physical quantities on the volume of the body. The technique chosen here combines time derivatives, volumes integral of the vorticity momentum—like in Formula (26)—and vorticity boundary values as well as fluxes on a surface away from the body, where these quantities are accurately computed. We follow the approach proposed in [28] and rewrite the force according to the *momentum equation* as follows:

$$\mathcal{F} = -\frac{d}{dt}\int_V \mathbf{u}\, d\mathbf{x} + \int_\Sigma \mathbf{n}\cdot\boldsymbol{\gamma}\, d\mathbf{x}, \tag{29}$$

where V is a domain containing S, Σ denotes its boundary, and

$$\begin{aligned}\boldsymbol{\gamma} =& \frac{1}{2}|\mathbf{u}|^2\mathbf{I} - \frac{1}{N-1}\mathbf{u}\cdot(\mathbf{x}\times\boldsymbol{\omega}) + \frac{1}{N-1}\boldsymbol{\omega}\cdot(\mathbf{x}\times\mathbf{u})\\ &- \frac{1}{N-1}\left[\left(\mathbf{x}\cdot\frac{\partial\mathbf{u}}{\partial t}\right)\mathbf{I} - \mathbf{x}\cdot\frac{\partial\mathbf{u}}{\partial t}\right] + \frac{1}{N-1}\left[\mathbf{x}\cdot(\nabla\cdot\mathcal{T})\mathbf{I} - \mathbf{x}(\nabla\cdot\mathcal{T})\right] + \mathcal{T}.\end{aligned} \tag{30}$$

In the aforementioned equation, $\mathcal{T}$ denotes the stress tensor

$$\mathcal{T} = \mu(\nabla\mathbf{u} + \nabla\mathbf{u}^{\mathbf{t}}), \tag{31}$$

where μ is the viscosity. For the sake of simplicity, we develop this formula in the 2D case where the computational box D and the volume control V are two nested rectangles. We use the notations

DOI: 10.1002/fld

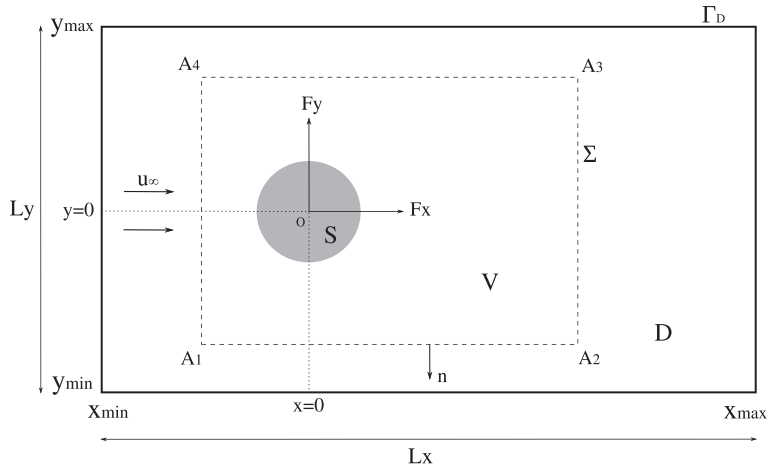

Figure 1. Computational domain D and control volume V.

given in Figure 1. We denote the velocity by $\mathbf{u} = (u, v)^{\mathbf{t}}$. The streamwise and vertical components of the force can then be written computed as follows:

$$\begin{aligned}
\mathcal{F}_x = &-\frac{d}{dt}\int_V u(1-\chi_S)\,dxdy \\
&+\int_{A_1}^{A_2}\left[uv + v\omega y - y\frac{\partial u}{\partial t} + \frac{1}{\mathrm{Re}}\left(2\frac{\partial^2 u}{\partial x^2} + \frac{\partial^2 u}{\partial y^2} + \frac{\partial^2 v}{\partial x \partial y}\right)y - \frac{1}{\mathrm{Re}}\left(\frac{\partial u}{\partial y} + \frac{\partial v}{\partial x}\right)\right]dx \\
&+\int_{A_2}^{A_3}\left[\frac{1}{2}(v^2-u^2) - u\omega y - y\frac{\partial v}{\partial t} + \frac{1}{\mathrm{Re}}\left(2\frac{\partial^2 v}{\partial y^2} + \frac{\partial^2 v}{\partial x^2} + \frac{\partial^2 u}{\partial x \partial y}\right)y + \frac{2}{\mathrm{Re}}\left(\frac{\partial u}{\partial x}\right)\right]dy \\
&+\int_{A_3}^{A_4}\left[-uv - v\omega y + y\frac{\partial u}{\partial t} - \frac{1}{\mathrm{Re}}\left(2\frac{\partial^2 u}{\partial x^2} + \frac{\partial^2 u}{\partial y^2} + \frac{\partial^2 v}{\partial x \partial y}\right)y + \frac{1}{\mathrm{Re}}\left(\frac{\partial u}{\partial y} + \frac{\partial v}{\partial x}\right)\right]dx \\
&+\int_{A_4}^{A_1}\left[-\frac{1}{2}(v^2-u^2) + u\omega y + y\frac{\partial v}{\partial t} - \frac{1}{\mathrm{Re}}\left(2\frac{\partial^2 v}{\partial y^2} + \frac{\partial^2 v}{\partial x^2} + \frac{\partial^2 u}{\partial x \partial y}\right)y - \frac{2}{\mathrm{Re}}\left(\frac{\partial u}{\partial x}\right)\right]dy
\end{aligned}$$

and

$$\begin{aligned}
\mathcal{F}_y = &-\frac{d}{dt}\int_V v(1-\chi_S)\,dxdy \\
&+\int_{A_1}^{A_2}\left[\frac{1}{2}(v^2-u^2) - v\omega x + x\frac{\partial u}{\partial t} - \frac{1}{\mathrm{Re}}\left(2\frac{\partial^2 u}{\partial x^2} + \frac{\partial^2 u}{\partial y^2} + \frac{\partial^2 v}{\partial x \partial y}\right)x - \frac{2}{\mathrm{Re}}\left(\frac{\partial v}{\partial y}\right)\right]dx \\
&+\int_{A_2}^{A_3}\left[-uv + u\omega x + x\frac{\partial v}{\partial t} - \frac{1}{\mathrm{Re}}\left(2\frac{\partial^2 v}{\partial y^2} + \frac{\partial^2 v}{\partial x^2} + \frac{\partial^2 u}{\partial x \partial y}\right)x + \frac{1}{\mathrm{Re}}\left(\frac{\partial v}{\partial x} + \frac{\partial u}{\partial y}\right)\right]dy \\
&+\int_{A_3}^{A_4}\left[-\frac{1}{2}(v^2-u^2) + v\omega x - x\frac{\partial u}{\partial t} + \frac{1}{\mathrm{Re}}\left(2\frac{\partial^2 u}{\partial x^2} + \frac{\partial^2 u}{\partial y^2} + \frac{\partial^2 v}{\partial x \partial y}\right)x + \frac{2}{\mathrm{Re}}\left(\frac{\partial v}{\partial y}\right)\right]dx \\
&+\int_{A_4}^{A_1}\left[uv - u\omega x - x\frac{\partial v}{\partial t} + \frac{1}{\mathrm{Re}}\left(2\frac{\partial^2 v}{\partial y^2} + \frac{\partial^2 v}{\partial x^2} + \frac{\partial^2 u}{\partial x \partial y}\right)x - \frac{1}{\mathrm{Re}}\left(\frac{\partial v}{\partial x} + \frac{\partial u}{\partial y}\right)\right]dy.
\end{aligned}$$

For a 2D viscous flow past a circular obstacle of diameter d with free stream velocity u_∞, drag and lift coefficients are expressed by the following formulas:

$$C_D = \frac{2\mathcal{F}_x}{\rho u_\infty^2 d}, \quad C_L = \frac{2\mathcal{F}_y}{\rho u_\infty^2 d}. \tag{32}$$

DOI: 10.1002/fld

3. VALIDATION FOR FLOW PAST A TWO-DIMENSIONAL CIRCULAR CYLINDER

The vortex penalization has been validated in 2D and 3D fluid structure interaction problems at low Reynolds numbers [11], in the context of multi-resolution [29] and in GPU implementations for 2D flows [15]. To evaluate the accuracy of the method, in particular with respect to the value of the penalization parameter, we consider here validations on the classical benchmark of the flow around a 2D circular cylinder for a wide range of Reynolds numbers.

There is an important literature about the classical benchmark of the 2D circular cylinder. This benchmark is covered by an important literature. A thorough survey of this subject can be found in Williamson (1996) [1].

Vortex methods using vorticity flux boundary conditions have allowed to obtain reference results for a wide range of Reynolds numbers [2]. Recently, the penalization–vortex method has been implemented on GPU processor. The accuracy and performance of this implementation against traditional CPU implementations have been tested on this benchmark in an explicit formulation of the penalization. We use here the same benchmark to illustrate the efficiency of the implicit formulation (Equation (20)).

3.1. Numerical setup and flow conditions

The computational domain and the geometrical setup are shown in Figure 1, where D is a rectangle delimited by its boundaries Γ^D. The non-dimensional diameter d of the circular cylinder is equal to 1, and the body is centered at the origin. The whole computational domain is covered by a uniform Cartesian grid.

In this section, periodic boundary conditions on the box boundary Γ_D were prescribed for system (17). A correction of the velocity field was performed at each time step in order to satisfy free stream velocity $\mathbf{u}_\infty = (u_\infty, 0) = (1, 0)$ imposed at the inlet. In all cases, the size of the computational box was chosen large enough so that the effect of these boundary conditions was found to be negligible.

3.2. Convergence studies

First, we consider the case of an impulsively started cylinder flow with $\mathrm{Re} = 550$ and study the convergence of the method with respect to the penalization parameter and the grid size. The left picture of Figure 2 shows the mean velocity profiles inside the cylinder, averaged over the time window $T = [0, 3]$. The results corresponding to the implicit penalization scheme for three values of λ are compared with the profile obtained with the explicit formulation for a mesh size $h = 0.005$. The explicit formulation of (18) requires a maximum value of $\lambda = 1/\Delta t$ to guarantee stability.

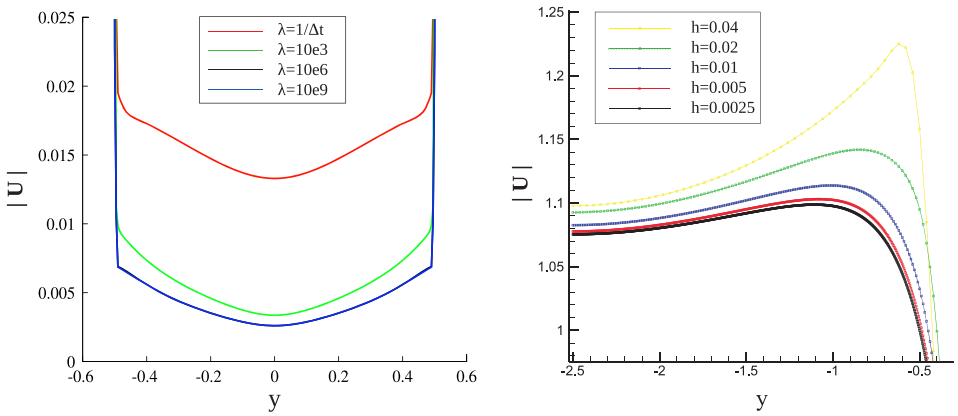

Figure 2. Left picture: mean velocity magnitude profiles in a section across the center of the cylinder, at $x = 0$, obtained with implicit penalization ($\lambda = 10^3, 10^6, 10^9$) and explicit penalization ($\lambda = 1/\Delta t$) at $\mathrm{Re} = 550$. Right picture: grid-refinement study for the axial velocity at $T = 3$ on a cross section at $x = 1.5$ behind the cylinder.

DOI: 10.1002/fld

One can see from this experiment that, to obtain small values of the velocity inside the body, it is necessary to use larger value of λ and therefore to implement the implicit scheme (20). As already mentioned, one can also notice that velocity values inside the body remain in all cases larger than $1/\lambda$. Unlike for the velocity–pressure formulation, indeed, in the vorticity formulation, there is no direct relationship between the velocity in the body and the parameter λ.

To have a more precise idea of the sensitivity of the results to the value of the penalization parameter, a λ-convergence study is carried out at $\mathrm{Re} = 550$ with $h = 0.005$ and $\Delta t = 0.0025$. The value of λ ranges from 1 to 10^6, with $\lambda = 10^8$ as reference case (solid case). We evaluate the L^1, L^2, and L^∞ norms of the error $e(y)$ in the mean velocity magnitude profile $|\bar{\mathbf{u}}|$ (at $x = 0$) with respect to the reference case

$$e(y)_{L^1} = \int_{y_{\min}}^{y_{\max}} \left| \, |\bar{\mathbf{u}}|_{\lambda=10^8}(y) - |\bar{\mathbf{u}}|(y) \, \right| \mathrm{d}y, \tag{33}$$

$$e(y)_{L^2} = \left(\int_{y_{\min}}^{y_{\max}} \left| \, |\bar{\mathbf{u}}|_{\lambda=10^8}(y) - |\bar{\mathbf{u}}|(y) \, \right|^2 \mathrm{d}y \right)^{1/2}, \tag{34}$$

$$e(y)_{L^\infty} = \sup_{y \in [y_{\min}, y_{\max}]} \left| \, |\bar{\mathbf{u}}|_{\lambda=10^8}(y) - |\bar{\mathbf{u}}|(y) \, \right|. \tag{35}$$

As Figure 3(a) shows, the numerical error decreases as $O(\lambda^{-1/2})$ when $\lambda \leqslant 10^2$ and as $O(\lambda^{-1})$ when $\lambda \geqslant 10^2$. The same study was performed at $\mathrm{Re} = 100$ with a smaller grid size and time step, respectively, equal to $h = 0.0025$ and $\Delta t = 0.001$. The results are given in Figure 3(b) and show that the error behaves as $O(\lambda^{-1/2})$ when $\lambda \leqslant 10^4$ and $O(\lambda^{-1})$ when $\lambda \geqslant 10^4$. These convergence rates are in agreement with the numerical results found out in [9] where it is stated that to increase λ to high values ($\lambda \geqslant 10^6$), a mesh refinement is necessary. Moreover, these numerical results are slightly better compared with the theoretical result given in [9], attesting that the upper bound on the global L^∞ error of the penalization is $\|\mathbf{u}_\lambda - \mathbf{u}\| \leqslant C\lambda^{-1/2}$. Furthermore, we can see in this figure that the circular cylinder reaches the solid state from $\lambda = 10^4$, where $e(y) \leqslant 10^{-4}$. Thus, a permeable medium can be defined by setting the λ-values between 1 and 10^3, with very low permeability for the latter one.

Finally, the right picture of Figure 2 shows a grid-refinement study performed at $\mathrm{Re} = 550$ for a section located in the wake at $x = 1.5$ and a penalization parameter $\lambda = 10^{10}$ in the implicit formulation. It depicts the instantaneous velocity magnitude at time $T = 3$ for different grid sizes and

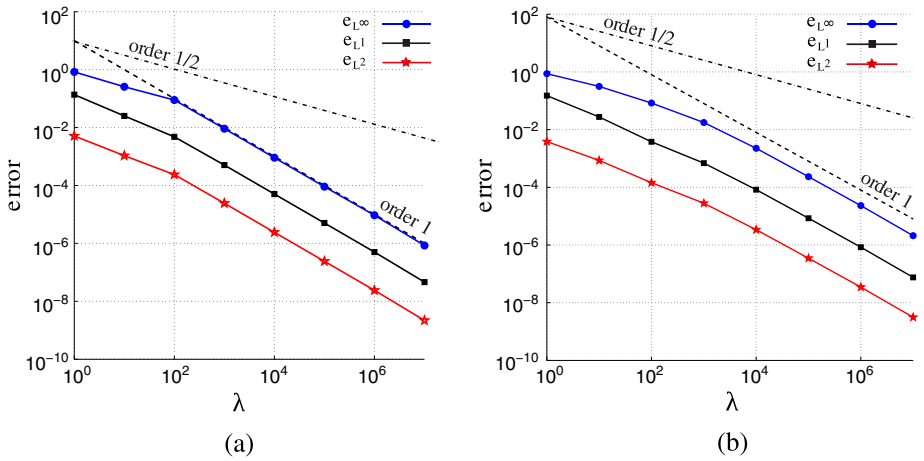

Figure 3. λ-convergence study for flow past a circular cylinder at $\mathrm{Re} = 550$ with $h = 0.005$ and $\Delta t = 0.0025$ (a) and at $\mathrm{Re} = 100$ with $h = 0.0025$ and $\Delta t = 0.001$ (b). The errors e_{L^∞}, e_{L^1}, and e_{L^2} are plotted against λ values.

DOI: 10.1002/fld

indicates that for this flow, one can consider that convergence is reached for $h \leqslant 0.005$. Additional validations are given in the next section.

3.3. Flow analysis and validations

The first part of the study is related to the low Reynolds number analysis where the viscous effects are predominant. Following [8], the adimensional time step Δt is determined by the condition $\Delta t/(h^2\ \mathrm{Re}) \sim O(1)$. Various tests have been carried out by increasing the blockage ratio $1/L_y$, where L_y denotes the height of the computational box, as shown in Figure 1. The size of the computational domain was chosen such that the effects of the boundaries on the shedding frequencies were negligible. Moreover, a careful convergence study with respect to the domain size has been performed in [4] for flow past a 2D circular cylinder using vortex methods. This study shows a first-order convergence for the lift coefficient and Strouhal number and third-order convergence for the drag coefficient. It demonstrates that a domain extending to about 6 cylinder diameters downstream is sufficient to provide reliable flow diagnostics. The subsequent simulations have been performed in a computational box with dimensions $[-7.5,\ 25] \times [-7.5,\ 7.5]$ with 3250×1500 grid points. This corresponds to a mesh size $h = 0.01$. The penalization was introduced using the implicit formulation (20), and the penalization parameter was set to $\lambda = 10^{10}$. For $\mathrm{Re} < \mathrm{Re}_{crit} = 49$, the flow regime is laminar, and the solution is steady and stable [1].

For larger Reynolds numbers, the flow regime is still laminar, but the steady solution becomes unstable ($\mathrm{Re} > \mathrm{Re}_{crit}$). On the left-hand side picture of Figure 4, the amplitude A_ω of the fluctuation of the vorticity on a monitoring point $P = (2.5,\ 0.5)$ is plotted for various Reynolds numbers. For a flow regime close to the bifurcation point Re_{crit} ($\mathrm{Re} < 60$), the wake instabilities grow very slowly, so the oscillation study is started at $\mathrm{Re} = 60$. Nevertheless, the exact critical Reynolds number is obtained with a linear extrapolation of the amplification factor curve. The right-hand side picture of Figure 4 shows the Strouhal number (given by the shedding frequency) as a function of the Reynolds number, obtained in our calculations and in the experimental work [1]. An estimate of the mean relative error between the two curves yields $\bar{\epsilon} = \frac{1}{N}\sum_N |St_{\mathrm{ref}} - St| \approx 0.6\%$, where N denotes the number of points on each curve (i.e., $N = 13$).

The evaluation of forces has been carried out using the *momentum equation* (29). The mean values and the amplitudes of the fluctuations of drag and lift coefficients for flows at $\mathrm{Re} = 100$ and $\mathrm{Re} = 200$ are computed and given in Table I. These results are very close to experimental and numerical data collected by Russell and Jane Wang [30] and Braza *et al.* [31].

To address a transitional case, we focus now on an impulsively started flow at $\mathrm{Re} = 550$ and compare our results to those of Koumoutsakos and Leonard [2] and Ploumhans and Winckelmans [8]. The time evolution of the drag coefficient is reported in Figure 5(a). In our computations, the grid convergence in a computational domain $[-4,\ 8] \times [-5,\ 5]$ is achieved with parameters $h = 0.005$,

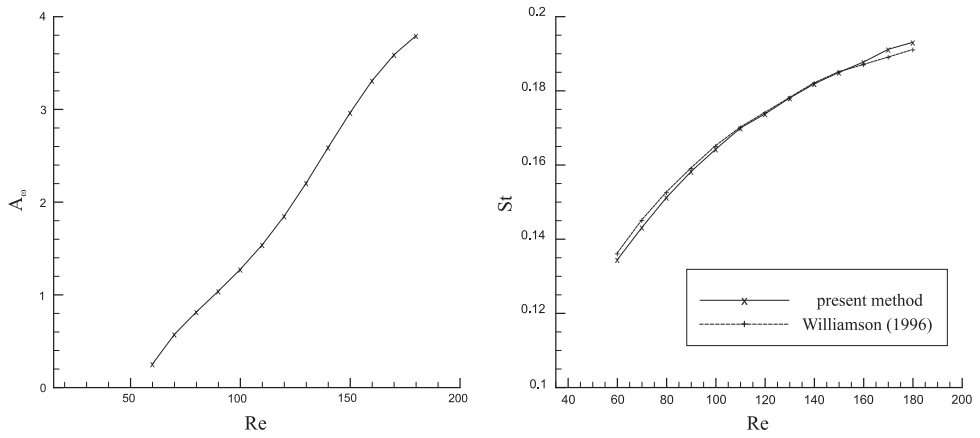

Figure 4. Amplification factor A_ω curve (left). Strouhal–Reynolds curve (right).

DOI: 10.1002/fld

Table I. Comparison of drag coefficient, lift coefficient, and Strouhal number for flow past a circular cylinder at Re = 100 and Re = 200.

	Re = 100			Re = 200		
Authors	$c_{\bar{D}}$	$c_{\bar{L}}$	S_t	$c_{\bar{D}}$	$c_{\bar{L}}$	S_t
Braza *et al.* [31]	1.36 ± 0.015	0 ± 0.25	0.160	1.40 ± 0.050	0 ± 0.75	0.190
Russel and Wang [30]	1.43 ± 0.009	0 ± 0.322	0.172	1.45 ± 0.036	0 ± 0.63	0.201
Present method	1.40 ± 0.010	0 ± 0.32	0.165	1.44 ± 0.05	0 ± 0.75	0.200

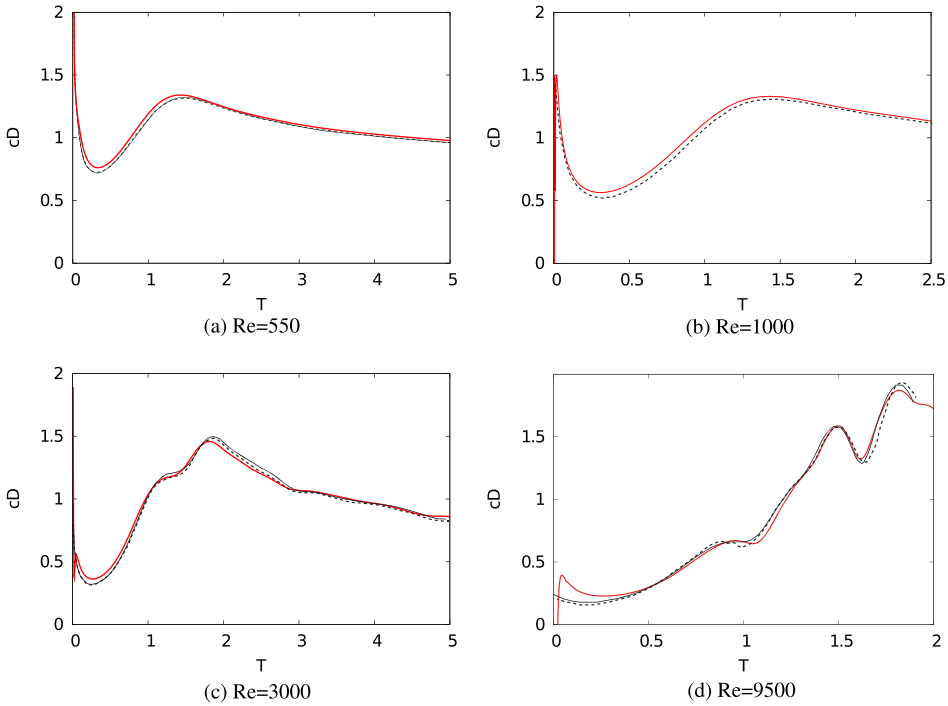

Figure 5. Drag evolution for Re = 550 (a), Re = 1000 (b), Re = 3000 (c), and Re = 9500 (d). Comparisons of present method (solid red line) with Koumoutsakos and Leonard [2] (dashed line). Solid black line are results from Ploumhans and Winckelmans [8] in (a), (b), (c) and from Rasmussen *et al.* [29] in (d).

$\Delta t = 0.005$, and $\lambda = 10^8$. The various results are in excellent agreement. Figure 6(a) depicts the vorticity isocontours, which are very similar to the vorticity field presented by Ploumhans and Winckelmans [8], where $h = 6.03 \times 10^{-3}$.

The next simulation was performed at Re = 1000. At this regime, advection effects become predominant in the flow field. The boundary layer thickness decreases, requiring a finer grid. The mesh size is consequently set to $h = 0.0025$ in a computational domain $[-4,\ 8] \times [-5,\ 5]$, and the time step is set to $\Delta t = 0.003$. The non-dimensional time evolution of the drag coefficient is given in Figure 5(b) and compared with the result in [2]. Table II shows the comparison of mean drag coefficient, amplitude fluctuation of lift coefficient, and Strouhal number with other studies [32, 33] for long time simulations. All these comparisons confirm an excellent agreement between our results and the reference results in the literature.

For Re = 3000, the flow is unstable, and the shedding generates complex vortex pairings [1]. In this case, grid convergence was obtained in our method for $\lambda = 10^8$, $h = 0.0025$, and $\Delta t = 0.0025$. Figure 5(c) shows again a very good agreement in the drag history between our results and those in [8] and [2]. In [8], h is about 0.002. Vortex contours in Figure 6(b) confirm this agreement.

The last simulation addresses the flow around the impulsively started cylinder at Re = 9500. Let us emphasize that a 2D validation study at such a regime makes sense because we only consider here the impulsive start of the flow, before the onset of 3D instabilities. In order to capture small

DOI: 10.1002/fld

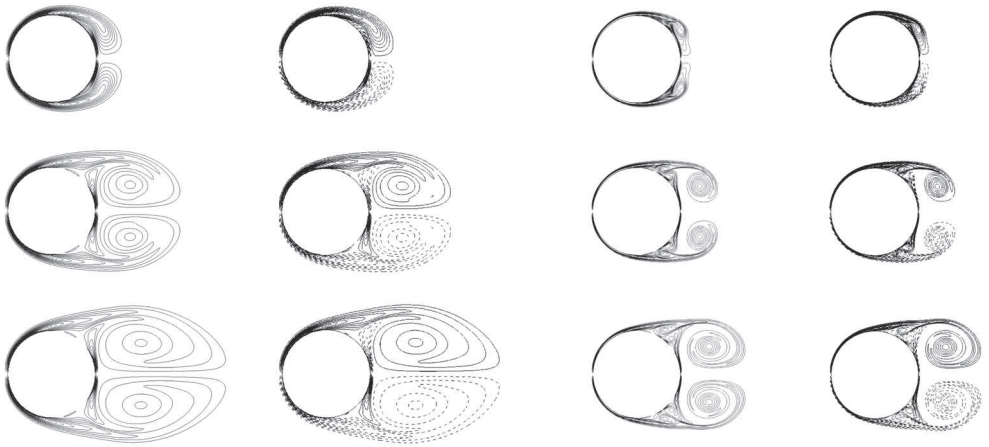

(a) Re=550 (b) Re=3000

Figure 6. Comparison of vorticity isocontours for the impulsively started cylinder between the present method (left columns) and Ploumhans and Winckelmans [8] (right columns) at (a) $T = 1, 3, 5$ at Re $= 550$ and (b) $T = 1, 2, 3$ at Re $= 3000$.

Table II. Comparison of mean drag coefficient, mean lift coefficient, and Strouhal number for flow past a circular cylinder at Re $= 1000$.

	Re $= 1000$		
Authors	$\bar{c_D}$	$\bar{c_L}$	S_t
Apte *et al*. [32]	1.50	0 ± 1.36	0.238
Mittal *et al*. [33]	1.48 ± 0.21	0 ± 1.65	0.250
Present method	1.51 ± 0.23	0 ± 1.54	0.245

Table III. Justification of the choice of mesh size h based on the boundary layer thickness δ, for the circular cylinder validation study.

Re	Boundary layer thickness (δ)	Chosen mesh size (h)	Number of mesh cells in boundary layer
550	~ 0.043	0.005	8.6
1000	~ 0.032	0.0025	12.8
3000	~ 0.018	0.0025	7.2
9500	~ 0.010	0.00125	8

spatial structures and the thin boundary layer, the grid size was reduced to the value $h = 0.00125$ in the same computational domain as the one used in the previous cases. The time step was set to 0.002 and $\lambda = 10^8$. The comparison of our results to those obtained by Rasmussen *et al*. [29] as well as Koumoutsakos and Leonard [2] is reported in Figure 5(d). In [29], a multilevel vortex method was used with a minimal grid resolution corresponding to $h_{min} = 1/1024$. The discrepancy observed in Figure 5(d) at early times of the drag history indicates that the penalization method has difficulties to establish the strong initial vortex sheet on the body of the cylinder. For later times, our results are in excellent agreement with [2, 29].

To conclude this section, Table III is given to confirm that the choice of the grid resolution h at each flow regime is appropriate to capture the boundary layer thickness, expressed by $\delta \approx D/\sqrt{Re}$.

The validation study just performed for the 2D circular cylinder benchmark enables us to determine the appropriate grid resolutions and time steps needed to obtain accurate results in the more challenging cases that will be considered in the following.

DOI: 10.1002/fld

4. APPLICATION TO FLOW PAST A MOVING TWO-DIMENSIONAL VERTICAL AXIS TURBINE

In this section, our goal is to take advantage of the flexibility of the vortex penalization method to handle moving bodies. Here, we apply this technique to the 2D flow past a VAT.

The main problem encountered with the aerodynamics of a VAT architecture turbine is the complex unsteady flow phenomena occurring during its working cycle. For each revolution, the blades undergo a highly unsteady relative motion with large variation of incidence and absolute value of the relative velocity. This complexity in the flow motion is mainly characterized by flow detachment, vortex shedding, dynamic stall, and turbulence.

The study of the turbulent flow past VAT has been addressed recently by some authors [34–36]; however, the basic characteristics of the turbulent wake for such a kind of flow remains essentially an open issue.

Cottet *et al*. [37] and van Rees *et al*. [38] provide validation studies of remeshed vortex methods against reference spectral methods in 3D laminar and turbulent flows. These studies give confidence that remeshed vortex methods, combined with penalization methods, can be efficient and flexible tools to handle VAT flows.

The VAT is rotating at a given velocity Ω and is immersed in a stream with a uniform far field velocity u_∞. The blade radius and the airfoil chord are denoted by R and c, respectively (Figure 7(a)).

The motion of a solid obstacle can be described with the vortex–penalization method as follows [11]. $S = S(t)$ is a moving multi-connected solid region. If one denotes by ϕ a level set function, which is negative inside S and positive outside, the characteristic function of S is defined by $\chi = \mathcal{H}(\phi)$, where $\mathcal{H}(\cdot)$ is a suitable step function. Moreover, in a rigid body motion, the level set function has to satisfy

$$\frac{\partial \phi}{\partial t} + (\mathbf{u}_s \cdot \nabla)\, \phi = 0. \tag{36}$$

The aforementioned equation enables to evaluate the body trajectory. Equation (36) can be interpreted as a material derivative $D\phi/Dt = 0$, and the movement of the blade can be integrated using a Lagrangian method. Figure 7(b) shows some levels of the function ϕ defining the airfoil on a Cartesian equispaced grid.

The blade section used in this VAT is a symmetrical Kármán–Trefftz airfoil with a slightly smoothed trailing edge. The frame of reference is set on the rotation axis of the turbine, and the computational domain is $D = [-6,\ 6] \times [-3.5,\ 3.5]$ with 3001×1751 grid points (corresponding to $h = 0.004$) and the penalization parameter $\lambda = 10^{10}$. The Poisson equation is solved using

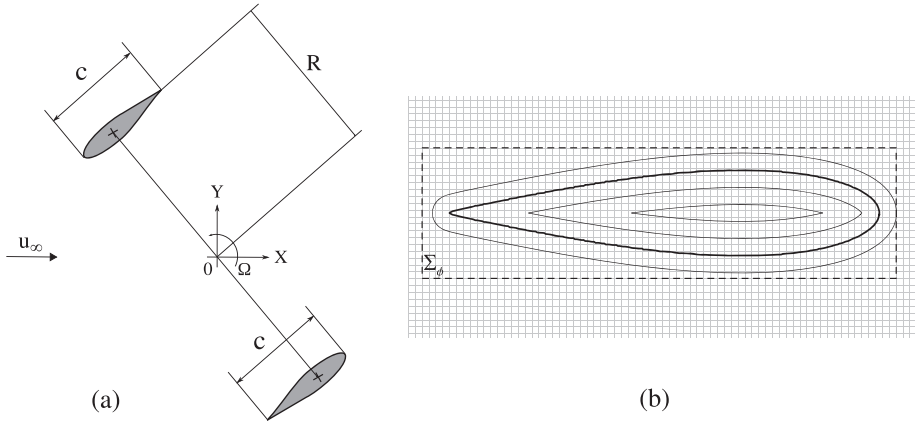

Figure 7. (a) Geometrical setup of VAT. (b) Distance function ϕ isocontours, the dashed rectangle Σ_ϕ is the support of ϕ.

DOI: 10.1002/fld

a fourth-order finite differences-based solver, provided by the Fishpack library [39]. The boundary conditions prescribed on the stream function ψ are the following: on the upstream/downstream boundaries, a Neumann condition is imposed, and on the horizontal boundaries, a Dirichlet condition enforces the flow mass rate through the domain. The Reynolds number for a VAT can be defined choosing the blade section chord c as reference length and the maximum relative velocity $\mathbf{u}_{rel}^{max}$ as reference velocity, where this velocity is given by $\mathbf{u}_{rel}^{max} = |u_\infty| + |\Omega R|$. For a realistic simulation of a medium/small wind or water turbine, it is located in the range of 10^4–10^6. The flow is transitional and is dominated by convective phenomena.

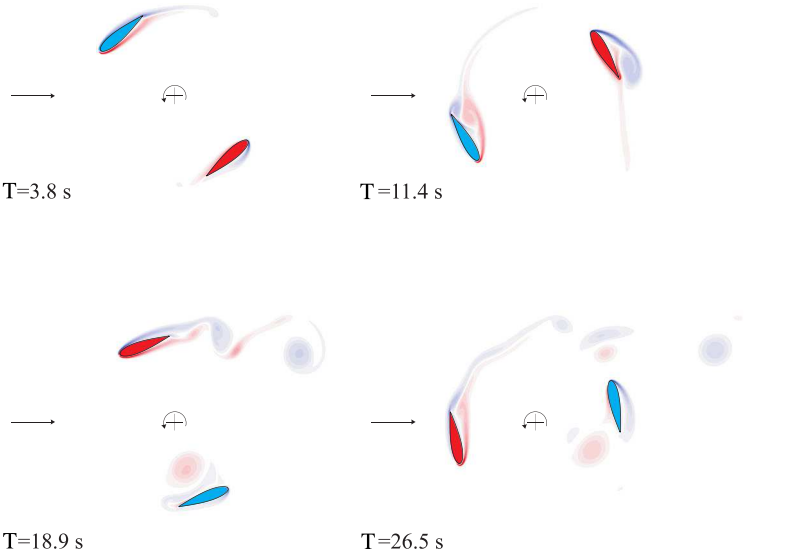

(a) Re=1000

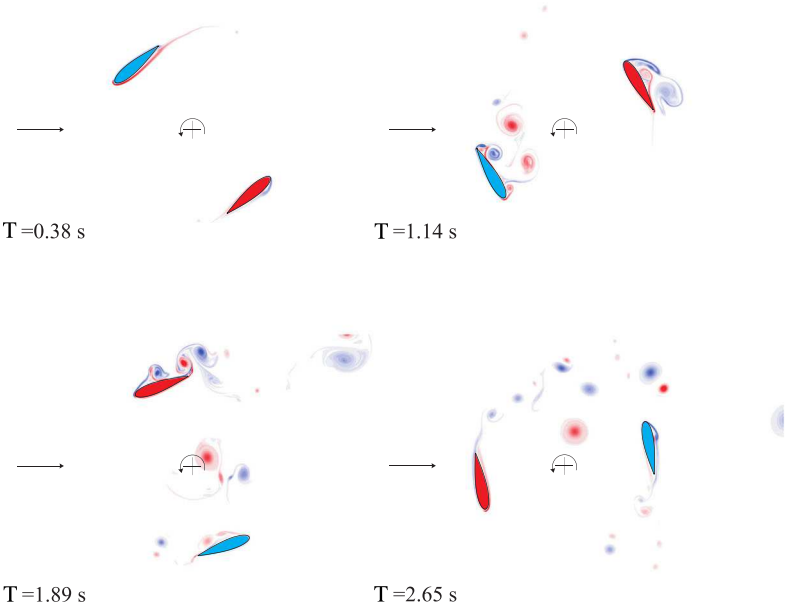

(b) Re=10000

Figure 8. Isovorticity lines of the wake past the VAT at Re $= 1000$ (a) and at Re $= 10,000$ (b). Snapshots, respectively, at times $T = 3.8,\ 11.4,\ 18.9$, and 26.5 s and $T = 0.38,\ 1.14,\ 1.89$, and 2.65 s.

DOI: 10.1002/fld

In this section, two values of the Reynolds numbers, Re $= 1000$ and Re $= 10,000$, are considered. This bench study mainly aims to highlight the great capability of the present method to supply realistic results for moving bodies with unfitted boundaries, and the grid resolution handled here is convenient to confirm the qualitative physical behavior of computations.

For the Reynolds number Re $= 1000$, a wind turbine with a blade section chord $c = 0.2$ m, radius $R = 0.3$ m, rotating speed $\Omega = 0.185$ rad/s, and immersed in a stream with $u_\infty = 0.025$ m/s is considered (where $\nu_{air} = 1.6\,10^{-5}$ m^2/s at 20°C). For this Reynolds number, which corresponds to a low transitional flow with viscous effects, the time step is taken as $\Delta t = 0.001$. A higher Reynolds number for a wind turbine operating at low wind speed is studied by considering this VAT geometry with the working conditions $\Omega = 1.85$ rad/s and $u_\infty = 0.25$ m/s. The corresponding Reynolds number is Re $= 10,000$, and the integration time step is chosen to be $\Delta t = 0.0002$. In Figure 8(a) and 8(b), instantaneous vorticity isolines for different rotating times of the blades at Re $= 1000$ and Re $= 10,000$ are, respectively, plotted. The varying incidence of the velocity occurring at each blade generates separation and vortex shedding; as the figures show, the flow is highly unsteady, and the blade strongly interacts with the wake. The flow for Re $= 1000$ generates an almost regular Von-Kármán-like wake with large structures. By contrast, the vortex shedding for the Re $= 10,000$ becomes very quickly unsteady where small high-frequency vortical structures interact with each other before being transported downstream.

A complementary description of the flow around the turbine is given by the averaged-in-time streamlines for the absolute flow field shown in Figure 9(a) and 9(b), for a wake at Re $= 1000$ and Re $= 10,000$. The isolines are displayed in the relative frame of reference, which is centered on the turbine axis and moves jointly with the blades. For the lower Reynolds number Re $= 1000$, the average is computed for a simulation time of $\approx$650 s, which corresponds to $\approx$19 loops of the blade. As Figure 9(a) shows, for this flow, the recirculation zones (one for each blade) are concentrated between the rotation axis and the inner surface of the blade. For the higher Reynolds number Re $= 10,000$, the mean flow is computed for a simulation time of $\approx$65 s, which still corresponds to $\approx$19 cycles. In this case, for each blade, three recirculating areas can be identified, as in Figure 9(b): two zones are close to the airfoil (outer and inner surfaces), and the third region is the average in time of the wake generated from the trailing edge of each blade due to complex vortex interactions.

Finally, we study the time evolution of the enstrophy ϵ and the number of vortex particles in order to better analyze the properties of these two flow regimes. The enstrophy is a quantity that measures the dissipation of energy in terms of kinetic energy. In a 2D flow field, the enstrophy is given by $Z = \int_D |\omega|^2 d\sigma$, where D is the computational domain. In Figure 10(a) and 10(b), the comparison between the time history of the enstrophy and the number of particles is shown for Re $= 1000$

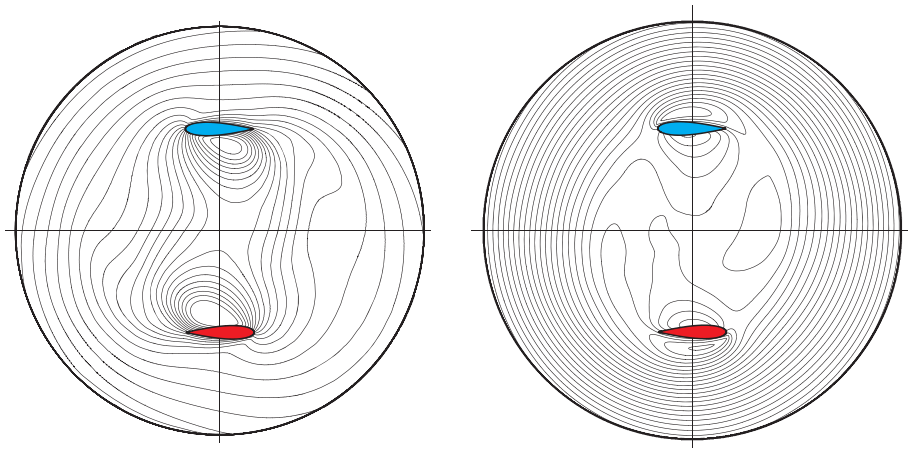

(a) (b)

Figure 9. Averaged-in-time streamlines for the VAT at Re $= 1000$ (a) and at Re $= 10,000$ (b). The isolines of the absolute flow field are represented in the relative frame of reference.

DOI: 10.1002/fld

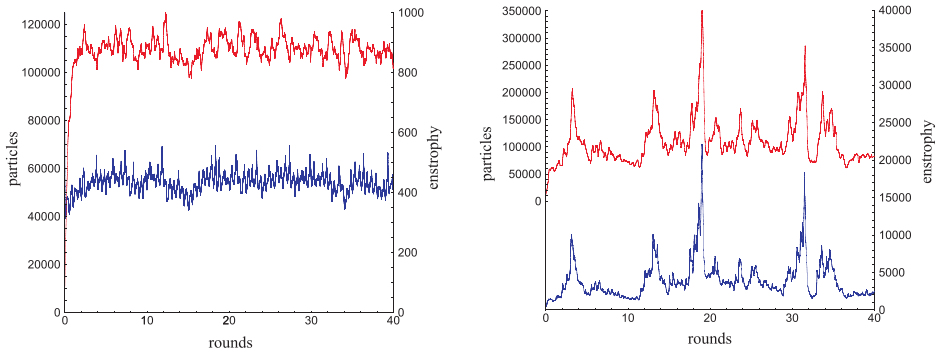

Figure 10. Time history of the dimensionless enstrophy Z (blue) and the number of vortex particles (red) for Re $=$ 1000 (a) and Re $=$ 10,000 (b). The axis of the abscissas represents the number of the cycles performed by the turbine.

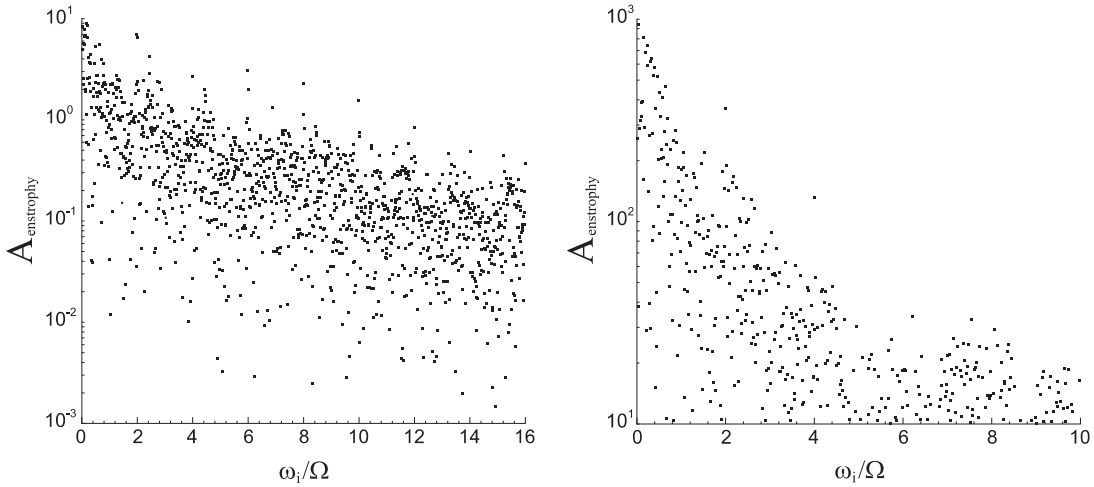

Figure 11. Frequency spectrum of the enstrophy signal computed for Re $=$ 1000 (a) and Re $=$ 10,000 (b). The horizontal axis reports the discrete frequency ω_i divided by the angular velocity Ω of the turbine.

and Re $=$ 10,000, respectively. As Figure 10(a) shows, the amplitude of the oscillations remains quite small compared with the Re $=$ 10,000 regime (Figure 10(b)), where the frequency of the shedding appears through large oscillations. The figures show the high correlation between the time evolution of the enstrophy and the number of particles. In addition, one can observe a characteristic frequency, roughly corresponding to 10 rotations of the blades, for which large vortices are shed outside the computational domain. Further computations would be needed to confirm and understand this phenomenon.

In the present cases, the flow regime is characterized by unsteady separations generated by the periodical interaction of the wake with the blades. For Re $=$ 1000, we notice that the principal vortex shedding frequency roughly corresponds to 2Ω, which is twice the angular velocity of the two-bladed VAT. For Re $=$ 10,000, different shedding frequencies can be distinguished from the rotational frequency of the blade. The investigation on the shedding frequencies is meaningful because it allows to relate the interaction of the vortex wake with the structure of the turbine. If some vortex shedding frequencies match the proper frequencies of the turbine, the structure can resonate with a self-sustained motion, and the turbine is liable to aeroelastic phenomena. To evaluate the principal frequencies of vortex shedding, we performed a discrete Fourier analysis of the enstrophy signal. In Figure 11(a) and 11(b), the spectra of the enstrophy versus the frequency of the signal are presented, where $A_{enstrophy}$ is the amplitude of the enstrophy, and ω_i / Ω is the non-dimensional

DOI: 10.1002/fld

discrete frequency of the signal. The spectra do not report the mean value corresponding to the first coefficient $i = 0$ of the Fourier series. To avoid the effect of the initial transient stage, the Fourier analysis was applied on the signals after the first three cycles of the turbine.

In Figure 11(a), the shedding principal harmonic at two times the angular velocity of the turbine is confirmed: the wake interacts with a blade two times for each cycle of the turbine. Further couplings with the principal frequency can be identified at 4, 6, and 8. Some high energy contributions are visible at frequencies lower than 2. A reason may be that the flow is not fully developed and did not achieve a statistical steady state yet.

In Figure 11(b), the spectrum exhibits shedding frequencies at two and four times the angular velocity. The enstrophy signal is noisy and characterized by random peaks at low frequency (Figure 10(b)).

Following [40], because the turbulent dissipation rate is equal to the turbulent kinetic energy production, the ratios of the Kolmogorov scale to the largest scales are determined readily by means of the approximation $\epsilon \sim \frac{U^3}{L}$, and the results are as follows: $\eta \sim \left(\frac{\nu^3 L}{U^3}\right)^{\frac{1}{4}}$, $\tau_\eta \sim \left(\frac{\nu L}{U^3}\right)^{\frac{1}{2}}$, and $u_\eta = \frac{\eta}{\tau_\eta}$. Finally, the Kolmogorov scales for the cases at $\mathrm{Re} = 1000$ and $\mathrm{Re} = 10,000$ are, respectively, $\eta = 1.1 \times 10^{-3}$ m, $u_\eta = 1.4 \times 10^{-2} \frac{\mathrm{m}}{\mathrm{s}}$, and $\tau_\eta = 7.8 \times 10^{-2}$ s and $\eta = 2.0 \times 10^{-4}$ m, $u_\eta = 8.0 \times 10^{-2} \frac{\mathrm{m}}{\mathrm{s}}$, and $\tau_\eta = 2.5 \times 10^{-3}$ s.

Higher couplings with the principal rotational frequency are not visible in the spectrum, because the energy is transferred from the large geometrical scale to the Kolmogorov scale. The large energetic contribution occurring at frequencies lower than 2 probably means that the flow is not yet fully developed.

5. EXTENSION TO SOLID–POROUS–FLUID MEDIA AND FLOW CONTROL

This section is devoted to the study of flows in solid–porous–fluid media. It illustrates the efficiency of the vortex penalization method to handle problems where the physical properties or boundary conditions vary in the body.

5.1. Modeling and numerical setup

The penalization method has been used to model the porous–fluid–solid problems with primitive pressure–velocity formulations [20, 23, 41]. This work is dedicated to the extension of this approach to the vorticity equations and to different configurations. We consider a solid body surrounded by a porous layer and immersed in an incompressible fluid. In such a system, one can identify five

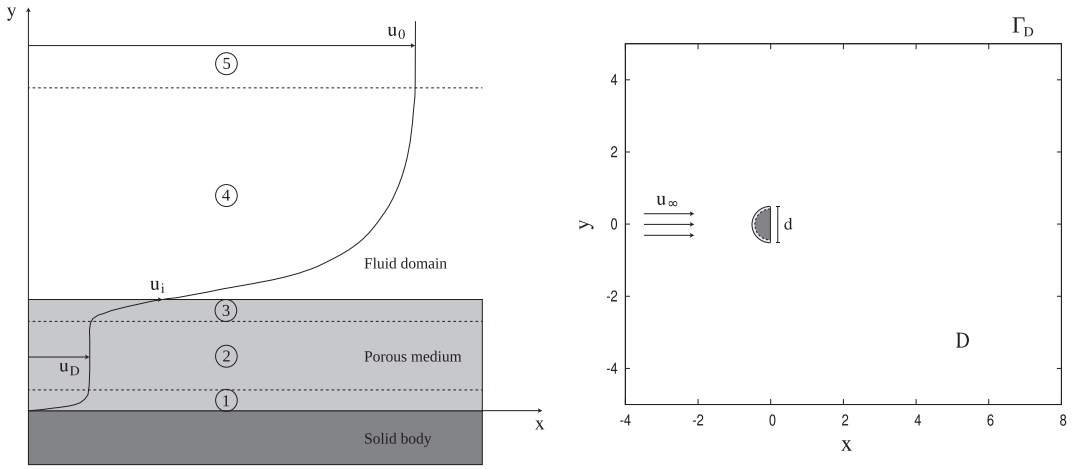

Figure 12. Velocity profile in the vicinity of a porous medium (left). Computational domain for flow control past semi-circular cylinder (right)

DOI: 10.1002/fld

different flow regimes corresponding to different regions in the fluid. The first region is the boundary layer inside the porous medium, close to the solid wall. This region is very thin compared with the second region, which is characterized by the homogeneous porous flow with Darcy velocity (regions numbered 1 and 2 in Figure 12 (left)). In the vicinity of the porous–fluid interface, two transient layers can be recognized (numbered 3 and 4 in Figure 12 (left)). The first one corresponds to the porous layer where the velocity increases to reach a value $\mathbf{u}_i$ at the interface and the second one to the fluid boundary layer leading to the free external flow. The size of the fluid boundary layer is determined by $\mathbf{u_0} - \mathbf{u}_i$ where $\mathbf{u_0}$ denotes the velocity of the main fluid flow (numbered 5 in Figure 12 (left)). The goal is thus to compute the flow simultaneously in the porous medium, the fluid region, and at the interface between the two media. Several approaches have already been proposed to handle this problem. The first one, which is mainly used to model flows past a solid with permeable walls [42, 43], avoids to solve the porous flow by enforcing appropriate porous–fluid boundary conditions [44]. This method neglects the physics of the porous medium and does not allow to have an overall view of the problem. The second approach considers that the porous flow has to be accurately computed and solves the governing equations in each region by coupling the Darcy equations and the Navier–Stokes equations through an appropriate condition at the interface [45, 46]. This approach is very delicate to handle especially because of the requirement of this appropriate boundary condition. The method presented here, based on the vortex–penalization technique, considerably simplifies the task because a unique equation is used for the whole domain and enables to accurately model each of the different regions by varying the value of the dimensionless penalization factor λ. In two dimensions, the penalized vorticity equation reads as follows:

$$\frac{\partial \omega}{\partial t} + (\mathbf{u}.\nabla)\omega = \frac{1}{\mathrm{Re}}\Delta\omega + \nabla \times [\lambda\ \chi_S(\mathbf{u}_s - \mathbf{u})]. \tag{37}$$

We recall that λ essentially depends, in the inverse proportion, on the physical intrinsic permeability of the medium k, which directly derives from the Darcy law (Equation (7)). Varying the value of λ thus directly characterizes the different media.

Modeling the physics of three different regions enables one to deal with engineering problems involving porous media. In the following, this approach is validated for a simple but informative passive flow control problem: the solid–porous–fluid configuration is applied to cover a semi-circular cylinder geometry with a porous coating. The porous coating is applied on the obstacle external surface in order to modify the vorticity generation of the boundary layer and the vortex shedding. The presence of a porous medium at the solid–fluid interface indeed imposes a kind of mixed boundary condition intermediate between the no-slip and the slip one on the solid boundary [47]. As a result, the shear forces are reduced, and the flow dynamics is smoothed [20, 23, 41, 48]. This control technique, which allows to keep the obstacle geometry unchanged, is expected to reduce drag forces and vortex-induced vibrations, thereby improving the aerodynamic properties of the obstacle. The semi-circular cylinder can be considered as a simplified section of an outside rear-view mirror of a vehicle. The mirrors, because of their spanwise location, indeed generate a non-negligible wake, which interferes with the vehicle sides. This provides a good motivation to perform flow control past such obstacles. Moreover, as it was shown in [49, 50], a flow past a square back obstacle is not dominated by longitudinal vortical structures, therefore, a preliminary 2D study can be useful to supply information on general trends for a control.

In the following, the semi-circular cylinder has a total dimensionless diameter of $d = 1$ including a porous layer of thickness τ. The backward face of the obstacle is centered at the point $(0, 0)$ (Figure 12 (right)). In the sequel, we will consider flows both at transitional ($\mathrm{Re} = 550$) and highly transitional ($\mathrm{Re} = 3000$) regimes.

5.2. Validation and convergence studies for flow past a solid semi-circular cylinder

Compared with the circular cylinder considered in the previous section, the semi-circular cylinder presents singular points, which make its simulation more challenging. In order to verify the accuracy of the method in the case of flow past a solid semi-circular cylinder, we proceed like in Section 3. We first compare the results obtained using the present method with the ones of the literature, for

DOI: 10.1002/fld

different Reynolds numbers. Second, we present the convergence of the method with respect to the penalization parameter and the grid size.

5.2.1. Validation. The benchmark of incompressible flow past a semi-circular cylinder is not a classical one, and only few references already exist on this subject. Nevertheless, we aim at least to compare our results to numerical and experimental ones. To do so, we, respectively, consider the works of Farhadi *et al.* [51] and Boisaubert and Texier [52]. The flow analysis presented hereafter is based on the near-wake length measurement, the Strouhal number, and the drag and lift coefficients. The Reynolds number ranges between 100 and 300 in this study.

As can be seen in Table IV, the results obtained at Re $=$ 100 and Re $=$ 300 show a good agreement with the numerical values given by [51]. A more detailed comparison is performed at Re $=$ 200, and the related results are reported in Figure 13. As regards drag and lift coefficients, one can say according to Figure 13(a) that our results coincide very well with those of Farhadi *et al.* [51] because we achieve $\bar{c_D} = 1.85 \pm 0.15$, $\bar{c_L} = 0 \pm 0.53$, and $S_t = 0.230$ against $\bar{c_D} = 1.85 \pm 0.12$, $\bar{c_L} = 0 \pm 0.50$, and $S_t = 0.215$ in [51]. Figure 13(b) gives a comparison of the normalized near-wake length L with the numerical results of Farhadi *et al.* [51] and the experimental data of Boisaubert and Texier [52]. The near-wake length is defined as the x-coordinate of the point located on the centreline in the x-direction, where the streamwise component of the velocity vanishes. As can be seen in the figure, the values obtained with the present method greatly coincide with the numerical and experimental reference results.

5.2.2. Convergence studies. In this section, we present convergence studies of the vortex–penalization method for the flow past a solid semi-circular cylinder at Re $=$ 550 and Re $=$ 3000. We first focus on the convergence of the present method with respect to the penalization parameter λ. The way this convergence study is carried out is exactly the same as presented in Section 3.2.

Table IV. Comparison of mean drag coefficient and Strouhal number for flow past a semi-circular cylinder at Re $=$ 100 and Re $=$ 300.

	Re $=$ 100		Re $=$ 300	
Authors	$\bar{c_D}$	S_t	$\bar{c_D}$	S_t
Farhadi *et al.* [51]	1.73	0.180	1.955	0.22
Present method	1.70	0.192	1.90	0.24

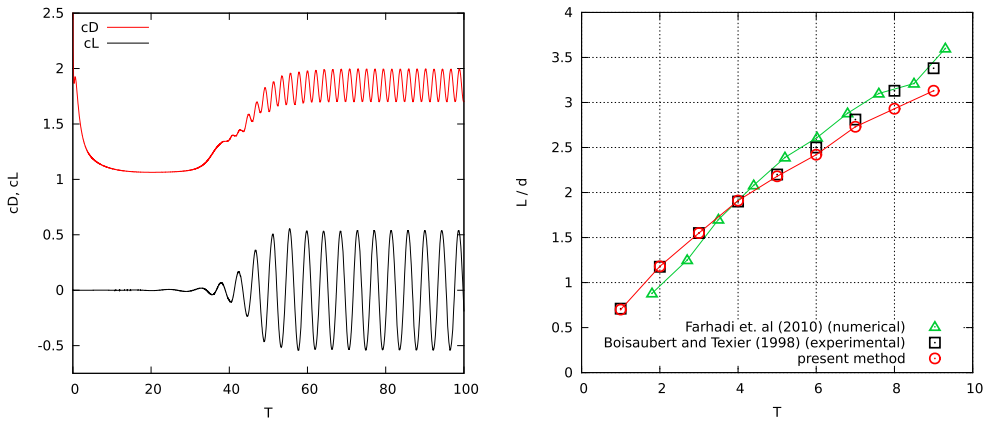

(a) (b)

Figure 13. (a) Drag and lift evolution for flow past a semi-circular cylinder at Re $=$ 200. (b) Normalized near-wake length L/d of a semi-circular cylinder at Re $=$ 200: comparison with numerical results [51] (green triangles) and experimental data [52] (black squares).

DOI: 10.1002/fld

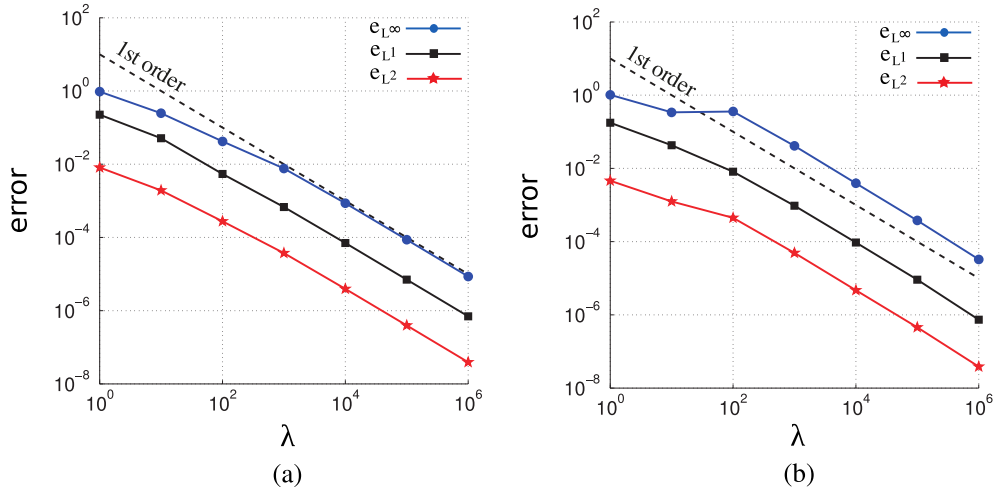

Figure 14. λ-convergence study for flow past a semi-circular cylinder: the errors e_{L^∞}, e_{L^1}, and e_{L^2} are plotted against λ values at Re = 550 (a) and Re = 3000 (b).

Table V. Convergence study for flow past a semi-circular cylinder at Re = 550 and Re = 3000. $\bar{c_D}$ and $\bar{Z}$, respectively, denote the mean values of drag coefficient and enstrophy.

	Re = 550		Re = 3000	
Grid	$\bar{c_D}$	$\bar{Z}$	$\bar{c_D}$	$\bar{Z}$
$h = 0.01$	1.49	122	—	—
$h = 0.005$	1.91	158	1.89	313
$h = 0.0025$	1.98	161	1.94	292
$h = 0.00125$	—	—	1.96	280

As Figure 14 shows, the semi-circular cylinder reaches the solid state from $\lambda = 10^5$, where $e(y) \leqslant 10^{-4}$, for both regimes. A permeable area can thus be defined with λ-values lower than 10^4. In the upcoming control study, we will vary the penalization parameter until 10^3 inside the added porous layer in order to model a permeable medium.

We now turn to a grid convergence study. It is performed on three grid levels. For Re = 550, we consider three mesh sizes as follows: $h = 0.01$, $h = 0.005$, and $h = 0.0025$ in the computational domain $D = [-4,\ 8] \times [-5,\ 5]$. For Re = 3000, as the boundary layer is thinner, we perform the convergence study with three finer mesh sizes, respectively, $h = 0.005$, $h = 0.0025$, and $h = 0.00125$. The simulations are carried out in a smaller domain $D = [-2.5,\ 5] \times [-3,\ 3]$ in order to reduce the computational cost induced by the finest grid. The mean drag and enstrophy values are reported in Table V. At Re = 550, on the basis of these results, one can consider that the grid convergence is achieved for $h = 0.005$ with $\Delta t = 0.0025$. At Re = 3000, grid convergence is obtained with $h = 0.0025$ and $h = 0.00125$, which lead us to choose $h = 0.0025$ and $\Delta t = 0.002$ for the upcoming simulations. Let us emphasize the interest of the vortex methods, which enable here to handle a highly transitional regime using a relatively large time step compared with classical Eulerian methods.

5.3. Parametric study with respect to the penalization parameter λ

In this section, we study the influence of the porous layer permeability on the flow behavior and the efficiency of such a passive control. This parametric study is performed at Re = 550 and Re = 3000 with different values of the porous permeability inside the layer, ranging from $\lambda = 0.125$ (very high permeability) to 10^3 (very low permeability). The results are compared with the one

DOI: 10.1002/fld

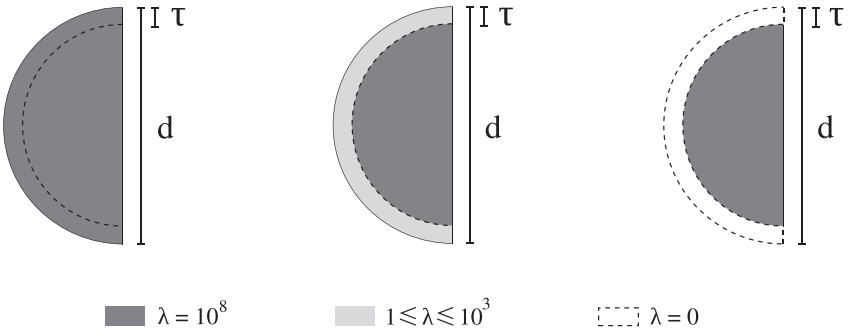

Figure 15. (left) Solid/uncontrolled case, (center) porous case, (right) fluid case.

Table VI. Reduction effects in terms of mean drag force, mean enstrophy, and Strouhal number brought by the different layer permeabilities in comparison with the uncontrolled case at Re = 550.

	Re = 550		
Cases	$\bar{\mathcal{F}}_x$	$\bar{Z}$	S_t
Uncontrolled case	0.957	158.4	0.248
Porous case $\lambda = 1000$	0.957 (−0%)	154.0 (−3%)	0.248 (+0%)
Porous case $\lambda = 100$	0.968 (+1.1%)	143.3 (−10%)	0.248 (+0%)
Porous case $\lambda = 10$	0.970 (+1.4%)	114.4 (−28%)	0.252 (+1.6%)
Porous case $\lambda = 5$	0.893 (−7%)	100.6 (−36%)	0.257 (+4%)
Porous case $\lambda = 2.5$	0.788 (−19%)	93.7 (−41%)	0.268 (+8%)
Porous case $\lambda = 1$	0.695 (−27%)	97.5 (−38%)	0.284 (+15%)
Porous case $\lambda = 0.5$	0.664 (−31%)	101.9 (−36%)	0.291 (+17%)
Porous case $\lambda = 0.25$	0.648 (−32%)	105.5 (−33%)	0.296 (+19%)
Porous case $\lambda = 0.125$	0.643 (−33%)	107.7 (−32%)	0.298 (+20%)
Fluid case	0.640	110.9	0.300

corresponding to the solid ($\lambda = 10^8$) and fluid ($\lambda = 0$) cases. In the first place, the thickness of the coating is set to 10% of the diameter: $\tau = 0.1$ (Figure 15) for all the cases. According to the grid convergence performed in the previous section (Table V), the numerical simulations are performed on a 2400×2000 grid (corresponding to $h = 0.005$) for $\mathrm{Re} = 550$ and on a 4800×4000 grid (corresponding to $h = 0.0025$) for $\mathrm{Re} = 3000$ in a computational domain $D = [-4,\ 8] \times [-5,\ 5]$ (Figure 12 (right)).

In order to analyze the effects of our control approach, we compare global flow quantities like the drag force ($\mathcal{F}_x$), computed according to the *momentum equation* (29), the enstrophy (Z) allowing to measure the dissipation effects in the flow as well as the delay of transition to turbulence, and the Strouhal number (S_t). Note that in this study, we consider drag forces instead of drag coefficients because the C_D formula (32) involves the diameter d of the obstacle, which is not clearly defined because of the porous coating.

The results of the parametric study performed at $\mathrm{Re} = 550$ are given in Table VI. Concerning the Strouhal number S_t, one can notice that it continuously increases as the λ value decreases. The presence of a permeable layer around the obstacle indeed enables to raise the shedding frequency, and in the limit $\lambda \to 0$, one tends to the flow dynamics of the fluid case, which is characterized by smaller vortices swirling at higher frequency (Figure 16(a)). Regarding $\bar{\mathcal{F}}_x$, Table VI shows that, as expected, the drag reduces as the controlled case tends to the fluid case. Nevertheless, one can observe a slight increase of the drag force for intermediate values of λ, namely, $\lambda = 100$ and $\lambda = 10$. In fact, this range of permeability values is responsible for a high resistance of the flow inside the layer inducing higher friction forces at the interface and thus a higher total drag. The quantitative results reported in Table VI are also highlighted in Figures 17 and 18, respectively, depicting the mean velocity and mean vorticity fields. As already emphasized in the literature [48, 50], the main source of drag forces for bluff bodies with square back is the low-pressure recirculation

DOI: 10.1002/fld

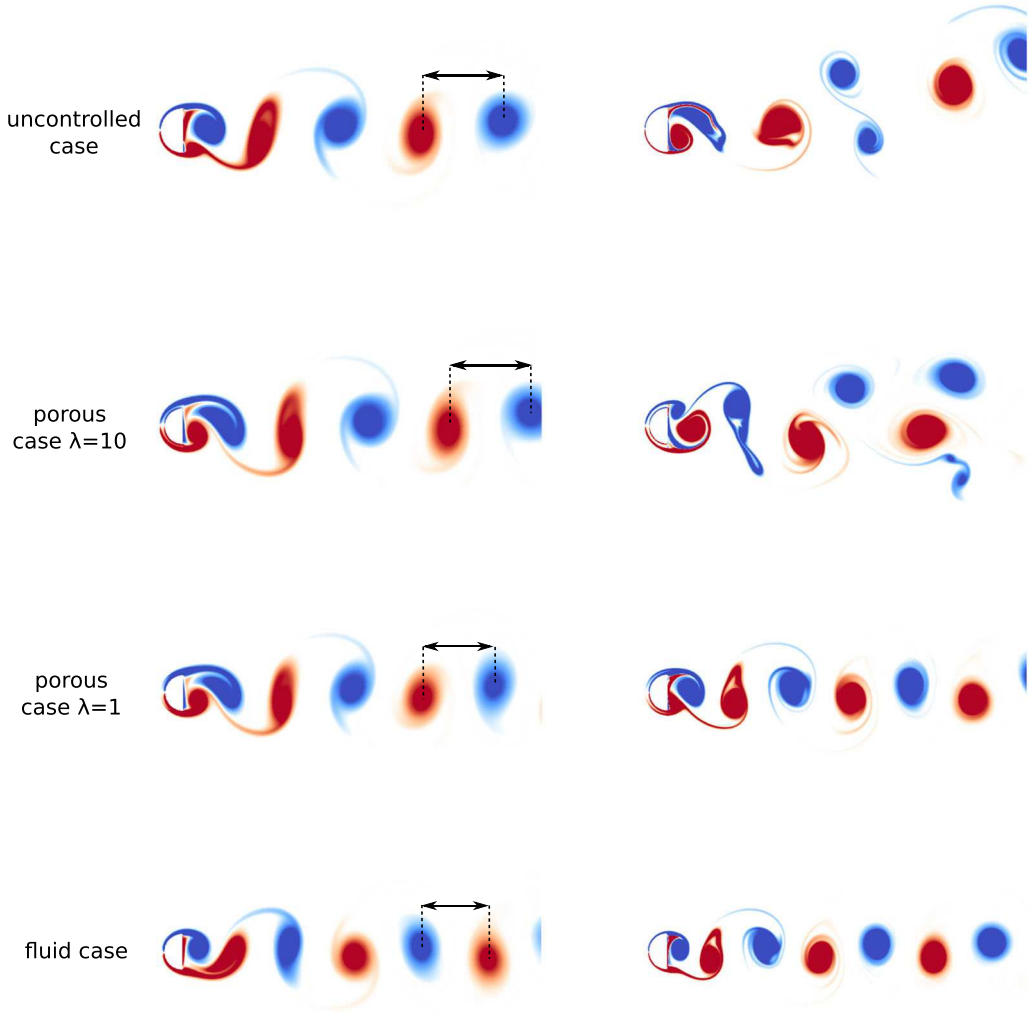

Figure 16. Instantaneous vorticity fields for flow past a semi-circular cylinder at Re $=$ 550 (a) and Re $=$ 3000 (b). The vortex shedding of the two controlled cases ($\lambda = 10$ and $\lambda = 1$, with $\tau = 0.1$) is compared with one of the uncontrolled and fluid cases (reduced obstacle).

zone in the near wake of the vertical wall. With $\lambda = 1$, the near-wake structures are smaller, and the back recirculation zone is drastically reduced (Figure 18). Moreover, the mean velocity of the wake clearly diminishes (Figure 17), and the structure of the global and near wake resembles one of the fluid cases. This feature explains the important drag reduction observed in Table VI for $\lambda = 1$ (-27%) and in general for small values of λ. On the contrary, the flow behavior obtained with $\lambda = 10$ looks very similar to one of the uncontrolled cases with an important transversal extent of the wake (Figure 18) and high velocities in the flow compared with the uncontrolled case (Figure 17). This confirms the results given in Table VI and allows us to conclude that this value of λ is not suitable at this regime to achieve drag reduction. However, with $\lambda = 10$, we obtain an important reduction of the enstrophy, which implies an efficient wake regularization and thus a delay in flow transition. This observation leads us to the analysis of control efficiency in terms of enstrophy, for which we observe a more complex behavior. Indeed, as can be read in Table VI, the enstrophy decreases with λ to reach an optimal value, for $\lambda = 2.5$ (-41% compared with uncontrolled case). Below this λ value, the enstrophy increases again to finally reach the value corresponding the reduced obstacle (fluid case). Therefore, when $\lambda \leqslant 10$, then $\bar{Z}_\lambda < \bar{Z}_{\text{fluid}}$, which demonstrates the non-monotonic

DOI: 10.1002/fld

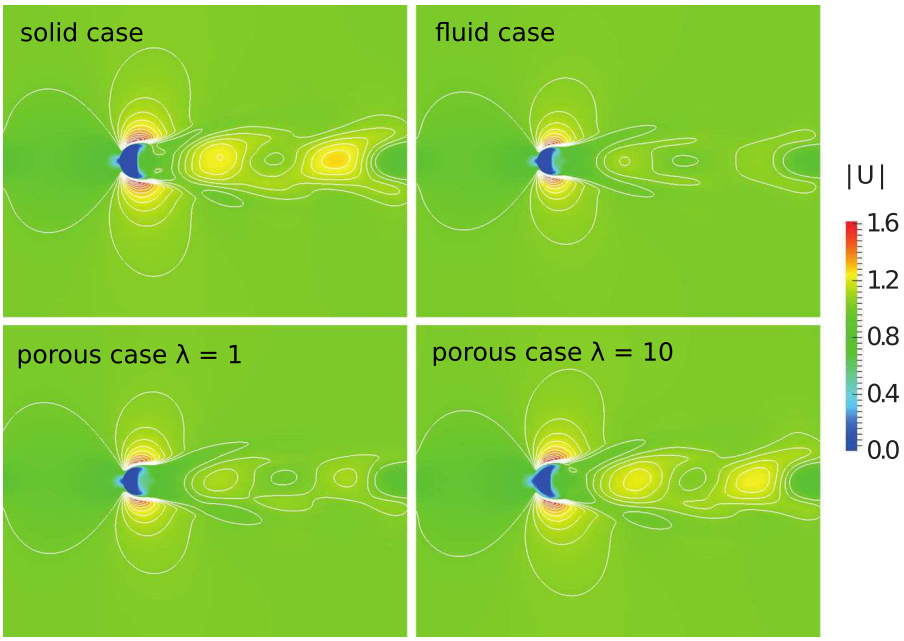

Figure 17. Isolines of mean velocity magnitude for the flow past a semi-circular cylinder at Re = 550.

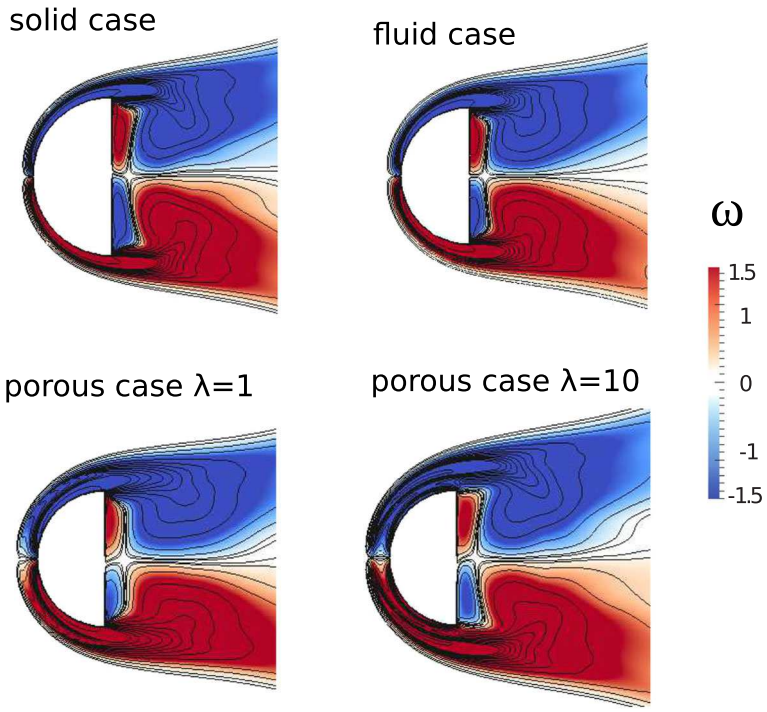

Figure 18. Zoom of the mean vorticity fields and isolines for the flow past a semi-circular cylinder at Re = 550.

behavior of the enstrophy, in the range of permeabilities taken into account in this parametric study (for all values of λ in $\{0.125, 1000\}$, $\bar{Z}_\lambda < \bar{Z}_{\text{solid}}$). Figure 19(a) summarizes these observations made from Table VI and shows the evolution of the mean drag force and the mean enstrophy with respect to the λ parameter.

DOI: 10.1002/fld

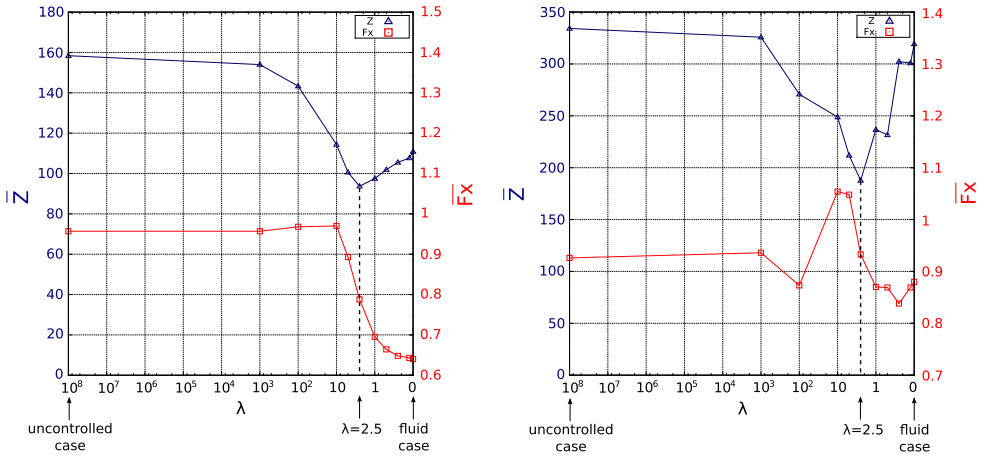

Figure 19. Effects of various layer permeabilities on the mean drag force $\bar{\mathcal{F}}_x$ (red curves) and the mean enstrophy $\bar{Z}$ (blue curves) for flow past a semi-circular cylinder at Re $=$ 550 (a) and Re $=$ 3000 (b) with $\tau = 0.1$.

Table VII. Reduction effects in terms of mean drag force, mean enstrophy, and Strouhal number brought by the different layer permeabilities in comparison with the uncontrolled case at Re $=$ 3000.

	Re $=$ 3000		
Cases	$\bar{\mathcal{F}}_x$	$\bar{Z}$	S_t
Uncontrolled case	0.926	334.2	0.238
Porous case $\lambda = 1000$	0.936 (+1%)	325.8 (−2.5%)	0.236 (−0.84%)
Porous case $\lambda = 100$	0.873 (−6%)	270.0 (−19%)	0.211 (−11%)
Porous case $\lambda = 10$	1.054 (+14%)	248.8 (−26%)	0.246 (+4%)
Porous case $\lambda = 5$	1.048 (+13%)	211.9 (−37%)	0.282 (+19.5%)
Porous case $\lambda = 2.5$	0.933 (+0.76%)	187.7 (−44%)	0.295 (+25%)
Porous case $\lambda = 1$	0.870 (−6%)	236.7 (−29%)	0.313 (+33%)
Porous case $\lambda = 0.5$	0.869 (−6%)	261.6 (−22%)	0.323 (+37%)
Porous case $\lambda = 0.25$	0.838 (−9.5%)	302.3 (−9.5%)	0.321 (+36%)
Porous case $\lambda = 0.125$	0.869 (−6%)	300.9 (−10%)	0.328 (+39%)
Fluid case	0.880	319.3	0.331

At Re $=$ 3000, the evolution of the Strouhal number as a function of λ is similar to the one observed at Re $=$ 550: the more permeable the added layer is, the higher the shedding frequency is. This behavior is represented by the vorticity fields of Figure 16(b), where one can clearly see the benefits of the porous coating, which enables to go from a chaotic wake with large eddies of strong intensity (uncontrolled case) to an axisymmetric Von Kármán street composed of numerous small vortices, similar to one of the fluid cases (controlled case with $\lambda = 1$). On the other hand, the results obtained in terms of mean drag force and mean enstrophy are also comparable with those obtained at Re $=$ 550, with a more pronounced behavior. Concerning the drag force, we indeed notice in Table VII and Figure 19(b) that intermediate permeabilities ($\lambda \approx 10$) completely deteriorate the performances. On the contrary, below $\lambda = 5$, the drag reduction is enhanced. This assessment is confirmed by Figures 20 and 21 showing in a case of a very permeable layer ($\lambda = 1$) a symmetric, thin and regular wake as well as low velocity gradients and low vorticity values in the vicinity of the detachment points and the recirculation zone. Regarding enstrophy, similarly as in the Re $=$ 550 study, we identify an optimum λ value, still equal to 2.5, for which the enstrophy reaches a global minimum value leading to a reduction of 44% (Table VII and Figure 19(b)). In a general way, this non-monotonic behavior of the enstrophy proves that the regularization effects reported here are not due to a change of the Reynolds number, because we have for instance $\bar{Z}_{\lambda=2.5} < \bar{Z}_{\lambda=1} < \bar{Z}_{\text{fluid}}$,

DOI: 10.1002/fld

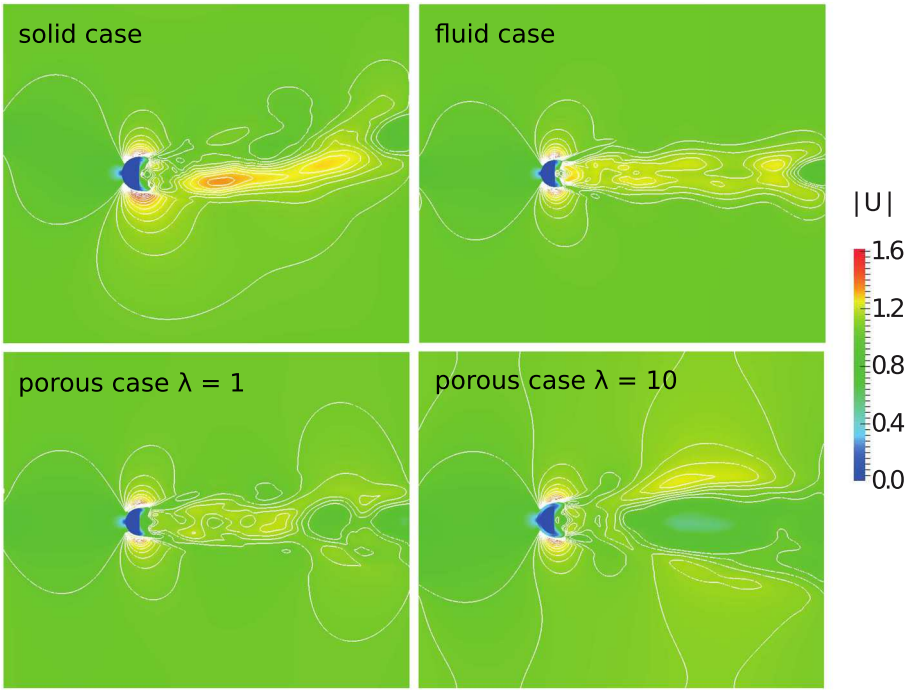

Figure 20. Isolines of mean velocity magnitude for the flow past a semi-circular cylinder at Re = 3000.

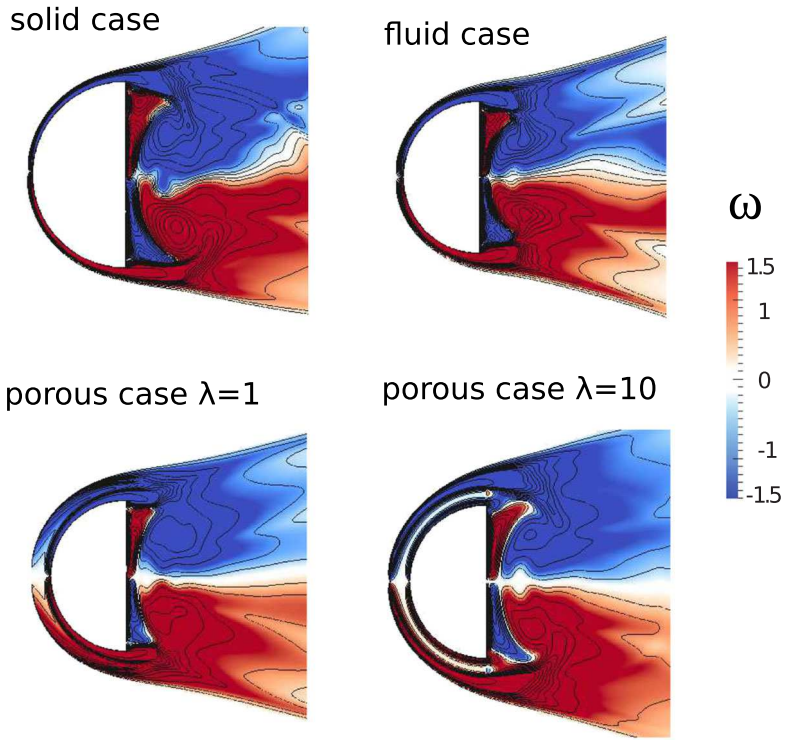

Figure 21. Zoom of the mean vorticity fields and isolines for the flow past a semi-circular cylinder at Re = 3000.

DOI: 10.1002/fld

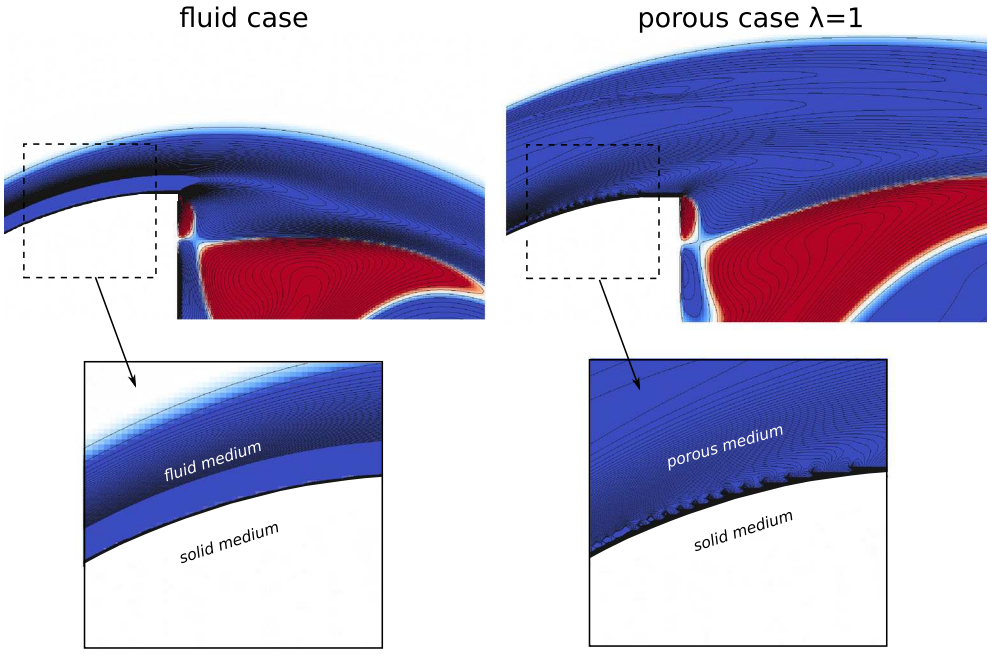

Figure 22. Zoom of the instantaneous vorticity fields and isolines at $T = 80$ in the vicinity of the solid interface at $\mathrm{Re} = 3000$ for the two following cases: the fluid case (left) and the controlled case with $\lambda = 1$ and $\tau = 0.1$ (right).

whereas $\mathrm{Re}_{\lambda=2.5} > \mathrm{Re}_{\lambda=1} > \mathrm{Re}_{\mathrm{fluid}}$. In fact, the introduction of a porous layer generates Kelvin–Helmoltz instabilities at the solid–porous interface. These instabilities, depicted in Figure 22 at $\mathrm{Re} = 3000$ for the $\lambda = 1$ test case, for example, change the shear forces at the interface and therefore modify the vortex shedding mechanism and the global flow dynamics. The presence of such instabilities explains in particular the qualitative and quantitative differences between the fluid case and the very permeable cases.

Finally, the most important observation that emerges from this parametric study is the difference of behavior between the enstrophy and the drag evolution. We indeed highlighted the systematic enstrophy reduction in the presence of a porous coating, regardless of its permeability, whereas some λ values were found to be responsible for a non-negligible drag increase, especially at $\mathrm{Re} = 3000$. This is directly due to the way these two quantities are evaluated. The enstrophy quantifies the energy dissipation of the whole system, it is therefore evaluated in the entire domain. Thus, the laminar velocities caused by the presence of the permeable layer and appearing in the vicinity of the detachment points lead to a delay in transition to turbulence and directly impact the transport of the vorticity, which is regularized. On the contrary, the drag force is evaluated on the walls of the obstacle or in the vicinity of the body (Section 2.3) and is directly linked to the vorticity generation. Therefore, the high friction phenomenon caused by some permeabilities (namely, intermediate permeabilities) and implying a resistance of the flow in the front part of the obstacle is directly reported in the drag diagnostic and in the very near-wake analysis. The $\lambda = 10$ test case at $\mathrm{Re} = 3000$ clearly illustrates these statements: one can indeed notice the beneficial effects of the permeable coating on the wake, which becomes axisymmetric (Figure 16(b)) and does not show high velocity gradients anymore (Figure 20). As a consequence, we achieve a reduction of enstrophy (Table VII). On the opposite, the effects on the very near-wake and on the drag in particular are clearly not beneficial (Table VII) as can be seen in Figure 21. The case $\lambda = 10$ shows important recirculation zones in the rear back of the solid, responsible for a pressure decrease and thus for a drag growth. Therefore, the drag forces are more sensitive to the permeability values.

To conclude this λ-parametric study, we can assert that the control should be implemented with high permeability coefficients ($\lambda \leqslant 2.5$) in order to combine both significant drag reduction and regularization of the wake.

DOI: 10.1002/fld

Table VIII. Effects of the porous layer thickness τ on the control efficiency at Re $=$ 550 (top part) and Re $=$ 3000 (bottom part). The two controlled cases considered in this study are the porous case with $\lambda = 10$ and the one with $\lambda = 1$.

	$\bar{\mathcal{F}}_x$	$\bar{Z}$	S_t
Re $=$ 550			
Uncontrolled case	0.957	158.4	0.248
$\tau = 0.1$			
Porous case $\lambda = 10$	0.970 (+1.4%)	114.4 (−28%)	0.252 (+1.6%)
Porous case $\lambda = 1$	0.695 (−27%)	97.5 (−38%)	0.284 (+15%)
$\tau = 0.05$			
Porous case $\lambda = 10$	0.914 (−4.5%)	123.5 (−22%)	0.253 (+2%)
Porous case $\lambda = 1$	0.774 (−19%)	123.7 (−22%)	0.269 (+8.5%)
$\tau = 0.025$			
Porous case $\lambda = 10$	0.879 (−8%)	134.5 (−15%)	0.254 (+2.5%)
Porous case $\lambda = 1$	0.821 (−14%)	139.3 (−12%)	0.260 (+5%)
Re $=$ 3000			
uncontrolled case	0.926	334.2	0.238
$\tau = 0.1$			
Porous case $\lambda = 10$	1.054 (+14%)	248.8 (−26%)	0.246 (+4%)
Porous case $\lambda = 1$	0.870 (−6%)	236.7 (−29%)	0.313 (+33%)
$\tau = 0.05$			
Porous case $\lambda = 10$	0.979 (+6%)	253.7 (−24%)	0.225 (−5.5%)
Porous case $\lambda = 1$	0.999 (+8%)	285.2 (−15%)	0.290 (+22%)
$\tau = 0.025$			
Porous case $\lambda = 10$	1.018 (+10%)	283.7 (−15%)	0.251 (+6%)
Porous case $\lambda = 1$	1.011 (+9%)	318.4 (−5%)	0.278 (+17%)

5.4. Influence of the layer thickness τ on the flow control efficiency

In the previous section, the effects of the control were studied for different permeabilities using a constant layer thickness $\tau = 0.1$. In this section, the effect of the thickness is investigated, and a special focus is made on thin layers in order to reduce the use of porous materials and to find out a compromise between practical engineering constraints and control efficiency. The same cases (Figure 15) are now considered with the thickness of the layer set to $\tau = 5\%d = 0.05$ and $\tau = 2.5\%d = 0.025$. Table VIII reports the control performances in terms of global flow quantities, obtained for two controlled cases, $\lambda = 10$ and $\lambda = 1$, with $\tau = 0.05$ and $\tau = 0.025$. Generally, as expected, for both regimes (Re $=$ 550 and Re $=$ 3000), a slight decrease of control efficiency is observed when τ diminishes. Nevertheless, at Re $=$ 3000, one can observe a change of trend. We indeed achieve a drag increase for both controlled cases ($\lambda = 1$, $\lambda = 10$), even if the enstrophy reduction is still maintained. Thus, to achieve a significant drag reduction, it becomes necessary to think about the position of the permeable areas around the obstacle in order to reduce the high resistance currently experienced by the flow only in the front part of the layer. This question is the purpose of a companion paper [53], where it is in particular shown that an efficient solution consists in locating the permeable zones only on top and bottom of the body, in the vicinity of the flow detachment points.

6. CONCLUSION

In this paper, a method combining penalization, vorticity formulation, and particle discretization was described and applied to complex fluid–solid configurations. The penalization approach greatly simplifies the implementation of vortex particle methods to handle the no-slip boundary conditions. It enables to consider the governing equations in the whole computational domain and enables the use of simple Cartesian grids and fast Poisson solvers to compute velocity fields. After a detailed validation on the circular cylinder benchmark, the first application to moderate and high Reynolds

DOI: 10.1002/fld

flows around a moving VAT was presented. The results showed the efficiency of this method to realistically model flows past moving obstacles. The second application illustrated the capability of the method to handle solid–fluid–porous media. The distinction between the three different media is indeed performed by varying the value of the penalization parameter without prescribing a boundary condition at the solid boundary or at the porous–fluid interface. An application to passive flow control past a semi-circular cylinder was performed at transitional and highly transitional regimes, consisting in adding a porous sheath on the obstacle surface in order to smooth the flow dynamics. The presence of a porous layer at the solid–fluid interface is responsible for a decrease of the shear forces and the vorticity generation of the boundary layer, leading to significant wake stabilization and drag reduction.

REFERENCES

1. Williamson CHK. Vortex dynamics in the cylinder wake. *Annual Review of Fluid Mechanics* 1996; **28**:477–539.
2. Koumoutsakos P, Leonard A. High-resolution simulations of the flow around an impulsively started cylinder using vortex methods. *Journal of Fluid Mechanics* 1995; **296**:1–38.
3. Ploumhans P, Winckelmans GS, Salmon JK, Leonard A, Warren MS. Vortex methods for direct numerical simulation of three-dimensional bluff body flows: applications to the sphere at $Re = 300$, 500 and 1000. *Journal of Computational Physics* 2002; **178**:427–463.
4. Cottet G-H, Poncet P. Advances in direct numerical simulation of 3D wall-bounded flows by vortex-in-cell methods. *Journal of Computational Physics* 2003; **193**:136–158.
5. Poncet P. Topological aspects of the three-dimensional wake behind rotary oscillating circular cylinder. *Journal of Fluid Mechanics* 2004; **517**:27–53.
6. Cottet GH, Koumoutsakos PD. *Vortex Methods—Theory and Practice*. Cambridge University Press: New York, 2000.
7. Koumoutsakos P, Leonard A, Pépin F. Boundary conditions for viscous vortex methods. *Journal of Computational Physics* 1994; **113**(1):52–61.
8. Ploumhans P, Winckelmans GS. Vortex methods for high-resolution simulations of viscous flow past bluff bodies of general geometry. *Journal of Computational Physics* 2000; **165**:354–406.
9. Angot P, Bruneau CH, Fabrie P. A penalization method to take into account obstacles in incompressible viscous flows. *Numerische Mathematik* 1999; **81**:497–520.
10. Kevlahan N, Ghidaglia JM. Computation of turbulent flow past an array of cylinders using a spectral method with brinkman penalization. *European Journal of Mechanics* 2001; **B 20**:333–350.
11. Coquerelle M, Cottet GH. A vortex level-set method for the two-way coupling of an incompressible fluid with colliding rigid bodies. *Journal of Computational Physics* 2008; **227**:9121–9137.
12. Gazzola M, van Rees WM, Koumoutsakos P. C-start: optimal start of larval fish. *Journal of Fluid Mechanics* 2012; **698**:5–18.
13. van Rees WM., Gazzola M, Koumoutsakos P. Optimal shapes for anguilliform swimmers at intermediate Reynolds numbers. *Journal of Fluid Mechanics* 2013; **722**.
14. Gazzola M, Hejazialhosseini B, Koumoutsakos P. Reinforcement learning and wavelet adapted vortex methods for simulations of self-propelled swimmers. *SIAM Journal on Scientific Computing* 2014; **36**(3):B622–B639.
15. Rossinelli D, Bergdorf M, Cottet G-H, Koumoutsakos P. Gpu accelerated simulations of bluff body flows using vortex particle methods. *Journal of Computational Physics* 2010; **229**:3316–3333.
16. Chorin AJ. Numerical study of slighly viscous flow. *Journal of Fluid Mechanics* 1973; **57**:785–796.
17. Chorin AJ. Vortex sheet approximation of boundary layers. *Journal of Computational Physics* 1978; **27**:428–442.
18. Creusé E, Giovannini A, Mortazavi I. Vortex simulation of active control strategies for transitional backward-facing step flows. *Computers & Fluids* 2009; **38**:1348–1360.
19. Caltagirone JP. Sur l'intéraction fluide-milieu poreux: application au calcul des efforts exercés sur un obstacle par un fluide visqueux. *Comptes Rendus de l'Académie des Sciences Paris* 1994; **318**:571–577.
20. Bruneau CH, Mortazavi I. Passive control of the flow around a square cylinder using porous media. *International Journal for Numerical Methods in Fluids* 2004; **46**:415–433.
21. Nield DA, Bejan A. *Convection in Porous Media*. Springer: New York, 1999.
22. Whitaker S. *The Method of Volume Averaging*. Kluwer: Dordercht, 1999.
23. Bruneau CH, Mortazavi I. Numerical modelling and passive flow control using porous media. *Computers & Fluids* 2008; **37**:488–498.
24. Monaghan JJ. Extrapolating B splines for interpolation. *Journal of Computational Physics* 1985; **60**(2):253–262.
25. Magni A, Cottet GH. Accurate, non-oscillatory remeshing schemes for particle methods. *Journal of Computational Physics* 2012; **231**(1):152–172.
26. Cottet GH, Etancelin J-M, Perignon F, Picard C. High order semi-Lagrangian particles for transport equations: numerical analysis and implementation issues. *ESAIM: Mathematical Modelling and Numerical Analysis* 2014; **48**:1029–1064.
27. Saffman PG. *Vortex Dynamics*. Cambridge University Press: New York, 1992.

DOI: 10.1002/fld

28. Noca F, Shiels D, Jeon D. A comparison of methods for evaluating time-dependent fluid dynamic forces on bodies, using only velocity fields and their derivatives. *Journal of Fluids and Structures* 1999; **13**:551–578.
29. Rasmussen JT, Cottet GH, Walther JH. A multiresolution remeshed vortex-in-cell algorithm using patches. *Journal of Computational Physics* 2011; **230**:6742–6755.
30. Russell D, Wang ZJ. A cartesian grid method for modeling multiple moving objects in 2D incompressible viscous flow. *Journal of Computational Physics* 2003; **191**:177–205.
31. Braza M, Chassaing P, Minh HH. Numerical study and physical analysis of the pressure and velocity fields in the near wake of a circular cylinder. *Journal of Fluid Mechanics* 1986; **165**:79–130.
32. Apte SV, Martin M, Patankar NA. A numerical method for fully resolved simulation (FRS) of rigid particle-flow interactions in complex flows. *Journal of Computational Physics* 2008; **228**:2712–2738.
33. Mittal S, Kumar V. Flow-induced vibrations of a light circular cylinder at Reynolds numbers 1000 to 10,000. *Journal of Sound and Vibration* 2001; **245**:923–946.
34. Shamsoddin S, Porté-Agel F. Large eddy simulation of vertical axis wind turbine wakes. *Energies* 2014; **7**:890–912.
35. Tescione G, Ragni D, He C, Simao Ferreira CJ, van Bussel GJW. Near wake flow analysis of a vertical axis wind turbine by stereoscopic particle image velocimetry. *Renewable Energy* 2014; **70**:47–61.
36. McNaughton J, Billard F, Revell A. Turbulence modelling of low Reynolds number flow effects around a vertical axis turbine at a range of tip-speed ratios. *Journal of Fluids and Structures* 2014; **47**:124–138.
37. Cottet GH, Michaux B, Ossia S, Vanderlinden G. A comparison of spectral and vortex methods in three-dimensional incompressible flows. *Journal of Computational Physics* 2002; **175**:702–712.
38. van Rees WM, Leonard A, Pullin DI, Koumoutsakos P. A comparison of vortex and pseudo-spectral methods for the simulation of periodic vortical flows at high Reynolds numbers. *Journal of Computational Physics* 2011; **230**: 2794–2805.
39. Adams JC, Swarztrauber P, Sweet R. Fishpack90 - Fortran library. (Available form: http://www2.cisl.ucar.edu/resources/legacy/fishpack90) [Accessed on July 1975].
40. Pope SB. *Turbulent Flows*. Cambridge University Press: New York, 2000.
41. Bruneau CH, Mortazavi I. Control of vortex shedding around a pipe section using a porous sheat. *Journal of Offshore and Polar Engineering* 2006; **16**:90–96.
42. Hahn S, Je J, Choi H. Direct numerical simulation of turbulent channel flow with permeable walls. *Journal of Fluid Mechanics* 2002; **450**:259–285.
43. Jimenez J, Uhlmann M, Pinelli A, Kawahara G. Turbulent shear flow over active and passive porous surfaces. *Journal of Fluid Mechanics* 2001; **442**:89–117.
44. Beavers GD, Joseph DD. Boundary conditons at a naturally permeable wall. *Journal of Fluid Mechanics* 1967; **30**:197–207.
45. Breugem WP, Boersma BJ, Uittenbogaard RE. The laminar boundary layer over a permeable wall. *Transport in Porous Media* 2005; **59**:267–300.
46. Hanspal NS, Waghode AN, Nassehi V, Wakeman RJ. Numerical analysis of coupled stokes/darcy flows in industrial filtrations. *Transport in Porous Media* 2006; **64**:73–101.
47. Carbou G. Brinkmann model and double penalization method for the flow around a porous thin layer. *Journal of Mathematical Fluid Mechanics* 2008; **10**:126–158.
48. Bruneau CH, Gilliéron P, Mortazavi I. Passive control around a two-dimensional square back Ahmed body using porous media. *Journal of Fluids Engineering* 2008; **130**:061101-1-12.
49. Rouméas M, Gilliéron P, Kourta A. Analysis and control of the near-wake flow over a square-back geometry. *Computers & Fluids* 2009; **38**:60–70.
50. Bruneau CH, Creusé E, Depeyras D, Gilliéron P, Mortazavi I. Coupling active and passive techniques to control the flow past the square back Ahmed body. *Computers & Fluids* 2010; **38**:1875–1892.
51. Farhadi M, Sedighi K, Fattahi E. Effect of a splitter plate on flow over a semi-circular cylinder. *Journal of Aerospace Engineering* 2010; **224**(3):321–330.
52. Boisaubert N, Texier A. Effect of a splitter plate on the near-wake development of a semi-circular cylinder. *Experimental Thermal and Fluid Science* 1998; **16**:100–111.
53. Mimeau C, Mortazavi I, Cottet GH. Passive flow control around a semi-circular cylinder using porous coatings. *International Journal of Flow Control* 2014; **6**:43–60.

DOI: 10.1002/fld

Passive Flow Control Around a Semi-Circular Cylinder Using Porous Coatings

Chloé Mimeau
Univ. Grenoble-Alpes, LJK
51, rue des Mathématiques
F-38041 Grenoble FRANCE
Email: Chloe.Mimeau@imag.fr

Iraj Mortazavi
IMB Université de Bordeaux
MC^2 INRIA Bordeaux Sud-Ouest
351, cours de la Libération
F-33405 Talence FRANCE
Email: Iraj.Mortazavi@math.u-bordeaux1.fr

Georges-Henri Cottet
Univ. Grenoble-Alpes, LJK
51, rue des Mathématiques
F-38041 Grenoble FRANCE
Email: Georges-Henri.Cottet@imag.fr

ABSTRACT

In this paper, the passive control of flow past a semi-circular cylinder is investigated. This control is achieved by adding a porous medium between the solid obstacle and the incompressible fluid in order to reduce drag forces and regularize the flow. A vortex-penalization method is chosen to easily model the flow in the different media. Several configurations of the porous layer are investigated and parametric studies are performed in order to determine the most efficient passive flow control devices. This control study can be considered as a first step to propose efficient strategies to regularize the flow around a side-view mirror.

Nomenclature

C_D drag coefficient
D computational domain
F, S fluid domain and solid domain
F_D drag force
Re Reynolds number
Z enstrophy
d non-dimensional diameter
h reference mesh size
k intrinsic permeability
l_{ref} height of the obstacle
u_{ref} reference velocity
$\mathbf{u} = (u, v)$ velocity field
$\mathbf{u_s}$ body rigid motion
$\bar{\mathbf{u}}$ mean velocity magnitude
$\mathbf{u}_\infty$ free stream velocity
Γ_D computational domain boundaries
Δt time step
Φ porosity
λ penalization parameter
μ dynamic viscosity
ν kinematic viscosity
ρ density of the fluid

τ porous layer thickness
χ_S characteristic function
ω vorticity field

1 Introduction

On a ground vehicle, the outside mirrors, due to their spanwise position, indeed generate a non-negligible wake which interferes with the flow past car sides. They are responsible of up to 10% of the total vehicle drag but they only represent 0.5% of the total projected surface, which accounts for a good motivation to perform flow control past these obstacles. This work is devoted to the control of flow past a two-dimensional semi-circular cylinder which can be considered as a simplified section of a side-view mirror. As it was shown in [1,2], a flow past a square back obstacle is not dominated by longitudinal three-dimensional vortical structures, therefore a preliminary two-dimensional study can be useful to supply information and general trends for a further control study in three dimensions around a hemisphere. The aim is to use a control device easy to set up, low cost and allowing to keep the geometry unchanged. As active control devices can be hardly implemented in such a case, an efficient passive strategy seems to be a good alternative. A suitable solution has already been proposed by Bruneau and Mortazavi in [3–7]. It consists in adding a porous sheath on the obstacle surface in order to reduce the vorticity generation of the boundary layer. The presence of a porous medium at the solid-fluid interface indeed imposes a kind of mixed boundary condition intermediate between the no-slip and the slip one on the solid boundary [8]. As a result, the shear forces are decreased and the flow dynamics is smoothed. Consequently, the problem we have to solve involves three different media, namely the solid obstacle, the porous layer and the fluid. An easy way to tackle it is to use the penalization method [9]. This method is based on a unique model, the Brinkman-Navier-Stokes equations, which are obtained by adding in the Navier-Stokes equations a penalization term, depending on the intrinsic permeability. Three values of this coefficient represent the three different media. This method can be easily implemented since it enables to consider the governing equations in the whole computational domain. Moreover it does not require to prescribe a boundary condition at the solid boundary or a condition at the porous-fluid interface. The penalization method has been recently implemented in vortex methods to deal with fluid-structure interaction problems [10–12]. It was extended to deforming bodies and applied to find optimal swimming modes of fishes [13,14]. In the present work, we consider a two-dimensional viscous and incompressible flow past a semi-circular cylinder. We also introduce some porous coatings on the obstacle in order to manipulate the flow. The Brinkman-Vorticity Transport Equations are solved using remeshed vortex methods [15–17] which are characterized by their efficiency and robustness at high Reynolds numbers since they allow to focus the computational task on the rotational zones and to solve the flow equations in a fast Lagrangian way.

In the following we first describe the methodology and show some validations and convergence studies. Then we present the results of two-dimensional passive flow control for several devices differing from each other in terms of the permeability, the thickness and the geometrical configuration of the added porous layer. A careful comparison is carried out between controlled and uncontrolled flows at transitional (Re = 550) and highly transitional regime (Re = 3000).

2 Vorticity Formulation And Vortex Methods

The dynamics of an incompressible flow is governed by the incompressible Navier-Stokes equations :

$$\nabla.\mathbf{u} = 0 \quad \text{in } D \tag{1}$$

$$\frac{\partial \mathbf{u}}{\partial t} + (\mathbf{u}\cdot\nabla)\mathbf{u} = -\nabla p + \frac{1}{\mathrm{Re}}\Delta\mathbf{u} \quad \text{in } D, \tag{2}$$

where D is the computational domain, $\mathbf{u}$ the velocity and Re the Reynolds number. In this work, flow simulations are based on particle methods. The fluid particles which are displaced by convection and diffusion are characterized by their position and their vorticity. The vorticity transport is expressed by the Helmholtz equation (or Vorticity Transport Equation), obtained taking the curl of the incompressible Navier-Stokes equations (Eqn. 2) and given in 2D by :

$$\frac{\partial \omega}{\partial t} + \mathbf{u}.\nabla\omega = \frac{1}{\mathrm{Re}}\Delta\omega \quad \text{in } D, \tag{3}$$

where ω denotes the vorticity. The Poisson equation

$$\nabla^2\mathbf{u} = -\nabla\times\omega, \tag{4}$$

obtained from continuity equation (Eqn. 1), enables to recover velocity field once the vorticity field is known. The previous equations are approximated using a Vortex method [15, 18]. These methods are very robust and low-cost to simulate high Reynolds number recirculating flows since the computationel task is mainly focused on vortical structures (see for example [19, 20]). In this kind of approach, the VTE equation (Eqn. 3) is solved using a two-fractional step (or viscous splitting) method. It relies on approximating separately the diffusion and convection terms at each time step. The convective part is solved using a "Vortex-In-Cell (VIC)" method (see e.g. [15] and [21] for its application to active flow control) with a semi-Lagrangian resolution. In this fractional step a convective velocity is associated to each finite vortex element through a high order interpolation procedure, and the displacement is achieved using a Runge-Kutta method. In order to avoid Lagrangian distortion, particles are then remeshed on the original grid using the same interpolation kernel as the one used previously to interpolate grid velocity values onto the particles. Finally, for computational efficiency and accuracy, diffusion and Poisson equation are solved on the grid using Fast Fourier Transforms (FFT).

3 Vortex Penalization Method in Vorticity Formulation

Before all, we show how the penalization method can be used successfully to model the flow of an incompressible fluid around an obstacle [9]. In the penalization technique the system is considered as a single flow, subject to the Navier-Stokes equation with a penalization term that enforces continuity at the solid-fluid interface and rigid motion inside the solid. In this work, the penalization term is expressed using vorticity formulation. The main interest of the penalized vorticity formulation is that it replaces the usual vorticity creation algorithm in order to satisfy the no-slip boundary condition for vortex methods. This new technique avoids the convergence difficulties due to the particle creation on the solid boundaries (see [10] and [17]). We solve simultaneously the Brinkman equations in the solid and the Navier-Stokes equations in the fluid, considering whole the domain as a porous medium with zero (solid) or infinite permeabilities (fluid). Thus, defining the Reynolds number as $\mathrm{Re} = u_{ref}\, l_{ref}/\nu$, the non-dimensional penalized vorticity equation (or Brinkman-Navier-Stokes equation) reads

$$\frac{\partial \omega}{\partial t} + (\mathbf{u}.\nabla)\omega = \frac{1}{\mathrm{Re}}\Delta\omega + \nabla \times [\lambda\, \chi_S(\mathbf{u_s} - \mathbf{u})], \tag{5}$$

where χ_S denotes the characteristic function that yields 0 in the fluid and 1 in the solid, $\mathbf{u_s}$ indicates the rigid body velocity which is zero in all this work since the body is fixed and $\lambda = \mu\Phi\, l_{ref}/\rho k\, u_{ref}$ is the non-dimensional penalization parameter, in inverse proportion to the permeability of the medium (with k the intrinsic permeability, μ the viscosity, Φ the porosity of the porous material, l_{ref} the height of the obstacle, ρ the density and u_{ref} the reference velocity). The main advantage of this method is that it needs neither the mesh to fit the boundaries nor to specify no-slip boundary conditions. In addition it allows to compute the pressure as a continuous field on the whole domain including the solids.

The zone variation is realized changing the penalization coefficient that defines the permeability of each region. Numerically, the fluid is considered as a porous medium with a very high permeability ($\lambda = 0$) and the bodies are considered as porous media with a very small permeability ($\lambda = 10^8$).

To discretize the penalized vorticity equation (Eqn. 5) in a vortex method, the equation is split in substeps. At each time step, one successively solves the unsteady penalization-convection-diffusion equations:

$$\frac{\partial \omega}{\partial t} = \nabla \times (\lambda\, \chi_S(\mathbf{u_s} - \mathbf{u})) \tag{6}$$

$$\frac{\partial \omega}{\partial t} + (\mathbf{u} \cdot \nabla)\, \omega = 0 \tag{7}$$

$$\frac{\partial \omega}{\partial t} = \frac{1}{Re}\Delta\omega. \tag{8}$$

To solve Eq. 6 we use an implicit scheme ([10]) and we set:

$$\widetilde{\omega}^{n+1} = \nabla \times \left[\frac{\mathbf{u}^n + \lambda \Delta t \chi_S \mathbf{u_s}^n}{1 + \lambda \Delta t \chi_S} \right]. \tag{9}$$

where Δt is the time step. The right hand side above is evaluated by second order centered finite differences.

At this stage, grid vorticity above a certain cut-off is used to create particles in grid point surrounding cells and Eq. 7 is solved by a classical vortex-in-cell method [15]. Particles are pushed with a RK4 time-stepping and are then remeshed on the original grid using the third order interpolation kernel M_4' [22]. Then, diffusion (Eq. 8) and Poisson equation (Eq.

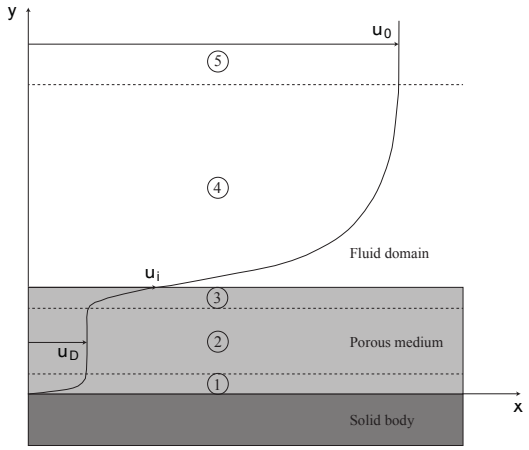

Fig. 1. Velocity profile in the vicinity of a porous medium.

4) are solved on the grid using FFT-based evaluations as described in [23]. Grid values for vorticity and velocity are now available for time t_{n+1} and a new cycle of iterations can start. Moreover, the no-slip boundary conditions are naturally satisfied penalizing the vorticity transport equations.

This hybrid vortex penalization method has already been successfully used to simulate high Reynolds flow regimes past bluff bodies [12, 24].

4 Vortex Penalization Method for Solid-Porous-Fluid Media

This section is devoted to the study of flows in solid-porous-fluid media and aims to highlight the efficiency of the vortex penalization method to solve such problems. For three different solid, porous and fluid media configurations, it is of great importance to clearly understand the flow behavior at the fluid-porous interface in order to model the physics correctly. As described in [6], we can consider five different flow regions from the solid to the free flow in the fluid. The first one is the boundary layer inside the porous medium, close to the solid wall. This one is very thin compared to the second region which is characterized by the homogeneous porous flow with Darcy velocity (numbers 1 and 2 in Fig. 1). In the vicinity of the porous-fluid interface, two transient layers can be recognized (numbers 3 and 4 in Fig. 1). The first one corresponds to the increase of the porous layer velocity reaching $\mathbf{u}_i$ value at the interface and the second one to the fluid boundary layer standing from the interface to the free flow. The fluid boundary layer growth is then determined by $\mathbf{u}_0 - \mathbf{u}_i$ where $\mathbf{u}_0$ denotes the velocity of the main fluid flow (number 5 in Fig. 1). The aim is thus to find out a way to solve the flow both in the porous medium, the fluid region and at the interface between the two media. Several approaches have already been proposed to handle this problem like avoiding to solve the porous flow enforcing appropriate porous-fluid boundary conditions [25] or solving the governing equations of each region coupling Darcy equations and Navier-Stokes equations with a right treatment at the interface [26, 27]. Nevertheless, these two approaches present some drawbacks since the first one neglects the porous medium physics and does not permit to have overall view of the problem and the second one is particularly difficult to handle especially because of the interface problem. The method presented here, based on the vortex-penalization technique, appears as a suitable alternative since it involves a unique equation (Eq. 5) for the whole domain and ensures an accurate modeling of each of the different regions thanks to the dimensionless penalization factor λ. Here, λ is expressed as $\lambda = \mu\Phi\, l_{ref}/\rho k\, u_{ref}$ where $l_{ref}, \rho, u_{ref} = 1$ in this study and the porosity Φ is close to 1 as imposed by Brinkman equations [28]. Therefore λ essentially depends, in the inverse proportion, on the intrinsic permeability k of the medium. Varying the λ value directly defines the different media according to the following equation obtained using implicit Euler scheme for the penalization velocity discretization:

$$\widetilde{\mathbf{u}}^{n+1} = \frac{\mathbf{u}^n}{1 + \lambda \Delta t \chi_S}. \tag{10}$$

Indeed, in the fluid, the intrinsic permeability coefficient k goes to infinity, thus the fluid can be considered numerically as a porous media with a very high permeability. We set $\lambda = 0$ in this region. According to Eq. 10, the velocity in the fluid is not penalized ($\widetilde{\mathbf{u}}^{n+1} = \mathbf{u}^n$) and since $\lambda = 0$, the penalization term vanishes in Eq. 5, and we naturally recover the Vorticity Transport Equation (Eq. 3). On the contrary, the solid has a permeability coefficient k which goes to zero, it can be consequently modeled setting the penalization parameter λ to a very high value. In this study λ equals 10^8 in the solid, which vanishes the flow velocity in this region according to Eq. 10 ($\widetilde{\mathbf{u}}^{n+1} \to 0$) .

It has been proved in [9] that solving Eq. 5 with such a value of λ was equivalent to solve Darcy's law in the solid. Furthermore, setting the λ parameter to an intermediate value, reasonably chosen between these two extreme values ($\lambda = 0$ and $\lambda = 10^8$), would model a porous medium in which the flow has a Darcy velocity $\mathbf{u}_D$ (Fig. 1). For example $\lambda = 1000$ corresponds to a very low permeable medium and $\lambda = 1$ represents a very high permeability. The variation of λ corresponds to the variation of k that specifies the intrinsic porous material permeability. The accuracy and efficiency of the penalization method come from its capability to take into account these variations of λ and to capture the induced steep velocity variations at the different interfaces with a minimum number of discretization points.

5 Validation and grid convergence study

In order to verify the accuracy of the method, we present in this section a validation study of the computational method employed in this work. First we consider flows past semi-circular and circular cylinders at different regimes, and we compare the results with the ones of the literature. Secondly we present a grid convergence study for flow past a semi-circular cylinder, the obstacle of interest in this work. Each simulation presented in the following is performed considering the same geometrical setup: the obstacle under study has a dimensionless diameter of $d = 1$ and its center (in the case of a circular cylinder) or its back wall (in the case of a semi-circular cylinder) is located at $(x,y) = (0,0)$ in the computational domain D. The whole domain is meshed by an equispaced Cartesian orthogonal grid. As we use FFT-based evaluations to solve diffusion and Poisson equations, periodic boundary conditions are considered on the box walls and a correction of velocity is performed at each time step in order to satisfy the free stream velocity $\mathbf{u}_\infty = (u_{ref}, 0) = (1,0)$ imposed at the inlet.

5.1 Validation for flow past a circular and a semi-circular cylinder

The first part of this validation study deals with incompressible flow past a semi-circular cylinder.We compare our results to numerical and experimental results of Farhadi et al. [29] and Boisaubert and Texier [30]. The flow analysis presented hereafter are based on the near-wake length measurement, the Strouhal number S_t (given by the shedding frequency) and the drag and lift coefficients, expressed by:

$$C_D = \frac{2F_D}{\rho u_{ref}^2 d}, \qquad C_L = \frac{2F_L}{\rho u_{ref}^2 d}. \tag{11}$$

where the drag and lift forces, respectively noted F_D and F_L, are computed according to the *momentum equation* given by Noca et al. in [31]. The Reynolds number ranges between 100 and 300 in this study.

As can be seen in Table 1, the results obtained at $\mathrm{Re} = 100$ and $\mathrm{Re} = 300$ show a good agreement with the numerical values given by [29]. A more detailed comparison is performed at $\mathrm{Re} = 200$ and the related results are reported in Fig. 2. Concerning in particular drag and lift coefficients, one can see from the left picture in this figure that our results coincide very well with those of [29]. Indeed we find $\bar{c_D} = 1.85 \pm 0.15$, $\bar{c_L} = 0 \pm 0.53$ and $S_t = 0.230$ to be compared with $\bar{c_D} = 1.85 \pm 0.12$, $\bar{c_L} = 0 \pm 0.50$ and $S_t = 0.215$ in [29]. The right hand side picture of Fig. 2 gives a comparison of the normalized near-wake length L with the numerical results of [29] and the experimental data of [30]. The near-wake length is defined as the x-coordinate of the point located on the centerline in the x-direction where the streamwise component of the velocity vanishes. Again, our results agree rather well with the literature.

We complete this validation study by investigating the circular cylinder benchmark for which references addressing higher Reynolds numbers can be found in the literature. The Reynolds numbers considered in this part are the one we selected to perform the passive control study, that is to say $\mathrm{Re} = 550$ (transitional regime) and $\mathrm{Re} = 3000$ (highly transitional regime). The early-time evolution of the drag coefficient for both regime is reported in Fig. 3 and one can see that the results are in excellent agreement with the considered references.

	Re = 100		Re = 300	
Authors	$\bar{c_D}$	S_t	$\bar{c_D}$	S_t
Farhadi et al. [29]	1.73	0.180	1.955	0.22
Present method	1.70	0.192	1.90	0.24

Table 1. Comparison of mean drag coefficient ($\bar{c_D}$) and Strouhal number (S_t) for flow past a semi-circular cylinder at Re=100 and Re=300.

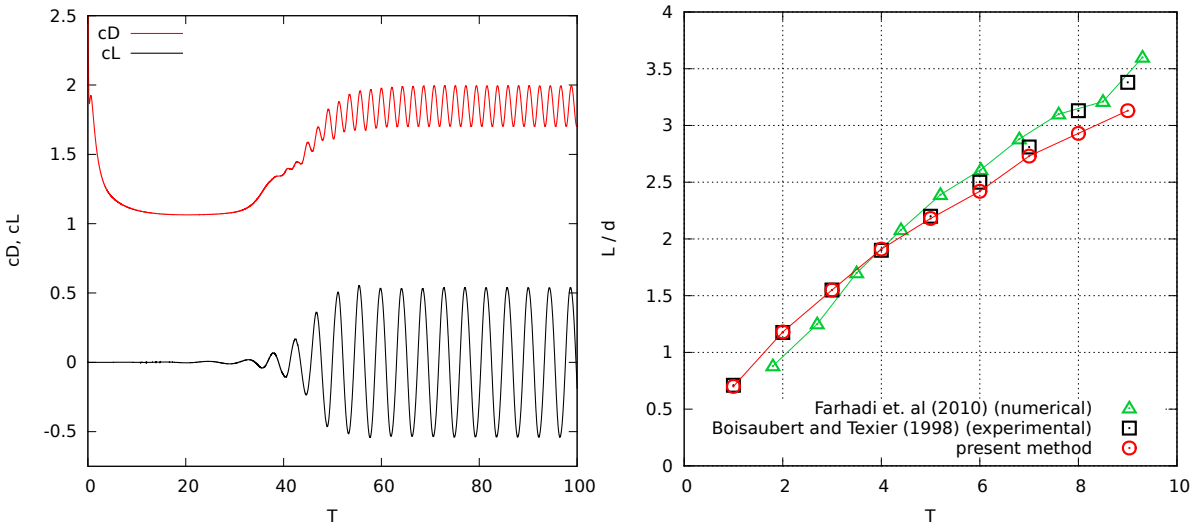

Fig. 2. (Left) Drag and lift evolution for flow past a semi-circular cylinder at Re=200. (Right) Normalized near-wake length L/d of a semi-circular cylinder at Re=200: comparison with numerical results [29] (green triangles) and experimental data [30] (black squares).

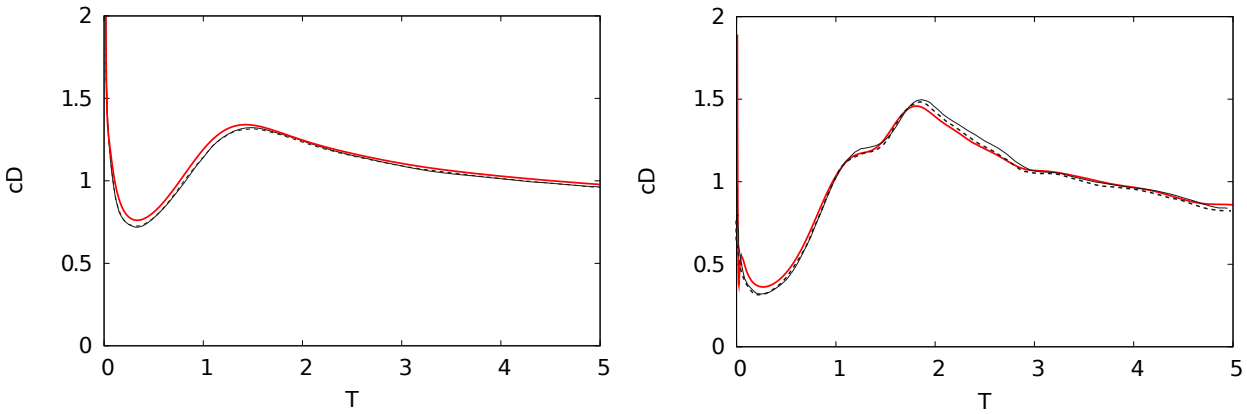

(a) Re=550 (b) Re=3000

Fig. 3. Drag evolution for flow past a circular cylinder at Re=550 and Re=3000. Comparisons of present method (solid red line) with Koumoutsakos & Leonard [16] (dashed line) and Ploumhans & Winckelmans [32] (solid black line).

5.2 Grid convergence

We perform herein a grid convergence study of the vortex penalization method for flow past a solid semi-circular cylinder at Re $= 550$ and Re $= 3000$. This grid convergence is carried out on three grid levels. For Re $= 550$ the three consecutive mesh sizes are: $h = 0.01$, $h = 0.005$ and $h = 0.0025$ in the computational domain $D = [-4,\ 8] \times [-5,\ 5]$. For Re $= 3000$, as the boundary layer is thinner, we perform the convergence study with three finer mesh sizes, respectively $h = 0.005$, $h = 0.0025$ and $h = 0.00125$. The simulations are carried out in a smaller domain $D = [-2.5,\ 5] \times [-3,\ 3]$ in order to reduce the computational cost induced by the finest grid. The results reported in Table 2, give the mean values of drag and enstrophy. For Re $= 550$, the results on the two finest consecutive grids are very close (Table 2). We can consider that the grid convergence is achieved and the adopted grid size for the further flow control simulations is $h = 0.005$ with $\Delta t = 0.0025$. For Re $= 3000$ the grid convergence is achieved with $h = 0.0025$ and $h = 0.00125$. The corresponding studies will thus be performed using $h = 0.0025$ as the grid size and $\Delta t = 0.002$ as the time step. Let us emphasize the interest of the vortex methods which enables here to handle a highly transitional regime using a relatively large time step compared to classical Eulerian methods.

	Re = 550		Re = 3000	
Grid	$\bar{c_D}$	$\bar{Z}$	$\bar{c_D}$	$\bar{Z}$
$h = 0.01$	1.49	122	-	-
$h = 0.005$	1.91	158	1.89	313
$h = 0.0025$	1.98	161	1.94	292
$h = 0.00125$	-	-	1.96	280

Table 2. Grid convergence study for flow past a semi-circular cylinder at Re=550 and Re=3000 through the mean values of drag coefficient ($\bar{c_D}$) and enstrophy ($\bar{Z}$).

6 Passive control

In this work, the vortex penalization method is applied to passive flow control around a two-dimensional semi-circular cylinder. The control is achieved covering this obstacle with a porous coating. The expected effect of a porous medium at the solid-fluid interface is to modify the vorticity generation of the boundary layer and the vortex shedding, and therefore to reduce drag forces and vortex induced vibrations improving the aerodynamic properties of the obstacle.

The subsequent flow control simulations are performed at transitional (Re = 550) and highly transitional regime (Re = 3000). As at these two regimes the flow is not turbulent, Direct Numerical Simulations (DNS) are performed to numerically solve Eq. 5. The semi-circular cylinder has a total dimensionless diameter of $d = 1$ including a porous layer of thickness τ, whose back wall is centered at $(x, y) = (0,\ 0)$ in the computational domain $D = [-4,\ 8] \times [-5,\ 5]$ depicted in Fig. 4.

In order to analyze the effects of the control approach we will compare velocity, vorticity and pressure fields as well as global flow quantities like the drag force (F_x) and the enstrophy (Z) which measures the dissipation effects in the flow and defined by $Z = \int_D |\omega|^2 \, \mathrm{d}\mathbf{x}$. Note that in this study we will consider the drag force instead of the drag coefficient since the computation formula of the latter involves the diameter d of the obstacle which includes the porous layer.

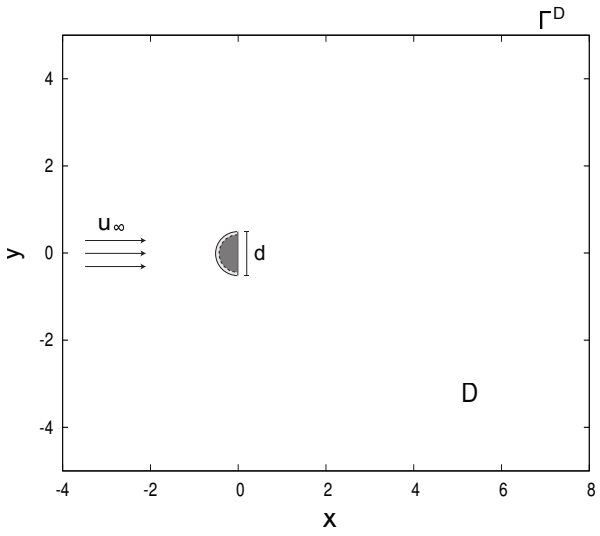

Fig. 4. Computational domain used for passive flow control.

6.1 Parametric study on penalization parameter λ for homogeneous porous layer

This section relies on the influence of the added porous layer permeability on the flow control behaviour and the efficiency of such a passive control. We perform a parametric study at Re = 550 and Re = 3000 considering four consecutive values of λ inside the porous coating, namely $\lambda = 1$ (high permeability), 10, 10^2, 10^3 (low permeability) and compare the results to the fluid case ($\lambda = 0$) and the uncontrolled case. The fluid case means a semi-cylinder including a porous layer with permeability $\lambda = 0$, which corresponds to a smaller semi-cylinder with diameter $d - 2\tau$. In this section, the thickness of the layer is set to $\tau = 10\% d = 0.1$ for each case (Fig. 5).

As can be seen in Fig. 6, which represents dimensionless time history of global flow quantities at Re = 550, setting $\lambda = 1$ inside the layer clearly appears as the best solution in terms of flow regularization. Indeed, the mean value of drag

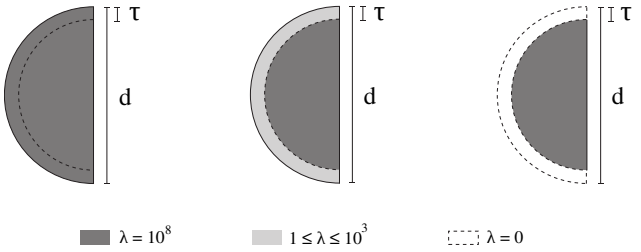

Fig. 5. (left) Uncontrolled case, (center) porous case, (right) fluid case.

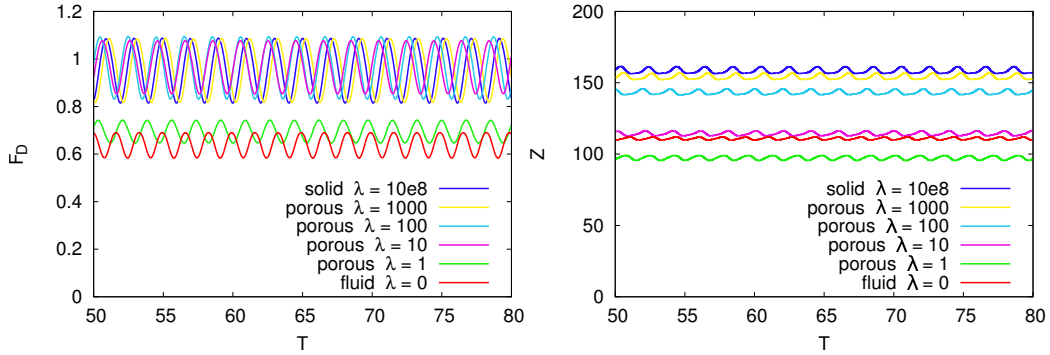

Fig. 6. Effects of various layer permeabilities on drag force (left) and enstrophy (right) for the flow past a semi-circular cylinder at Re=550.

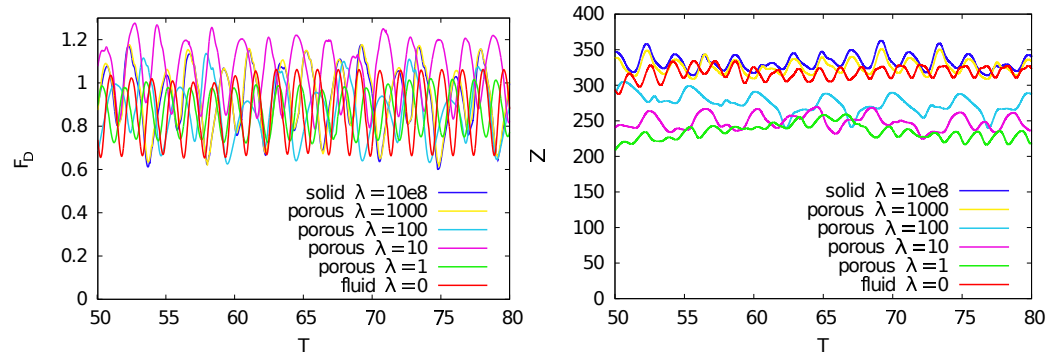

Fig. 7. Effects of various layer permeabilities on drag force (left) and enstrophy (right) for the flow past a semi-circular cylinder at Re=3000.

force (Fig. 6 (left)) reaches for $\lambda = 1$ an optimum value close to the one of the fluid case, showing a drag reduction of 27% compared to uncontrolled case. For all the other values of porous λ, the drag reduction effects are nearly nonexistent. Results of enstrophy evolution (Fig. 6 (right)) show a progressive reduction of the dissipation and the delay to transition with the decrease of λ values. Moreover, we note that the result with $\lambda = 1$ is even better than the one of fluid case and represents an improvement of nearly 40% compared to uncontrolled case.

At $Re = 3000$ the best solution for global flow regularization is also achieved setting $\lambda = 1$ inside the porous coating. This configuration leads to a drag and enstrophy reduction of respectively 6% and 30% compared to the uncontrolled case and one can see on Fig. 7 the important decrease of the signals amplitude. In terms of control effects, the main difference one can notice here in comparison to the parameter study performed at $Re = 550$ concerns the flow behaviour observed when $\lambda = 10$ inside the layer. Contrary to the other λ values, the flow field obtained with the latter is non-periodic (Fig. 7). This flow irregularity impacts the mean drag value, which is increased of about 15% compared to the uncontrolled case. We can summarize that except for a very permeable porous layer ($\lambda = 1$), a porous coating covering the whole face of the semi-cylinder is not a convenient tool to reduce the drag. It is only useful to regularize the wake. The problem seems due to the separation point that is located inside the porous medium.

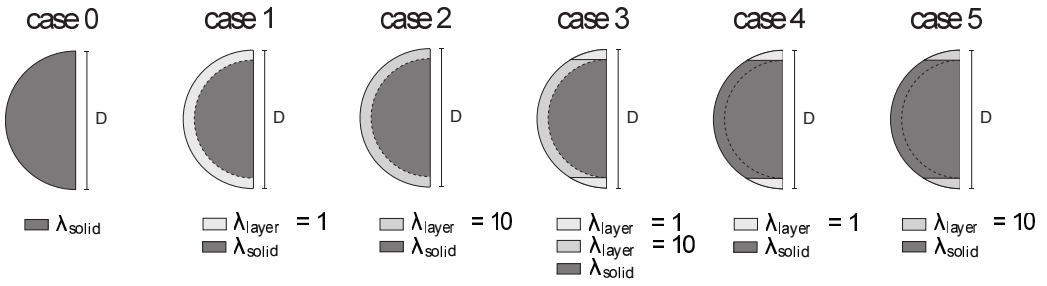

Fig. 8. Cases 1 to 5 corresponding to different porous layer configurations. Case 0 depicts the uncontrolled case.

6.2 Influence of the porous layer configuration on flow control efficiency

This section aims to determine control devices which are both efficient in terms of flow regularization and easy to set up in terms of manufacturing constraints. According to the parametric study presented in the previous section, setting the λ function to 1 in the surrounding sheath enables important flow reduction effects. Nevertheless, this configuration turns out to be industrially difficult to implement because of the very high permeability of the added layer. On the contrary, intermediate permeabilities obtained fixing $\lambda = 10$ inside the porous interface are easier to handle but show quite poor improvements in terms of flow control, as reported in the parametric study. Taking into account these observations, we propose to compare the six test cases depicted in Fig. 8. Case 0 refers to the uncontrolled case, cases 1 and 2 correspond to homogeneous layer cases where λ respectively equals 1 and 10, and cases 3 to 5 refer to heterogeneous cases where the porous layer is split in two regions with different permeabilities. The simulations were performed taking the same numerical parameters as the one used for the parametric study. In a first place, the thickness of the layer is kept to $10\%d = 0.1$. The asymptotic mean values of global flow quantities and the time averaged vorticity, velocity and pressure fields are respectively given for each case in Table 3, and Figures 9 to 14.

First of all, the results reported here give further information concerning cases 1 and 2. They confirm that case 2 is not competitive as it increases the drag for $\mathrm{Re} = 550$ and $\mathrm{Re} = 3000$ compared to uncontrolled case (Table 3). They also highlight the efficiency of case 1 which induces a significant reduction of drag force (-27% and -6%) and enstrophy (-38% and -29%). These quantitative results are confirmed by the mean vorticity and velocity fields showing the smoothing of wake dynamics generated by the presence of the highly permeable layer. Indeed, the near wake structures are smaller and the back recirculation zone is sharply reduced (Figs. 9 and 12), implying an increase of downstream pressure (Figs. 11 and 14) and thus a reduction of drag forces. Finally, the vortices swirl with lower velocity and for $\mathrm{Re} = 3000$ the mean wake becomes axisymmetric (Fig 10 and 13).

Let us now focus on the heterogeneous devices. For both regime, the case 3 shows benefits which are very comparable to those of case 1. We note that the only difference with case 2 is the presence of highly permeable poles in the layer. This change allows an eddy detachment from the wall with larger shedding structures, diminishing the back wall recirculation zone (Figs. 9 and 12) and a drastic increase of downstream near wall pressure for the $\mathrm{Re} = 550$ regime (Fig. 11). The case 3 also enables to significantly regularize the flow in the wake with lower velocities, using highly permeable material introduced in both edges of the body (Figs. 10 and 13). Nevertheless, the mix of high and intermediate permeabilities induces difficulties to industrially build such a coating and has no practical interest.

The cases 4 and 5 are more interesting for industrial applications. For these cases, the front part of the coating is no more permeable, but completely solid and porous layers are only placed in the two edge parts of the obstacle, which makes the practical implementation much more easier. Here, for both Reynolds numbers 550 and 3000, the enstrophy and the drag force undergo a tremendous decrease except for the case 5 at $\mathrm{Re} = 3000$ where the drag force drop is limited to 7% because of the lower permeability of the porous layer (Table 3). Figures 9 to 14 confirm these results. They show a significant reduction of the mean velocity of the flow in the near and far wake (Figs. 10 and 13) as well as the decrease of the crosswise dimension of the two counter-rotating vortical structures at the back of the obstacle (Figs. 9 and 12). Also, the near wall pressure values (Figs. 11 and 14), especially for the case 4, are sensibly diminished which is in agreement with drag results. These results emphasize the importance of the positions of the permeable zones that should be chosen considering the flow separation phenomenon as it preferably should not occur inside the porous material. Finally, test case 5, made of intermediate permeabilities on both edges of the body, corresponds to a more realistic device compared to the case 4 with very permeable edges. It can be considered as a suitable and affordable device for flow control.

6.3 Influence of the porous layer thickness τ on flow control efficiency

In the previous sections, the control effects were studied for different configurations using a constant porous layer thickness $\tau = 10\%d$. In this section, the effect of the thickness for different configurations will be investigated, and a special

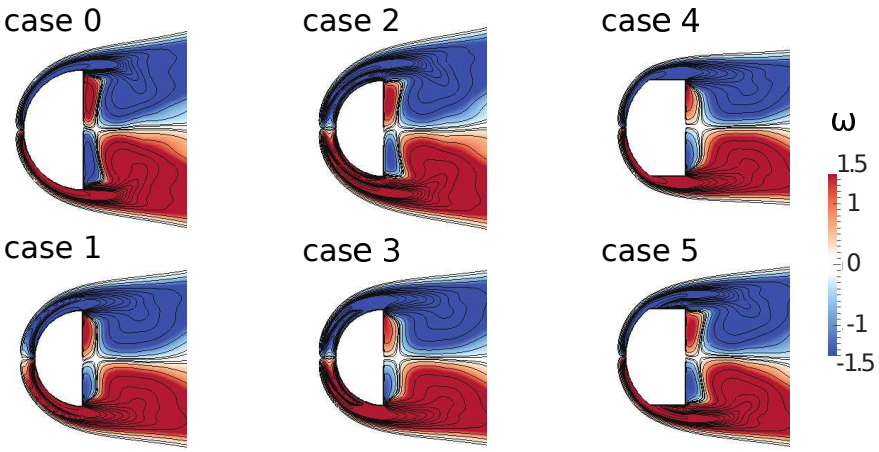

Fig. 9. Zoom of the mean vorticity fields and isolines for the flow past a semi-circular cylinder at Re=550 with $\tau = 10\%d$.

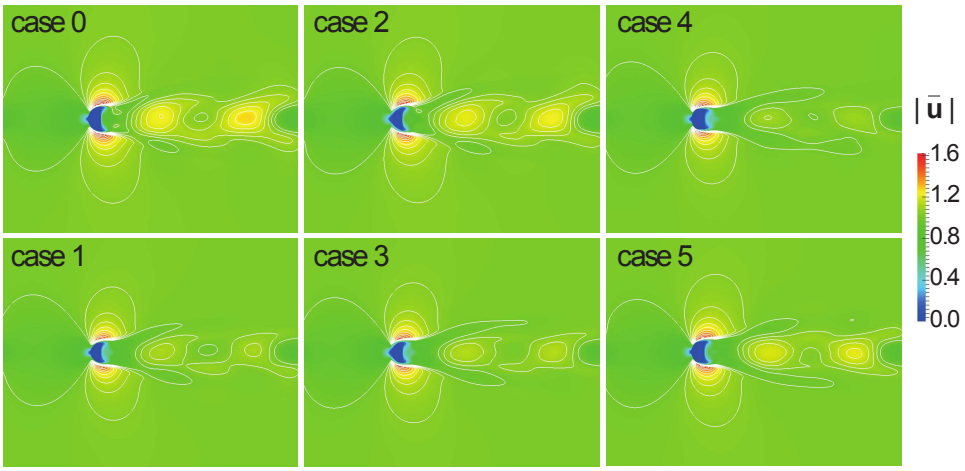

Fig. 10. Fields and isolines of mean velocity magnitude for the flow past a semi-circular cylinder at Re=550 with $\tau = 10\%d$.

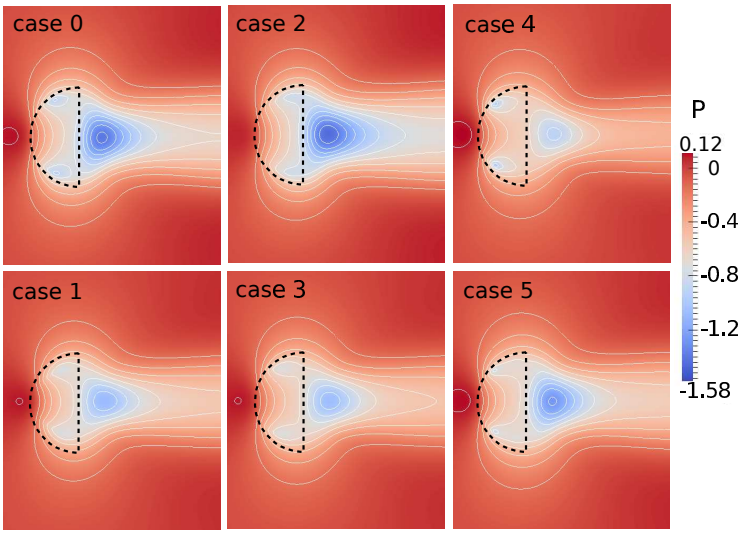

Fig. 11. Zoom of the mean pressure fields and isolines for the flow past a semi-circular cylinder at Re=550 with $\tau = 10\%d$.

	Re = 550		Re = 3000	
$\tau = 10\%d$	F_x	Enstrophy	F_x	Enstrophy
case 0 (uncontrolled case)	0.957	158.4	0.926	334.2
case 1	0.695 (-27%)	97.5 (-38%)	0.870 (-6%)	236.7 (-29%)
case 2	0.970 (+1.4%)	114.4 (-28%)	1.054 (+14%)	248.8 (-26%)
case 3	0.668 (-30%)	87.4 (-45%)	0.922 (-0.4%)	223.2 (-33%)
case 4	0.551 (-40%)	110.2 (-30%)	0.737 (-20%)	270.6 (-19%)
case 5	0.738 (-23%)	125.2 (-21%)	0.860 (-7%)	281.3 (-16%)

Table 3. Reduction effects brought by the different porous layer configurations in comparison to the uncontrolled case at Re=550 and Re=3000 with $\tau = 10\%d$.

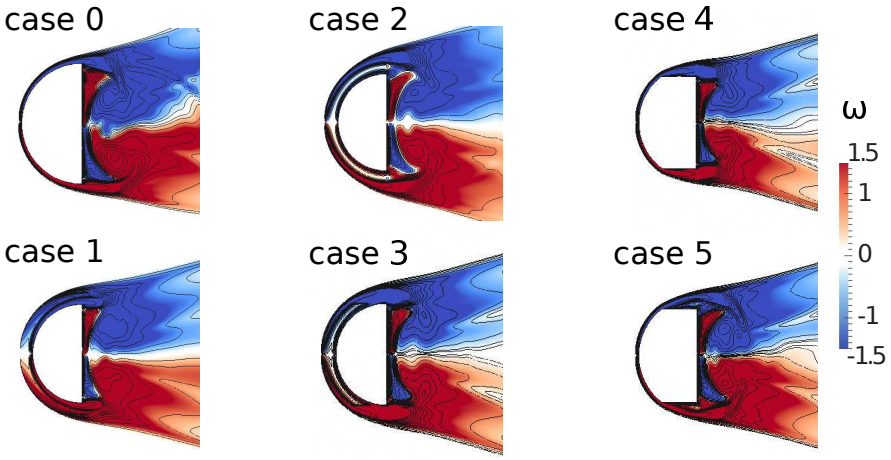

Fig. 12. Zoom of the mean vorticity fields and isolines for the flow past a semi-circular cylinder at Re=3000 with $\tau = 10\%d$.

focus will be made for thin layers in order to reduce the use of porous materials and to find out a compromise between practical constraints and control efficiency. The same test cases (Fig. 5) are now considered setting the thickness of the layer to $\tau = 5\%d = 0.05$ and to $\tau = 2.5\%d = 0.025$. Table 4 and 5 respectively report the control performances in terms of mean global flow quantities, obtained for each case with $\tau = 5\%d$ and $\tau = 2.5\%d$.

For both regimes Re = 550 and Re = 3000, when comparing Tables 3, 4 and 5, a slight decrease of control effects is observed. This can be explained looking at the mean profiles of the streamwise component of the velocity, u at $x = -0.05$ plotted in Figures 16 and 18. These profiles show higher acceleration of the flow field inside the layer when its thickness drops, inducing higher velocity gradients in the vicinity of the solid-porous-fluid interface and make the vortex shedding occurring earlier, resulting in a little reduction of beneficial effects. Nevertheless, the decrease of drag and enstrophy remains important for thinner porous layers, which enables to consider them as interesting passive control devices. Also, as shown in Figure 15, a direct correlation between the drag reduction and the back wall pressure forces is noticeable at Re = 550: when drag drops the back wall pressure rises. This fact is more unstable for the Re = 3000 as the flow is highly transitional (figure 17). Furthermore, for the later flow regime, decreasing the layer thickness in cases 1, 2 and 3 deteriorate the drag performances as the flow velocity slows down inside the thin layer around the body and the skin friction effects increase the drag forces.

Now let focus on cases 4 and 5. One can observe in Tables 3, 4, 5 that case 4 remains the best control device in terms of drag reduction, regardless of the coating thickness and Reynolds number. As discussed in the previous section, this is due to the fact that the front part of the obstacle is completely solid and that highly permeable zones are precisely located in the vicinity of the boundary layer separation point where the shedding starts. On one hand this configuration enables to efficiently decrease the shedding velocity of the flow damped by porous edges (see Figures 16 and 18), on the other hand it prevents from the negative effect of porous coatings implemented in the front part of the semi-cylinder. For both cases 4 and 5, Figs. 16 and 18 show for all thicknesses a uniform and relatively low acceleration of the flow field inside the layer. As the case 5 is the most practical benchmark (more than all other cases as the porous materials with moderate permeability and edge locations are easier to handle for the manufacturing of a real device), its control efficiency is important to be studied

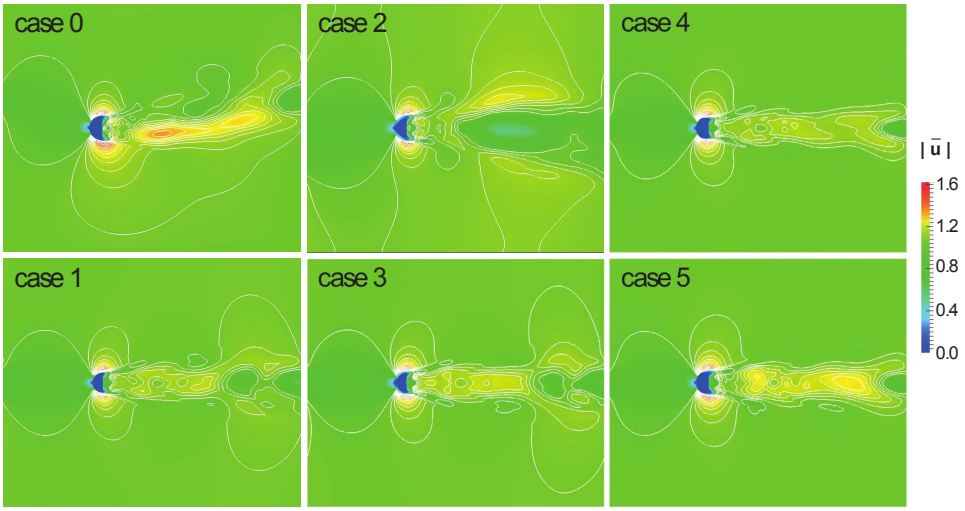

Fig. 13. Fields and isolines of mean velocity magnitude for the flow past a semi-circular cylinder at Re=3000 with $\tau = 10\%d$.

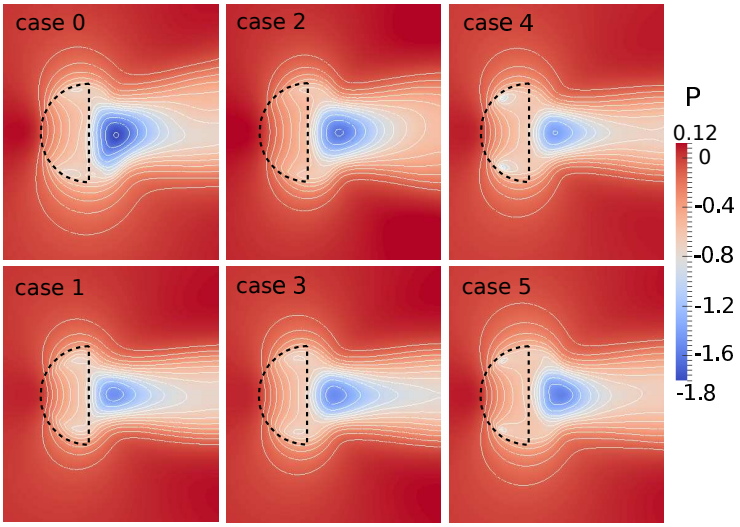

Fig. 14. Zoom of the mean pressure fields and isolines for the flow past a semi-circular cylinder at Re=3000 with $\tau = 10\%d$.

for all thicknesses: the control efficiency of case 5 is inversely proportional to the porous layer thickness τ. Indeed, in Tables 3, 4 and 5 one can clearly see that with $\tau = 2.5\%d$ the drag reduction achieved with case 5, leads to -15% for $\mathrm{Re} = 550$ and -10.5% for $\mathrm{Re} = 3000$. This promising assessment seems to be due to the fact that the flow resistance inside a thin porous layer is less than a thick layer but the shedding is still well tuned thanks to the position of porous coatings in the body corners.

	Re = 550		Re = 3000	
$\tau = 5\%d$	F_x	Enstrophy	F_x	Enstrophy
case 0 (uncontrolled case)	0.957	158.4	0.926	334.2
case 1	0.774 (-19%)	123.7 (-22%)	0.999 (+8%)	285.2 (-15%)
case 2	0.914 (-4%)	123.5 (-22%)	0.979 (+6%)	253.7 (-24%)
case 3	0.751 (-22%)	110.4 (-30%)	0.947 (+2%)	247.6 (-26%)
case 4	0.618 (-35%)	127.6 (-19%)	0.819 (-12%)	326.2 (-2%)
case 5	0.753 (-21%)	135.4 (-15%)	0.847 (-8.5%)	312.3 (-6.5%)

Table 4. Reduction effects brought by the different porous layer configurations in comparison to the uncontrolled case at Re=550 and Re=3000 with $\tau = 5\%d$.

	Re = 550		Re = 3000	
$\tau = 2.5\%d$	F_x	Enstrophy	F_x	Enstrophy
case 0 (uncontrolled case)	0.957	158.4	0.926	334.2
case 1	0.821 (-14%)	139.3 (-12%)	1.011 (+9%)	318.4 (-5%)
case 2	0.879 (-8%)	134.5 (-15%)	1.018 (+10%)	283.7 (-15%)
case 3	0.824 (-14%)	129.6 (-18%)	0.929 (+0.4%)	271.1 (-19%)
case 4	0.768 (-20%)	140.2 (-11%)	0.806 (-13%)	331.4 (-0.8%)
case 5	0.810 (-15%)	143.4 (-10%)	0.828 (-10.5%)	320.6 (-4%)

Table 5. Reduction effects brought by the different porous layer configurations in comparison to the uncontrolled case at Re=550 and Re=3000 with $\tau = 2.5\%d$.

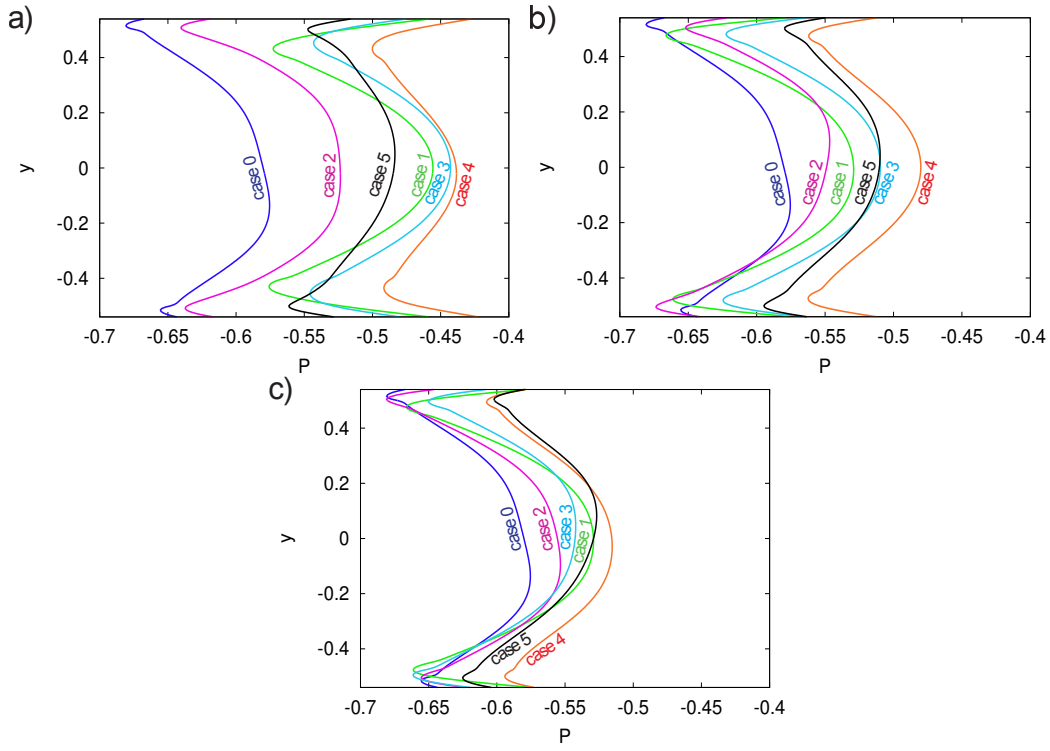

Fig. 15. Mean pressure profiles at the rear end of the body with a) $\tau = 10\%d$, b) $\tau = 5\%d$ and c) $\tau = 2.5\%d$ at Re=550.

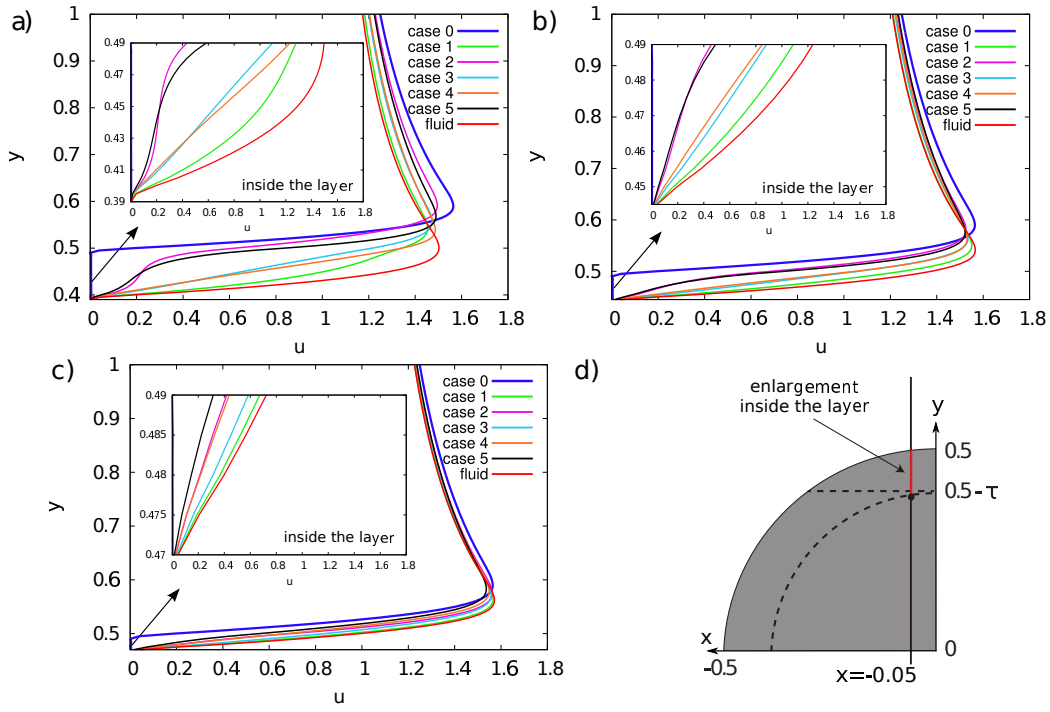

Fig. 16. Mean profiles of the streamwise component of the velocity u at $x = -0.05$ with a) $\tau = 10\%d$, b) $\tau = 5\%d$ and c) $\tau = 2.5\%d$ at Re=550. d) Pattern of profile configuration at $x = -0.05$ showing the location of the profiles enlargement inside the layer proposed in a), b) and c).

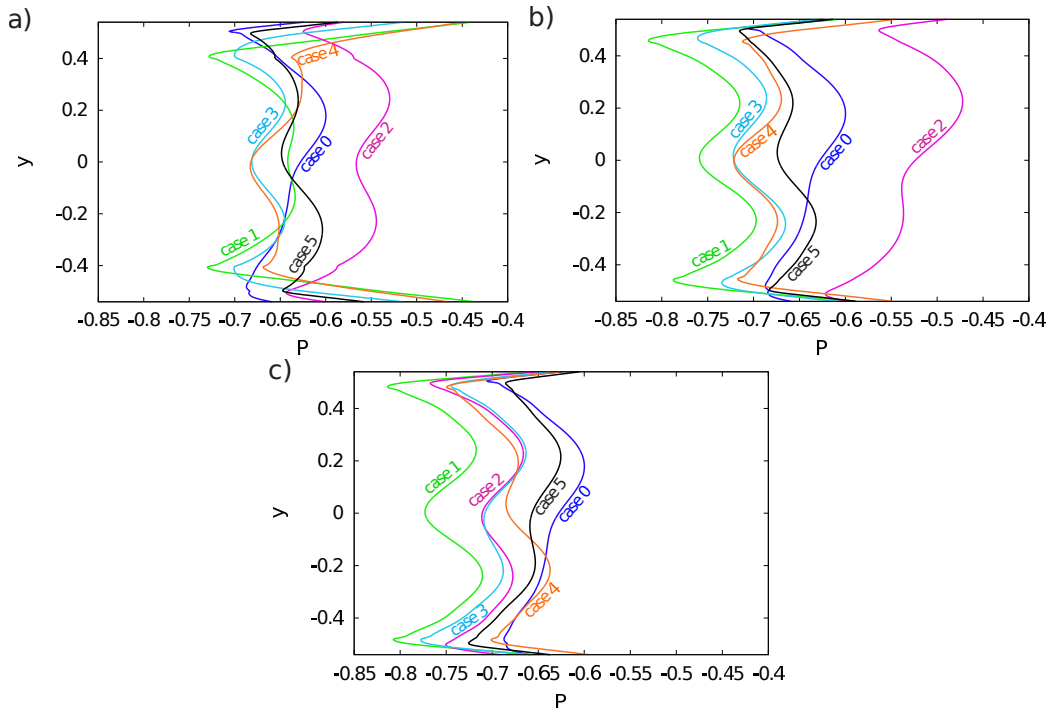

Fig. 17. Mean pressure profiles at the rear end of the body with a) $\tau = 10\%d$, b) $\tau = 5\%d$ and c) $\tau = 2.5\%d$ at Re=3000.

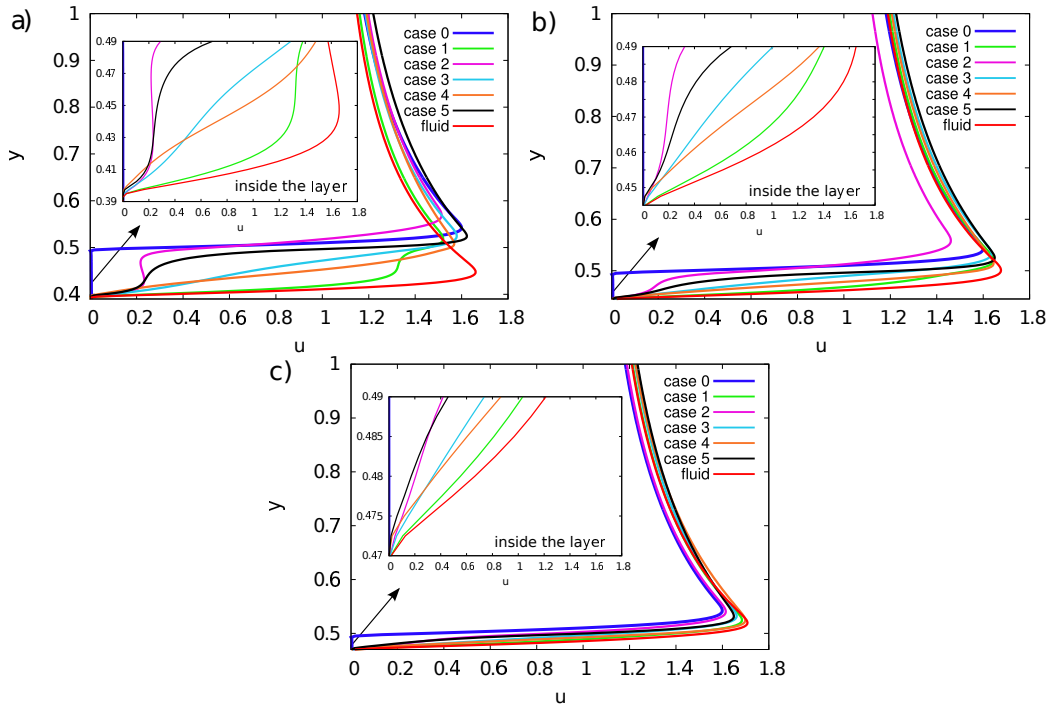

Fig. 18. Mean profiles of the streamwise component of the velocity u at $x = -0.05$ with a) $\tau = 10\%d$, b) $\tau = 5\%d$ and c) $\tau = 2.5\%d$ at Re=3000 (cf Fig. 16 d) for profiles location.)

7 CONCLUSION

In this work a passive control technique with porous coatings was implemented around a semi-circular cylinder in order to regularize flow and reduce drag forces for laminar and transitional flows. The direct numerical simulations were performed using vortex-penalization method which allows to compute simultaneously the three fluid-porous-solid media. In the numerical study, the effect of the porous layer permeability on the control results was first analyzed. Highly permeable media were more efficient, as expected. Then, several configurations of porous devices were compared. The results showed that introducing porous layers only at the top and bottom of the solid body permits to better manipulate the vortex shedding and to achieve relevant control performances. A further study on the influence of the porous layer thickness on the control efficiency was performed. It showed that a thin layer with intermediate permeability, introduced in both edges of the back wall, generates a significant drag reduction. As the ultimate target of this work is the drag reduction related to side mirrors, this type of configuration would be easy to implement industrially and at low cost, since it only consists in adding an intermediate-porous ring on the edge wall of the mirror. Although the present work needs to be complemented by three-dimensional studies to confirm the quantitative control trends that were observed in the 2D experiments, it thus opens interesting perspectives towards efficient drag control devices.

References

[1] Rouméas, M., Gilliéron, P., and Kourta, A., 2009. "Analysis and Control of the Near-Wake Flow Over a Square-Back Geometry". *Computers & Fluids,* **38**, pp. 60–70.

[2] Bruneau, C. H., Creusé, E., Depeyras, D., Gilliéron, P., and Mortazavi, I., 2010. "Coupling Active and Passive Techniques to Control the Flow Past the Square Back Ahmed Body". *Computers & Fluids,* **38**, pp. 1875–1892.

[3] Bruneau, C. H., and Mortazavi, I., 2004. "Passive Control of the Flow Around a Square Cylinder Using Porous Media". *International Journal for Numerical Methods in Fluids,* **46**, pp. 415–433.

[4] Bruneau, C. H., and Mortazavi, I., 2006. "Control of Vortex Shedding Around a Pipe Section Using a Porous Sheat". *Journal of Offshore and Polar Engineering,* **16**.

[5] Bruneau, C. H., Gilliéron, P., and Mortazavi, I., 2007. "Flow Manipulation Around the Ahmed Body With a Rear Window Using Passive Strategies". *Comptes Rendus Mecanique,* **335**.

[6] Bruneau, C. H., and Mortazavi, I., 2008. "Numerical Modelling and Passive Flow Control Using Porous Media". *Computers & Fluids,* **37**, pp. 488–498.

[7] Bruneau, C. H., Gilliéron, P., and Mortazavi, I., 2008. "Passive Control Around a Two-Dimensional Square Back Ahmed Body Using Porous Media". *Journal of Fluids Engineering,* **130**.

[8] Carbou, G., 2008. "Brinkmann Model and Double Penalization Method for the Flow Around a Porous Thin Layer". *Journal of Mathematical Fluid Mechanics,* **10**, pp. 126–158.

[9] Angot, P., Bruneau, C. H., and Fabrie, P., 1999. "A Penalization Method to Take Into Account Obstacles in Incompressible Viscous Flows". *Numerische Mathematik,* **81**, pp. 497–520.

[10] Coquerelle, M., and Cottet, G. H., 2008. "A Vortex Level Set Method for the Two-Way Coupling of an Incompressible Fluid with Collinding Rigid Bodies". *Journal of Computational Physics,* **227**, pp. 9121–9137.

[11] Rossinelli, D., M.Bergdorf, Cottet, G.-H., and Koumoutsakos, P., 2010. "Gpu accelerated simulations of bluff body flows using vortex particle methods". *Journal of Computational Physics*.

[12] Cottet, G. H., Gallizio, F., Magni, A., and Mortazavi, I., 2011. "A Vortex Penalization Method for Flows with Moving Immersed Obstacles". In Proceedings of ASME-JSME-KSME Joint Fluids Engineering Conference, July, 2011, ASME, pp. 3703–3708. Paper number AJK2011-20015.

[13] Gazzola, M., van Rees, W., and Koumoutsakos, P., 2012. "C-start: optimal start of larval fish". *Journal of Fluid Mechanics,* **698**, pp. 5–18.

[14] van Rees, W., Gazzola, M., and Koumoutsakos, P., 2013. "Optimal shapes for anguilliform swimmers at intermediate reynolds numbers". *Journal of Fluid Mechanics,* **722**.

[15] Cottet, G. H., and Koumoutsakos, P. D., 2000. *Vortex Methods - Theory and Practice*. Cambridge University Press.

[16] Koumoutsakos, P., and Leonard, A., 1995. "High-resolution simulations of the flow around an impulsively started cylinder using vortex methods". *Journal of Fluid Mechanics,* **296**, pp. 1–38.

[17] Cottet, G. H., and Maitre, E., 2004. "A Level-Set Formulation of Immersed Boundary Methods for Fluid-Structure Interaction Problems". *Comptes Rendus de l'Acadmie des Sciences de Paris,* **338**, pp. 51–56.

[18] Chorin, A. J., 1974. "Numerical Study of Slighly Viscous Flow". *Journal of Fluid Mechanics,* **57**, pp. 785–796.

[19] Ghoniem, A. F., and Gagnon, Y., 1987. "Vortex Simulation of Laminar Recirculating Flows". *Journal of Computational Physics,* **68**, pp. 346–377.

[20] Sethian, J. A., and Ghoniem, A. F., 1988. "Validation Study of Vortex Methods". *Journal of Computational Physics,* **74**, pp. 283–317.

[21] Creusé, E., Giovannini, A., and Mortazavi, I., 2009. "Vortex Simulation of Active Control Strategies for Transitional Backward-Facing Step Flows". *Computers & Fluids,* **38**, pp. 1348–1360.

[22] Monaghan, J. J., 1985. "Extrapolating b-Splines for Interpolation". *Journal of Computational Physics,* **60**, pp. 253–262.
[23] Chatelain, P., and Koumoutsakos, P., 2010. "A Fourier-Based Elliptic Solver For Vortical Flows With Periodic and Unbounded Directions". *Journal of Computational Physics,* **229**, pp. 2425–31.
[24] Cottet, G. H., Gallizio, F., Magni, A., and Mortazavi, I., 2010. "A Vortex Immersed Boundary Method for Bluff Body Flows". In Proceedings of 3rd Joint US-European ASME Fluids Engineering Summer Metting, August, 2010, ASME, pp. 2409–2414. Paper number FEDSM-ICNMM2010-30787.
[25] Beavers, G. D., and Joseph, D. D., 1967. "Boundary Conditons at a Naturally Permeable Wall". *Journal of Fluid Mechanics,* **30**, pp. 197–207.
[26] Breugem, W. P., Boersma, B. J., and Uittenbogaard, R. E., 2005. "The Laminar Boundary Layer Over a Permeable Wall". *Transport in Porous Media,* **59**, pp. 267–300.
[27] Hanspal, N. S., Waghode, A. N., Nassehi, V., and Wakeman, R. J., 2006. "Numerical Analysis of Coupled Stokes/Darcy Flows in Industrial Filtrations". *Transport in Porous Media,* **64**, pp. 73–101.
[28] Nield, D. A., and Bejan, A., 1999. *Convection in Porous Media*. Springer.
[29] Farhadi, M., Sedighi, K., and Fattahi, E., 2010. "Effect of a Splitter Plate on Flow Over a Semi-Circular Cylinder". In Proceedings of the Institution of Mechanical Engineers, Part G: Journal of Aerospace Engineering, pp. 224–321.
[30] Boisaubert, N., and Texier, A., 1998. "Effect of a Splitter Plate on the Near-Wake Development of a Semi-Circular Cylinder.". *Experimental Thermal and Fluid Science,* **16**, pp. 100–111.
[31] Noca, F., Shiels, D., and Jeon, D., 1999. "A Comparison of Methods for Evaluating Time-Dependent Fluid Dynamic Forces on Bodies, Using Only Velocity Fields and Their Derivatives". *Journal of Fluids and Structures,* **13**, pp. 551–578.
[32] Ploumhans, P., and Winckelmans, G. S., 2000. "Vortex methods for high-resolution simulations of viscous flow past bluff bodies of general geometry". pp. 354–406.

Conception et mise en oeuvre d'une méthode vortex hybride avec pénalisation pour des écoulements en milieux solides-fluides-poreux : application au contrôle passif d'écoulements

Résumé :
Dans cette thèse nous mettons en œuvre une méthode vortex hybride pénalisée (HVP) afin de simuler des écoulements incompressibles autour de corps non profilés dans des milieux complexes solides-fluides-poreux. Avec cette approche particulaire hybride, le phénomène de convection est modélisé à l'aide d'une méthode vortex afin de bénéficier du caractère peu diffusif et naturel des méthodes particulaires. Un remaillage des particules est alors réalisé systématiquement sur une grille cartésienne sous-jacente afin d'éviter les phénomènes de distorsion. D'autre part, les effets diffusifs et d'étirement ainsi que le calcul de la vitesse sont traités sur la grille cartésienne, à l'aide de schémas eulériens. Le traitement des conditions de bords aux parois de l'obstacle est effectué à l'aide d'une technique de pénalisation, particulièrement bien adaptée au traitement de milieux solides-fluides-poreux.

Cette méthode HVP est appliquée au contrôle passif d'écoulement. Cette étude de contrôle est effectuée respectivement en 2D et en 3D autour d'un demi-cylindre et d'un hémisphère par l'ajout d'un revêtement poreux à la surface de l'obstacle. La présence de cette couche poreuse modifiant la nature des conditions aux interfaces, permet de régulariser l'écoulement global et de diminuer la traînée aérodynamique de l'obstacle contrôlé. A travers des études paramétriques sur la perméabilité, l'épaisseur et la position du revêtement poreux, ce travail vise à identifier des dispositifs de contrôles efficaces pour des écoulements autour d'obstacles comme des rétroviseurs automobiles.

Mots clés : Méthode vortex hybride, méthode de pénalisation, contrôle passif d'écoulements, milieux poreux.

Conception and implementation of a hybrid vortex penalization method for solid-fluid-porous media: application to the passive control of incompressible flows

Abstract :
In this work we use a hybrid vortex penalization method (HVP) to simulate incompressible flows past bluff bodies in complex solid-fluid-porous media. In this hybrid particle approach, the advection phenomenon is modeled through a vortex method in order to benefit from the natural description of the flow supplied by particle methods and their low numerical diffusion features. A particle remeshing is performed systematically on an underlying Cartesian grid in order to prevent distortion phenomena. On the other hand, the viscous and stretching effects as well as the velocity calculation are discretized on the mesh through Eulerian schemes. Finally, the treatment of boundary conditions is handled with a penalization method that is well suited for the treatment of solid-fluid-porous media.

The HVP method is applied to passive flow control. This flow control study is realized past a 2D semi-circular cylinder and a 3D hemisphere by adding a porous layer on the surface of the body. The presence of such porous layer modifies the characteristics of the conditions at the interfaces and leads to a regularization of the wake and to a decrease of the aerodynamic drag of the controlled obstacle. Through parametric studies on the permeability, the thickness and the position of the porous coating, this works aims to identify efficient control devices for flows around obstacles like the rear-view mirrors of a ground vehicle.

Keywords : Hybrid vortex method, penalization method, passive flow control, porous media.